Fluorescence of PDT Photosensitizers for Quantitative Cancer Diagnosis and Treatment Monitoring

FLUORESCENCE OF PDT PHOTOSENSITIZERS FOR QUANTITATIVE CANCER DIAGNOSIS AND TREATMENT MONITORING

By

SHU-CHI YEH, B.Sc.

A Thesis

Submitted to the School of Graduate Studies

In Partial Fulfilment of the Requirements for the Degree

Doctor of Philosophy

McMaster University

Doctor of Philosophy (2015) McMaster University

School of Biomedical Engineering Hamilton, Ontario

TITLE: Fluorescence of PDT Photosensitizers for Quantitative Cancer Diagnosis and Treatment Monitoring

AUTHUR: Shu-Chi Yeh, B.Sc., Chung-Shan Medical University

SUPERVISOR: Qiyin Fang, Ph.D.

NUMBER OF PAGES: xxiii, 179

Abstract

Photodynamic therapy (PDT) has been considered a favorable approach in certain oncology applications for its little invasiveness and better targeting specificity compared to conventional therapies. In PDT, localized photosensitizers can be activated by light to produce cytotoxic oxygen species. However, the prescribed drug and light doses do not provide satisfying outcomes as the PDT efficacy relies strongly on the interplay between localized dose factors. Therefore, the fluorescence emission from active photosensitizers has been investigated extensively for real-time PDT dosimetry.

This dissertation focuses on characterizing fluorescence properties of two photosensitizers, Photofrin® and PpIX, in cellular models and discusses about their potential clinical applications. First, we introduce time-resolve fluorescence (TRF) of photosensitizers as a potential tool in PDT dosimetry. TRF acquires fluorescence decay profiles and it is sensitive to drug-microenvironment interactions that occur frequently in PDT. Therefore, it provides complementary information in addition to fluorescence spectra that could be subject to intensity artifacts. In this dissertation, we review TRF studies on PDT photosensitizers, and quantify TRF parameters of Photofrin® at various subcellular locations. Moreover, analytical solutions are developed to correct distorted TRF measurements from commonly used time-domain data acquisition.

Second, we report a new concept – integrated detection and treatment of Barrett's Esophagus (BE). BE is a pre-cancerous lesion considered as a major risk factor in developing esophageal cancers. However, early intervention of BE has remained a challenging issue as tissue biopsy introduces significant sampling errors and the separate procedures between diagnosis and treatment add relocation errors. We proposed to use PpIX fluorescence to highlight morphological features at the cellular level for quantitative classification, followed by well-characterized treatment. Current proof-of-concept studies were performed separately, whilst the detection and treatment can be integrated using confocal endomicroscopy technology. Overall, these studies examine the potential benefits provided by fluorescence of photosensitizers for cancer diagnosis and treatment monitoring.

.

Acknowledgments

I am very grateful to my Ph.D. supervisor, Dr. Qiyin Fang, for his patience in teaching, his thoughtful advices, and valuable learning opportunities he has provided throughout my studying period. I would also like to thank my supervising committee members, Dr. Michael S. Patterson, Dr. Kevin R, Diamond, and Dr. Joseph E. Hayward for their helpful discussions in each project meeting, and for their time and effort on guiding me and editing the manuscripts. In addition, I would like to express my thanks to Dr. David Andrews and Dr. Tony Collins, who had provided me with valuable advices when I was struggled in cell experiments.

Moreover, I would like to say thank you to all of my good friends and colleagues, who have been always so helpful and caring to me, and giving me such a great experience at McMaster during these years. In particular, I want to thank Dr. Samir Sahli and Regina Leung for giving me insight in image processing. Many thanks to Sharon Goh and Celine Ling for their efforts on dealing with cells, and also to Zhaojun Nie, Jin Ning, Roy Wang, Anthony Tsikouras, Fiona Du, and Du Le for their helpful discussions in math, physics, and optical instrumentation. In addition, I would like to appreciate people who used to work in McMaster Biophotonics Facility together, including Dr. Fei Geng, Dr. Qian Liu, Weijia Zhu, Jennifer Russell, and Nehad Hirmiz for their great helps and guidance. In addition to those helps related to my project; most importantly, we have been through those good years with so much fun.

Finally, I would love to thank my parents, my in-laws, my siblings and my close family members for their warm support. Special thanks to my “roommates” - my husband Leo, my daughter Naomi, and my sister Joyce for giving me so much love and joy during these years.

Contents

List of Figures

List of Tables

List of Abbreviations

5-ALA:	5-Aminolevulinic acid
AFI:	Autofluorescence imaging
AOTF:	Acousto-optic tunable filter
APC:	Argon plasma coagulation
AUC:	Area under the curve
BE:	Barrett's Esophagus
CLE:	Confocal laser endomicroscopy
EAC:	Esophageal Adenocarcinoma
EBL:	Endoscopic band ligation
EMR:	Endoscopic mucosal resection
FAD:	Flavin-adenine dinucleotide
FD:	Frequency-domain
FDA:	US Food and drug administration
FDOT:	Fluorescence diffuse optical tomography
FLIM:	Fluorescence lifetime imaging microscopy
FRET:	Föster resonance energy transfer
FSS:	Forward sequential selection
GERD:	Gastroesophageal reflux disease
GI:	Gastrointestinal
GLCM:	Gray-level co-occurrence matrix
HGD:	High-grade dysplasia
HpD:	Hematoporphyrin derivative
HPPH:	2-(1-Hexyloxyethyl)-2-devinyl pyropheophorbide-a
HRME:	High-resolution microendoscopy
hTERT:	Human telomerase reverse transcriptase
IC:	Internal conversion
ICCD:	Intensified charge-coupled device
ISC:	Intersystem crossing
IRF:	Impulse response function
KTP:	potassium-titanyl-phosphate
LGD:	Low-grade dysplasia
LOH:	Loss of heterozygosity

LY:	Lucifer Yellow
MCP:	Micro-channel plate
MLE:	Maximum likelihood estimation
MLL:	Mat-lylu cell line
MTG:	Mito-Tracker Green
mTHPC:	meta-tetra (hydroxyphenyl) chlorine
NADH:	Reduced nicotinamide adenine dinucleotide
NBI:	Narrow band imaging
Nd:YAG:	Neodymium-doped yttrium aluminum garnet
NIR:	Near infrared
NLLS:	Non-linear least squares
NSCLC:	Non-small cell lung cancer
OCT:	Optical coherence tomography
PBS:	Phosphate buffered saline
PBR:	Peripheral benzodiazepine receptor
PBG:	Porphobilinogen
Pc:	Phthalocyanie
PDT:	Photodynamic therapy
PI:	Propidium Iodide
PMT:	Photo-multiplier tube
PPIX:	Protoporphyrin IX
PS:	Photosensitizer
RBF:	Radial basis function
RdmB:	Rhodamine B
RF:	Radio frequency
RLD:	Rapid lifetime determination
ROC:	Receiver operating characteristic
ROS:	Reactive oxygen species
SLIM:	Spectral-resolved lifetime imaging microscopy
SNR:	Signal-to-noise ratio
SVM:	Support vector machine
TRF:	Time-resolved fluorescence
TCSPC:	Time-correlated single photon counting
TD:	Time-domain
UV:	Ultraviolet

Chapter 1.

Introduction

Photodynamic therapy (PDT) has been used in various medical applications [1–3]. The photosensitizers used in PDT may accumulate preferentially in the targeted tissue, and be activated selectively by light of desired wavelengths to generate cytotoxic oxygen species [4]. Although this helps PDT achieve a better targeting selectivity, the PDT efficacy depends strongly on dose factors, such as the amount of localized light, drug, oxygen, and the interplay between them [5]. The fluorescence of photosensitizers has been studied as a potential non-invasive dosimetric tool to probe localized dose factors in real time [3]. In this dissertation, we focus on oncology applications of PDT and the benefit given by the fluorescent PDT photosensitizers. In particular, we introduce the potential advantage of using time-resolved fluorescence (TRF) of PDT photosensitizers for PDT dosimetry (**Chapter 2 – Chapter 4**). We also bring in a new application using fluorescence of PDT photosensitizer – integrated detection and treatment of Barrett's Esophagus (BE). In this study, the photosensitizer serves as a contrast agent for automatic detection of high-grade dysplasia using the supervised classification algorithm (**Chapter 5**), and also serves as a therapeutic agent for real time treatment following the initial detection (**Chapter 6**).

In **Chapter 1**, we briefly introduce PDT and its clinical use (**1.1**), fluorescence properties of PDT photosensitizers (**1.2**), followed by introduction of the two applications mentioned above (**1.3 – 1.4**). **Section 1.3** briefly introduces existing fluorescence and phosphorescence approaches for PDT dosimetry. As TRF studies of photosensitizers have not been extensively reviewed, we prepared a separate review manuscript that wraps up a more detailed background of TRF and its potential application in PDT dosimetry, as presented in **Chapter 2**. However, clinical and pre-clinical management for BE and its limitations have been reviewed comprehensively; therefore, we summarize these reviews in **section 1.4** to provide a detailed overview of the proposed concept.

1.1. Introduction of PDT and its clinical use

The first success of photodynamic therapy (PDT) in oncology was back in the 1970's, when Dougherty established the clinical efficacy of the photosensitizer, HpD (hematoporphyrin derivative), for treating cancer [6]. A detailed review of PDT history can be found in the review from Fukumura and Jain *et al*. [6]. In PDT, photosensitizers that may accumulate preferentially in malignant tissues are administrated to patients. A time delay allows for redistribution to the malignant tissues, where cellular uptake occurs. The light source that matches the absorption peaks of photosensitizers activates the process. Photosensitizers excited to the triplet state will interact with biological substrates and/or undergo energy transfer with oxygen molecules, creating reactive oxygen species (ROS, type I reactions) and cytotoxic singlet oxygen ($^1O_2$, type II reactions), respectively. Owing to the preferential drug uptake and finite diffusion range of cytotoxic species, PDT has a higher targeting specificity compared to chemotherapy, radiation therapy, and surgical intervention [4]. Clinical applications of PDT in oncology [6] and other medical conditions [3] are summarized in **Table 1.1**.

Table 1.1 Major clinical applications of photodynamic therapy

Approved clinical indications	**Photosensitizers**	**PDT Activation wavelength**
Dermatology (*e.g*. actinic keratosis) [1]	5-aminolevulinic acid (5-ALA)	635 nm
Age-related macular degeneration [2]	Veteporfin (Visudyne®)	680- 695 nm
Localized infection (*e.g*. Periodontitis) [7]	Methylene blue	632 nm
Oncology [6,8]		
Cervical, endobronchial, bladder, and esophageal cancers	Porfimer sodium (Photofrin®)	630 nm
Head and neck tumors	m-THPC (Foscan®)	652 nm
Basal-cell carcinoma	5-ALA-methylesther (Metvix®)	635 nm

1.2. PDT Photosensitizers and their fluorescence properties

PDT photosensitizers are fluorescent after activation by light of desired wavelengths. Fluorescence is a form of radiative energy released when the fluorophore returns to its ground state upon photo-excitation, and is considered to be proportional to the quantum yield and the concentration of the fluorophores [9]. Fluorescence lifetime is then defined as the time it takes for a fluorophore to return to its ground state, typically happening in nanoseconds.

1.2.1. Fluorescence properties of PDT photosensitizers

Fluorescence properties of photosensitizers, including the emission peak, spectral shape, and the fluorescence lifetime, may change while there are photobleaching, formation of photoproducts, structural changes of the compound, molecular aggregation, collisional quenching, and energy transfer [9]. These transitions and interactions occur frequently in PDT photosensitizers during treatment, and can be monitored through fluorescence measurements [10–12]. **Table 1.2** summarizes the fluorescence properties of PDT photosensitizers compared to endogenous fluorophores that account for cellular metabolism [13]. Typically, photosensitizers have greater fluorescence emission in red and near-infrared regions, and exhibit slow fluorescence decay kinetics. In contrast, autofluorescence emission is in blue and green, with faster fluorescence lifetimes within 4 ns. This distinct spectral information enables fluorescence monitoring *in vitro* and *in vivo* to probe photosensitizer location, concentration, and mechanisms of PDT. Detailed review of autofluorescence can be found in work from Ramanujam [13]. Steady-state and time-resolved studies of PDT photosensitizers are reviewed more in detail in **Chapter 2**.

Table 1.2 Fluorescence properties of photosensitizers and endogenous fluorophores

Common photosensitizers	**Fluorescence emission peaks**	**Fluorescence lifetime***
Photofrin [14]	635 nm, 700 nm	1 – 15 ns
5-ALA [11]	635 nm, 705 nm	2 – 17 ns
m-THPC [15]	720 nm	4 – 10 ns
Endogenous fluorophores [13]	(Typically < 600 nm)	(Typically < 4 ns [14,16])
NADH	440 nm, 460 nm	Unbound: < 1 ns Bound: 3.6 ns
FAD	535 nm	Bound: < 1 ns Unbound: 2.8 ns
Collagen	405 nm	350 ps, 2.8 ns
Porphyrins	635 nm, 700 nm	Typically > 10 ns

* The fluorescence lifetime depends strongly on drug-molecular interactions, resulting in a wide range of measured values. This is discussed further in Chapter 2.

Photofrin® is a FDA-approved photosensitizer for various applications in oncology. 5-ALA (5-Aminolevulenic acid) induced proptoporphyrin IX (PpIX) has been investigated extensively in clinical trials for its superior mucosal selectivity in the GI tract [17]. Therefore, these two photosensitizers are used in our work in an attempt to achieve easier translation from bench work to clinical

studies. In this thesis, Photofrin® is mainly used to investigate time-resolved fluorescence of photosensitizers (**Chapter 3**), while the fluorescence of 5-ALA induced PpIX is used in integrated detection and treatment of Barrett's Esophagus (**Chapter 5 and 6**). The following sections briefly introduce Photofrin® and 5-ALA in terms of their indications, biological targets, and mechanisms of action.

1.2.2. Photofrin

Photofrin® (porfimer sodium) is a photosensitizing agent originally approved by the FDA to be used in photodynamic therapy for various types of solid tumors. It is a combination of oligomers includes monomeric hematoporphyrin, protoporphyrin, and oligomeric porphyrins, with an average molecular weight of 600 g/mol. During the manufacturing process, it is purified to contain more photoactive components in comparison to the earlier generation photosensitizer, hematoporphyrin derivative (HpD) [18]. The main indications of Photofrin®-based PDT are obstructing esophageal cancers, ablation of High-Grade Dysplasia (HGD) in BE, and endobronchial non-small cell lung cancer (NSCLC). In clinical usages, it is injected intravenously after mixing its dried powder with 5% Dextrose or 0.9% Sodium Chloride (FDA). An interval of 24 to 48 hours is given to allow drug uptake, followed by light treatment.

Mitochondria, which play important roles in cell metabolism and in regulation of cell death, are the final targets of Photofrin® after drug administration [19]. Several studies have examined the cellular uptake to understand its mechanisms of action [19–21]. Photofrin® is initially taken up by the plasma membrane. Then, it enters the cytoplasm and sensitizes enzymes such as pyruvate kinase, which affects cell metabolism. In a few hours, Photofrin® will bind to the receptor on the outer mitochondrial membrane, PBR (Peripheral Benzodiazepine Receptor), which is also a binding site for naturally occurring porphyrins and is usually overexpressed in many types of cancers. A voltage-dependent anion channel will be created at this point, which further causes accumulation of Photofrin® at cardiolipin in the inner mitochondrial membrane. At this stage, mitochondrial depolarization could happen which results in reduced energy production and drug relocation. Damage to mitochondria thus induces downstream events, such as release of cytochrome c and activation of the caspase 3 pathways that eventually contribute to cell apoptosis [21,22].

1.2.3. 5-Aminolevulenic acid (5-ALA)

5-ALA induced proptoporphyrin IX (PpIX) has been approved by the FDA to be used in PDT for treating actinic keratosis [23]. ALA-PpIX holds some desired features as a clinical PDT photosensitizer, including easy administration (oral) with short activation time (4-5 hours) [24], minimized side effects due to the fast clearance rate within 24 hours [25], and most importantly, its mucosal

selectivity [26]. Therefore, BE is considered as a suitable application and clinical trials have been performed extensively on Barrett's Esophagus [27–29].

To understand its mechanisms of action, haem biosynthesis pathways are illustrated in **Fig. 1.1**. Haem is a vital component in mitochondria; it plays a role in all biological oxidation reactions. 5-ALA works as a precursor for the endogenous photosensitizing agent, protoporphyrin IX (PpIX) during haem biosynthesis pathways [30]**.** As demonstrated in **Fig. 1.1,** 5-ALA is synthesized when the enzyme Succinyl CoA (from the citric acid cycle) is present with glycine. It is then condensed to form porphobilinogen (PBG) and water molecules in cytosol, where four PBG molecules are catalyzed by uroporphyrin I synthase to the intermediate compound, Hydroxymethylbilane. This will be mainly converted to uroporphyrinogen III in normal conditions while some uroporphyrinogen I can be formed as well. Through decarboxylation of the acetate groups, uroporphyrinogen III is converted to coproporphyrinogen III that re-enters the mitochondria. Eventually, PpIX is formed in the mitochondria and haem is synthesized by incorporating ferrous iron to PpIX. There are two important regulations during this process: (i) haem production activates the negative feedback to control the synthesis rate of 5-ALA, and (ii) Haem synthesis is a relatively slow process regulated by Ferrochelatase, the enzyme that chelates ferrous iron to PpIX. These regulations contribute to certain degrees of tumor selectivity using exogenous ALA because it overwhelms the negative feedback and leads to increased PpIX accumulation. Therefore, the photosensitizer PpIX accumulates more in tumor areas where ferrochelatase activity is limited [30,31].

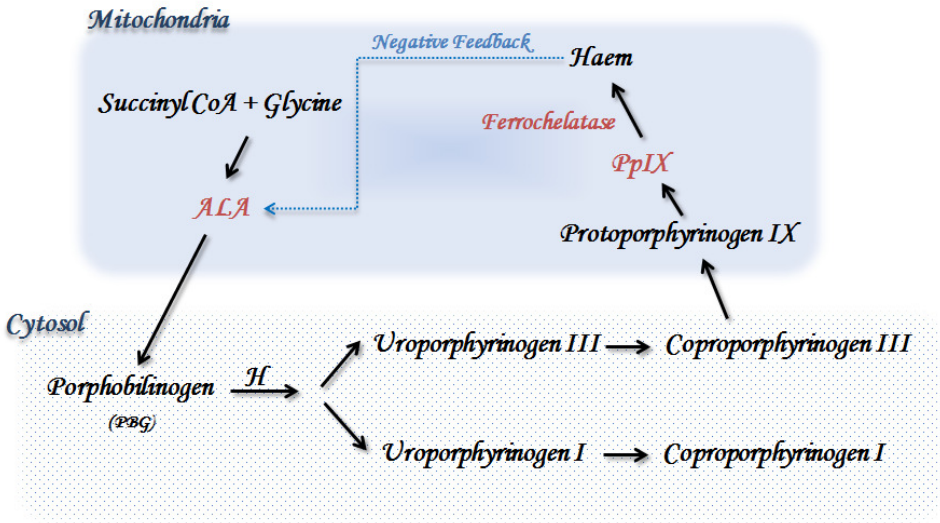

Figure 1.1 Haem biosynthesis pathways

Since the mitochondria is also the targeted intracellular organelle, 5-ALA induced PpIX works similarly to Photofrin ® and results in mitochondrial depolarization and cascade apoptosis reactions [32]. However, cell death pathways vary between different cell lines and has been seen in cells demonstrating less apoptotic capability [33]. 5-ALA has also been investigated for its better diagnostic power than HpD [26]. However, the comparison of PpIX accumulation between normal and tumor areas did not show significant differences. For example, it has been demonstrated that the maximum concentration of PpIX was found earlier in BE (4.6 hrs) than in other sites (6.6 hrs), while normal squamous cells contain more PpIX than BE after prolonged incubation [34–36]. These results suggest other identification features should be investigated to improve detection sensitivity.

In **section 1.3**, we introduce the first potential application, PDT dosimetry, using fluorescence of photosensitizers.

1.3. Application I - PDT Dosimetry

As mentioned in **section 1.1**, PDT efficacy replies strongly on the precise control of localized dose factors, but is challenging to probe these factors accurately in real-time. In **section 1.3**, existing PDT dosimetric approaches are reviewed, including explicit, implicit [3], and singlet oxygen luminescence dosimetry [37]. Detailed reviews and comparisons of these approaches can be found in the review from Wilson and Patterson [3]. The limitations of these approaches and the potential use of time-resolved fluorescence for probing parameters in PDT dosimetry is reviewed and discussed in **Chapter 2**.

1.3.1. Explicit dosimetry

To date, explicit dosimetry is the most commonly used dose metric, which assumes that the product of local photosensitizer concentration and light fluence may be able to predict the treatment outcome. The overall concept of explicit dosimetry is to calculate three dose factors directly. Light fluence can be calculated by modeling the radiative transport equation [38] when tissue optical properties are known. Experimental measurements at some discrete points can be used to verify simulation results, and are considered important for measurements at tissue boundaries. As for probing the localized photosensitizer concentration, fiber-based fluorescence measurements have been reported [39,40], which could be suitable for both superficial and interstitial measurements. The major concern of explicit dosimetry is that singlet oxygen production is not just proportional to the light and drug product, but also dependent on local oxygen concentration and dose interdependencies (elaborated in **section 2.1**) that could be altered during the treatment. This leads to failure in predicting tissue responses in some cases by just measuring light-drug products.

1.3.2. Implicit dosimetry

Implicit dosimetry has been proposed to account for the dose interdependencies and the downstream photophysical and photochemical effects from PDT [5]. As the photosensitizer can be destroyed photochemically by highly reactive oxygen species generated from PDT, or interact with biological substrates (type I reaction), it is assumed that the extent of photosensitizer photobleaching can be related to the photobiological effect from PDT. This is then the key concept of implicit dosimetry – using an indirect parameter, photobleaching, to account for intermediate pathways that occur during the treatment process. Therefore, depending on how abundant the localized oxygen supply is, photobleaching is affected by various degrees of oxygen coupling, and can be interpreted using two extreme situations. First, uncoupled photobleaching usually occurs at hypoxic or anoxic areas, where no singlet oxygen is produced from PDT. In this case, the integration of fluorescence intensity over the treatment time represents the overall active photosensitizer concentration. On the contrary, fully coupled photobleaching can be related to the amount of singlet oxygen production. Therefore, a faster photobleaching kinetic indicates a stronger PDT efficacy. Although there is always some degree of coupling in practice, photobleaching is used in implicit dosimetry as an indirect parameter to correlate all intermediate transitions, and can be performed simply by fluorescence measurements. Detailed review of implicit dosimetry can be found in work from Wilson *et al.* [5], and the photobleaching kinetics of various photosensitizers have been modeled *in vitro* to correlate photobleaching with PDT effects [41–43].

1.3.3. Singlet oxygen luminescence dosimetry

In addition to the fluorescence measurements of photosensitizers mentioned in **section 1.3.1** and **1.3.2**, the amount of cytotoxic singlet oxygen can be measured directly by its phosphorescence at 1270 nm. The equation that describes singlet oxygen generation and its phosphorescence decay after a short excitation pulse can be simplified to **Eq. 1.1** [37] :

$$\left[{}^1O_2\right](t) = A\,\frac{\tau_D}{\tau_T}e^{\left(-\frac{t}{\tau_T}\right)} \qquad \textbf{(1.1)}$$

where *A* represents the coefficient term, describing the process of light absorption and singlet oxygen production. The concentration of singlet oxygen as a function of time is expressed by the exponential decay related to two pathways, the triplet state lifetime of the photosensitizer (τ_T), as well as the singlet oxygen phosphorescence decay (τ_D). Assuming that the luminescence signal is proportional to the singlet oxygen concentration, it is possible to recover τ_T by fitting the curve of luminescent signal, and further estimate the ground-state oxygen concentration [37]. Although this approach can probe the singlet oxygen concentration and estimate ground-state oxygen depletion, it assumes that the

PDT efficacy is solely based on the amount of cytotoxic singlet oxygen, which is not always true. In reality, other factors such as vascular responses and inflammatory responses also play important roles [6]. In addition, it still suffers from technical challenges including low signal to noise ratio of measured decays, as well as complicated and expensive instrumentation involving detectors sensitive to this wavelength range and the short-pulsed light source that has to be coupled efficiently for interstitial measurements. In **Chapter 2**, we compare these dosimetric approaches and review the potential benefits of using time-resolved fluorescence for PDT dosimetry.

In **section 1.4**, integrated detection and treatment of Barrett's Esophagus, a new application that uses fluorescence of photosensitizers, is introduced. **Section 1.4** introduces the background and motivation of the concept in detail, followed by the introduction of its research methodology in **section 1.5**.

1.4. New application – Integrated detection and treatment of Barrett's Esophagus

The incidence rate of esophagus adenocarcinoma (EAC) has increased by 300% in the US over the past few decades [44]. This has brought particular concerns as EAC has been reported to have an overall 5-year survival rate of just 12% [45], and this low survival rate is highly associated with the lack of early diagnosis and treatment [46]. Barrett's Esophagus (BE) is a precancerous condition that is deemed the major risk factor for esophageal cancer. Studies have shown 0.5% of patients with BE develop esophageal cancer per year [47]. The malignancy transformation process of metaplasia-dysplasia-adenocarcinoma suggests that early detection and treatment of dysplasia in BE is essential to reduce the risk of cancer development. However, current clinical protocols perform tissue biopsy, histopathological analysis, and treatment in separate procedures, leading to significant mis-sampling and treatment rate [46]. The discrepancy between tissue level (endoscopy) and cellular level (histopathology) observation, as well as intra-observer and inter-observer variation further impede accurate diagnosis and treatment. Therefore, there is an urgent need to develop integrated diagnosis and treatment technique: the lesion can be visualized and classified robustly with cellular resolution imaging followed by real-time treatment plans. In **section 1.4**, we introduce a new application using fluorescence of photosensitizers – integrated detection and treatment of Barrett's Esophagus. We start with histopathological progress of BE and limitations of clinical standards for BE diagnosis and treatment (**1.4.1**). Next, we review advances and limitations of recent biophotonics techniques for detecting and managing BE (**1.4.2 – 1.4.4**). In **1.4.5**, we conclude our motivation behind integrated diagnosis and therapy and present the overall concept of the proposed research.

1.4.1. Introduction to Barrett's Esophagus

Barrett's Esophagus (BE) mostly develops as a result of chronic gastroesophageal reflux disease (GERD), which is a common condition with a prevalence of 10 to 20% in North America [48]. **Fig. 1.2** demonstrates the anatomical layers of esophageal mucosa [49]. The inner lining of esophagus is normally layered with squamous epithelium with flat and smooth surface. In GERD, gastric or bile acid leads to chronic inflammation and possible erosion of the esophageal-gastric junction and the lower end of esophagus. Prolonged GERD thus transforms normal squamous cells to intestinalized columnar epithelium that contains mucus- secreting goblet cells [50].

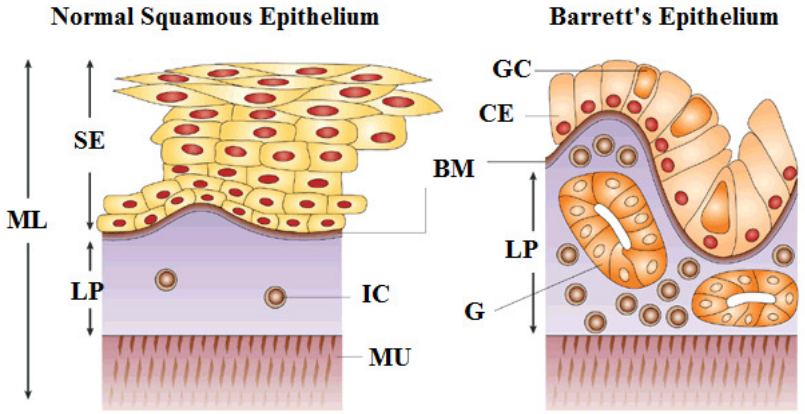

Figure 1.2 Anatomical structure of esophageal mucosal layers. Mucosal layer (ML) is the inner surface of esophagus, which is normally composed of squamous epithelium (SE), lamina propia (LP), and muscularis mucosa (MU). Barrett's Esophagus can develop with chronic GERD, where columnar epithelium (CE) replaces the SE surface. In addition, Goblet cells (GC), inflammatory cells (IC) and mucus-secreting glands (G) are also found (Adapted by permission from Macmillan Publishers Ltd: Ref. [49], copyright (2003))

Histopathological analysis following tissue biopsy is currently a clinical gold standard for confirming diagnosis: BE is diagnosed when there are positive histopathological findings of intestinal metaplasia from biopsied samples (American College of Gastroenterology), as this most common subtype of metaplasia demonstrates the highest malignant potential [51]. Pathological standards for diagnosis of metaplasia and dysplasia include cytological and architectural abnormities, as summarized in **Table 1.3** [50,52].

Table 1.3 Summary of histopathological standards for BE diagnosis

Conditions	Histopathological Standards
Metaplasia	**Cytology:** well-spaced cell nuclei; rounder and basally oriented nuclei;
	Gross observation: non-distorted architecture, existence of goblet cells and less stratified morphology
Low-grade dysplasia (LGD)	**Cytology:** mild cytological atypia; nuclear overlapping; irregular contour
	Gross observation: mild architectural distortion; dystrophic goblet cells;
High-grade dysplasia (HGD)	**Cytology:** Loss of cell polarity**;** crowded nucleus distribution**;** nuclear pleomorphism; enlarged cell nuclei; immature cytoplasm**;** nuclear stratification
	Gross observation: Increased crypt complexity**;** no goblet cells

Upon diagnosis, routine endoscopic surveillance is performed using the biopsy interval of 2 cm for metaplasia and 1 cm for dysplasia [51]. In addition, advanced treatment to eliminate the dysplastic area (*e.g.* surgical intervention) is given to reduce the risk of developing esophageal cancer. Esophagectomy, a clinical routine used to treat high-grade dysplasia, has shown to cause increased morbidity and mortality (*e.g.* major respiratory complications). Detailed review of major complications has been documented in work from Low *et al.* [53,54]. Consequently, alternative optical imaging and photo-ablative techniques have been proposed to access and treat affected mucosa using minimally invasive ways [44,46,55–60], which will be reviewed later in this chapter.

Although the rationale of tissue biopsy, histopathology, and treatment followed by regular surveillance seems reasonable and practical for detecting and managing Barrett's esophagus, the incidence of EAC still remains high. In other words, certain drawbacks of these procedures should be considered. (i) Sampling error: BE lesion can be focal and distributed irregularly, while the sampling procedures are usually performed at the most affected area [61]. This poses increased sampling errors and the errors are associated with the number of biopsies and the sampling area. For example, it has been reported that the sensitivity of 8 biopsies in a metaplasia segment away from the esophageal-gastric junction is just 68% [50]. (ii) Intra-observer variation of histopathological interpretation reduces robustness in diagnosis [61,62] (iii) Relocation errors: this is introduced from separate diagnosis and treatment procedures; in particular, the mismatch between the observation scales of histopathological analysis (microscopic) and endoscopy examination (macroscopic) results in potential relocation errors when giving treatment [46]. To address challenges mentioned

above, several biophotonics approaches have been proposed to improve the detection and treatment of Barrett's esophagus. These techniques are reviewed in **section 1.4.2** and **1.4.3**.

1.4.2. Biophotonics approaches for BE detection

Biophotonics approaches for detection of BE include wide-field and optical biopsy techniques. The former one uses endoscopic observation with either endogenous fluorophores (*e.g.* narrow band imaging, autofluorescence endoscopy) [63] or exogenous contrast (*e.g.* chromoendoscopy) [64,65] to visualize the dysplastic region. The latter, on the contrary, illuminates the target at the cellular level to retrieve Barrett's-associated characteristics by the use of point spectroscopy [66,67], high-resolution microendoscopy [62,68], or endomicroscopy [58,59,69].

1.4.2.1. Wide field Endoscopy

Autofluorescence endoscopy and narrow band imaging (NBI) are two common wide-field techniques without the use of exogenous contrast. Autofluorescence used to be a favored option in clinical diagnosis as no exogenous contrast agent is required, thus there is no safety concern. This technique takes advantages of proportional changes in endogenous fluorophore concentration due to neoplasia formation [67]. In general, neoplastic regions are found to have degraded collagen structure, and increased cell metabolism that affects a variety of enzymes such as NADH, FAD, and porphyrins. The spectral features of these endogenous fluorophores are shown in **Fig. 1.3**. Due to these characteristics, autofluorescence bronchoscopy has been approved by FDA as a supplementary technique for detecting early stage bronchial lesions [70]. Overall, the degraded collagen and mucosal thickening cause reduction of collagen fluorescence as well as increased attenuation. Therefore, neoplastic regions may appear more brownish when compared to normal tissue that shows greenish color. The technique has also shown promising results in differentiating precancerous polyps in colon [71] and BE [67,72]. Although it is not being listed as one of the discriminative characteristics in autofluorescence bronchoscopy, attenuation from absorption of hemoglobin also helps to reveal the microvascular pattern. This will be mainly used in narrow band imaging (NBI) discussed in the next paragraph.

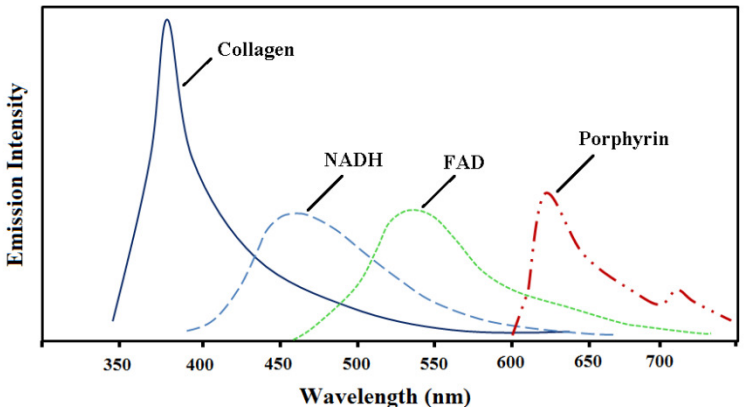

Figure 1.3 Important endogenous fluorophores for autofluorescence endoscopy. Loosened structure and mucosal thickening lead to decreased signal of collagen. Increased signal of porphyrin, FAD, and NADH can be observed due to increased metabolism. The emission spectra demonstrated here are just for illustrative purposes, not the measured values.

In NBI, a broad band light source is passed through a filter disk containing red, green, and blue (RGB) band-pass filters, or more commonly the green (540-560 nm) and blue (400-420 nm) filters. The mucosa is illuminated sequentially by the RGB light source, and the narrow-band signal is collected by a monochrome CCD. The imaging contrast is built based on the altered attenuation of these wavelength bands. Due to absorption of hemoglobin at blue and green channels, it is capable of showing mucosal morphology and microvasculature of neoplastic areas. The blue band also helps with observing superficial layers due to its shallow penetration depth [63].

Instead of using endogenous fluorophores, white light chromoendoscopy or fluorescence endoscopy use organic or synthetic dyes in an attempt to highlight BE. Common dyes used in clinical GI endoscopy have been reviewed extensively by Song *et al.* [64], and summarized in **Table 1.4**. It should be noted that these dyes can also be used at microscopic scales.

Table 1.4 Common endoscopic contrast agents

Contrast Agents	Properties and Applications
Fluorescein	Highlights vasculatures and intracellular space. Goblet cells and epithelial mucin appear dark
Methylene Blue	Highlights actively absorbing columnar epithelium but with little discrimination for HGD
Toluidine Blue	Stains nuclei of columnar cells

Lugol's Solution	Only stains normal mucosa for its affinity to iodinated agents
Cresyl Violet	Stains the cytoplasm, so also highlighting cell nuclei, while the staining pattern is not discriminative
Acriflavin	Stains cell nuclei directly, but is considered to be mutagenic.
Acetic Acid	Highlights columnar mucosa, but low specificity for HGD
Indocyanine Green	Less used in chromoendoscopy, but only for marking locations.

1.4.2.2. Point spectroscopy and imaging

Fluorescence and autofluorescence spectroscopy are alternatives for endoscopy for its low cost and easier implementation. However, in the case of Barrett's esophagus, spectroscopic techniques are not preferred owing to certain major challenges, such as individual variability and substantial artifacts from changes of imaging geometry [67], which will be discussed further in **section 1.4.4**.

Moving towards cellular resolution, optical coherence tomography (OCT) has been used to obtain cross-sectional images non-invasively using low coherence light. Similar to the concept of ultrasonic pulse-echo imaging, OCT is based on the scattering events from tissue microstructures due to the mismatch of refractive indices. The structures of the targeted volume can be reconstructed based on the interference patterns between the incident and reflected light [73]. Recently, high-resolution OCT has also been developed as a potential tool for imaging stratified layers of esophageal epithelium [74–77], achieving lateral resolution of a few micrometers, axial resolution down to 2 μm in tissue, and a penetration depth of 2 to 3 mm [75]. This allows visualization of tissue architecture such as crypts, blood vessels, *etc.*, and differentiate BE from normal squamous epithelium. The greater imaging depth compared to confocal microscopy is particularly valuable for visualizing submucosal invasion and staging of neoplastic lesions [75]. However, as the contrast from OCT is built upon the mismatch of refractive index, subcellular organelles may not easily visible using this technique, thus classification within BE is challenging and further correlation may be required.

Based on the clinical standards of histological analysis, morphological features of cell nuclei may provide the most robust criteria for detection of HGD areas [50,52]. *In vivo* histology is a promising technique whose resolution approaches that of gold standard histopathological analysis. This includes the use of high-resolution microendoscopy (HRME) [62,78], and confocal laser endomicroscopy (CLE) [58,59,69,79]. Both HRME and CLE render imaging resolution down to cellular level.

In particular, CLE yields cytology-comparable resolution using miniaturized confocal optics placed at the distal end of the optical fiber, as shown in **Table 1.5**. The depth of imaging acquisition is up to 250 µm (EC3870CILK, Pentax, Tokyo, Japan), which allows microscopic visualization of mucosal layers and capillaries [79]. As a result, BE has become an important focus as the pathology is mostly limited to mucosal layers [47]. Unlike axial sectioning used in standard histopathology, the image sectioning using CLE is performed on the plane parallel to the surface (*en face* acquisition), which is similar to images acquired by laboratory confocal microscope. As the features of CLE images are in agreement with mucosal histopathology, Kiesslich and colleagues have shown that CLE is capable of differentiating BE and adenocarcinoma with the use of fluorescein for visualizing cellular and vascular patterns. Mainz Confocal Barrett's Classification system was developed based on the morphological characteristics to stage BE [59]. This BE classification system achieved high diagnosis accuracy (97.5 %) and successfully enabled targeted HGD biopsy, while it is still considered to be highly dependent on intra-observer agreement [62].

The comparison of wide-field and point-biopsy technology is summarized in **Table 1.5**. These techniques make real-time diagnosis feasible, and may allow on-site detection and treatment when imaging devices and treatment technologies are integrated into the endoscopic head. To explore treatment options, common phototherapeutic technologies are introduced in the following section.

Table 1.5 Summary of wide-field and point-biopsy imaging techniques

Instrument	FOV	Resolution (µm)	Classification techniques
Wide-field	100 – 300 K pixels FOV: a few cm^2	Lateral: 100	Visual observation by trained endoscopist. Requires histopathological analysis
OCT	FOV: up to 1 mm x 1mm	Lateral: 5.6 Axial: 2 Axial range: 2 – 3 mm	Visual observation by the trained endoscopist and pathologists
CLE	1024 x 1024 pixels FOV: up to 500 x 500 µm	Lateral: 0.7 – 3.5 Axial: 5 - 7 Axial range: up to 250	Gastroenterologists and pathologists perform classification based on cellular and vascular changes
HRME	400 to 850 K pixels 1400 µm x 530 µm	Lateral 4.4 µm	Using automatic image classification algorithm.

1.4.3. Phototherapeutics for Barrett's Esophagus

As mentioned in **section 1.4.1**, esophagectomy has been considered to cause increased morbidity and mortality [45,53,54]. To avoid these adverse effects, alternative photo-ablative techniques have been proposed to access and treat affected mucosa using minimal invasiveness. The main concept is to remove the HGD epithelium and stimulate the regrowth of normal squamous layers in an anacidic environment [80]. It is also based on the rationale that metastatic rate in HGD is nil [81,82]. Endoscopic mucosal resection (EMR) for treating BE was initially adapted by Soetikino *et al*. to deal with the flat neoplastic lesions present in esophagus [83]. A plastic cap, typically used in the endoscopic band ligation (EBL) device can be used with a suction force from the endoscope to remove the lesion. Another method is to lift the affected mucosa by injecting saline into the submucosa, thus the HGD mucosa can be snared for electrocoagulation (multipolar electrocautery) [57,80]. The main advantage of this technique is that it may remove the pathological area including some of submucosa, which can achieve complete resection of lesion and help determine the stage of the disease. However, EMR is only practical when the lesion area is known, thus other photo-ablative techniques described below may be used to treat spotted lesions.

Current photo-ablative methods include the use of photochemical (*e.g.* photodynamic therapy, PDT) [17,28,84,85], photothermal (*e.g.* argon plasma coagulation, APC) [56,57,86,87] techniques, and radiofrequency ablation [88,89]. This section focuses on the review of PDT and APC, the most extensively studied photo-ablative techniques in treating BE.

1.4.3.1. PDT for treating Barrett's Esophagus

Photodynamic therapy is based on the cytotoxicity generated by photochemical reactions [4]. PDT using Photofrin® (porfimer sodium) has been approved for treating patients with HGD in North America and Europe [85]. The specific applications of PDT in BE are reviewed in this section.

Overholt *et al.* compared results from multi-center phase III clinical trials in 2007 [85], where BE patients diagnosed with HGD were placed into two groups: a control group that only took proton pump inhibitors (Omeprazole), and an experimental group that received both Omeprazole and PDT. In PDT, Photofrin® of 2mg/kg was administrated intravenously. Light activation at 630 nm was delivered 40 to 50 hours after drug administration, using 130 J per centimeter of the cylindrical diffuser. The cylindrical diffuser fiber was introduced to the center of the targeted BE segment using an inflatable balloon device. The follow up light treatment was given 4 to 6 days after drug administration, and 1 or 2 more treatment sessions can be applied depending on the completeness of the treatment. This comparative study affirmed the PDT efficacy for treating Barrett's esophagus, where the complete elimination was enhanced from 39 % to 77%, and

it eventually lead to FDA approval of using Photofrin® for Barrett's neoplasia. 5-aminolevulinic acid (5-ALA) is another topical photosensitizer that has been studied extensively for treating BE owing to its better mucosal selectivity [28,29,34,90]. This unique advantage significantly reduces unwanted esophageal stricture from the low targeting specificity of Photofrin.

1.4.3.2. Laser ablation

Focal laser ablation techniques include a wide range of mechanisms from photothermal to plasma-mediated ablation using different combinations of light irradiance and exposure time [91]. Of these, photothermal reaction is the most commonly used technique in BE, where light of the wavelengths that matches the absorption peaks of tissue achieves mucosal coagulation in BE segment. It can be performed using Nd:YAG or KTP lasers, while more commonly with Argon plasma beam (APC) or multipolar electrocoagulation [57] in recent years. During clinical procedures, the APC probe is passed through endoscopic biopsy channel and placed at about 1 cm further to the distal end. The ablation is usually performed from the gastro-esophageal junction, and moved upward towards the upper boundary of the HGD segment. With APC, a mucosal strip of 2 mm wide can be coagulated at a time. Kelty *et al*. performed a large randomized controlled trial to compare the efficacy of PDT and APC in treating Barrett's esophagus [56], where 68 patients were divided into a 5-ALA based PDT group, and the APC group. Patients receiving 5-ALA of 30 mg/kg were given the light fluence of 68 mJ/cm^2 during the treatment. APC group received light treatment with a power setting of 65 W. Results showed that both techniques led to a significant reduction of Barrett's epithelium, while APC demonstrated a much better treatment efficacy in terms of complete reversal of squamous epithelium (97 % vs. 50% of treated patients).

In summary, photochemical reactions are not limited to focal lesions and are intended to treat the entire BE regions. Other ablative techniques are more time-consuming when treating focal spots but demonstrated relatively better prediction of treatment results. These treatment technologies may be integrated with diagnostic techniques to achieve early detection and treatment. To examine clinical feasibility, potential limitations of these techniques in BE applications are discussed.

1.4.4. Clinical limitations

Although biophotonics techniques mentioned in **1.4.2** and **1.4.3** help approaching integrated *in vivo* diagnosis and real time treatment without taking tissue biopsy, commonly used wide field endoscopy (*e.g.* AFI, NBI, chromoendoscopy), and optical biopsy (*e.g.* point spectroscopy, endomicroscopy)

still yield insufficient detection sensitivity and specificity in the reported trials [68]. In general, current techniques pose certain major limitations, as detailed in the following:

(i) Autofluorescence-based techniques do not have adequate specificity mostly because non-dysplastic areas in esophagus also present high level of autofluorescence signal. Thus the pathological and normal areas do not show significant differences in terms of autofluorescence features [63,72]. As a result, combinations of multiple modalities, multiple spectral bands, or adding exogenous contrast agents are required.

(ii) Significant patient to patient variability is a major uncertainty when using spectroscopic techniques, thus making a robust detection algorithm almost impossible. Other technical difficulties were also reported [46]. For example, it is difficult to reproduce the same point of measurement when trying to perform tissue biopsy to validate spectroscopic results. The varied endoscopic observation geometry (particularly in esophagus) and artifacts from heartbeat lead to further variation in measurement. To deal with these problems, providing extra spectroscopic information (*e.g.* such as time-resolved fluorescence, detailed in **Chapter 2**) can be one of the options. Using imaging techniques can be a more preferred way to account for individual variability.

(iii) Clinical histopathological standards are mainly based on distinct nucleus contrast given by various pathological progresses. However, when attempting to use exogenous contrast in endoscopy (*e.g.* fluorescence endoscopy, chromoendoscopy), either organic dyes or PDT photosensitizers do not show sufficient targeting specificity [64,84] except for some nucleus stains that are considered mutagenic. For example, PDT used to be deemed as an approach with both diagnostic and therapeutic powers. Although 5-ALA based diagnosis achieved acceptable sensitivity (> 80%), the specificity is only up to 56 % [92]. Therefore, not only is a contrast agent demonstrating nucleus contrast desired, a proper quantitative algorithm should also be employed to alleviate problems from variability in targeting specificity. Limitations of the above biophotonics techniques are summarized in **Table 1.6.**

Table 1.6 Limitations of diagnostic techniques for BE

Diagnostic Techniques	**Limitations**
Autofluorescence Endoscopy	Insufficient contrast, scale mismatch (sampling errors)
Autofluorescence Spectroscopy	Insufficient contrast, large individual variability, no spatial information
Narrow-band Imaging	Insufficient contrast, scale mismatch
Chromoendoscopy*	Lacking safe dyes that highlight HGD, scale mismatch

OCT	Lacking subcellular contrast
Molecular Imaging	Requires extensive clinical trials to address safety concerns.

*including fluorescence endoscopy and the use of fluorescent PDT photosensitizers

To overcome these challenges, we proposed the integrated detection and treatment using a PDT photosensitizer as an exogenous contrast agent with potential treatment power. It is combined with microscopic-based imaging analysis and classification to address the issue of insufficient targeting specificity from the photosensitizer. We illustrate the overall concept of the proposed research and intermediate research objectives in **section 1.4.5**.

1.4.5. Integrated detection and treatment of HGD using photosensitizers

As mentioned in the preceding sections, integrated detection and treatment is in urgent need to address the sampling and relocation errors arising from traditional tissue biopsy, while the limitations from current biophotonics approaches still exist. These challenges lead to our research motivation for integrated detection and treatment. More specifically, it may be feasible to detect HGD areas with better sensitivity and specificity using statistical classification algorithms at a microscopic level. In addition, the diagnostic step is followed immediately by well-characterized treatment plans that avoid relocation errors and render predictable results. The schematics of the research concept are shown in **Fig. 1.4**.

Integrated detection and treatment compatible with current confocal laser endomicroscopy (CLE) techniques may improve the diagnostic accuracy. We propose to use the FDA-approved photosensitizer, 5-aminolevulenic acid (5-ALA) induced protoporphyrin IX (PpIX), as a nucleus contrast agent for highlighting the HGD area. 5-ALA is selected for its ability to stain peri-nucleus region (mitochondria), mucosal selectivity *in vivo*, and fast clearance rate (less side effects). However, as mentioned in **section 1.4.4**, 5-ALA shows limited targeting selectivity due to heterogeneous PpIX synthesis. Therefore, instead of relying on the targeting selectivity by the contrast agent, machine learning and pattern recognition are more robust to extract histological features and distinguish HGD from normal areas. In other words, the integrated detection and treatment comprise two components: (i) quantitative morphological and textural extraction is performed based on the nucleus contrast given by PpIX (ii) Treatment immediately following the classification can be achieved through photodynamic therapy (PDT) or laser ablation. The use of photosensitizers with machine

learning techniques may solve the dilemma of selecting contrast agents, as well as the low selectivity of traditional "wide field" PDT.

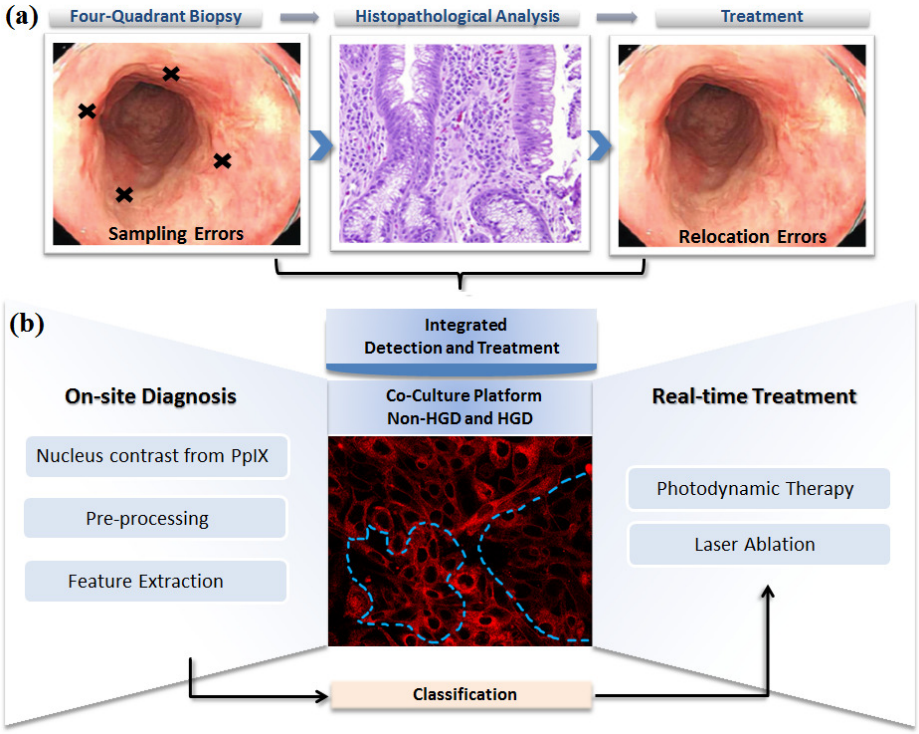

Figure 1.4 Schematics of concepts. (a) Substantial sampling and relocation errors exist in endoscopic surveillance due to the mismatch of resolution between endoscopy and histology. The separate procedures between diagnosis and treatment can lead to undiagnosed focal dysplasia that increases the risk of esophageal cancer. (b) Integrated detection and treatment compatible with current confocal laser endomicroscopy (CLE) techniques may improve the diagnostic accuracy. We propose to use the FDA-approved photosensitizer, 5-ALA induced PpIX, as a nucleus contrast agent for quantitative morphological and textural extraction. Treatment immediately following the classification can be achieved through photodynamic therapy (PDT) or laser ablation.

The overall goal of this project is to enable an integrated diagnostic and treatment technique for early detection of Barrett's esophagus. To achieve this goal, the logical intermediate steps include: *in vitro* models such as mono- and co-culture studies, organotypic (3D) mono- and co-culture studies; *in vivo* animal models, and eventually moving towards clinical studies. Towards this end, the flow of specific research objectives is summarized in **Fig. 1.5**.

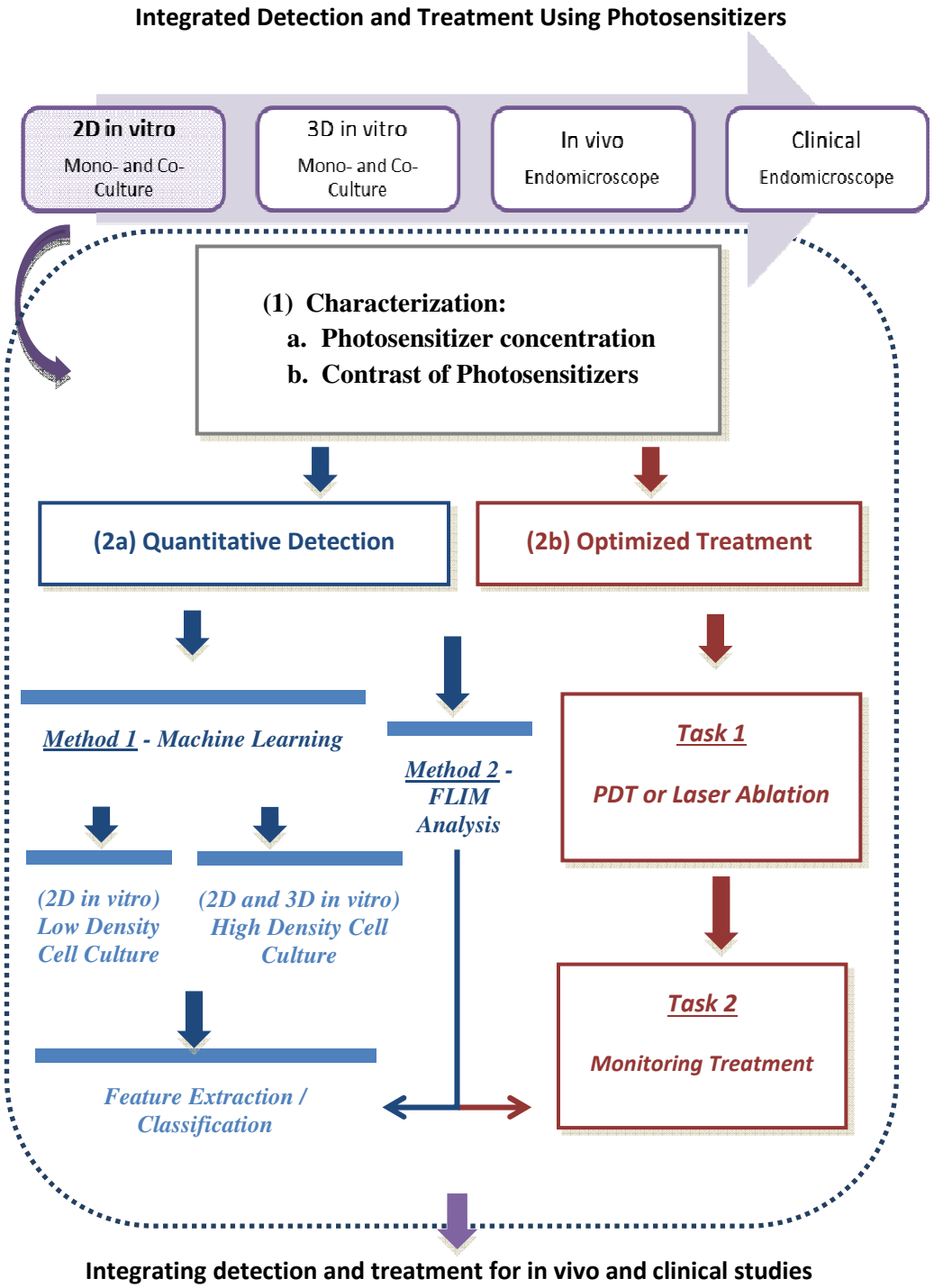

Figure 1.5 The flow chart of individual research objectives.

We started with an *in vitro* platform to study quantitative detection and characterize treatment efficacy using 5-ALA. This *in vitro* characterization step can be divided to several step-by-step tasks, as shown in **Fig. 1.5**. These tasks include using machine learning techniques or time-resolved fluorescence imaging for quantitative detection. Current work is focused on investigating basic morphological and textural features provided by a low density co-culture model for classification of HGD cells. The preliminary features acquired from this simple platform can be expanded and adapted for high-density co-culture and organotypic platforms. In addition to quantitative detection, there are also research questions to answer in order to optimize the treatment efficacy. Treatment efficacy should be characterized when applying different treatment options (e.g. PDT or laser ablation). The work presented in this thesis used PDT as a main treatment option and characterized cell viability in the *in vitro* platform. Moreover, we investigated the feasibility of using time-resolved imaging for probing photosensitizer-molecular interactions, in an attempt to obtain information of drug concentration, intracellular localization, and cell function. This could also be potentially useful for classification as previous studies have reported that the fluorescence lifetime of PpIX in tumor area is significantly longer than normal area [93].

In **section 1.5**, we briefly introduce relevant background to the research methodologies used in the BE project, including BE cell culture platform (**1.5.1**), principles of pattern recognition and light treatment (**1.5.2**).

1.5. Background of research methodology

1.5.1. BE experimental models

Several laboratory BE models have been used to investigate research questions in BE and esophageal cancer. These models are necessary for investigating diagnosis, preventive and treatment strategies. A detailed review of BE experimental models from *in vitro* platform to laboratory animals can be found in work published by Garman *et al* [94]. The selection of an experimental platform is usually based on the context of research questions. For example, an *in vitro* platform possesses a main advantage that research questions can be characterized in a controlled culture setting. This applies to the context of current work that ALA- PpIX is first used as a contrast agent for feature extraction and classification. In addition, a co-culture model is usually preferred to demonstrate the diverse cell types of Barrett's epithelium [95,96]. Moving forwards, 3D BE cultures can provide sufficient closeness to the *in vivo* environment, and has advantages over the animal models. For example, animal models create

metaplasia by surgical anastomosis of jejunum of intestine and the distal end of the esophagus [97], which may cause atypical bile reflux and increased experimental variability. The requirement of surgical expertise is also an issue. As shown in the **Fig. 1.5**, we started our project using two-dimensional mono- and co-culture BE models to investigate how ALA-PpIX can be used for integrated quantitative detection and treatment. Characteristics of these cell lines are described below.

CP-A (metaplasia), and CP-B / CP-C / CP-D (high-grade dysplasia) are telomerase-immortalized (hTERT-immortalized) cell lines first developed by Palanca Wessels *et al* in 1998 [98,99]. Typically, primary esophageal squamous cells only survive for a week. Telemorase-immortalized cells can be maintained in culture environment for a longer period, thus enables studies of long term or organotypic (3D) cell culture. With this transformation, gene expression and morphological characteristics have been investigated to show genetic and morphological similarity to primary cells.

Molecular genetic abnormality is one of the hallmarks in neoplastic progression of BE. Such changes include nonrandom loss of heterozygosity (LOH) at some chromosome arms (9p, 17p) and mutation of certain cell-cycle regulated proteins (*i.e.* p53). Palanca-Wessels *et al* has demonstrated that all cell lines have close similarities as primary culture, where all HGD cell strains contain mutation of p53 and 17p LOH. Slight genetic differences were present among these cell lines: LOH was found at chromosome arm (9p) in just CP-A and CP-B, while CP-D exhibited consistent losses of one copy of chromosomes at certain homozygous sites. Also, mutations in p16 were only found in CP-B (missense mutation; leucine to glutamine) and CP-D (deletion of p16). Details of these studies can be found in work from Palanca-Wessels in 2003 [99].

Emphasis should be put on comparison of morphological patterns from *in vitro* platforms to *in vivo* observation, as the consistency in morphological features is essential for translating classification studies to tissue or *in vivo* levels. In terms of morphology, these cell lines have been well-characterized in co-culture and organotypic culture [95,100]. Mono-culture cell studies have demonstrated various cell shapes, doubling time, and metabolic activities between cell lines, while all cells exhibited large nucleus to cytoplasm ratio [98,99]. When grown in three dimensional environment, co-culture of BE cell strains with fibroblast-embedded collagen revealed distinct morphological patterns between these HGD cell lines and between HGD and metaplastic cells (CP-A). In particular, CP-A cells showed a significant difference in terms of goblet cell formation and the phenotype of columnar cells; multilayered stratified epithelium was formed in both CP-B and CP-D cells and CP-D cells were found to mildly invade the collagen matrix. In contrast, CP-C cells only spread in a single layer [100]. The morphological patterns of different experimental models are summarized in **Table 1.7**.

Table 1.7 Morphological patterns at different experimental models

Levels	Literature review: Morphological features at different levels
Single cell lines	All cell lines exhibit enlarged nucleus to cytoplasm ratio. CP-A cells have rounder shape and well-spaced distribution, while other HGD cell lines exhibit slender morphology and crowded distribution.
2D co-culture	No obvious morphological changes when compared to single cell culture, while cells demonstrate competitive responses to the chemical stimulants [95].
3D co-culture (Organotypic culture)	Metaplasia and HGD yielded different growth patterns and behaviors similar to histopathological observation. Metaplastic cells formed goblet cells, and HGD lines become multilayered stratified epithelium except for CP-C cell line [100].
Ex vivo/ In vivo	Metaplasia demonstrates honey comb-like patterns with goblet cells. Cells have regular basal-oriented nuclei and basal border. Villiform shapes can be observed at the basal membrane layer. In contrast, HGD shows severe pleomorphysm, nuclear membrane irregularity, large nuclei and no nuclear polarity [59].

The correlation between different experimental models is mainly based on nucleus distribution. The distribution in organotypic and tissue level leads to distinct patterns shown in a 2D culture. This is demonstrated using a simple cartoon illustration in **Fig 1.6**, where the *xy* plane represents *en face* acquisition using CLE or a confocal microscope, and the *xz* plane shows a regular axial sectioning performed in histopathological analysis**.**

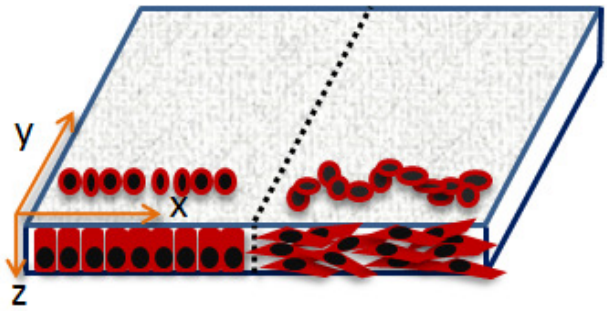

Figure 1.6 Illustration of morphological features shown in different image acquisition planes.

As shown in the figure**,** the nucleus distribution of columnar metaplastic cells in *xz* plane (*e.g.* single layer, basal-oriented nuclei) yields well-spaced, rounder shape in *xy* plane. In contrast, the irregular cell shape and stratified layers of HGD cells in *xz* plane lead to crowded and uneven distribution seen in *xy* images. Therefore, microendoscopy (CLE) acquires images have been shown to yield meaningful information for differentiating HGD areas [59], and these nucleus

morphological features can be correlated between all levels of BE experimental models.

In summary, these well-characterized cell lines were shown to be genetically and morphologically close to *in vivo* BE, and provide a better platform to avoid unwanted contamination from endoscopically biopsied specimens. In this work, we use this cell culture platform as an initial model for studying cellular-resolution classification and treatment. The specific machine learning and light activation techniques are introduced in the next section.

1.5.2. Cellular-resolution classification and treatment

Section 1.5.1 introduces the experimental platforms used in our work. With cell mitochondria and nucleus patterns highlighted by fluorescent photosensitizers (PpIX), cellular resolution classification and treatment can be performed. For quantitative detection of HGD area, image processing combined with machine learning algorithms may be the most objective and robust approach. Image processing and feature extraction is first performed to extract morphological, textural, and pattern descriptors [101], thus the computer learning algorithm can be trained based on the extracted features. In this section, support vector machine (SVM), the classification technique used in our work will be presented. In addition, comparisons of potential treatment strategies using one-photon or two-photon light sources are reviewed.

1.5.2.1. Support vector machines (SVM)

Support vector machine (SVM) was introduced by Boser *et al* in 1992, and has been widely used as a supervised learning approach in bioinformatics for its capability of dealing with high dimensional data and data variability [102]. SVM is essentially a linear two-class classifier, as represented in **Fig 1.7 (a)**, where data can be classified to two groups (+1, -1) using the separating line:

$$\boldsymbol{f(x) = w^T x + b} \qquad \textbf{(1.2)}$$

where $f(x)$ is the linear discriminant function; $w^T x$ is the dot product between coefficient vectors (w) and sample vectors (x), and b is the bias that translates the line away from the origin. In most cases, training data cannot be divided to two groups easily in a two-dimensional space. Therefore, SVM projects training data into a higher-dimensional feature space, where the decision boundary is termed a hyperplane. As shown in **Fig. 1.7 (b)**, SVM separates two training classes by optimizing the hyperplane: maximizing the margin ($1/\|w\|$) as denoted in **Fig. 1.7 (a)**, and minimizing the sum of errors. The training examples on the margin are called support vectors, noted by the concentric circle in **Fig. 1.7 (a)**.

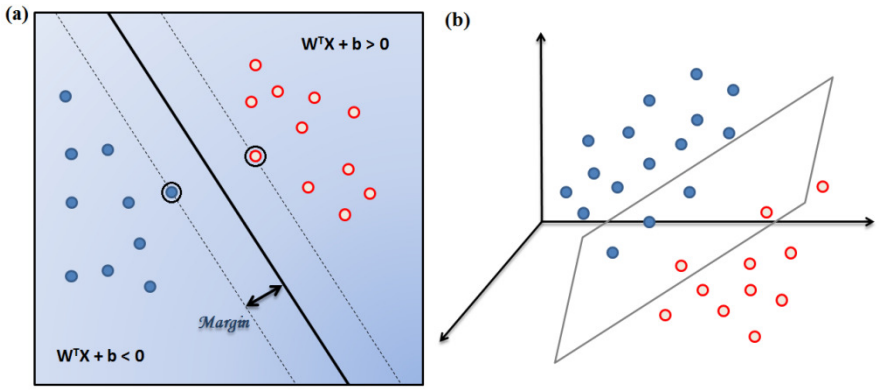

Figure 1.7 Support vector machines.

Typically, when a set of data is transformed from linear to non-linear space, it can be mapped using a non-linear function, $\phi(x)$, then the discriminant function becomes a soft margin:

$$\boldsymbol{f(x) = w^T \emptyset(x) + b} \qquad \textbf{(1.3)}$$

However, computing non-linear functions explicitly can increase the use of memory and is considered computationally expensive. Therefore, kernel methods are proposed to solve this non-linear complexity. Assume the weight function w^T can be represented as a linear combination of training data ($\alpha_i x_i$), thus **Eq. (1.2)** and **(1.3)** can be rewritten to **Eq. (1.4)** and **(1.5)**, respectively:

$$\boldsymbol{f(x) = \sum_{i=1}^{n} \alpha_i x_i^T x + b} \qquad \textbf{(1.4)}$$

$$\boldsymbol{f(x) = \sum_{i=1}^{n} \alpha_i \emptyset(x_i)^T \emptyset(x) + b} \qquad \textbf{(1.5)}$$

where x_i is the i^{th} vector of the dataset, which is associated with a class label, y_i. Therefore, a kernel (k) can be introduced to replace the non-linear functions in **Eq. (1.5)** such that:

$$\boldsymbol{f(x) = \sum_{i=1}^{n} \alpha_i k(x, x_i) + b} \qquad \textbf{(1.6)}$$

In particular, Gaussian kernel is commonly used to increase flexibility of the classifier [103], which can be expressed as:

$$\boldsymbol{k(x, x_i) = \exp\left(-\gamma \left|\left|x - x_i\right|\right|^2\right)} \qquad \textbf{(1.7)}$$

Based on this **Eq. (1.7)**, the radius of the kernel is controlled by Υ. A small Υ (large variance) yields a nearly linear decision boundary. A proper setting of this value achieves moderate flexibility and avoids unwanted over-classification that is difficult to be generalized when more samples are recruited.

In addition, as SVM is an optimization process to maximize the margin, the flexibility of the classifier can also be determined by the tolerance of misclassification, a penalty parameter, *C*. This parameter is also useful when processing datasets with unbalanced groups. Unbalanced groups can usually cause bias during classification because classifying most samples to the majority group may yield the best accuracy. Therefore, this issue can be solved by adjusting the tolerance of misclassification (*C*) proportional to the group size. An optimal classifier based on a Gaussian kernel can be achieved by using the grid search of parameters Υ and *C* that yields the best SVM accuracy [104].

1.5.2.2. Light treatment and monitoring

To achieve integrated detection and treatment, cellular-resolution light treatment and monitoring is complementary to on-site detection, and can be achieved by the use of point-scanning instrumentation. We have mentioned confocal laser endomicroscopy (CLE) in **1.4.2**. This section also introduces considerations of treatment strategies compatible with existing CLE platforms.

As mentioned in **section 1.4.3**, light treatment can be given by photodynamic therapy (PDT) or laser ablation requiring a high irradiance. PDT has some degree of selectivity from preferential accumulation of photosensitizers, while laser ablation of the whole cell or certain subcellular areas holds better precision in cell killing. The correspondence of power density and ablative mechanisms is shown in **Fig. 1.8**.

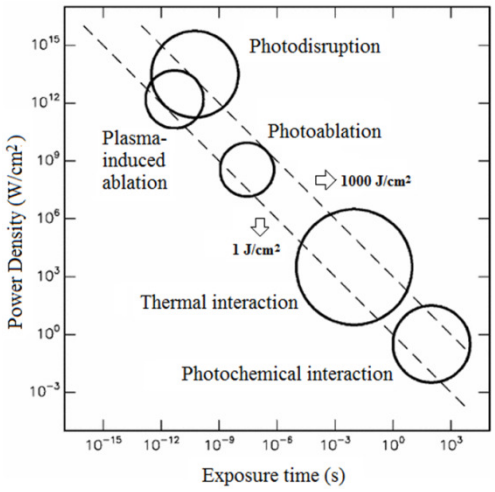

Figure 1.8 The power density and exposure time for laser ablation. (The figure was adapted from Ref. [105], with kind permission of Springer Science + Business Media).

One-photon and two-photon excitation are two common light activation principles used in fluorescence microscopy. One-photon excitation is usually coupled with confocal optics to achieve imaging sectioning capability. In contrast, ultra-short pulsed two-photon (or multi-photon) sources with high peak power of approximately 10^{11} W can provides better contrast due to the quadratic dependency of fluorescence emission on excitation [106]. Main differences between the two techniques are listed in **Table 1.8**. Among the listed characteristics, excitation volume, penetration depth, and ablation mechanisms are important considerations when using light as a treatment tool in BE. For example, a relatively larger excitation volume given by one-photon excitation may yield higher energy deposition and provide an overall better phototoxicity. However, two-photon activation can achieve a more suitable penetration depth for Barrett's epithelium, and potentially provide immediate and targeted photo-disruptive effects when the power density is sufficiently high. Details of one-photon and two-photon principles can be found in work from Zipfel *et al*. and Karotki *et al* [106,107].

Table 1.8 One-photon and two-photon excitation

Characteristics	One - photon excitation	Two-photon excitation
Light sources	Deposit the energy using *cw* or pulsed light sources in UV-VIS wavelength ranges (*e.g.* UV or Argon-ion lasers).	Deposit the energy using ultra-short (fs) pulsed near-infrared light (*e.g.* Mode-locked Ti:Sapphire lasers).
Activation	Single photon of higher energy is absorbed by the molecule. Linear dependence to excitation intensity.	Two-photons of equal energy and physical properties simultaneously produce the same energy level of single photon excitation. Quadratic dependence on excitation intensity
Excitation volume	The whole light path is activated, with the energy focused at the focal point.	Mostly activates the focal spot due to higher two-photon probability. Loss of ballistic photons in tissue may result in reduced two-photon capability.
Fluorescence emission	Linear dependence. Emission is summed from emitted photons of the light path.	Quadratic dependence. Emission is only from the focal spot.

Optimal Resolution	Lateral: diffraction limited Axial: approximately 1 µm	Lateral: diffraction limited Axial: approximately 1 µm
Penetration depth	A few micrometers due to absorption of hemoglobin and increased scattering.	A few hundred microns more than one-photon excitation due to less absorption from endogenous chromophores. The actual penetration depth may be affected by loss of ballistic photons in tissue.
Ablation mechanisms	Typically contributes to photochemical or photothermal ablation	Common light sources for photo-disruptive and plasma-mediated ablation

In summary, cellular resolution detection and treatment can be achieved by quantitative imaging analysis and classification algorithms (*e.g.* SVM) based on the morphological and textural features given by the photosensitizer. Upon diagnosis, it is followed by appropriate light activation to achieve either PDT or ablative effects. Both detection and treatment technologies can be coupled to existing CLE systems in the future for *in vivo* applications.

1.6. Dissertation overview and organization

The overall background of research questions, motivation and specific aims of the study are presented in the introduction chapter. The dissertation is organized based on the two applications using fluorescence of PDT photosensitizers, which includes five journal papers. The presentation sequence starts with (i) PDT dosimetry using time-resolved fluorescence (**Chapter 2 to 4**), followed by (ii) quantitative detection (**Chapter 5**) and (iii) treatment (**Chapter 6**) of Barrett's Esophagus. A short introduction to the paper is also given at the beginning of each article.

Chapter 2 is a review article regarding time-resolved fluorescence of PDT photosensitizers. This chapter reviews current limitations in PDT dosimetry, technologies time-resolved fluorescence, and provides literature review to examine the feasibility of using time-resolved fluorescence in monitoring PDT treatment efficacies.

Chapter 3 investigates changes of fluorescence lifetime during intracellular uptake of photosensitizers, which can be correlated with cell function and drug-molecular interactions. The results showed that the fluorescence lifetime of Photofrin is significantly shorter when it is bound to cell membrane compared

to other intracellular locations. This suggests fluorescence lifetime may be a potential indicator for drug-cell interactions.

Chapter 4 follows the topic of time-domain fluorescence lifetime technology used in **Chapter 3**. It investigates the problems of incomplete fluorescence decays that could lead to inaccurate lifetime estimation, which can be substantial when using long-lived fluorophores such as PDT photosensitizers. Analytical solutions are developed to perform correction based on measured time-resolved parameters, and validated using bulk solution experiment. Results showed the lifetime estimation can be distorted significantly when two fluorophores have comparable concentration or large differences in decay rate.

Chapters 5 and **6** investigate the feasibility of quantitative detection and treatment of BE using 5-ALA as a fluorescent marker. **Chapter 5** focuses on the detection part. 5-ALA uptake is first characterized in BE cell lines, followed by image processing, feature extraction, and classification using SVM. Results confirmed that 5-ALA does not yield targeting specificity during cellular uptake process, while yielding sufficient nucleus contrast for quantitative imaging analysis. Metaplasia and high-grade dysplasia (HGD) can be classified using two fluorescence features – eccentricity and contrast, with the sensitivity and specificity of 95% and 87%, respectively.

Chapter 6 focuses on the treatment side using the same experimental platform. Subcellular treatment involving cell nuclei, mitochondria, or whole cell is given at 3 hours after 5-ALA is administered. Cell viability is then compared between various treatment regimens, and between one-photon and two-photon irradiation. Results showed that HGD cells are more susceptible to the photosensitizer when the same light dose is given. In addition, treatment involving the photosensitizer-localized area (mitochondria) provides better killing efficacy in both cell lines. One-photon excitation also led to more photo-toxicity than two-photon excitation due to its increased excitation volume.

Chapter 7 concludes the dissertation and also presents future directions for both applications.

1.7. Contributions to articles

The research work in this dissertation is presented as five journal articles from **Chapters 2 – 6**. As for the first application – time-resolved fluorescence of photosensitizers, Professors Qiyin Fang, Michael S. Patterson, Kevin R. Diamond, and Joseph E. Hayward provided the initial ideas and guided the research direction, and I continued the development of initial ideas through literature searches, experimental design and data analysis. As for the second application – integrated detection and treatment of Barrett's Esophagus, Professors Qiyin Fang, Michael S. Patterson, and David W. Andrews proposed the initial concept and the

cellular model, and I worked on the investigation of suitable experimental methods and data interpretation.

I prepared the first drafts of articles in **Chapters 2, 3, 5, and 6** and the final manuscripts were revised based on all co-authors' feedback. For the published articles, I made required changes and generated the preliminary responses according to reviewers' comments, and the revisions were finalized by the co-authors.

In particular, Professors Michael S. Patterson, Qiyin Fang, and Joseph Hayward guided me through the initial outline of the review article (**Chapter 2**), and provided critical comments that contribute to a more comprehensive review. Prof. Kevin R. Diamond assisted in proofreading of papers in **Chapters 3 and 6**. Dr. Samir Sahli had provided valuable discussions for the paper in **Chapter 5** regarding image processing and classification techniques. Prof. Andrews' lab provided the mcerulean-3 plasmid for creating the stably transfected cell lines, and the stable cell strains were purified with the help of Liang Hong from McMaster flow cytometry facility. Cell imaging experiments were performed in McMaster Biophotonics Facility, with the initial guidance for troubleshooting from Dr. Tony Collins.

As for **Chapter 4,** Professor Qiyin Fang provided the initial ideas for the necessity of fluorescence lifetime correction. The paper was contributed equally by Regina W-K. Leung and I. I reviewed the concept of time-domain techniques and completed its introduction section. Regina guided me through the development of analytical solutions, performed data simulation, and completed the corresponding method and result sections. Then, I performed experimental validation, data analysis, and completed experimental result and discussion. The final manuscript incorporated the revisions from Prof. Qiyin Fang.

References

1. K. Kalka, H. Merk, and H. Mukhtar, "Photodynamic therapy in dermatology.," J. Am. Acad. Dermatol. **42**, 389–413; quiz 414–6 (2000).

2. R. Weinreb, E. Cotlier, U. Schmidt-erfurth, and T. Hasan, "Mechanisms of action of photodynamic therapy with verteporfin for the treatment of age-related macular degeneration," Surv. Ophthalmol. **45**, 195–214 (2000).

3. B. C. Wilson and M. S. Patterson, "The physics, biophysics and technology of photodynamic therapy.," Phys. Med. Biol. **53**, R61–109 (2008).

4. T. J. Dougherty, C. J. Gomer, B. W. Henderson, G. Jori, D. Kessel, M. Korbelik, J. Moan, and Q. Peng, "Photodynamic therapy.," J. Natl. Cancer Inst. **90**, 889–905 (1998).

5. B. C. Wilson, M. S. Patterson, and L. Lilge, "Implicit and explicit dosimetry in photodynamic therapy : a new paradigm," Lasers Med. Sci. **12**, 182–199 (1997).

6. D. E. J. G. J. Dolmans, D. Fukumura, and R. K. Jain, "Photodynamic therapy for cancer," Nat. Rev. Cancer **3**, 380 – 387 (2003).

7. M. Wilson, "Lethal photosensitisation of oral bacteria and its potential application in the photodynamic therapy of oral infections.," Photochem. Photobiol. Sci. **3**, 412–418 (2004).

8. S. B. Brown, E. A. Brown, and I. Walker, "The present and future role of photodynamic therapy in cancer treatment Photodynamic therapy," Lancet Oncol. **5**, 497–508 (2004).

9. J. R. Lakowicz, *Principles of Fluorescnece Spectroscopy*, 3rd ed. (Springer, 2006).

10. K. König, H. Wabnitz, and W. Dietel, "Variation in the fluorescence decay properties of haematoporphyrin derivative during its conversion to photoproducts.," J. Photochem. Photobiol. B. **8**, 103–11 (1990).

11. H. Schneckenburger, R. Steiner, and A. Rueck, "In vivo photoproduct formation during PDT with ALA-induced endogenous porphyrins," In Vivo (Brooklyn). **18**, 287–290 (1993).

12. A. C. Rueck, "FLIM and SLIM for molecular imaging in PDT," Proc. SPIE **5700**, 182–187 (2005).

13. N. Ramanujam, "Fluorescence spectroscopy of neoplastic and non-neoplastic tissues," Neoplasia **2**, 89 – 117 (2000).

14. A. Ruck, C. Hulshoff, I.Kinzler, W. Becker, and R. Steiner, "SLIM : A new method for molecular imaging," Microsc. Res. Tech. **492**, 485–492 (2007).

15. C. Hopper, A. Kübler, H. Lewis, I. B. Tan, and G. Putnam, "mTHPC-mediated photodynamic therapy for early oral squamous cell carcinoma.," Int. J. Cancer **111**, 138–46 (2004).

16. A. Ruck, "Fluorescence lifetime imaging in PDT. An overview," Med. Laser Appl. **20**, 125–129 (2005).

17. D. Mitton and R. Ackroyd, "Photodynamic therapy in oesophageal carcinoma : an overview A brief history of photodynamic therapy," Photochem. Photobiol. Sci. **3**, 839–850 (2004).

18. P. G. Calzavara-Pinton, M. Venturini, and R. Sala, "Photodynamic therapy: update 2006. Part 1: Photochemistry and photobiology.," J. Eur. Acad. Dermatol. Venereol. **21**, 293–302 (2007).

19. J. Morgan and A. Oseroff, "Mitochondria-based photodynamic anti-cancer therapy.," Adv. Drug Deliv. Rev. **49**, 71–86 (2001).

20. R. Hilf, "Mitochondria are targets of photodynamic therapy.," J. Bioenerg. Biomembr. **39**, 85–9 (2007).

21. N. L. Oleinick, R. L. Morris, and I. Belichenko, "The role of apoptosis in response to photodynamic therapy: what, where, why, and how," Photochem. Photobiol. Sci. **1**, 1–21 (2002).

22. R. D. Almeida, B. J. Manadas, A. P. Carvalho, and C. B. Duarte, "Intracellular signaling mechanisms in photodynamic therapy.," Biochim. Biophys. Acta **1704**, 59–86 (2004).

23. E. H. Tschen, D. S. Wong, D. M. Pariser, F. E. Dunlap, A. Houlihan, and M. B. Ferdon, "Photodynamic therapy using aminolaevulinic acid for patients with nonhyperkeratotic actinic keratoses of the face and scalp: phase IV multicentre clinical trial with 12-month follow up.," Photobiology **155**, 1262–9 (2006).

24. C. S. Loh, a J. MacRobert, J. Bedwell, J. Regula, N. Krasner, and S. G. Bown, "Oral versus intravenous administration of 5-aminolaevulinic acid for photodynamic therapy.," Br. J. Cancer **68**, 41–51 (1993).

25. J. C. Kennedy, P. Nadeau, Z. J. Petryka, R. H. Pottier, and G. Weagle, "Clearance times of porphyrin derivatives from mice as measured by in vivo fluorescence spectroscopy," Photochem. Photobiol. **55**, 729–34 (1992).

26. J. Bedwell, a J. MacRobert, D. Phillips, and S. G. Bown, "Fluorescence distribution and photodynamic effect of ALA-induced PP IX in the DMH rat colonic tumour model.," Br. J. Cancer **65**, 818–24 (1992).

27. C. J. Kelty, N. J. Brown, M. W. R. Reed, and R. Ackroyd, "The use of 5-aminolaevulinic acid as a photosensitiser in photodynamic therapy and photodiagnosis," Photochem. Photobiol. Sci. **1**, 158–168 (2002).

28. R. Ackroyd, N. Brown, D. Vernon, D. Roberts, T. Stephenson, S. Marcus, C. Stoddardl, and M. Reed, "5-aminolevulinic acid photosensitization of dysplastic Barrett's esophagus: a pharmacokinetic study," Photochem Photobiol. **70**, 656–662 (1999).

29. C. J. Kelty, R. Ackroyd, N. J. Brown, S. B. Brown, and M. W. R. Reed, "Comparison of high- vs low-dose 5-aminolevulinic acid for photodynamic therapy of Barrett's esophagus.," Surg. Endosc. **18**, 452–8 (2004).

30. J. C. Kennedy, R. H. Pottier, and D. C. Pross, "Photodynamic therapy with endogenous protoporphyrin IX: basic principles and present clinical experience.," J. Photochem. Photobiol. B. **6**, 143–8 (1990).

31. P. Hinnen, "Biochemical aspects of ALA-PDT basic mechanisms and optimization for the treatment of Barrett ' s oesophagus," (2001).

32. J. Webber, Y. Luo, R. Crilly, D. Fromm, and D. Kessel, "An apoptotic response to photodynamic therapy with endogenous protoporphyrin in vivo.," J. Photochem. Photobiol. B. **35**, 209–11 (1996).

33. B. B. Noodt, K. Berg, T. Stokke, Q. Peng, and J. M. Nesland, "Apoptosis and necrosis induced with light and 5-aminolaevulinic acid-derived protoporphyrin IX.," Br. J. Cancer **74**, 22–9 (1996).

34. P. Hinnen, F. W. M. De Rooij, W. C. J. Hop, A. Edixhoven, H. Van Dekken, J. H. P. Wilson, and P. D. Siersema, "Timing of 5-aminolaevulinic acid-induced photodynamic therapy for the treatment of patients with Barrett's oesophagus," J. Photochem. Photobiol. B Biol. **68**, 8–14 (2002).

35. K. Lang, K. Bolsen, W. Stahl, T. Ruzicka, H. Sies, P. Lehmann, and C. Fritsch, "The 5-aminolevulinic acid-induced porphyrin biosynthesis in benign and malignant cells of the skin.," J. Photochem. Photobiol. B. **65**, 29–34 (2001).

36. M. C. Milanetto, H. Imasato, and J. R. Perussi, "The importance of protoporphyrin IX efflux for ALA-PDT dosimetry," Laser Phys. Lett. **6**, 611–615 (2009).

37. M. T. Jarvi, M. J. Niedre, M. S. Patterson, and B. C. Wilson, "Singlet oxygen luminescence dosimetry (SOLD) for photodynamic therapy: current status, challenges and future prospects.," Photochem. Photobiol. **82**, 1198–210 (2006).

38. J. L. Sandell and T. C. Zhu, "A review of in-vivo optical properties of human tissues and its impact on PDT," **4**, 773–787 (2012).

39. K. R. Diamond, P. P. Malysz, J. E. Hayward, and M. S. Patterson, "Quantification of fluorophore concentration in vivo using two simple fluorescence-based measurement techniques.," J. Biomed. Opt. **10**, 024007 (2005).

40. K. R. Diamond, M. S. Patterson, and T. J. Farrell, "Quantification of fluorophore concentration in tissue-simulating media by fluorescence measurements with a single optical fiber.," Appl. Opt. **42**, 2436–42 (2003).

41. J. S. Dysart and M. S. Patterson, "Photobleaching kinetics, photoproduct formation, and dose estimation during ALA induced PpIX PDT of MLL cells under well oxygenated and hypoxic conditions.," Photochem. Photobiol. Sci. **5**, 73–81 (2006).

42. J. S. Dysart and M. S. Patterson, "Characterization of Photofrin photobleaching for singlet oxygen dose estimation during photodynamic therapy of MLL cells in vitro.," Phys. Med. Biol. **50**, 2597–616 (2005).

43. J. S. Dysart, M. S. Patterson, T. J. Farrell, and G. Singh, "Relationship between mTHPC fluorescence photobleaching and cell viability during in vitro photodynamic treatment of DP16 cells.," Photochem. Photobiol. **75**, 289–95 (2002).

44. N. Thekkek, S. Anandasabapathy, and R. Richards-Kortum, "Optical molecular imaging for detection of Barrett's-associated neoplasia.," World J. Gastroenterol. **17**, 53–62 (2011).

45. E. Sihvo, M. Luostarinen, and J. Salo, "Fate of patients with adenocarcinoma of the esophagus and the esophagogastric junction: a population-based analysis.," Am. J. Gastroenterol. **99**, 419–24 (2004).

46. B. C. Wilson, "Detection and treatment of dysplasia in Barrett's esophagus: a pivotal challenge in translating biophotonics from bench to bedside.," J. Biomed. Opt. **12**, 051401 (2007).

47. S. J. Spechler, "The Natural History of Dysplasia and Cancer in Barrett's Esophagus," J. Clin. Gastroenterol. **36**, 2–5 (2003).

48. J. Dent, H. B. El-Serag, M. Wallander, and S. Johansson, "Epidemiology of gastro-oesophageal reflux disease: a systematic review.," Gut **54**, 710–7 (2005).

49. C. P. Wild and L. J. Hardie, "Reflux, Barrett's oesophagus and adenocarcinoma: burning questions.," Nat. Rev. Cancer **3**, 676–84 (2003).

50. R. Fiocca, L. Mastracci, M. Milione, P. Parente, and V. Savarino, "Microscopic esophagitis and Barrett's esophagus: the histology report.," Dig. Liver Dis. **43 Suppl 4**, S319–30 (2011).

51. K. K. Wang and R. E. Sampliner, "Updated guidelines 2008 for the diagnosis, surveillance and therapy of Barrett's esophagus.," Am. J. Gastroenterol. **103**, 788–97 (2008).

52. J. R. Goldblum, "Barrett's esophagus and Barrett's-related dysplasia.," Mod. Pathol. **16**, 316–24 (2003).

53. D. E. Low and A. Bodnar, "Update on clinical impact, documentation, and management of complications associated with esophagectomy.," Thorac. Surg. Clin. **23**, 535–50 (2013).

54. G. Portale, J. A. Hagen, J. H. Peters, L. S. Chan, S. R. DeMeester, T. A. K. Gandamihardja, and T. R. DeMeester, "Modern 5-year survival of resectable

esophageal adenocarcinoma: single institution experience with 263 patients.," J. Am. Coll. Surg. **202**, 588–96; discussion 596–8 (2006).

55. P. K. Nijhawan and K. K. Wang, "Endoscopic mucosal resection for lesions with endoscopic features suggestive of malignancy and high-grade dysplasia within Barrett's esophagus.," Gastrointest. Endosc. **52**, 328–32 (2000).

56. C. J. Kelty, R. Ackroyd, N. J. Brown, T. J. Stephenson, C. J. Stoddard, and M. W. R. Reed, "Endoscopic ablation of Barrett's oesophagus: a randomized-controlled trial of photodynamic therapy vs. argon plasma coagulation.," Aliment. Pharmacol. Ther. **20**, 1289–96 (2004).

57. G. S. Dulai, D. M. Jensen, G. Cortina, L. Fontana, and A. Ippoliti, "Randomized trial of argon plasma coagulation vs. multipolar electrocoagulation for ablation of Barrett's esophagus," Gastrointest. Endosc. **61**, 232–240 (2005).

58. K. B. Dunbar, P. Okolo, E. Montgomery, and M. I. Canto, "Confocal laser endomicroscopy in Barrett's esophagus and endoscopically inapparent Barrett's neoplasia: a prospective, randomized, double-blind, controlled, crossover trial.," Gastrointest. Endosc. **70**, 645–54 (2009).

59. R. Kiesslich, L. Gossner, M. Goetz, A. Dahlmann, M. Vieth, M. Stolte, A. Hoffman, M. Jung, B. Nafe, P. R. Galle, and M. F. Neurath, "In vivo histology of Barrett's esophagus and associated neoplasia by confocal laser endomicroscopy.," Clin. Gastroenterol. Hepatol. **4**, 979–87 (2006).

60. H. C. Wolfsen, "Present Status of Photodynamic Therapy for High-Grade Dysplasia in Barrett's Esophagus," J. Clin. Gastroenterol. **39**, 189–202 (2005).

61. L. Mastracci, P. Spaggiari, F. Grillo, P. Zentilin, P. Dulbecco, P. Ceppa, P. Baccini, C. Mansi, V. Savarino, and R. Fiocca, "Microscopic esophagitis in gastro-esophageal reflux disease: individual lesions, biopsy sampling, and clinical correlations.," Virchows Arch. **454**, 31–9 (2009).

62. T. J. Muldoon, N. Thekkek, D. Roblyer, D. Maru, N. Harpaz, J. Potack, S. Anandasabapathy, and R. Richards-Kortum, "Evaluation of quantitative image analysis criteria for the high-resolution microendoscopic detection of neoplasia in Barrett's esophagus.," J. Biomed. Opt. **15**, 026027 (2010).

63. M. a Kara and J. J. Bergman, "Autofluorescence imaging and narrow-band imaging for the detection of early neoplasia in patients with Barrett's esophagus.," Endoscopy **38**, 627–31 (2006).

64. L. M. Wong Kee Song, D. G. Adler, B. Chand, J. D. Conway, J. M. B. Croffie, J. a Disario, D. S. Mishkin, R. J. Shah, L. Somogyi, W. M. Tierney, and B. T. Petersen, "Chromoendoscopy.," Gastrointest. Endosc. **66**, 639–49 (2007).

65. Y. Amano, Y. Kushiyama, S. Ishihara, T. Yuki, Y. Miyaoka, N. Yoshino, N. Ishimura, H. Fujishiro, K. Adachi, R. Maruyama, M. A. K. Rumi, and Y. Kinoshita, "Crystal violet chromoendoscopy with mucosal pit pattern diagnosis is useful for surveillance of short-segment Barrett's esophagus.," Am. J. Gastroenterol. **100**, 21–6 (2005).

66. S. Brand, T. D. Wang, K. T. Schomacker, J. M. Poneros, G. Y. Lauwers, C. C. Compton, M. C. Pedrosa, and N. S. Nishioka, "Detection of high-grade dysplasia in Barrett's esophagus by spectroscopy measurement of 5-aminolevulinic acid-induced protoporphyrin IX fluorescence.," Gastrointest. Endosc. **56**, 479–87 (2002).

67. M. A. Kara, R. S. DaCosta, C. J. Streutker, N. E. Marcon, J. J. G. H. M. Bergman, and B. C. Wilson, "Characterization of tissue autofluorescence in Barrett's esophagus by confocal fluorescence microscopy.," Dis. Esophagus **20**, 141–50 (2007).

68. M. H. Lee, K. Buterbaugh, R. Richards-Kortum, and S. Anandasabapathy, "Advanced endoscopic imaging for Barrett's Esophagus: current options and future directions.," Curr. Gastroenterol. Rep. **14**, 216–25 (2012).

69. K. B. Dunbar and M. I. Canto, "Confocal endomicroscopy," Tech. Gastrointest. Endosc. **12**, 90–99 (2010).

70. S. Lam, T. Kennedy, M. Unger, Y. E. Miller, D. Gelmont, V. Rusch, B. Gipe, D. Howard, J. C. LeRiche, a Coldman, and a F. Gazdar, "Localization of bronchial intraepithelial neoplastic lesions by fluorescence bronchoscopy.," Chest **113**, 696–702 (1998).

71. A. L. McCallum, J. T. Jenkins, D. Gillen, and R. G. Molloy, "Evaluation of autofluorescence colonoscopy for the detection and diagnosis of colonic polyps.," Gastrointest. Endosc. **68**, 283–90 (2008).

72. M. A. Kara, F. P. Peters, F. J. W. ten Kate, S. J. van Deventer, P. Fockens, and J. J. G. H. M. Bergman, "Endoscopic video autofluorescence imaging may improve the detection of early neoplasia in patients with Barrett's esophagus," Gastrointest. Endosc. **61**, 679–685 (2005).

73. D. Huang, E. A. Swanson, C. P. Lin, J. S. Schuman, W. G. Stinson, W. Chang, M. R. Hee, T. Flotte, K. Gregory, C. A. Puliafito, G. Fujimoto, and E. A. Swanson, "Optical coherence tomography," Science (80-.). **254**, 1178–1181 (1991).

74. B. E. Bouma, G. J. Tearney, C. C. Compton, and N. S. Nishioka, "High-resolution imaging of the human esophagus and stomach in vivo using optical coherence tomography," Gastrointest. Endosc. **51**, 467–474 (2000).

75. M. J. Cobb, J. H. Hwang, M. P. Upton, Y. Chen, B. K. Oelschlager, D. E. Wood, M. B. Kimmey, and X. Li, "Imaging of subsquamous Barrett's epithelium with ultrahigh-resolution optical coherence tomography: a histologic correlation study.," Gastrointest. Endosc. **71**, 223–30 (2010).

76. C. Pitris, C. Jesser, S. a Boppart, D. Stamper, M. E. Brezinski, and J. G. Fujimoto, "Feasibility of optical coherence tomography for high-resolution imaging of human gastrointestinal tract malignancies.," J. Gastroenterol. **35**, 87–92 (2000).

77. M. Wojtkowski, V. J. Srinivasan, T. H. Ko, J. G. Fujimoto, A. Kowalczyk, and J. S. Duker, "Ultrahigh-resolution, high-speed, Fourier domain optical coherence tomography and methods for dispersion compensation," Opt. Express **12**, 707–709 (2004).

78. T. J. Muldoon, M. C. Pierce, D. L. Nida, M. D. Williams, A. Gillenwater, and R. Richards-Kortum, "Subcellular-resolution molecular imaging within living tissue by fiber microendoscopy.," Opt. Express **15**, 16413–23 (2007).

79. M. I. Canto, "Endomicroscopy of Barrett's Esophagus.," Gastroenterol. Clin. North Am. **39**, 759–69 (2010).

80. R. E. Sampliner, B. Fennerty, and H. S. Garewal, "Reversal of Barrett's esophagus with acid suppression and multipolar electrocoagulation: preliminary results," Gastrointest. Endosc. **44**, 532–535 (1996).

81. J. J. Nigro, T. R. Demeester, S. R. DeMeester, J. H. Peters, S. Oberg, J. Theisen, M. Kiyabu, P. F. Crookes, and C. G. Bremner, "Prevalence and location of nodal metastases in distal esophageal adenocarcinoma confined to the wall: implications for therapy," Gen. Thorac. Surg. **117**, 16–25 (1999).

82. H. J. Stein, M. Feith, J. Mueller, M. Werner, and J. Ru, "Limited resection for early adenocarcinoma in Barrett's esophagus," Ann. Surg. **232**, 733–742 (2000).

83. R. Soetikno, T. Kaltenbach, R. Yeh, and T. Gotoda, "Endoscopic mucosal resection for early cancers of the upper gastrointestinal tract.," J. Clin. Oncol. **23**, 4490–4498 (2005).

84. C. J. Kelty, S. L. Marcus, and R. Ackroyd, "Photodynamic therapy for Barrett's esophagus: a review," Dis. Esophagus **15**, 137–144 (2002).

85. B. F. Overholt, K. K. Wang, J. S. Burdick, C. J. Lightdale, M. Kimmey, H. R. Nava, M. V Sivak, N. Nishioka, H. Barr, N. Marcon, M. Pedrosa, M. P. Bronner, M. Grace, and M. Depot, "Five-year efficacy and safety of photodynamic therapy with Photofrin in Barrett's high-grade dysplasia.," Gastrointest. Endosc. **66**, 460–8 (2007).

86. C. Saul, E. B. Toneloto, C. B. Rynkowski, C. Blaya, and P. Alegre, "High power setting argon plasma coagulation for the eradication of Barrett's esophagus," Am. J. Gastroenterol. **95**, 1661–1668 (2000).

87. J. P. Byrne, G. R. Armstrong, and S. E. A. Attwood, "Restoration of the normal squamous lining in Barrett's esophagus by argon beam plasma coagulation," Am. J. Gastroenterol. **93**, 1–6 (1998).

88. F. G. I. van Vilsteren, R. E. Pouw, S. Seewald, L. Alvarez Herrero, C. M. T. Sondermeijer, M. Visser, F. J. W. Ten Kate, K. C. Yu Kim Teng, N. Soehendra, T. Rösch, B. L. a M. Weusten, and J. J. G. H. M. Bergman, "Stepwise radical endoscopic resection versus radiofrequency ablation for Barrett's oesophagus with high-grade dysplasia or early cancer: a multicentre randomised trial.," Gut **60**, 765–73 (2011).

89. D. E. Fleischer, B. F. Overholt, V. K. Sharma, A. Reymunde, M. B. Kimmey, R. Chuttani, K. J. Chang, R. Muthasamy, C. J. Lightdale, N. Santiago, D. K. Pleskow, P. J. Dean, and K. K. Wang, "Endoscopic radiofrequency ablation for Barrett's esophagus : 5-year outcomes from a prospective multicenter trial," Endoscopy **42**, 781–789 (2010).

90. P. E. Claydon and R. Ackroyd, "5-Aminolaevulinic acid-induced photodynamic therapy and photodetection in Barrett's esophagus," Dis. Esophagus **17**, 205–212 (2004).

91. A. Vogel and V. Venugopalan, "Mechanisms of pulsed laser ablation of biological tissues.," Chem. Rev. **103**, 577–644 (2003).

92. E. Endlicher, R. Knuechel, T. Hauser, R. Szeimies, J. Schölmerich, and H. Messmann, "Endoscopic fluorescence detection of low and high grade dysplasia in Barrett's oesophagus using systemic or local 5-aminolaevulinic acid sensitisation," Gut **48**, 314–319 (2001).

93. S. R. Kantelhardt, H. Diddens, J. Leppert, V. Rohde, G. Hüttmann, and A. Giese, "Multiphoton excitation fluorescence microscopy of 5-aminolevulinic acid induced fluorescence in experimental gliomas.," Lasers Surg. Med. **40**, 273–81 (2008).

94. K. S. Garman, R. C. Orlando, and X. Chen, "Review: Experimental models for Barrett's esophagus and esophageal adenocarcinoma.," Am. J. Physiol. Gastrointest. Liver Physiol. **302**, G1231–43 (2012).

95. L. M. F. Merlo, R. E. Kosoff, K. L. Gardiner, and C. C. Maley, "An in vitro co-culture model of esophageal cells identifies ascorbic acid as a modulator of cell competition.," BMC Cancer **11**, 461 – 471 (2011).

96. Y. Miki, K. Ono, S. Hata, T. Suzuki, H. Kumamoto, and H. Sasano, "The advantages of co-culture over mono cell culture in simulating in vivo environment.," J. Steroid Biochem. Mol. Biol. **131**, 68–75 (2012).

97. Y. Su, X. Chen, M. Klein, M. Fang, S. Wang, C. S. Yang, and R. K. Goyal, "Phenotype of columnar-lined esophagus in rats with esophagogastroduodenal anastomosis: similarity to human Barrett's esophagus.," Lab. Investig. **84**, 753–65 (2004).

98. M. C. Palanca-Wessels, M. T. Barrett, P. C. Galipeau, K. L. Rohrer, B. J. Reid, and P. S. Rabinovitch, "Genetic analysis of long-term Barrett's esophagus epithelial cultures exhibiting cytogenetic and ploidy abnormalities," Gastroenterology **114**, 295–304 (1998).

99. M. C. a Palanca-Wessels, A. Klingelhutz, B. J. Reid, T. H. Norwood, K. E. Opheim, T. G. Paulson, Z. Feng, and P. S. Rabinovitch, "Extended lifespan of Barrett's esophagus epithelium transduced with the human telomerase catalytic subunit: a useful in vitro model.," Carcinogenesis **24**, 1183–90 (2003).

100. R. E. Kosoff, K. L. Gardiner, L. M. F. Merlo, K. Pavlov, A. K. Rustgi, and C. C. Maley, "Development and characterization of an organotypic model of Barrett's esophagus.," J. Cell. Physiol. **227**, 2654–9 (2012).

101. R. C. Gonzalez, R. E. Woods, and P. Hall, *Digital Image Processing*, 2nd ed. (Prentice Hall, 2008).

102. V. N. Vapnik, "An overview of statistical learning theory.," IEEE Trans. Neural Netw. **10**, 988–99 (1999).

103. C. Hsu, C. Chang, and C. Lin, "A Practical Guide to Support Vector Classification," **1**, 1–16 (2010).

104. A. Ben-hur and J. Weston, "A user's guide to support vector machines," Methods Mol. Biol. **209**, 223–239 (2010).

105. M. H. Niemz, *Laser-Tissue Interactions: Fundamentals and Applications. Chapter 3 - Interaction Mechanisms*, 3rd ed. (Springer, 2004), p. 46.

106. W. R. Zipfel, R. M. Williams, and W. W. Webb, "Nonlinear magic: multiphoton microscopy in the biosciences.," Nat. Biotechnol. **21**, 1369–77 (2003).

107. A. Karotki, M. Khurana, J. R. Lepock, and B. C. Wilson, "Simultaneous two-photon excitation of photofrin in relation to photodynamic therapy.," Photochem. Photobiol. **82**, 443–52 (2006).

Chapter 2.

Paper I – Time-resolved fluorescence in photodynamic therapy

Shu-Chi Allison Yeh[1], Michael S. Patterson[2], Joseph E. Hayward[2], and Qiyin Fang[1,3,*]

[1]School of Biomedical Engineering, McMaster University, 1280 Main Street West, Hamilton, ON, L8S 4K1, Canada

[2]Department of Medical Physics and Applied Radiation Sciences, McMaster University

[3]Department of Engineering Physics, McMaster University

Published in Photonics; 1(4):530-564, 2014

Introduction to paper I

This chapter summarizes fundamental processes of photodynamic therapy (PDT) and associated PDT dosimetry schemes. Then, discusses the potential of using time-resolved fluorescence (TRF) technique in PDT dosimetry.

Recent time-resolved fluorescence studies on interactions between PDT photosensitizers and biomolecules both *in vitro* and *in vivo* are summarized and critically reviewed. From *in vitro* studies, TRF has been shown to be able to reveal drug bindings to subcellular molecules and the changes of active amount of photosensitizers, such as photoproduct formation or photobleaching. *In vivo* imaging also studies endogenous fluorophores for probing cell responses, and the effects of complex microenvironment such as oxygenation and pH.

Based on the outcome of the studies, potential PDT dosimetry scheme of incorporating time-resolved fluorescence from photosensitizers, their photoproducts, and endogenous fluorescence of the targeted tissue have been proposed. Moreover, challenges and advances of TRF-based PDT dosimetry are discussed, including issues in data analysis, tissue optics, and instrumentation development.

This work provides an overview of potential indications of TRF in PDT treatment monitoring, and addresses potential challenges. The targeted audience of this review may include researchers working on TRF-based cancer diagnosis and treatment monitoring using photosensitizers or any contrast agent, and /or using TRF as a potential tool to probe cellular and tissue responses, and/or TRF instrumentation development for clinical applications. The manuscript was prepared initially as an independent study course (BME 799) supervised by Dr. Hayward. The report was written by me and then further developed into a comprehensive review in this subject area by the co-authors.

Contents of Paper I

Abstract

Photodynamic therapy (PDT) has been used clinically for treating various diseases including malignant tumors. The main advantages of PDT over traditional cancer treatments are attributed to the localized effects of the photochemical reactions by selective illumination, which then generate reactive oxygen species and singlet oxygen molecules that lead to cell death. To date, over- or under-treatment still remains one of the major challenges in PDT due to the lack of robust real-time dose monitoring techniques. Time-resolved fluorescence (TRF) provides fluorescence lifetime profiles of the targeted fluorophores. It has been demonstrated that TRF offers supplementary information in drug-molecular interactions and cell responses compared to steady-state intensity acquisition. Moreover, fluorescence lifetime itself is independent of the light path; thus it overcomes the artifacts given by diffused light propagation and detection geometries. In this review, principles of PDT and TRF technologies are summarized, followed by elaborating the current progress in TRF- PDT research. In particular, in order to examine the feasibility of using TRF in PDT dosimetry, this report emphasizes on the correlation between time-resolved measurements and PDT dosimetric factors, as well as discussion of instrumentation and data analysis issues in the context of clinical implementation.

2.1. Introduction

Photodynamic therapy (PDT) has been applied in various clinical fields including dermatology [1], age-related macular degeneration [2], oncology [3], *etc.* In treatment of malignant lesions, it was first used for treating superficial bladder cancer [4], and subsequently approved for esophageal [5], lung [6], and high-grade dysplasia of Barrett's Esophagus [7] by the use of the photosensitizer Photofrin®. Treating skin basal cell carcinomas with 5-aminolevulinic acid (5-ALA) administration has been shown to have high efficacy and was approved in Europe [5]. Other ongoing clinical trials include prostate [8], ovarian [9], and head/neck cancers [10,11]. The histories and principles of PDT were reviewed in detail by Dougherty [12], MacDonald [13], Brown [5], and Wilson [3].

Unlike traditional methods such as chemotherapy and radiotherapy, PDT allows a relatively higher degree of specificity by targeting malignant and pre-malignant cells. It is also preferred when surgical removal is considered risky in certain cases such as esophageal [14] and brain tumors [15,16]. The specificity of PDT is achieved by a two-fold process: the drug (*i.e.*, photosensitizer, which will be used interchangeably here) is first "preferentially" retained in tumor cells due to higher metabolic activities and a leaky vasculature at the tumor sites [12]. In addition, preferentially treating malignant/tumor tissue over normal tissue can be achieved by selective illumination of the target tissue volume by light sources matching the absorption peak of the photosensitizer. PDT-induced cellular effect can be achieved through two pathways: (i) Drugs in their triplet excited state couple with ground stage oxygen molecules (Type II PDT) and produce cytotoxic singlet oxygen. Due to its short diffusion range, it ultimately leads to apoptotic cell death and reduces unwanted damage to normal tissue. There are different apoptosis pathways induced by PDT, including the activation of plasma membrane death receptors, mitochondria, lysosomes, and endoplasmic reticulum (ER), which are all potential photosensitizer binding sites. Photosensitizers binding to these subcellular organelles can trigger cascade reactions involving proteins regulating apoptosis (e.g., Bcl-2 family), release of cathepsins (binding to lysosomes) and Ca^{2+} (binding to ER). These apoptotic mechanisms are preferred to necrotic cell death, but it is subject to cell types, intracellular photosensitizer localization, overall dose, and oxygenation [17–19]. (ii) Free radicals such as hydroperoxides can also be generated when photosensitizers in their triplet state interact with biological substrates (Type I PDT). This involves a one-electron oxidation-reduction reaction that produces reactive oxygen species (ROS), and consequently causes necrotic damage in most cases [20]. Photochemical processes of PDT have been reviewed extensively in work from Oleinick *et al.* and Calzavara-Pinton *et al.* [17,21].

2.1.1. Limitation factors in PDT dosimetry

As implied by its working mechanism, the efficacy of PDT depends strongly on factors that directly manipulate drug-tissue interactions, including (i) local concentration of the photosensitizer, (ii) the amount of light it absorbs (fluence), and (iii) oxygenation status of the lesion [3]. The effective dosage is eventually altered by additional biological factors such as different drug uptake [22–24], various tissue optical properties [25], changes in vasculature and perfusion [26,27], and inconsistencies in tissue oxygenation [28], as well as unexpected photophysical and photochemical changes of photosensitizers [29–31]. The schematics of the three main dose factors are illustrated in **Figure 2.1(a)**, and the interdependencies of dose factors [32] are summarized in **Table 2.1**. These interdependencies yield a problem: an optimum dose cannot be

provided based on the current clinical standards using prescribed drug and light doses. In other words, real-time monitoring of dose parameters to account for the interdependency of these factors may minimize the risks of collateral damage (overdose) and cancer recurrence (underdose). Systematic reviews of PDT dosimetry can be found in work by Wilson and Patterson [3,32].

Table 2.1 Interdependencies of Dose Factors

Dose Factors	Interdependencies	Results
Photosensitizer	Individual variability	Variation in uptake, local location and concentration;
	Light fluence	Large extinction coefficient leads to self-shielding from light
	Oxygen	Chemically deplete oxygen molecules
Light Fluence	Individual variability	Variation in distribution
	Photosensitizers	High fluence rate can photobleach photosensitizers
	Oxygen	High fluence rate can deplete oxygen molecules [33]
Oxygen	Individual variability	Variation in vasculature, perfusion and oxygen saturation
	Photosensitizer	Variation in photobleaching rate
	PDT treatment	Potential vasculature occlusion that reduces oxygen supply

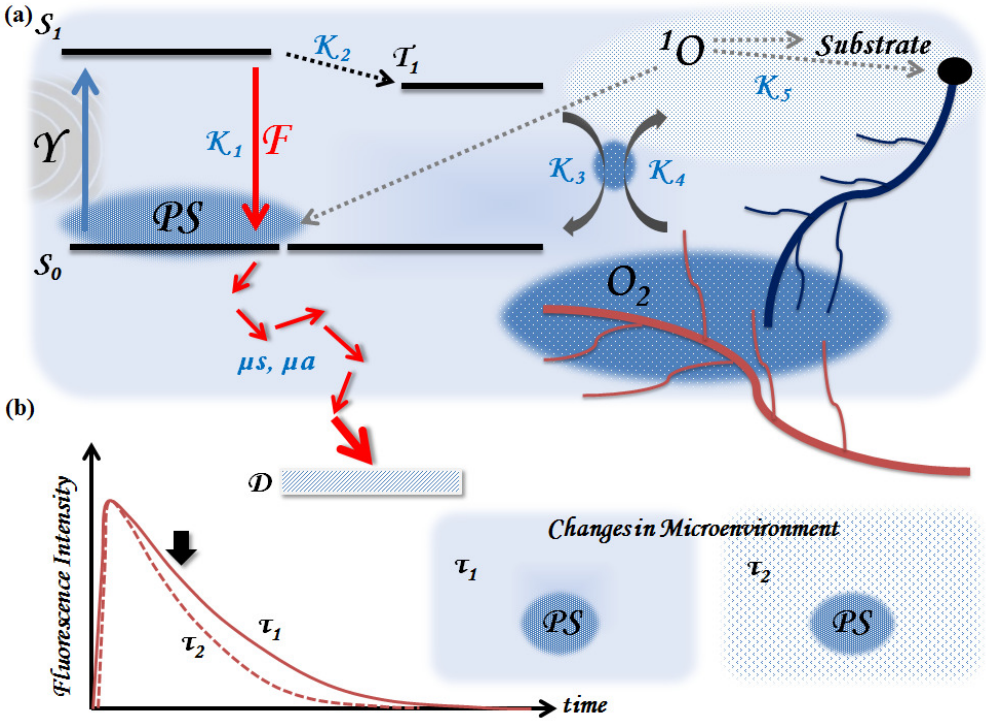

Figure 2.1(a) Schematics of PDT principles and the interdependencies between dose factors. The photosensitizers (*PS*) are pumped to an excited state (S_1) by the light source (Υ). With intersystem crossing, *PS* at the triplet excited state (T_1) go through energy transfer with the ground state oxygen molecules (O_2) and yield cytotoxic singlet oxygen ($^1O_2$). $^1O_2$ eventually result in various treatment effect including apoptosis/ necrosis, and vasculature occlusion. During the PDT procedures, all of the following factors contribute to challenges in dosimetry, including the interdependencies of dose factors (as indicated in **Table 2.1**), dynamics in the PDT process (various rate constants, *K*), and heterogeneous tissue optical properties (μ_s,μ_a) that affects both light delivery (Υ) and detection (*D*). (b) Steady-state fluorescence only measures a single time point during the decay dynamics (as indicated by the black arrow). Time-resolved fluorescence decay measures the temporal profiles that are sensitive to non-radiative energy transfer such as the changes in microenvironment and drug-molecular interactions (as indicated by τ_1 and τ_2).

As mentioned previously, local drug concentration is one of the major factors that affects treatment efficacy. Fluorescence emission of the photosensitizer has been considered as a good candidate to reflect local drug concentration in PDT [34,35], which may mitigate its dosimetric dilemma. These strategies include explicit dosimetric approaches that measure the main influencing factors independently [36]; implicit approaches, which take every interdependency into account and eventually model an indirect parameter (photobleaching) to reflect singlet oxygen production [29,37,38]; and direct

dosimetry that measures the phosphorescence to reveal singlet oxygen concentration [39]. Descriptions and limitations of each technique are summarized in **Table 2.2**. Nonetheless, there still exists a major challenge in steady-state fluorescence measurement: the measured fluorescence intensity suffers from intensity artifacts due to heterogeneity of tissue optical properties, changes in local environment, unknown chromophores and photoproducts of the original photosensitizing agents with overlapped spectra, and detection geometry [35]. That is**,** although analytical models have been proposed to solve light propagation before entering the detector [25], the corrected steady-state signal may not be sufficient to represent drug–molecular interactions and tissue response. As a result, investigation of physiological (e.g., local environment) and photosensitizer changes (e.g., photoproduct formation) is still required to interpret local drug concentration and effectiveness.

Table 2.2 Dose metrics of PDT

Dose metrics	Measured Parameters	Limitations
Explicit	Main dose factors: Photosensitizer concentration; light fluence; oxygen concentration	Difficult to acquire complete data set and require a model to combine all these for the effective dose; ignored all microdosimetric changes induced from interdependencies of dose factors [32]
Implicit	Photobleaching	Need photosensitizers or a second reporter that can be photobleached; Need to know the degree of photosensitizer coupling to cytotoxic photoproduct (*e.g.* $^1O_2$); Accurate modeling in tissue optics is required
Direct	Singlet oxygen phosphorescence	Low SNR and technically difficult [39,40]

2.1.2. The potential role of time-resolved fluorescence (TRF) for PDT dosimetry

TRF Fluorescence lifetime (τ) can be defined as the average time a fluorophore remains in the excited state after excitation; in other words, lifetime is the time it takes for the number of excited molecules to decay to 1/e of the original population. The decay of the intensity as a function of time can be expressed as $I_t = Ae^{-t/\tau}$, where I is the intensity at time t, and A is the normalization term [41]. TRF parameters τ and A have been used to probe a range of biological phenomena [42–44] due to the following reason. The rate of de-

excitation of the fluorophore depends on the total rate constant of both radiative (fluorescence) and non-radiative (*i.e*., energy transfer) processes, as illustrated in **Fig. 2.1(a).** In other words, the decay dynamics are sensitive to intermolecular interactions and changes of adjacent microenvironment, while relatively independent of the artifact existing in the steady-state measurements [42], as illustrated in **Fig. 2.1(b).** For example, photosensitizers can exhibit various degrees of toxicity when they bind to different intracellular organelles, or form aggregates and photoproducts. Nevertheless, these events yield similar emission spectra and cannot be detected using steady-state measurement. Therefore, additional contrast based on time-domain parameters may help distinguish these changes, and reveal the drug-molecular interactions for further correlation with treatment efficacy [31,45]. Note that TRF measurements of photosensitizers could be performed with the same wavelength used for treatment, providing convenience for treatment monitoring. In the following sections, the principles of time-domain fluorescence will be briefly summarized (**Section 2.2**), followed by a review of time-resolved fluorescence studies in PDT photosensitizers (**Section 2.3**) and a survey of its clinical challenges and feasibility in terms of instrumentation and data analysis (**Section 2.4**)

2.2. Principles of TRF Spectroscopy and Imaging

Time-resolved fluorescence spectroscopy (TRFS) is able to measure fluorescence decay profiles at each wavelength [41]. The time-domain parameters retrieved from each decay curve (as shown in **Fig. 2.1(b)**) can be a combination of n exponential terms from various fluorescence species, expressed as:

$$F(t) = \sum_{i=1}^{n} A_i * \exp^{-(\frac{t}{\tau_i})} \quad \textbf{(2.1)}$$

where where $F(t)$ is the fluorescence intensity at time t and A_i are normalized coefficients that denote the relative contributions of individual fluorescence lifetime components (τ_i). Non-linear least squares (NLLS) analysis is a widely used approach that estimates A_i and τ_i using multiple exponential approximation [46,47]. With individual parameters, the average lifetime (τ) can be calculated using fractional or amplitude-weighted approaches to represent the decay dynamics [41]. The challenges of using NLLS will be further discussed in **Section 2.4**.

Since changes of fluorescence lifetime are subject to non-radiative and emission processes that occur between 10^{-13} to 10^{-8} s, TRFS has been widely used in chemistry for liquid samples to probe a variety of phenomena such as solvent dynamics, polymer photophysics, molecular reorientation, *etc.* [48]. For

biomedical applications, single-point spectroscopic analysis can be further extended to fluorescence lifetime imaging that measures the TRF parameters of each pixel with a point-scanning interface or wide-field detectors.

When measuring the TRF parameters of PDT photosensitizers in a complex microenvironment, time resolution and the measuring accuracy covering a broad range of decay times play key roles. For instance, most of the photosensitizers exhibit multiple exponential decay behavior with an average lifetime in the range of several nanoseconds [45]. The absorption-emission spectra of these photosensitizers also overlap with many intrinsic fluorophores (*i.e.*, autofluorescence) with lifetimes ranging between hundreds of picoseconds to a few nanoseconds. Therefore, TRF measurement and analysis in this regime are challenging and only become feasible owing to advances in high-speed optoelectronics [49]. In this section, we briefly review two main approaches to measure TRF: time-domain and frequency domain techniques, followed by a discussion of their clinical feasibility. Detailed review of TRFS techniques and analysis were presented in references from Lakowicz [41] and Marcu [49].

2.2.1. Time domain fluorescence spectroscopy and imaging

In time-domain (TD) measurement, the use of short pulsed lasers enables the recording of the fluorescence emission after each pulse to establish the emission decay curve.

Time correlated single photon counting (TCSPC)

TCSPC is based on the detection of single photons after excitation by a pulsed source. A single photon is detected from an excitation pulse at random and the arrival time of each detected single photon relative to the excitation pulse is converted to voltage signals with a time resolution up to a few picoseconds. A probability histogram was then built from repetitive measurements of the arrival time of a detected single photon emission, as illustrated in **Fig. 2.2(a)** [50]. TCSPC is a well-established technique with single photon sensitivity and high temporal resolution. It is also a relatively low cost option comparing to other time-resolved measurement techniques in the nanosecond to picosecond regime. However, in order to achieve good statistical accuracy while maintaining low detection rate (1%) to avoid pulse pile-up, there are trade-offs between data acquisition time, SNR and the measurement accuracy. Since only a single photon is detected for each pulse, TCSPC is not an efficient detection method that requires high repetition rate excitation sources, and the sample may suffer photobleaching. Nonetheless, TCSPC is the most widely used time-resolved fluorescence measurement technique.

TCSPC-FLIM (Fluorescence Lifetime Imaging Microscopy) can be achieved by the combination of TCSPC electronics and a scanning interface, as shown in **Fig. 2.2(a)**. It is also possible to perform multi-spectral TCSPC imaging by simultaneously recording several spectral bands with the photo detector arrays and multi-channel counting electronics. One problem associated with multi-spectral imaging may be the trade-off between the number of pixels and the number of detector channels because of a limited memory space [50].

Pulse sampling techniques

Fluorescence decay can also be measured using pulse sampling or time-gated techniques. In pulse sampling techniques, as shown in **Fig. 2.2(b)**, the full decay profile after each pulse excitation is repetitively sampled by a photodetector (e.g., PMT or photodiode) followed by a digitizer. Since acquisition can be done with a single detector and digitizer pair, such measurements can be performed with good temporal and spectral resolution [41,49,51]. When the fluorophores exhibit high quantum yield, decay profiles from a single excitation pulse may be adequate for retrieving TRF parameters, which is considered one of the main advantages of the pulse sampling technique. The potential fast data acquisition (e.g., ns laser pulses) thus provides a unique advantage for clinical applications [51]. For example, flexible fiber probes can be coupled to endoscopy systems for clinical surveillance [52–56]. Multiple time-resolved spectra can either be acquired by sequentially scanning in the spectral domain (e.g., via a monochromator) [57] or using a multiple fiber delay arrangement [58]. Although this technique is more often used for single-point spectroscopy measurements, fluorescence lifetime imaging has also been reported recently [59,60].

Instead of sampling the full fluorescence decay, the time-gated technique only measures integrated fluorescence intensities in the gated window delayed by a different time relative to the excitation pulse. The whole fluorescence decay can be reconstructed by repeating the gated detection process. This is also a preferred FLIM (**Fig. 2.2(b)**) technology in clinical application as faster data acquisition can be achieved using an intensified charge-coupled device (ICCD) [61]. In particular, fast two-gate detection scheme (also termed rapid lifetime determination) is an efficient method to estimate fluorescence lifetimes, which measures the ratio of the integrated intensities acquired in two time windows with equal width. Detailed descriptions may be found in work from Sharman and Agronskaia [62,63]. Due to the low frame rate of the ICCD, only a limited number of time-delayed windows can be used in this technique, hence limiting its application to rather simple decay profiles. In addition, the spatial resolution of this technique is limited by that of the ICCD.

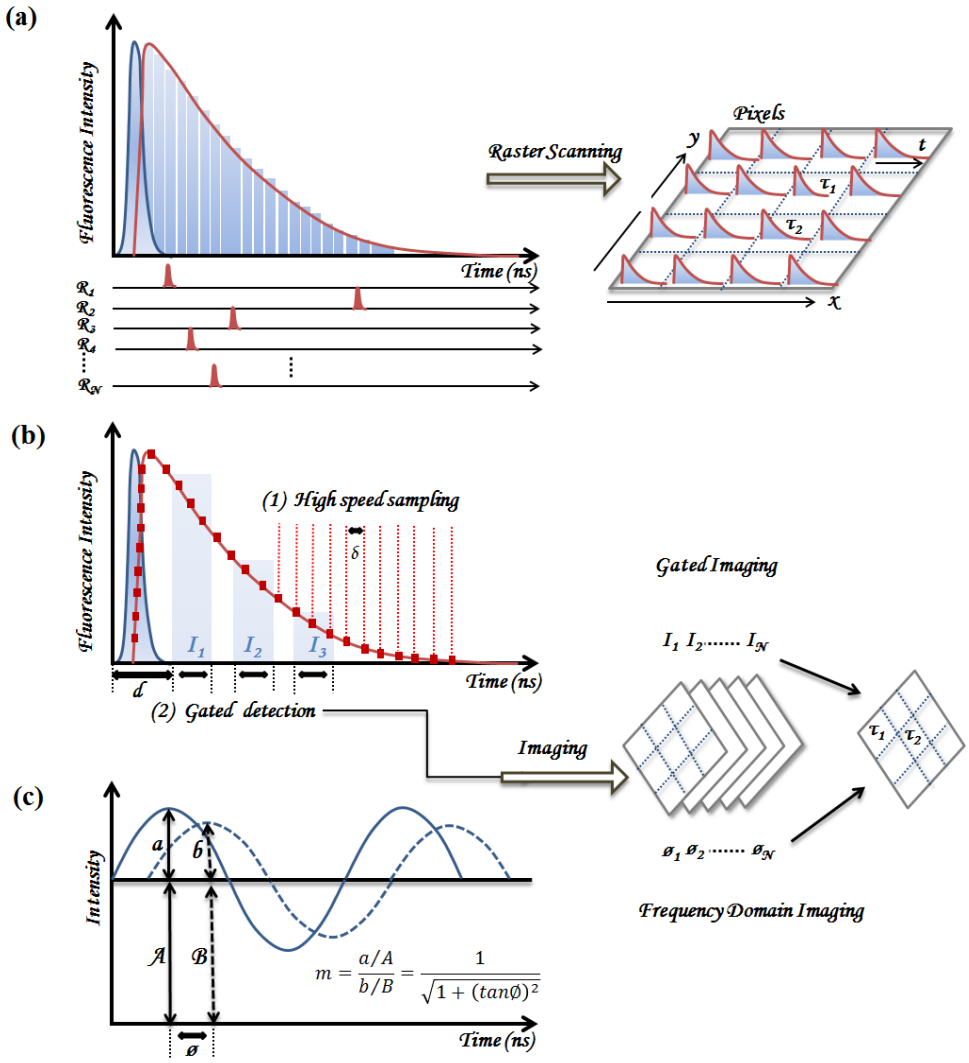

Figure 2.2 (a) The histogram built using TCSPC and the raster-scanning techniques used for fluorescence lifetime images. (b) Principles of high-speed sampling and time gated techniques. The fluorescence decay can be collected through different time gates (I_1 to I_3). In time-gated imaging technique, immediately after the excitation pulse, intensity information within several delays of gating pulse will attribute to a stack of intensity images (I_1 to I_N). Ultimately, for each pixel, the processed lifetime image can be constructed from the measured stack of the fluorescence images. (c) Principles of frequency domain spectroscopy, where the fluorescence lifetime can be calculated based on the phase delay (ø) and the demodulation ratio, m. Fluorescence lifetime imaging can also be reconstructed using an ICCD with various phase delay (ϕ_1, ϕ_2... ϕ_N).

2.2.2. Frequency Domain Fluorescence Spectroscopy

Frequency domain (FD) measurement utilizes a periodically modulated excitation source to obtain the phase shift (ϕ) between the emission and excitation waveforms, and the demodulation ratio represents the change in modulation depth of fluorescence signals with respect to the waveform of the exciting light [64], as illustrated in **Fig. 2.2(c)**. Assuming a molecule with single exponential decay excited by the modulated source of an angular frequency, the estimation of fluorescence lifetime can be simply retrieved by the phase shift and demodulation ratio. These two parameters can be measured through a range of modulation frequency to resolve multiple exponential components [41]. FD-FLIM is usually implemented in wide-field techniques, but can also be used in the confocal scanning system [64]. Typically, the homodyne method is used, where the electronic gain of imaging intensifier is modulated at the same frequency as the excitation light. The coming fluorescence light with certain modulated frequency will mix with the modulated gain in the imaging intensifier to achieve phase shift and demodulation ratio at different locations. After acquiring a stack of steady-state phase images ($\phi_1, \phi_2 \ldots \phi_N$) in which the detector phases are distributed between 0 and 2π, the lifetime can be measured for each pixel by extracting the demodulation ratio and the phase lag (**Fig. 2.2(c)**)

2.2.3. Summary of instrumentation requirement for clinical implementation

As typical fluorescence lifetimes of organic fluorophores are around a few nanoseconds, lifetime changes caused by non-radiative energy transfer in hundreds of picoseconds are not trivial. Therefore, temporal resolution, fast acquisition, and accurate analysis are the main considerations in clinical settings. There are usually trade-offs in the selection of instrumentation. For example, TCPSC is capable of achieving time resolution down to tens of picoseconds, while the acquisition time is limited by detection efficiency. Time-gated or pulse sampling techniques are more desirable for clinical implementation due to their high data acquisition speed and the potential use of rapid lifetime determination (RLD) algorithms [63]. For example, pulse sampling and time-gated FLIM can rapidly acquire fluorescence decay in parallel. In addition, it is very efficient to reject unwanted background from short-lived fluorescence. This method is later used in time-domain endoscopic FLIM for real-time imaging acquisition [65]. However, higher fluence and fluorescence quantum yield are required to achieve sufficient signal-to-noise ratio (SNR). Their temporal resolution is also limited by the laser pulse shape, instrumental responses and the detection gate (*i.e.*, down to ~100 ps) when compared to TCPSC. **Table 2.3** summarized the advantages and limitations of TD technology. FD technique has less stringent requirements regarding electronics, light source (e.g., no ultrafast lasers), and computation (e.g., no deconvolution). In addition, time-domain yields certain artifacts while

detecting fluorophores with its fluorescence decay longer than the inter-pulse duration; therefore, frequency domain method used to be a more feasible way to perform lifetime analysis of long-lived fluorophores. However, repetitive measurements using various modulation frequencies are usually necessary to encompass the multiple fluorescence lifetime components in tissue; thus the long data acquisition time limits its applications in clinical settings. Phasor representation for fast FD-FLIM analysis is now under investigation and has been shown to achieve good performance [66].

Table 2.3 Summary of time-domain techniques [49].

Advantages	**Disadvantages**
TCSPC	
High sensitivity and temporal resolution	Very slow data acquisition to achieve desired signal
Low systematic errors	Require post-processing to correct distortions in long fluorescence lifetimes [67,68]
Suitable for resolving complex decays	
Easy implementation to existing scanning system	Cannot tolerate ambient light
Low cost	
Time-gated and pulse sampling	
Capable of single-shot detection	Difficult to predict instrument noise
Rapid data acquisition of fluorescence decays	Low sensitivity so requires sufficient quantum yield
Good for background subtraction	Time resolution is subject to the gate window
Immune to ambient lighting	High instrumentation cost
General	
Broad excitation spectra of short pulsed lasers	Complex opto-electronic systems for detector and light sources compared to FD –FLIM
Can be operated at room light (f *< 10 Hz)	

**f* represents pulse repetition rate.

2.3. Applications of TRF on PDT photosensitizers

In this section, we review previous TRF studies on PDT photosensitizers. PDT photosensitizers were known to go through multiple transitions after drug administration, which include photoproduct formation, self-aggregation, and compound formation through binding with adjacent molecules. These changes could greatly alter the PDT effect as they hinder the energy transfer between the excited-state photosensitizer and the adjacent oxygen molecules. However, steady-state fluorescence measurements alone are not sufficient to probe the above changes as these fluorescence species present significant spectral overlap [45,69]. Therefore, TRF measurements have become an attractive complementary tool to characterize these transitions and drug interactions with biological molecules. *In vitro* studies then offer a good platform to initiate the investigation in molecular perspectives. *In vivo* studies, however, are still quite limited due to the limitations in technology development (further discussed in **Section 2.4**); TRF measurements on endogenous fluorophores will also be discussed along with photosensitizers.

2.3.1. Time-resolved studies of PDT photosensitizers in solution and in vitro

TRF studies relevant to different PDT photosensitizers have been reported by several research groups in the past decades [31,43,45,70–76]. FDA-approved PDT photosensitizers include Photofrin®, 5-aminolevulinic acid-induced protoporphyrin IX (ALA-PpIX), and verteporphyrin, Other photosensitizing agents in research stage, such as mTHPC (m-tetrahydroxyphenylchlorin, Foscan®), phthalocyanine (Pc) compounds, and chlorin-based compounds (*i.e.*, HPPH), also showed promising results in terms of their singlet oxygen yield and more red-shifted absorption bands [77]. We summarized TRF measurements of photosensitizers in **Table 2.4**. In addition, the cellular environment is a more complex system when compared to bulk solutions. Other than the solvent effect, the distinct microenvironment of subcellular organelles (e.g., molecular binding) leads to various degrees of quenching effect on photosensitizers. Photosensitizers of various concentration and lipophilicity may result in self-aggregation, and the photodynamic process may generate a variety of photoproducts. Moreover, in an *in vivo* environment, a drastic change of oxygen level and abundant endogenous fluorophores also contribute to additional variations in TRF parameters. How these factors affect lifetime measurements of the photosensitizers will be further discussed.

Table 2.4 Summary of TRF studies of Photosensitizers

PS.	Lifetimes (τ) / Localization	PS. Conc.	Ex/ Em (nm)
HpD/ Photofrin	14 ns (Organic solution) [43]	5 µg/ml	364 / 615
	10 ns (Organic solution) [70]	0.06 - 6 µg/ml	405 / > 580
	5.5 ns (Mitochondria, MLL) [70]	10 µg/ml	810/ 600-750
	13.3 ns (Monomer, mitochondria) [70]	10 µg/ml	810/ 600-750
	13.6 ns (Monomer, mitochondria) [45]	2 µg/ml	398/ 627-651
	8.5 ns (Aggregates, mitochondria) [45]	2 µg/ml	398/ 651-687
	8.0 ns (Aggregates, mitochondria) [78]	5 µg/ml	514/ 600-700
	4.8 ns (Cell membrane) [78]	5 µg/ml	514/ 600-700
	1.0 ns (Aggregates, *mouse model*) [31]	20 mg/kg	514/ 630
	13 ns (Monomers, *mouse model*) [31]	20 mg/kg	514/6 30
PpIX	16.4 ns (Organic solution) [70] ;	10 mM	810/ 600-750
	6.3 ns (Averaged. mitochondria) [70]	10 mM	810/ 600-750
	7.5 ns (Averaged, mitochondria) [79]	1 mM	398/ >590
	2 - 4 ns (Photoproducts, cytoplasm) [69]	1 mM	398/ >590
	5.4 ns (PPp, Mitochondria) [71]	20 µM	670/ 674
mTHPC	10 ns (Ethanol solution) [72]	40 µM	355/ 456-794
	8.4 ns (Methanol) [73]	15 µM	590/ > 630
	4.8 ns (Macrophages, V79) [73]	15 µM	380/ > 630
$AlPcS_2$	4.0 ns (Macrophages, V79) [73]	100 µM	380/ > 630
ZnPPC	2.5 - 3 ns (Macrophages, V79) [73]	10- 50 µM	380/ > 630
HPPH	5.7 ns (PBS) [74]	100 µM	400/ 670-710
	7.6 ns (liposome confined) [74]	100 µM	400/ 670-710
	6.4 ns (tissue phantom) [75]	0.5 µM	660/ 720
	4.3 ns (mouse tumor, before PDT) [75]	3 µM/kg	660/ 720
	5.0 ns (mouse tumor, after PDT) [75]	3 µM/kg	660/ 720
Chlorin-e6	4.5 ns (Monomer, methanol) [76]	5 µM	800/ 635-740
	~ 0.5 ns (Aggregates, methanol) [76]	5 µM	800/ 740
	0.5 - 3 ns (Aggregates, Lysosome) [76]	5 µM	430/ >710
	~0.1 ns (Aggregates, Lysosome) [76]	5 µM	430/ >710

2.3.1.1. Solvent effect

Solvent effect is related to the solvent relaxation that can lead to both spectral shifts and lifetime changes. As shown in **Fig. 2.3**, fluorophores at the excited states exhibit larger dipole moment (μ_E) than ground state (μ_g). The solvent dipole reorientation is then driven by the dipole moment of the excited fluorophores, and the solvent with a higher polarity leads to an increased energy relaxation with a more red-shifted emission.

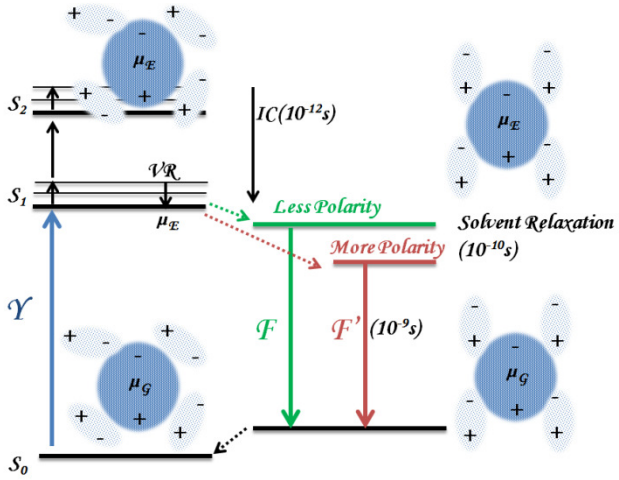

Figure 2.3 Schematics of solvent relaxation. The excited fluorophores has larger dipole moment (μ_E) than ground state fluorophores (μ_g). The solvent relaxation phenomenon is due to the reorientation of solvent molecule surrounding the excited fluorophores. The more polar the solvent is, the emission energy is further reduced. This leads to solvent-dependent spectral shift and lifetime changes. Fluorescence lifetime can be affected by the increase of non-radiative decay rates in non-solvent environment. *VR* and *IC* denote vibrational relaxation and internal conversion. Note that both *VR* and *IC* are independent of solvent relaxation because these transitions occur in shorter time frame (10^{-12} s). Non-radiative energy transfer (10^{-10} s) and fluorescence (10^{-9} s) are then affected by the solvent effect.

Connelly *et al.* investigated the fluorescence lifetime of mTHPC in living cells using time-gated fluorescence lifetime imaging technique in combination with the line-scanning confocal fluorescence microscope [73]. *In vitro* results showed mTHPC exhibited apparent photobleaching and had a significantly shorter lifetime (4.8 ± 0.3 ns) than in methanol solution (8 ± 0.4 ns). These results are found to be inconsistent with previous ethanol solution-based measurements using time-resolved excited-state absorption and emission spectra: the lifetimes of

10 ns correspond to the timescale of fluorescence (S_1), and are independent of oxygen concentration [72]. The inconsistency of the measurements in solution can be attributed to certain variables, including the solvent effect and the time resolution of the measurement techniques. In particular, as solvent effect is associated with energy relaxation from the surrounding solvent molecules, it also results in changes in non-radiative decay rates (K_{nr}). The increase of K_{nr} to adjacent biomolecules and the consequent lower quantum yield is found in less polar solvent. Hence, when using solvents such as water, ethanol, or methanol sorted with descending polarity, fluorescence lifetime can be quenched further in less-polar environments [41].

.

2.3.1.2. Binding to Biomolecules

It is noted that the fluorescence lifetimes of the photosensitizers were shortened significantly when measured in biological environment, as shown in the mTHPC experiment discussed above. This dynamic quenching effect is also consistent between types of cell lines and photosensitizers, while the extent of quenching depends on the drug localization. This phenomenon may serve as one of the advantages of using TRF to probe drug-molecular interactions. Several photosensitizers have been tested in a variety of cell lines and different binding sites were reported including mitochondria [80–83], lysosome [73], and cell membrane-based PDT [84,85].

Mitochondrial localization

5-aminolevulinic acid (ALA) induced protoporphyrin IX (PpIX) and Photofrin® are two common photosensitizers approved for clinical PDT treatments; hence, more photophysical and photobiological studies regarding these photosensitizers have been done. Although different pathways were involved in the drug internalization processes [17], mitochondrial depolarization is the main mechanism that induces apoptotic cell death [81]. 5-ALA is an endogenous heme precursor that can lead to phototoxic PpIX synthesis through ferrochelatase inside the mitochondria. The nature of reduced ferrochelatase enzyme activities in tumor cells gives exogenous 5-ALA an advantage to accumulate extra PpIX. Maximum intracellular PpIX level is typically reached within six hours, but high variability between cell lines were observed [86–89]. Unlike 5-ALA, Photofrin® is integrated into mitochondria with a different pathway. It goes through plasma membrane and cytoplasm (pyruvate kinase activation) within three hours and contacts outer mitochondrial membrane to form the voltage-dependent anion channel within five hours; eventually the more hydrophobic components will reach the mitochondrial inner membrane and bind to cardiolipin [17,80,82,90]. Thus, several TRF studies were performed in an

attempt to characterize the changes of time-domain parameters due to mitochondrial binding, and correlate these changes with treatment efficacy (apoptosis).

For example, Russell *et al.* characterized the lifetimes of Photofrin® and 5-ALA-induced PpIX inside living MLL (Mat-Lylu) cells using TCSPC-FLIM with the intention to help regulate the dosage of PDT in real time [70]. The fluorescence lifetimes of both drugs in methanol or cells agreed well with previous studies [31,43,45], as summarized in **Table 2.4**. Among different experimental settings that employed various modalities, cell lines, and drug concentrations, the measured lifetimes typically exhibited an average lifetime of more than 10 ns in solvent that correspond to monomers, while significantly quenched lifetimes of less than 8 ns were found when bound to mitochondria. These results suggested that the fluorescence lifetime-based technique might be able to provide a quantitative measurement of intermolecular interactions and may be a good candidate for *in vivo* PDT dosage monitoring. Further discussion of the slight discrepancy in individual lifetime components (short- or long-lived components) will be mentioned later in the photoproduct and self-aggregation section.

Lysosome localization

Studies have shown that anionic porphyrins tend to localize in lysosomes [91], and lysosomal localization has been proposed as one of the critical subcellular targets in PDT [92]. Subsequent studies demonstrated that the lysosome-localized photosensitizers are also capable of causing apoptotic cell death by indirect activation of mitochondria-associated apoptotic pathways after destruction of the lysosomal membrane. Chlorin-based compounds and Phthalocyanine are the main photosensitizers internalized via lysosomes [93]. AlPc (aluminum phthalocyanine chloride) and ZnPc are also photosensitizers with great potential in PDT because of their red-shifted excitation spectra, which could allow for better tissue penetration during clinical interventions. Connelly *et al.* compared the fluorescence lifetimes of AlPcS2 in aqueous solution and in living V79 cells. Similar values of mean lifetime (4.8 ns) were obtained in bulk solution and *in vivo*, but a broad lifetime histogram was observed when the drug was incubated in cells. These results agreed well with the value reported by MacRobert *et al*, where the unquenched monomers exhibit the fluorescence lifetime of 5.4 ns in cells [94]. A short-lived component of 1 ns was also found and could be attributed to the quenching from non-fluorescence aggregates, which agreed with the cell measurement performed by Moan *et al.* [95].

Cell membrane localization

Cell membrane is a relatively uncommon target in PDT, while it remains an interesting target of PDT due to its fast-reaction PDT effect. The phototoxic effect can be observed within a short time frame after light irradiation, which can cease cell proliferation with low dose of Photofrin® (7 μg/mL) using light fluence of 10 J/cm^2. Although efficient, the plasma membrane-mediated PDT was reported to manifest necrotic cell death [84]. Cell phenotype demonstrated swelling, blebbing, and disintegration of the membrane [12] without signs of apoptosis such as DNA fragmentation. Yeh *et al.* studied the lifetime changes of Photofrin® through the uptake process and correlated the lifetime changes to subcellular localization. The fluorescence lifetime of Photofrin® was found to be significantly shortened when the drug is first bound to plasma membrane at 1 h of incubation (4.3 ns compared to 7.3 ns at cytoplasm). This phenomenon can be attributed to specific intermolecular reactions between Photofrin and the receptors at the plasma membrane. Another explanation is that the increased photobleaching of Photofrin® monomers might be caused by a much higher fluence required for sufficient SNR during the initial uptake of Photofrin® [78]. This leads to the shortened average fluorescence lifetimes from Photofrin® aggregates [31]. The effect of irradiance will be further discussed in the section on "prolonged irradiation".

It is important to note that redistribution of the photosensitizers to the cell cytoplasm can occur in any types of photosensitizers that eventually disintegrate the membrane of subcellular organelles [81]. Therefore, characterization of lifetime changes throughout the drug uptake duration might provide an indicator for cell responses. Multiple endogenous fluorophores such as NADH and FAD should be taken into account together to represent cell function, and will be further discussed in **Section 2.3.3**.

2.3.1.3. Photoproducts and Self-aggregation

Photoproduct and self-aggregation could exhibit distinct fluorescence spectra, fluorescence lifetimes, and phototoxicity. These phenomena have been proved to be one of the major issues that introduce variability in PDT efficacy and inaccuracy during monitoring. Therefore, an effort has also been made to investigate their properties by manipulating drug concentration and the use of spectral-resolved TRF measurement.

In 1990, König *et al.* demonstrated aggregation studies by using different concentrations of Hematoporphyrin derivative (HpD), which is a previous generation of photosensitizer and is known to be a mixture of monomeric and aggregated porphyrins. Results showed that the short-lived component (~2 ns) increased while the photoproduct of HpD was formed. This phenomenon is

associated with the increase of photosensitizer concentration (10-5 to 10-3 M) and/or the light energy (80 mW for 0 to 120 min). This result first suggested the fact that photoproduct formation needs to be considered during lifetime imaging [31].

5-ALA induced PpIX is also known to produce several intermediate photoproducts, as shown in **Fig. 2.4** [29,69]. Its photoproducts with varying lipophilic characteristics can localize at different locations in the cells, and some of the photoproducts (*i.e.*, Ppp and its photoproducts) also play cytotoxic roles in treatment [30,96]. However, it is not easy to differentiate them with steady-state fluorescence measurements due to the significant spectrum overlap, while TRF may be an alternative candidate, as labeled in **Fig. 2.4**. Theodossiou *et al.* attempted to characterize the cell photosensitizing properties of Ppp in a murine keratinocyte cell line (PAM 212) by using fluorescence microscopy and time-resolved spectroscopy. Ppp is one of the photoproducts from 5-ALA induced PpIX and was shown to be effective in cell killing. Time-course fluorescence studies up to 400 min of incubation were performed to examine drug localization, quantum yields and decay times, and Ppp with the decay time of 5.35 ± 0.17 ns was found in cells after 4 h of incubation [71]. The study of photoproduct and self-aggregation can be further advanced with the development of spectral-resolved FLIM (SLIM). Lifetimes were obtained by TCSPC-FLIM and were further classified into eight wavelength channels. As a result, four-dimensional data including photon distribution (*x*, *y*), the wavelength (λ), and the lifetimes (τ) were built. SLIM studies measured in solution and cells both showed that different metabolites of 5-ALA exhibited significantly different decay rates compared to PpIX monomers, and also localized at different intracellular regions [69].

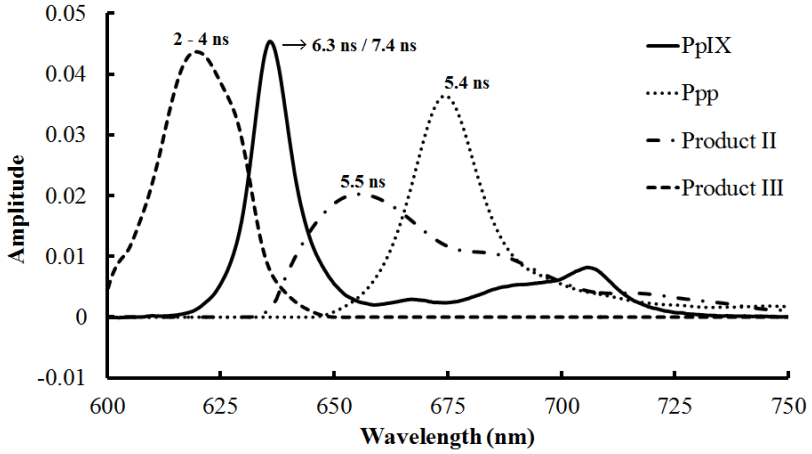

Figure 2.4 The emission spectrum of 5-ALA-induced PpIX and its photoproducts. The monomer and photoproducts of the photosensitizers demonstrate significant spectral overlap. Fluorescence lifetimes of different 5-ALA metabolites in cells are

also labeled. PpIX fluorescence lifetimes are quenched to 6.3 ± 1.2 ns [70] and 7.4 ± 0.6 ns [79] measured in different cell lines; Ppp (5.4 ± 0.2 ns) and its photoproduct (Product II, 5.5 ± 0.4 ns) have similar lifetimes, but both demonstrate faster decay compared to PpIX [71]; Product III corresponds to Uroporphyrins and other intermediate metabolites that show significant shorter lifetime of 2 to 4 ns and can be easily differentiated from PpIX [69] (Reproduced from data in [29]).

Photofrin® has also been extensively investigated by the fluorescence lifetime-based technique both in bulk solution and *in vitro* using SLIM [45]. Photofrin® at a concentration of 2 μg /mL was first incubated in HepG2 cells (Human hepatoblastoma cell line) for 24 h. The decay traces were then calculated by the bi-exponential model. As known by spectroscopic studies, Photofrin® has its main fluorescence emission bands at the wavelength ranges of 627–639 nm, 639–651 nm, and 687–699 nm. Accordingly, lifetime results from these three emission bands were approximately 12 ns (11.2–13.6 ns); however, at the emission band of 663–675 nm and 651–663 nm, which correspond to the photoproducts of Photofrin®, the measured lifetime values were apparently shorter (~ 8.9–9.3 ns) than the monomers. Furthermore, the spectral range of 508–520 nm can be attributed to autofluorescence of flavin molecules inside cancer cells and exhibited the lifetime value of 5.2 ns. In other words, analyzing fluorescence lifetimes at different spectral ranges can be an important approach to realize mitochondrial metabolism under PDT treatments. This is further supported by later studies, where Photofrin® exhibited a slower component of 11.6 ± 0.5 ns coming from monomers and a fast component of 4.8 ± 0.9 ns from aggregates or photoproducts using bulk measurement. A significantly quenched lifetime of 5.5 ± 1.2 ns was also found in cells after incubation of Photofrin® at10 μg/mL for 18 h [70]. It should be noted that the concentration of the photosensitizer can affect the extent of aggregation, and different fitting algorithms can also lead to discrepancy in lifetime estimation, but a consistent finding of quenched lifetimes in aggregates and photoproducts can still be a distinct feature when probing fluorescence lifetime changes. The degree of lipophilicity is a factor that can alter photosensitizer distribution inside the cells, where lysosome distribution is usually found in strongly lipophilic sensitizers (*i.e.*, Chlorin e6) and could lead to more aggregate formation [76].

2.3.1.4. Prolonged irradiation

The fluorescence lifetime components of photosensitizers were also found to be dependent on the irradiation dose. Studies have shown that prolonged irradiation can result in the production of an extra short-lived component in the lifetime range of hundreds of ps. König *et al.* performed *in vivo* fluorescence measurements and the results clearly showed that the intensity of short-lived components (1.0 ± 0.3 ns) increased when the excitation fluence was raised. This phenomenon could be explained by the photoproduct formation due to

photobleaching of HpD monomers. This agreed well with later research using Photofrin® and chlorin compounds [31,76,78].

2.3.2. Time-resolved studies of PDT photosensitizer in vivo

Photosensitizers have been shown to undergo fluorescence lifetime changes in the cell environment. The changes are significant and relatively independent of fluorophore concentration. Efforts have been made to direct this technique towards clinical applications including the investigation of the instrumentation and analysis in tissue phantom and *in vivo*, although photosensitizer studies were still quite limited. To achieve time-resolved mapping of photosensitizers in a thicker tissue volume, time-domain (TD) NIR fluorescence diffuse optical tomography (FDOT) has become an attractive option to account for light propagation in tissue by the use of multiple source-detector pairs across the targeted area [75,97–99]. Imaging reconstruction was then performed based on the normalized Born approximation [100]. Mo *et al.* in 2012 used a time-gated fluorescence tomography system to characterize the fluorescence lifetime of a PDT photosensitizer, 2-(1-hexyloxyethyl)-2-devinyl pyropheophorbide-a (HPPH), in a tissue phantom as well as a human head-and-neck xenograft in a mouse model [75]. HPPH-based PDT has shown effective results in superficial cancers such as Barrett's esophagus [101], head, and neck tumors [102]. In this experiment, the HPPH in a tube was embedded in a liquid phantom of which the optical properties match healthy mouse tissue. The correct location of the HPPH tube was extracted, which showed both the quantum yield and the mean lifetime of 6.4 ns. Results were further validated by consistent measurement from a standard fluorophore, Atto 655. Changes of fluorescence lifetimes of HPPH *in vivo* were characterized before and after PDT, with the scanning depth from 5 mm to 13 mm underneath the surface. Shorter fluorescence lifetimes were observed *in vivo* and an increase from 4.3 ns to 5.0 ns was obtained after treatment (**Fig. 2.5**). The tomographic results also showed a 20% increase in photosensitizer photobleaching at the surface of the tumor mass due to the increased fluence rate close to the irradiation plane. Fluorescence lifetimes of HPPH also increased by 16% after PDT treatment, which could be related to changes in physiological parameters. It is important to note that the change of physiological parameters, in particular oxygen level and blood perfusion, could all contribute to the changes in fluorescence lifetimes [103]. In addition, changes from the standard dose parameters—fluence distribution and photobleaching of the photosensitizers—should also be considered [75]. These influencing factors are discussed in the following sections.

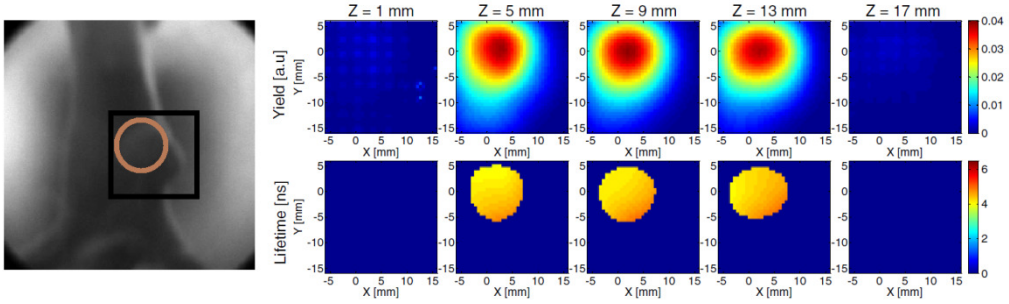

Figure 2.5 In vivo imaging of the HPPH-targeted tumor in mice before treatment. The mouse was immersed in the optical matching fluid (μ_a = 0.4 cm^{-1}; μ_s' = 10 cm^{-1}. Note: $\mu_s'= \mu_s$ (1-g), which accounts for anisotropic scattering dominating in tissue. g is the anisotropy factor with a typical value of 0.9).The reconstructed fluorescence lifetime and quantum yield at different depth agreed well with reported values (The figure is from [75], with permission from SPIE).

2.3.2.1. Endogenous fluorophores

Endogenous fluorophores that participate in oxidative phosphorylation are common fluorescence markers that reflect cell metabolism and mitochondrial function. These include reduced nicotinamide adenine dinucleotide (NADH), reduced NADH phosphate (NADPH), and flavin adenine dinucleotide (FAD) [104,105]. *In vitro* TRF measurement of photosensitizers focused more on the lifetime changes of the photosensitizers themselves; however, it is indispensable to take the interactions from abundant endogenous fluorophores into account for *in vivo* environment. In fact, though abundant endogenous fluorophores present in tissue provide insight for probing the phototoxicity of PDT, they also interfere with the fluorescence lifetime estimation to some extent, which will be further discussed in **Section 2.4.1**. With the potential to correlate biological effect (cell function) to the treatment dose, endogenous fluorescence lifetimes were studied alone or incorporated with photosensitizers to investigate cell function after PDT. Pogue *et al.* tackled the changes of NADH fluorescence lifetimes both *in vitro* and *in vivo* after the cell damage induced by verteporphyrin-mediated PDT [104]. Results have demonstrated that the NADH fluorescence was reduced both *in vitro* and in murine muscle after a toxic PDT dose was given that introduced immediate mitochondrial damage. This can be more likely attributed to compromised mitochondrial membrane that ceased the accumulation of NADH molecules [18], or the oxidation caused by the singlet oxygen induced by the photodynamic reactions. Fluorescence lifetimes remained the same at approximately 1.5 ns throughout the time course and were found to be shorter than the no-drug control groups (2.1 ns). Later cell experiments performed by Wang *et al.* [106] further characterized the NADH lifetimes in an attempt to differentiate staurosporine (STS)-induced apoptosis from hydrogen peroxide-

induced necrosis, which could be essential for monitoring cell responses to the treatment. It is noted that the fluorescence lifetime of NADH increased within 15 min after apoptosis was introduced, while no change was observed in necrotic cells. The observed changes were much earlier than regular apoptosis detection techniques that require 2 to 4 h for cytochrome *c* and caspase 3 activation [107]. These results are consistent with earlier work from Ghukasyan *et al.* that showed a significant increase of protein-bound NADH occurred only in apoptosis that caused an increase fluorescence lifetime to 3.6 ns [105]. Wang *et al.* further used 5-ALA-mediated PDT to induce cell apoptosis and have a consistent finding as STS-induced apoptosis (increased NADH lifetime) [108]. With the alteration of fluorescence properties of endogenous fluorophores during apoptosis, it is feasible to perform noninvasive treatment monitoring and detection of cell death by considering both the changes of fluorescence lifetimes from photosensitizer (the drug–molecular interactions), and the endogenous fluorophores (the treatment effect).

2.3.2.2. Microenvironment – oxygen level, vascularization, pH

The dynamic physiological factors induced by PDT can also alter fluorescence lifetimes of the photosensitizers and inevitably increase the complexity of data analysis. These factors include the size of tumor masses [75], oxygen saturation [103], vascularization [109], and pH [110]. For example, oxygen supplied by the surrounding capillary vessels plays an important role in PDT treatment. Large tumor masses usually manifest an oxygen level of nearly zero in tissue far away from the capillary supplies. Studies have been done to show the oxygen diffusion capability into the tissue and the kinetics between oxygen pressure and photosensitizer quenching using Photofrin [28,111], Pd-porphyrins [112], and mTHPC [113]. However, the oxygen pressure and the extent of oxygen depletion were not solely based on the blood perfusion, but also on the local photosensitizer concentration and light dose. High local drug concentration can bear multiple cycles of excitation before photobleaching and can use up oxygen easily; a dose of high irradiance also aggravates the depletion effect, thus limiting the overall PDT efficacy [33]. It is noted that these changes associated with the depletion of oxygen through the photosensitizing processes could possibly increase the fluorescence lifetime of photosensitizers in tissue due to reduced quenching effects [114]. PDT-associated blood perfusion changes can also cause consequent effects on oxygen supplies and photobleaching rates; occlusion of vessels and reduced vasculature deep within the tumor mass also affect delivery of the photosensitizers [32]. Changes in interstitial fluid pressure induced by PDT can also result in changes in pH [103]. Correlating all of these factors becomes essential to interpret fluorescence lifetime measurement *in vivo*.

2.3.3. Discussion

To discuss the feasibility of using TRF as a complementary tool for PDT dosimetry, one needs to first answer the following question: What information provided by TRF is relevant to PDT dosimetry? Abundant *in vitro* and some preliminary *in vivo* studies have demonstrated the capability of using TRF to probe the photosensitizers in a biological environment. Differences in TRF results were observed between photosensitizers and cell lines, but some key observations that are related to PDT dosimetry are summarized in **Table 2.5.**

Table 2.5 Implications from TRF-PDT

Key information for dosimetry	Information yielded by PDT-FLIM
Drug interactions with subcellular organelles	Quenching of photosensitizer fluorescence lifetime while binding to biomolecules [73,115].
	Changes of fluorescence lifetimes through the drug uptake process [78].
Photoproducts	FLIM is able to determine photoproduct species although significant spectral overlap exists. Understanding of photoproduct contribution is essential to avoid over-or under-dose estimation [31,45,69].
Apoptosis	NADH fluorescence lifetime would increase immediately after the initiation of apoptosis. This can be applicable to apoptosis-mediated PDT [105,116,117].
Necrosis	NADH fluorescence lifetime does not change through the necrosis procedures. This can be related to necrosis-mediated PDT (plasma membrane as a target) [116,117]
Cell function	Cell metabolism and mitochondrial malfunction can be revealed by the ratio of free NADH (short lifetime) and bound NADH [44,104,117].
Oxygen Sensing	Decreased oxygen level lead to increased lifetime [75].
	Instrument with low laser repetition rate and CCD detection is under development for sensing oxygen concentration and fluorescence lifetime [118].

To correlate TRF with PDT dosimetry, we first consider what the most important factors are to build up the effective PDT dose. These encompass the

local drug concentration, effective light fluence, and oxygen levels [3]. However, the approaches to accurately quantify these parameters are still under investigation [25,119] with either indirect [29,38] or direct dosimetry [25,40,118]. As for direct dosimetry, it may be noted that phosphorescence measurements of singlet oxygen provide a direct indicator as well as a measure of oxygen depletion, but certain practical issues have to be considered. It is a challenging task to probe short-lived singlet oxygen species because the phosphorescence signal is so weak and there is a significant background due to fluorescence. More importantly, singlet oxygen may not be solely responsible for the treatment effect. The overall efficacy still relies on the interdependencies indicated in **Table 2.1** and **Fig. 2.1(a)**, and free radicals could potentially be significant in hypoxic or anoxic conditions. Although TRF does not probe any of the three parameters directly, it is able to reveal another key dosimetry factor: the biological effect at the molecular/cellular level, which includes several transitional steps such as drug interactions with its targets, photoproduct formation, singlet oxygen quenching, and cell function alterations. For example, it is able to probe the quenched fluorescence lifetimes and the contribution of photoproducts when drugs are bound to various subcellular organelles. Cell function alterations such as mitochondrial depolarization and cell death pathways can be characterized according to the proportional intensity and lifetime changes of autofluorescence [116,117]. This can lead to overall changes in the amplitude-weighted average lifetime of the photosensitizers. More specifically, TRF may help discriminate apoptotic and necrotic responses after treatment. For example, autofluorescence lifetime could be correlated to type II (singlet-oxygen) PDT when NADH exhibits increased lifetime immediately after apoptosis, or type I (free radicals) PDT if no such change is observed. However, the presence of both cytotoxic oxygen species, free radicals and singlet oxygen, may result in a quenched fluorescence lifetime for photosensitizers. In other words, fitting the data with multiple exponents could be essential to delineate the differences and dependencies when different types of photosensitizers (type I or type II) are used in PDT. Overall, dynamic relationships should be taken into account while interpreting the results *in vivo*, where the supporting vasculature plays a role in the PDT parameters, including oxygen and photosensitizer concentration. Is TRF measured *in vitro* going to be independent of these *in vivo* changes? It is unlikely that the *in vitro* time-resolved features are still completely applicable when measured in animal models. Efforts have to be made to characterize the effect of the surrounding in vivo environment (*i.e.*, the change of oxygen level, drug delivery, light delivery, and pH) to the proportional changes of individual fluorescence lifetimes (*i.e.*, photosensitizers, photoproducts, endogenous fluorophores, and the overall changes of average lifetimes). This further poses an inherent challenge: the complexity of data analysis (**Section 2.4.1**). Furthermore, the self-aggregation and photoproduct phenomena discussed in **Section 2.3.1.3** raise another question: is fluorescence lifetime actually independent of fluorophore concentration and light delivery? In theory, within a

certain range of concentrations that do not cause aggregation of photosensitizers, the fluorescence lifetime of the fluorophore should remain unchanged. As a result, fluorescence lifetime alone cannot provide concentration information. In fact, it will be affected by the drug concentration accumulated at its target due to the formation of dimers at high concentration; the photobleaching of monomers also leads to an increase in the proportion of photoproducts, and changes the average fluorescence lifetime. These factors will play a more complicated role in animal models. To date, there is a lack of TRF studies that correlate TRF parameters to treatment efficacy. A practical question is how TRF may reflect treatment progress or the final effect. Contribution of the specific lifetime component can change significantly during the treatment progress and this eventually alters the amplitude-weighted average lifetime. Overall, the sensitivity of time-resolved parameters offers a great opportunity to look into biological responses after PDT, but also introduces significant complexity in terms of data analysis and interpretation. Development of clinical friendly instrumentation and analysis are in progress and will enable researchers to further tackle these questions (further discussed in **Section 2.4**).

2.4. Challenges and Advances of Using TRF for Clinical Applications

In vitro and *in vivo* results demonstrated the potential to employ TRF for dose monitoring. However, when implementing the in vitro technique at the tissue level or animal models, the questions become more complicated, as mentioned in **section 2.3.3**. In short, in vivo applications introduce the complexity in microenvironment, including diversity of fluorophores, variation in photosensitizer and light delivery, perfusion, etc. Therefore, the following perspectives must be taken into account:

(i) Robust data analysis that deals with substantial biological variables and low SNR. Time-domain parameters are typically retrieved from fitting the results with known decay dynamics. Fitting accuracy may be reduced in multiple exponential decay and low SNR from photosensitizer fluorescence. In addition, the typical fluorescence lifetime range of photosensitizers can be long enough to introduce pulse pile-up and incomplete decay problems using time-domain TRF techniques. To be practical, the first challenge to overcome is to have fast and robust algorithms to retrieve time-resolved parameters, τ_i (lifetime) and A_i (coefficients).

(ii) Tissue optics that affects light focusing and drug targeting efficiency. This can be approached by modeling light transport using diffuse optical tomography.

(iii) Compatible instrumentation for clinical implementation. It is desired to have compact instrumentation with accessibility to desired tissue target (*e.g.* coupled to endoscopy). In addition, spectral-resolved analysis (*e.g.* hyperspectral TRF) may provide additional advantages in terms of interpreting multiple sources of fluorophores.

2.4.1. Data Analysis

Fluorescence emission profiles of photosensitizers have been shown to exhibit multiple exponential decays with a relatively lower SNR. SNR is particularly important when analyzing multiple fluorescence lifetime components, and is usually one of the major considerations for data acquisition in clinical settings. In this section, we mainly review approaches in analyzing time-domain TRF for its feasibility in clinical implementation.

In time-domain TRF, the measured fluorescence decay curve is a convolution of the true fluorescence decay, F (**Eq. 2.1**), with the instrumental response function (IRF) of the optical system. The time-resolved parameters such as lifetime can be estimated through deconvolution [41]. Global analysis based on non-linear least squares (NLLS) [46,47] is a common approach that shows good accuracy in lifetime estimation. It assumes fluorescence lifetimes are spatially invariant, thus a high SNR decay profile averaged from all pixels can be used to retrieve fractional contributions of lifetime components. Another method particularly proposed in biological systems is the stretched exponential model [120]. This assumes a continuous distribution of lifetimes by using a single decay model that can be generalized, thus it does not require assumptions of the decay function and is considered computationally efficient compared to NLLS. However, the Fourier transform of the model for frequency-domain data cannot be expressed in analytical solutions, and numerical approximation has not been successfully presented. Also, data interpretation is challenging when considering a continuous lifetime distribution [121], thus limiting its use. When approaching complex tissue characterization in PDT, NLLS still suffers from certain limitations: (i) NLLS gives non-unique solutions of fluorescence decay times and their coefficients. The inaccurate local minima can be obtained due to the low SNR in multi-exponential fitting. (ii) The retrieved exponential components are usually not sufficient to represent the different types of fluorophores in tissue, and lead to difficulties in data interpretation [41,49]. (iii) Nonlinear optimization is computationally expensive. Therefore, several

techniques have been proposed to overcome computational challenges and estimation accuracy. For example, Maus *et al.* compared performance of maximum likelihood estimation (MLE) and NLLS on low SNR data and found that MLE resulted in better accuracy in multiexponential analysis with photon counts of 1000 to 20000, while NLLS underestimated the fluorescence lifetimes by about 5% [122]. Laguerre basis functions (LBF) are another alternative proposed in previous TCSPC and time-gated FLIM [123–125], where the intrinsic fluorescence decays are expanded to a set of orthonormal functions to provide unique estimation of fluorescence lifetime coefficients. To improve clinical compatibility, Jo *et al.* performed a global analysis based on a common LBF for data in every pixel obtained from a time-gated FLIM system. Results showed an improved computational speed in the order of a few seconds, which is at least two times faster than standard NLLS [125].

Incomplete decay of long-lived fluorophores can introduce estimation error in time-domain TRF using ultrafast lasers. As demonstrated in **Fig. 2.6**, when the fluorescence decay cannot be completed within the pulse duration (t), the decay tails from previous excitation pulses are superimposed to the currently measured decay curve, $I(t)$. The consequent estimation error can be critical when the lifetime changes of energy transfer can be as short as 0.1–0.2 ns [126]. Previous studies have used the forward model to estimate the measured parameters based on original values [67,68,127], as well as the inverse model to recover the original values from estimated results [68]. Leung *et al.* simulated the effect of incomplete decay using a bi-exponential model. It is noted that the pulse pile-up caused errors in individual coefficients (A_i), but not in the individual lifetimes (τ_i). In addition, an increased estimation error can be caused when there is an increased discrepancy of original lifetime components (τ_2- τ_1), or a convergence of individual coefficients to 0.5 ($A_i = 0.5$) [68]. The inverse model thus provided a way to correct the measured coefficients and the eventual average lifetimes for a more valid interpretation of fluorophore concentration and interactions.

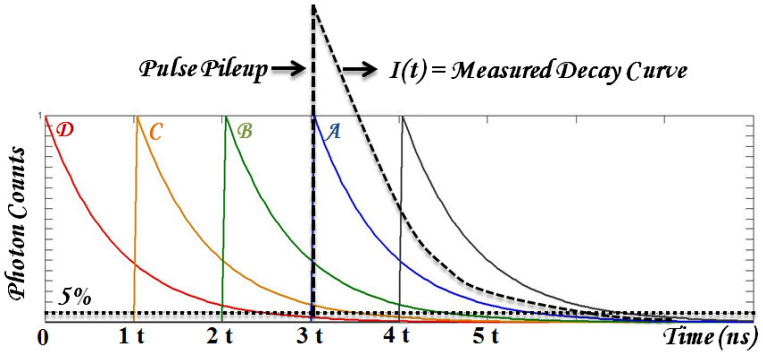

Figure 2.6 Schematics of incomplete decay when an ultrafast laser is used in time-domain TRF. Ultrafast laser pulses with an inter-pulse interval of t yield

fluorescence emission that follows exponential decay profiles, as indicated by the decay curves *A–D*, corresponding to each pulse. The tails of previous decays (*B–D*) are superimposed on the current decay (*A*) when *t* is not sufficiently long for a full fluorescence decay, causing distortion of the measured decay curve, I(t). The effect becomes more prominent when *t* is decreased or with a slow decay profile (adapted from [68], with permission from OSA).

2.4.2. Tissue Optics in PDT and lifetime measurement

In PDT, scattering dominates light transport when red to NIR light sources are used, although hemoglobin also plays a role in light absorption as a function of oxygen content. As turbid tissue is heterogeneous, spatial and individual variation of tissue optical properties is always one of the major concerns in light-mediated therapies. These factors alter PDT targeting efficiency due to attenuation of the effective light dose. For example, the fluence rate near the tissue surface could be several times greater than the delivered irradiance due to backscattering. This applies to both surface and intracavitary irradiation schemes. In interstitial treatment, the distribution of light dose is still affected by the effective attenuation coefficient, defined as $[3\ \mu_a(\mu_a + \mu'_s)\ ]^{1/2}$. The variation in light fluence can cause various extents of photosensitizer photobleaching and biological effect. Mathematical solutions to model light fluence and distribution in superficial, interstitial, and intracavitary applications were done to further account for the effect of scattering and absorption [25]. Detailed reviews of light propagation and modeling can be found in recent work from Zhu *et al.* and Jacques [25,128]. This may be further correlated with dose monitoring using time-resolved parameters.

In addition, light propagation of the emitted photons leads to distortion of measured data, although fluorescence lifetime estimation is supposed to be relatively more independent of light path when the propagation time is shorter than the fluorescence decay time. However, potential distortions still exist: (i) the measured fluorescence lifetime may not be attributed to the targeted location, and (ii) the penetration depth and the total light path can be increased when a NIR source is used. Therefore, both diffusion theories [129,130] and Monte Carlo simulations [131,132] can be applied in an attempt to retrieve intrinsic fluorescence yield and time decay based on source-detector geometries and tissue optical properties. A thorough modeling of these coefficients *in vivo* is essential for accurate data interpretation, while keeping the computational speed reasonable. Recent improvement including the use of TD-FDOT (**Fig. 2.5**), frequency-domain [97,133–135], and asymptotic TD (ATD) approach [136] have been proposed to reduce the computational complexity when dealing with non-linear problems [41,136,137]. Time-domain analysis can lead to computational challenges in order to solve non-linear problems (**Eq. 2.1**). Thus, frequency-domain that calculates the phase shifts between the fluorescence emission and

excitation simplifies the problem to a linear solution $Y(i) = Ax$. Y is the ratio of emission to excitation photon density from the measurements (i) that depends on the source location, detector location, modulation frequency, and wavelength. A represents the effect from each imaging voxel, where the two-point Green's function yields for light propagation in tissue by taking into account parameters such as detection geometry and tissue optical properties. Eventually, the reconstruction is to solve quantum yield and the fluorescence lifetime represented by x. The first approach to analyze time-resolved fluorescence tomography is using a normalized Born approximation, which was extensively reviewed to resolve 3D map of fluorescence distribution [133]. Ratiometric analysis of the excitation and emission sets is used to reconstruct the tomographic image, thus the normalized data are independent of parameters of the optical system and the coupling efficiency to the sample [97]. In addition to frequency-domain approaches, the asymptotic separation (ATD) approach has been proposed. Considering the contribution of each lifetime component (**Eq. 2.1**) is a function of time affected by light transport in tissue, it can be independent of time only when considering times longer than light propagation in the background medium. Therefore, ATD separates the analysis into temporal and spatial steps and has been shown to significantly simplify the complexity of the fitting process using NLLS on each source-detector pair. Performance of FD and ATD approaches were compared by Kumar *et al.* [136], where simulations and phantom studies were done to examine the accuracy of 3D fluorescence lifetime reconstruction. Results showed that ATD demonstrated better capability to resolve distinct lifetimes in the turbid medium, while the comparison of computation speed was not explicitly indicated in current FLIM tomography studies.

2.4.3. Instrumentation

To implement TRF technology for PDT treatment monitoring, it is necessary to have instrumentation that can access the treatment area other than superficial malignancies. In addition, instrumentation that can encompass spectral-resolved information may further improve data interpretation. The advances in these development are reviewed in **sections 2.4.3.1** regarding FLIM endoscopy, and **2.4.3.2** regarding hyperspectral TRF.

2.4.3.1. FLIM endoscopy

The output of light can be coupled to a flexible fiber bundle endoscope, which will be compatible with *in vivo* imaging of the gastrointestinal tract during PDT application. Wide-field time-domain FLIM has been proposed for clinical applications and a real-time flexible endoscopic FLIM system has been reported [61], which can achieve 29 frames per second when the RLD algorithm

is used. TCSPC-based FLIM endoscopy has also been developed to accommodate low SNR applications (*i.e.*, FRET) [138] and can potentially be used depending on the acquisition speed required by the application.

Most current clinical FLIM applications use UV to blue emission lasers to acquire fluorescence decays of the endogenous fluorescence [139]; however, when photosensitizers and their interactions with biomolecules are the main fluorophores, red to NIR lasers play an important role in matching the photosensitizer's absorption peaks and reducing unwanted autofluorescence background. In particular, absorption from hemoglobin typically reaches its minimum in the optical window between 600 and 900 nm. An NIR laser operating at this range provides an opportunity to achieve high-resolution optical imaging and better penetration depth comparable with the tissue thickness in histopathological analysis [139]. König *et al.* introduced the first multi-photon endoscope for clinical settings in 2003 using femtosecond two-photon excitation [140]; this has been tested on skin cancer diagnosis. Note that the mode-locked femtosecond Ti:Sapphire lasers are currently the primary light sources for multi-photon FLIM. Therefore, the incomplete decay effect should be considered when using it to probe photosensitizers and their interactions with biomolecules [67,68]. However, the two-photon endomicroscope is not widely used in current biomedical research field because several restrictions are posed when using optical fibers for delivering the femtosecond excitation pulses of the desired pulse energy.

2.4.3.2. Hyperspectral TRF imaging

As summarized in **Section 2.3**, photosensitizers go through photoproduct/aggregate transitions and an energy transfer with the microenvironment that lead to dynamic PDT efficacy. Moreover, when probing the biological, not only is the status of photosensitizers considered, but also the endogenous fluorophores that correlate with viability. In other words, the source of fluorophores can exhibit broad-band emission spectra with significant spectrum overlap, which leads to difficulties in data interpretation. Therefore, more comprehensive assessment may be required to deal with the complexity *in vivo*.

Spectral-resolved TRF techniques have been proposed by several research groups to probe the aforementioned biological reactions. The spectral partition can be achieved by scanning methods (hyperspectral) over the whole spectrum range, or parallel acquisition of multiple spectral bands. Typically, parallel acquisition is faster by using multiple band-pass filters [141] or multiple-delay optical fiber bundles [58], while it may not be sufficient to deal with significant spectral overlap in PDT application. In contrast, scanning methods such as grating-based monochromator [51], spectrometer with multichannel PMTs [142], and an acousto-optic tunable filter (AOTF) [57,59] can yield more detailed

spectrum information. Among these techniques, AOTF uses the acoustic wave to modulate spatial refractive index of a birefringent crystal, which diffracts light of different wavelengths [57]. The modulation frequency of acoustic waves is in the order of microseconds. Therefore, faster hyperspectral data acquisition becomes its main advantage for clinical implementation when compared to other approaches that typically need tens of seconds to complete a full spectral scan [51]. Moreover, Nie *et al.* reported an AOTF-based hyperspectral FLIM to render four dimensional data (x, y, τ, λ), and the system was validated using the standard fluorophores and porcine skin tissue [59]. Although current development is still used *ex vivo*, the development of hyperspectral TRF may render more thorough information and help the interpretation of PDT dynamics.

2.5. Conclusion and Outlook

In this report, we have reviewed dosimetric limitations in PDT as well as current progress of time-resolved fluorescence for its feasibility in PDT dosimetry. Up-to-date, explicit, implicit, or direct dosimetrics based on steady-state fluorescence measurement have been proposed to improve real-time monitoring of treatment efficacy, while the additional imaging contrast given by fluorescence lifetime can provide new information that looks into PDT dynamics. Towards this goal, time-resolved studies have been performed using common PDT photosensitizers in cellular and animal models. In particular, we reviewed influencing factors such as molecular bindings, photoproducts, irradiation doses, endogenous fluorophores, and the overall microenvironment that could lead to fluorescence lifetime changes of the photosensitizers. These studies have provided encouraging results that showed the potential to correlate changes of time-domain parameters to the eventual drug-molecular interactions and cell toxicity produced by PDT. Recently, time-resolved studies have been tested *in vivo* using mouse models and the retrieved 3D fluorescence yield and lifetime mapping demonstrated good agreement between phantom and animal studies. This advance has been successfully applied in PDT photosensitizer (HPPH) to study photobleaching and fluorescence lifetime changes before and after treatment. The eventual goal is to correlate “real time” biological effects at the molecular/cellular level to eventual tissue responses, and adjust treatment parameters based on the detected changes and this correlation. Hence, robust and rapid mapping of TRF results, the scope and speed of data acquisition, and penetration depth play key roles when considering the feasibility of PDT dosimetry *in vivo*. These challenges still exist and the use of TRF in PDT may actually introduce even more complexity for dosimetry. However, with the development of hyperspectral TRF, the use of TD-FDOT to account for tissue optics, robust data analysis for low

SNR data, and the rapidly emerging *in vivo* PDT-TRF studies, time-resolved fluorescence can still be promising in aiding PDT dosimetry.

References

1. K. Kalka, H. Merk, and H. Mukhtar, "Photodynamic therapy in dermatology.," J. Am. Acad. Dermatol. **42**, 389–413; quiz 414–6 (2000).

2. R. Weinreb, E. Cotlier, U. Schmidt-erfurth, and T. Hasan, "Mechanisms of action of photodynamic therapy with verteporfin for the treatment of age-related macular degeneration," Surv. Ophthalmol. **45**, 195–214 (2000).

3. B. C. Wilson and M. S. Patterson, "The physics, biophysics and technology of photodynamic therapy.," Phys. Med. Biol. **53**, R61–109 (2008).

4. U. O. Nseyo, B. Shumaker, E. Klein, and K. Sutherland, "Photodynamic therapy using porfimer sodium as an alternative to cystectomy in patients with refractory transitional cell carcinoma in situ of the bladder. Bladder Photofrin Study Group.," J. Urol. **160**, 39–44 (1998).

5. S. B. Brown, E. A. Brown, and I. Walker, "The present and future role of photodynamic therapy in cancer treatment Photodynamic therapy," Lancet Oncol. **5**, 497–508 (2004).

6. J. Usuda, H. Kato, T. Okunaka, K. Furukawa, K. Yamada, Y. Suga, H. Honda, Y. Nagatsuka, T. Ohira, M. Tsuboi, and T. Hirano, "Photodynamic Therapy (PDT) for lung cancers," J. Thorac. Oncol. **1**, 489–493 (2006).

7. B. F. Overholt, K. K. Wang, J. S. Burdick, C. J. Lightdale, M. Kimmey, H. R. Nava, M. V Sivak, N. Nishioka, H. Barr, N. Marcon, M. Pedrosa, M. P. Bronner, M. Grace, and M. Depot, "Five-year efficacy and safety of photodynamic therapy with Photofrin in Barrett's high-grade dysplasia.," Gastrointest. Endosc. **66**, 460–8 (2007).

8. S. E. Eggener, P. T. Scardino, P. R. Carroll, M. J. Zelefsky, O. Sartor, H. Hricak, T. M. Wheeler, S. W. Fine, J. Trachtenberg, M. a Rubin, M. Ohori, K. Kuroiwa, M. Rossignol, and L. Abenhaim, "Focal therapy for localized prostate cancer: a critical appraisal of rationale and modalities.," J. Urol. **178**, 2260–7 (2007).

9. K. L. Molpus, D. Kato, M. R. Hamblin, L. Lilge, M. Bamberg, and T. Hasan, "Intraperitoneal photodynamic therapy of human epithelial ovarian carcinomatosis in a xenograft murine model," Cancer Res. **56**, 1075–1082 (1996).

10. C. Hopper, A. Kübler, H. Lewis, I. B. Tan, and G. Putnam, "mTHPC-mediated photodynamic therapy for early oral squamous cell carcinoma.," Int. J. Cancer **111**, 138–46 (2004).

11. H. J. Nyst, R. L. P. van Veen, I. B. Tan, R. Peters, S. Spaniol, D. J. Robinson, F. Stewart, P. C. Levendag, and H. J. C. M. Sterenborg, "Performance of a dedicated light delivery and dosimetry device for photodynamic therapy of nasopharyngeal carcinoma: phantom and volunteer experiments.," Lasers Surg. Med. **39**, 647–53 (2007).

12. T. J. Dougherty, C. J. Gomer, B. W. Henderson, G. Jori, D. Kessel, M. Korbelik, J. Moan, and Q. Peng, "Photodynamic therapy.," J. Natl. Cancer Inst. **90**, 889–905 (1998).

13. I. J. Macdonald and T. J. Dougherty, "Basic principles of photodynamic therapy," J. Porphyr. Phthalocyanines **5**, 105–129 (2001).

14. G. Portale, J. A. Hagen, J. H. Peters, L. S. Chan, S. R. DeMeester, T. A. K. Gandamihardja, and T. R. DeMeester, "Modern 5-year survival of resectable esophageal adenocarcinoma: single institution experience with 263 patients.," J. Am. Coll. Surg. **202**, 588–96; discussion 596–8 (2006).

15. P. J. Muller and B. C. Wilson, "Photodynamic therapy of brain tumors--a work in progress.," Lasers Surg. Med. **38**, 384–9 (2006).

16. A. Johansson, G. Palte, O. Schnell, J.-C. Tonn, J. Herms, and H. Stepp, "5-Aminolevulinic acid-induced protoporphyrin IX levels in tissue of human malignant brain tumors.," Photochem. Photobiol. **86**, 1373–8 (2010).

17. N. L. Oleinick, R. L. Morris, and I. Belichenko, "The role of apoptosis in response to photodynamic therapy: what, where, why, and how," Photochem. Photobiol. Sci. **1**, 1–21 (2002).

18. D. Kessel, Y. Luo, Y. Deng, and C. K. Chang, "The role of subcellular localization in initiation of apoptosis by photodynamic therapy.," Photochem. Photobiol. **65**, 422–6 (1997).

19. M. Price, L. Heilbrun, and D. Kessel, "Effects of the oxygenation level on formation of different reactive oxygen species during photodynamic therapy," Photochem Photobiol. **89**, 683–686 (2013).

20. T. Vanden Berghe, N. Vanlangenakker, E. Parthoens, W. Deckers, M. Devos, N. Festjens, C. J. Guerin, U. T. Brunk, W. Declercq, and P. Vandenabeele, "Necroptosis, necrosis and secondary necrosis converge on similar cellular disintegration features.," Cell Death Differ. **17**, 922–30 (2010).

21. P. G. Calzavara-Pinton, M. Venturini, and R. Sala, "Photodynamic therapy: update 2006. Part 1: Photochemistry and photobiology.," J. Eur. Acad. Dermatol. Venereol. **21**, 293–302 (2007).

22. S. Gupta, B. S. Dwarakanath, K. Muralidhar, and V. Jain, "Cellular uptake, localization and photodynamic effects of haematoporphyrin derivative in human glioma and squamous carcinoma cell lines.," J. Photochem. Photobiol. B. **69**, 107–20 (2003).

23. H. Mojzisova, S. Bonneau, C. Vever-Bizet, and D. Brault, "Cellular uptake and subcellular distribution of chlorin e6 as functions of pH and interactions with membranes and lipoproteins.," Biochim. Biophys. Acta **1768**, 2748–56 (2007).

24. T. Kiesslich, J. Berlanda, K. Plaetzer, B. Krammer, and F. Berr, "Comparative characterization of the efficiency and cellular pharmacokinetics of Foscan- and Foslip-based photodynamic treatment in human biliary tract cancer cell lines.," Photochem. Photobiol. Sci. **6**, 619–27 (2007).

25. J. L. Sandell and T. C. Zhu, "A review of in-vivo optical properties of human tissues and its impact on PDT," **4**, 773–787 (2012).

26. C. Abels, "Targeting of the vascular system of solid tumours by photodynamic therapy (PDT).," Photochem. Photobiol. Sci. **3**, 765–71 (2004).

27. C. J. Chang, C. H. Sun, L. H. Liaw, M. W. Berns, and J. S. Nelson, "In vitro and in vivo photosensitizing capabilities of 5-ALA versus photofrin in vascular endothelial cells.," Lasers Surg. Med. **24**, 178–86 (1999).

28. I. Georgakoudi and T. H. Foster, "Singlet oxygen- versus nonsinglet oxygen-mediated mechanisms of sensitizer photobleaching and their effects on photodynamic dosimetry.," Photochem. Photobiol. **67**, 612–25 (1998).

29. J. S. Dysart and M. S. Patterson, "Photobleaching kinetics, photoproduct formation, and dose estimation during ALA induced PpIX PDT of MLL cells under well oxygenated and hypoxic conditions.," Photochem. Photobiol. Sci. **5**, 73–81 (2006).

30. H. Schneckenburger, R. Steiner, and A. Rueck, "In vivo photoproduct formation during PDT with ALA-induced endogenous porphyrins," In Vivo (Brooklyn). **18**, 287–290 (1993).

31. K. König, H. Wabnitz, and W. Dietel, "Variation in the fluorescence decay properties of haematoporphyrin derivative during its conversion to photoproducts.," J. Photochem. Photobiol. B. **8**, 103–11 (1990).

32. B. C. Wilson, M. S. Patterson, and L. Lilge, "Implicit and explicit dosimetry in photodynamic therapy : a new paradigm," Lasers Med. Sci. **12**, 182–199 (1997).

33. M. A. Weston and M. S. Patterson, "Monitoring oxygen concentration during photodynamic therapy using prompt photosensitizer fluorescence.," Phys. Med. Biol. **58**, 7039–59 (2013).

34. K. R. Diamond, P. P. Malysz, J. E. Hayward, and M. S. Patterson, "Quantification of fluorophore concentration in vivo using two simple fluorescence-based measurement techniques.," J. Biomed. Opt. **10**, 024007 (2005).

35. K. R. Diamond, M. S. Patterson, and T. J. Farrell, "Quantification of fluorophore concentration in tissue-simulating media by fluorescence measurements with a single optical fiber.," Appl. Opt. **42**, 2436–42 (2003).

36. M. S. Patterson, C. Wilson, and R. Graff, "In vivo tests of the concept of photodynamic threshold dose in normal rat liver photosensitized by aluminum pthalocyanine," Photochem. Photobiol. **51**, 343–349 (1990).

37. C. Sheng, P. J. Hoopes, T. Hasan, and B. W. Pogue, "Photobleaching-based dosimetry predicts deposited dose in ALA-PpIX PDT of rodent esophagus.," Photochem. Photobiol. **83**, 738–48 (2007).

38. J. S. Dysart and M. S. Patterson, "Characterization of Photofrin photobleaching for singlet oxygen dose estimation during photodynamic therapy of MLL cells in vitro.," Phys. Med. Biol. **50**, 2597–616 (2005).

39. M. Niedre, M. S. Patterson, and B. C. Wilson, "Direct near-infrared luminescence detection of singlet oxygen generated by photodynamic therapy in cells in vitro and tissues in vivo.," Photochem. Photobiol. **75**, 382–91 (2002).

40. M. T. Jarvi, M. J. Niedre, M. S. Patterson, and B. C. Wilson, "Singlet oxygen luminescence dosimetry (SOLD) for photodynamic therapy: current status, challenges and future prospects.," Photochem. Photobiol. **82**, 1198–210 (2006).

41. J. R. Lakowicz, *Principles of Fluorescnece Spectroscopy*, 3rd ed. (Springer, 2006).

42. K. Suhling, P. M. W. French, and D. Phillips, "Time-resolved fluorescence microscopy.," Photochem. Photobiol. Sci. **4**, 13–22 (2005).

43. R. Cubeddu, R. Ramponi, and G. Bottiroli, "Time-resolved fluorescence spectroscopy of hematoporphyrin derivative in micelles," Chem. Phys. Lett. **128**, 439–442 (1986).

44. Y. Wu, W. Zheng, and J. Y. Qu, "Sensing cell metabolism by time-resolved autofluorescence.," Opt. Lett. **31**, 3122–4 (2006).

45. A. Ruck, C. Hulshoff, I.Kinzler, W. Becker, and R. Steiner, "SLIM : A new method for molecular imaging," Microsc. Res. Tech. **492**, 485–492 (2007).

46. P. J. Verveer, A. Squire, and P. I. Bastiaens, "Global analysis of fluorescence lifetime imaging microscopy data.," Biophys. J. **78**, 2127–37 (2000).

47. S. Pelet, M. J. R. Previte, L. H. Laiho, and P. T. C. So, "A fast global fitting algorithm for fluorescence lifetime imaging microscopy based on image segmentation.," Biophys. J. **87**, 2807–17 (2004).

48. F. V Bright and C. A. Munson, "Time-resolved fluorescence spectroscopy for illuminating complex systems," Anal. Chim. Acta **500**, 71–104 (2003).

49. L. Marcu, "Fluorescence lifetime techniques in medical applications.," Ann. Biomed. Eng. **40**, 304–31 (2012).

50. W. Becker, A. Bergmann, and C. Biskup, "Multispectral fluorescence lifetime imaging by TCSPC," Microsc. Microanal. **70**, 403–409 (2007).

51. Q. Fang, T. Papaioannou, J. A. Jo, R. Vaitha, K. Shastry, and L. Marcu, "Time-domain laser-induced fluorescence spectroscopy apparatus for clinical diagnostics," Rev. Sci. Instrum. **75**, 151 (2004).

52. T. Papaioannou, N. W. Preyer, Q. Fang, A. Brightwell, M. Carnohan, G. Cottone, R. Ross, L. R. Jones, and L. Marcu, "Effects of fiber-optic probe design and probe-to-target distance on diffuse reflectance measurements of turbid media: an experimental and computational study at 337 nm," Appl. Opt. **43**, 2846–2860 (2004).

53. T. J. Pfefer, D. Y. Paithankar, J. M. Poneros, K. T. Schomacker, and N. S. Nishioka, "Temporally and spectrally resolved fluorescence spectroscopy for the detection of high grade dysplasia in Barrett's esophagus.," Lasers Surg. Med. **32**, 10–6 (2003).

54. M.-A. Mycek, K. T. Schomacker, and N. S. Nishioka, "Colonic polyp differentiation using time-resolved autofluorescence spectroscopy," Gastroenterol. Endosc. **48**, 390–394 (1998).

55. P. V Butte, Q. Fang, J. A. Jo, W. H. Yong, B. K. Pikul, K. L. Black, and L. Marcu, "Intraoperative delineation of primary brain tumors using time-resolved fluorescence spectroscopy.," J. Biomed. Opt. **15**, 027008 (2010).

56. P. V Butte, A. N. Mamelak, M. Nuno, S. I. Bannykh, K. L. Black, and L. Marcu, "Fluorescence lifetime spectroscopy for guided therapy of brain tumors.," Neuroimage **54**, S125–35 (2011).

57. Y. Yuan, J. Hwang, M. Krishnamoorthy, K. Ye, Y. Zhang, J. Ning, R. C. Wang, M. J. Deen, and Q. Fang, "High-throughput acousto-optic-tunable-filter-based time-resolved fluorescence spectrometer for optical biopsy," Opt. Lett. **34**, 1132–1134 (2009).

58. Y. Yuan, T. Papaioannou, and Q. Fang, "Single-shot acquisition of time-resolved fluorescence spectra using a multiple delay optical fiber bundle.," Opt. Lett. **33**, 791–3 (2008).

59. Z. Nie, R. An, J. E. Hayward, T. J. Farrell, and Q. Fang, "Hyperspectral fluorescence lifetime imaging for optical biopsy.," J. Biomed. Opt. **18**, 1-7 (2013).

60. Y. Sun, A. J. Chaudhari, M. Lam, H. Xie, D. R. Yankelevich, J. Phipps, J. Liu, M. C. Fishbein, J. M. Cannata, K. K. Shung, and L. Marcu, "Multimodal characterization of compositional, structural and functional features of human atherosclerotic plaques.," Biomed. Opt. Express **2**, 2288–98 (2011).

61. I. Munro, J. McGinty, N. Galletly, J. Requejo-Isidro, P. M. P. Lanigan, D. S. Elson, C. Dunsby, M. A. A. Neil, M. J. Lever, G. W. H. Stamp, and P. M. W. French, "Toward the clinical application of time-domain fluorescence lifetime imaging.," J. Biomed. Opt. **10**, 051403 (2005).

62. A. V Agronskaia, L. Tertoolen, and H. C. Gerritsen, "Fast fluorescence lifetime imaging of calcium in living cells.," J. Biomed. Opt. **9**, 1230–7 (2004).

63. K. K. Sharman, A. Periasamy, H. Ashworth, and J. N. Demas, "Error analysis of the rapid lifetime determination method for double-exponential decays and new windowing schemes.," Anal. Chem. **71**, 947–52 (1999).

64. M. J. Booth and T. Wilson, "Low-cost, frequency-domain, fluorescence lifetime confocal microscopy.," J. Microsc. **214**, 36–42 (2004).

65. Y. Sun, J. E. Phipps, J. Meier, N. Hatami, B. Poirier, D. S. Elson, D. G. Farwell, and L. Marcu, "Endoscopic fluorescence lifetime imaging for in vivo intraoperative diagnosis of oral carcinoma," Microsc. Microanal. **4**, 1 – 8 (2013).

66. A. Celli, S. Sanchez, M. Behne, T. Hazlett, E. Gratton, and T. Mauro, "The epidermal Ca(2+) gradient: Measurement using the phasor representation of fluorescent lifetime imaging.," Biophys. J. **98**, 911–21 (2010).

67. P. R. Barber, S. M. Ameer-Beg, J. Gilbey, L. . Carlin, M. Keppler, T. . Ng, and B. Vojnovic, "Multiphoton time-domain fluorescence lifetime imaging microscopy: practical application to protein-protein interactions using global analysis," J. R. Soc. Interface **6**, S93–S105 (2009).

68. R. W. K. Leung, S.-C. A. Yeh, and Q. Fang, "Effects of incomplete decay in fluorescence lifetime estimation.," Biomed. Opt. Express **2**, 2517–31 (2011).

69. A. Ruck, "Fluorescence lifetime imaging in PDT. An overview," Med. Laser Appl. **20**, 125–129 (2005).

70. J. A. Russell, K. R. Diamond, T. J. Collins, H. F. Tiedje, J. E. Hayward, T. J. Farrell, M. S. Patterson, and Q. Fang, "Characterization of fluorescence lifetime of Photofrin and delta-aminolevulinic acid induced protoporphyrin IX in living cells using single and two-photon excitation," IEEE J. Quantum Electron. **14**, 158–166 (2008).

71. T. Theodossiou and A. J. MacRobert, "Comparison of the photodynamic effect of exogenous photoprotoporphyrin and protoporphyrin IX on PAM 212 murine keratinocytes.," Photochem. Photobiol. **76**, 530–7 (2002).

72. L. Howe, A. Sucheta, O. Einarsdottir, and J. Z. Zhang, "Time-resolved studies of the excited-state dynamics of meso-Tetra (hydroxylphenyl) cholorin in Solution," Photochem. Photobiol. **69**, 617–623 (1999).

73. J. P. Connelly, S. W. Botchway, L. Kunz, D. Pattison, A. W. Parker, and A. J. MacRobert, "Time-resolved fluorescence imaging of photosensitiser distributions in mammalian cells using a picosecond laser line-scanning microscope," J. Photochem. Photobiol. A Chem. **142**, 169–175 (2001).

74. O. Mermut, I. Noiseux, J.-P. Bouchard, J.-F. Cormier, P. Desroches, M. Fortin, P. Gallant, S. Leclair, M. L. Vernon, K. R. Diamond, and M. S. Patterson, "Effect of liposomal confinement on photothermal and photo-oximetric fluorescence lifetimes of photosensitizers with varying hydrophilicity.," J. Biomed. Opt. **13**, 041314 (2008).

75. W. Mo, D. Rohrbach, and U. Sunar, "Imaging a photodynamic therapy photosensitizer in vivo with a time-gated fluorescence tomography system.," J. Biomed. Opt. **17**, 071306 (2012).

76. L. Kelbauskas and W. Dietel, "Internalization of aggregated photosensitizers by tumor cells : subcellular yime-resolved fluorescence spectroscopy on derivatives of pyropheophorbide-a ethers and chlorin e6 under femtosecond one- and two-photon excitation," Photochem. Photobiol. **76**, 686–694 (2002).

77. A. E. O'Connor, W. M. Gallagher, and A. T. Byrne, "Porphyrin and nonporphyrin photosensitizers in oncology: preclinical and clinical advances in photodynamic therapy.," Photochem. Photobiol. **85**, 1053–74 (2009).

78. S.-C. A. Yeh, K. R. Diamond, M. S. Patterson, Z. Nie, J. E. Hayward, and Q. Fang, "Monitoring photosensitizer uptake using two photon fluorescence lifetime imaging microscopy.," Theranostics **2**, 817–26 (2012).

79. M. Kress, T. Meier, R. Steiner, F. Dolp, R. Erdmann, U. Ortmann, and A. Rück, "Time-resolved microspectrofluorometry and fluorescence lifetime imaging of photosensitizers using picosecond pulsed diode lasers in laser scanning microscopes.," J. Biomed. Opt. **8**, 26–32 (2003).

80. R. Hilf, "Mitochondria are targets of photodynamic therapy.," J. Bioenerg. Biomembr. **39**, 85–9 (2007).

81. J. Morgan and A. Oseroff, "Mitochondria-based photodynamic anti-cancer therapy.," Adv. Drug Deliv. Rev. **49**, 71–86 (2001).

82. J. Saczko, M. Mazurkiewicz, a Chwiłkowska, J. Kulbacka, G. Kramer, M. Ługowski, M. Snietura, and T. Banaś, "Intracellular distribution of Photofrin in malignant and normal endothelial cell lines.," Folia Biol. (Praha). **53**, 7–12 (2007).

83. G. Singh, W. P. Jeeves, B. C. Wilson, and D. Jang, "Mitochondrial photosensitization by Photofrin II.," Photochem. Photobiol. **46**, 645–9 (1987).

84. Y.-J. Hsieh, C.-C. Wu, C.-J. Chang, and J.-S. Yu, "Subcellular localization of Photofrin determines the death phenotype of human epidermoid carcinoma A431 cells triggered by photodynamic therapy: when plasma membranes are the main targets.," J. Cell. Physiol. **194**, 363–75 (2003).

85. H.-P. Lassalle, M. Wagner, L. Bezdetnaya, F. Guillemin, and H. Schneckenburger, "Fluorescence imaging of Foscan and Foslip in the plasma membrane and in whole cells.," J. Photochem. Photobiol. B. **92**, 47–53 (2008).

86. A. Khursid, M. Atif, S. Firdous, S. S. Z. Zaidi, R. Salman, and M. Ikram, "Study of the efficacy of 5 ALA-mediated photodynamic therapy on human larynx squamous cell carcinoma (Hep2c) cell line," Laser Phys. **20**, 1673–1678 (2010).

87. M. S. AlSalhi, M. Atif, A. . AlObiadi, and a. S. Aldwayyan, "Photodynamic damage study of HeLa cell line using ALA," Laser Phys. **21**, 733–739 (2011).

88. M. Fakhar-e-Alam, M. Atif, T. Rehman, H. Sadia, and S. Firdous, "The role of sensitivity of ALA (PpIX)-based PDT on Human embryonic kidney cell line (HEK293T)," Laser Phys. **21**, 1428–1437 (2011).

89. M. Atif, M. Fakhar-e-Alam, S. Firdous, S. S. Z. Zaidi, R. Suleman, and M. Ikram, "Study of the efficacy of 5-ALA mediated photodynamic therapy on human rhabdomyosarcoma cell line (RD)," Laser Phys. Lett. **7**, 757–764 (2010).

90. A. Chwiłkowska, J. Saczko, T. Modrzycka, A. Marcinkowska, A. Malarska, J. Bielewicz, D. Patalas, and T. Banaś, "Uptake of photofrin II, a photosensitizer used in photodynamic therapy, by tumour cells in vitro.," Acta Biochim. Pol. **50**, 509–13 (2003).

91. K. W. Woodburn, N. J. Vardaxis, J. S. Hill, A. H. Kaye, and D. R. Phillips, "Subcellular localization of porphyrins using confocal laser scanning microscopy.," Photochem. Photobiol. **54**, 725–32 (1991).

92. M. Geze, P. Morli, J. C. Mazi, K. M. Smith, and R. Santw, "Lysosomes , a key target of hydrophobic for photochemotherapeutic applications photosensitizers proposed," **20**, 23–35 (1993).

93. A. Høgset, "Photochemical internalisation in drug and gene delivery," Adv. Drug Deliv. Rev. **56**, 95–115 (2004).

94. A. Scully, R. B. Ostler, D. Phillips, P. O'Neill, K. M. S. Townsend, A. W. Parker, and a J. MacRobert, "Application of fluorescence lifetime imaging microscopy to the investigation of intracellular PDT mechanisms," Bioimaging **5**, 9–18 (1997).

95. A. W. J Moan, K Berg, JC Bommer, "Action spectra of phthalocyanines with respect to photosensitization of cells," Photochem. Photobiol. **56**, 171–175 (1992).

96. L. Ma, S. Bagdonas, and J. Moan, "The photosensitizing effect of the photoproduct of protoporphyrin IX.," J. Photochem. Photobiol. B. **60**, 108–13 (2001).

97. R. E. Nothdurft, S. V Patwardhan, W. Akers, Y. Ye, S. Achilefu, and J. P. Culver, "In vivo fluorescence lifetime tomography.," J. Biomed. Opt. **14**, 024004 (2009).

98. A. T. N. Kumar, S. B. Raymond, A. K. Dunn, B. J. Bacskai, and D. A. Boas, "A time domain fluorescence tomography system for small animal imaging.," IEEE Trans. Med. Imaging **27**, 1152–63 (2008).

99. A. B. Milstein, S. Oh, K. J. Webb, C. A. Bouman, Q. Zhang, D. A. Boas, and R. P. Millane, "Fluorescence optical diffusion tomography.," Appl. Opt. **42**, 3081–94 (2003).

100. V. Ntziachristos and R. Weissleder, "Experimental three-dimensional fluorescence reconstruction of diffuse media by use of a normalized Born approximation.," Opt. Lett. **26**, 893–5 (2001).

101. H. R. Nava, S. S. Allamaneni, T. J. Dougherty, T. Michele, W. Tan, G. Wilding, and B. W. Henderson, "Photodynamic therapy (PDT) using HPPH for the treatment of precancerous lesions associated with Barrett's esophagus," Lasers Surg Med **43**, 705–712 (2011).

102. U. Sunar, D. Rohrbach, N. Rigual, E. Tracy, K. Keymel, M. T. Cooper, H. Baumann, and B. H. Henderson, "Monitoring photobleaching and hemodynamic responses to HPPH-mediated photodynamic therapy of head and neck cancer: a case report.," Opt. Express **18**, 14969–78 (2010).

103. D. Sud, W. Zhong, D. G. Beer, and M.-A. Mycek, "Time-resolved optical imaging provides a molecular snapshot of altered metabolic function in living human cancer cell models.," Opt. Express **14**, 4412–26 (2006).

104. B. W. Pogue, J. D. Pitts, M.-A. Mycek, R. D. Sloboda, C. M. Wilmot, J. F. Brandsema, and J. O'Hara, "In vivo NADH fluorescence monitoring as an assay for cellular damage in photodynamic therapy.," Photochem. Photobiol. **74**, 817–24 (2001).

105. V. V Ghukasyan and F. Kao, "Monitoring cellular metabolism with fluorescence lifetime of reduced nicotinamide adenine dinucleotide," J Phys Chem **113**, 11532–11540 (2009).

106. H.-W. Wang, V. Gukassyan, C.-T. Chen, Y.-H. Wei, H.-W. Guo, J.-S. Yu, and F.-J. Kao, "Differentiation of apoptosis from necrosis by dynamic changes of reduced nicotinamide adenine dinucleotide fluorescence lifetime in live cells.," J. Biomed. Opt. **13**, 054011 (2008).

107. E. Maeno, T. Shimizu, and Y. Okada, "Normotonic cell shrinkage induces apoptosis under extracellular low Cl conditions in human lymphoid and epithelial cells.," Acta physiol **187**, 217–22 (2006).

108. J.-S. Yu, H.-W. Guo, C.-H. Wang, Y.-H. Wei, and H.-W. Wang, "Increase of reduced nicotinamide adenine dinucleotide fluorescence lifetime precedes mitochondrial dysfunction in staurosporine-induced apoptosis of HeLa cells.," J. Biomed. Opt. **16**, 036008 (2011).

109. T. L. Becker, A. D. Paquette, K. R. Keymel, B. W. Henderson, and U. Sunar, "Monitoring blood flow responses during topical ALA-PDT.," Biomed. Opt. Express **2**, 123–30 (2010).

110. R. Niesner, B. Peker, P. Schlüsche, K.-H. Gericke, C. Hoffmann, D. Hahne, and C. Müller-Goymann, "3D-resolved investigation of the pH gradient in artificial skin constructs by means of fluorescence lifetime imaging.," Pharm. Res. **22**, 1079–87 (2005).

111. I. Georgakoudi, M. G. Nichols, and T. H. Foster, "The mechanism of Photofrin photobleaching and its consequences for photodynamic dosimetry.," Photochem. Photobiol. **65**, 135–44 (1997).

112. S. Mitra and T. H. Foster, "Photochemical oxygen consumption sensitized by a porphyrin phosphorescent probe in two model systems.," Biophys. J. **78**, 2597–605 (2000).

113. J. C. Finlay, S. Mitra, and T. H. Foster, "In vivo mTHPC photobleaching in normal rat skin exhibits unique irradiance-dependent features," Photochem. Photobiol. **75**, 282–288 (2002).

114. M. G. Nichols and T. H. Foster, "Oxygen diffusion and reaction kinetics in the photodynamic therapy of multicell tumour spheroids.," Phys. Med. Biol. **39**, 2161–81 (1994).

115. R. J. Errington, S. M. Ameer-Beg, B. Vojnovic, L. H. Patterson, M. Zloh, and P. J. Smith, "Advanced microscopy solutions for monitoring the kinetics and dynamics of drug-DNA targeting in living cells.," Adv. Drug Deliv. Rev. **57**, 153–67 (2005).

116. H.-W. Guo, C.-T. Chen, Y.-H. Wei, O. K. Lee, V. Gukassyan, F.-J. Kao, and H.-W. Wang, "Reduced nicotinamide adenine dinucleotide fluorescence lifetime separates human mesenchymal stem cells from differentiated progenies.," J. Biomed. Opt. **13**, 050505 (2008).

117. G.-C. Su, Y.-H. Wei, and H.-W. Wang, "NADH fluorescence as a photobiological metric in 5-aminolevlinic acid (ALA)-photodynamic therapy.," Opt. Express **19**, 21145–54 (2011).

118. W. Zhong, P. Urayama, and M.-A. Mycek, "Imaging fluorescence lifetime modulation of a ruthenium-based dye in living cells: the potential for oxygen sensing," J. Phys. D. Appl. Phys. **36**, 1689–1695 (2003).

119. J. P. Celli, B. Q. Spring, R. Imran, E. CL, K. S, S. Verma, B. W. Pogue, and T. Hasan, "Imaging and photodynamic therapy: Mechanisms, monitoring, and optimization," Chem Rev **110**, 2795–2838 (2010).

120. K. C. Lee, J. Siegel, S. E. Webb, S. Lévêque-Fort, M. J. Cole, R. Jones, K. Dowling, M. J. Lever, and P. M. French, "Application of the stretched exponential function to fluorescence lifetime imaging.," Biophys. J. **81**, 1265–74 (2001).

121. M. Budiman, R. L. Stroshine, and P. Cornillon, "Moisture measurement in cheese analogue using stretched and multi-exponential models of the magnetic resonance T2 relaxation curve," J. Dairy Res. **69**, 619–632 (2002).

122. M. Maus, M. Cotlet, J. Hofkens, T. Gensch, F. C. De Schryver, J. Schaffer, and C. a Seidel, "An experimental comparison of the maximum likelihood estimation and nonlinear least-squares fluorescence lifetime analysis of single molecules.," Anal. Chem. **73**, 2078–86 (2001).

123. J. M. Maarek, L. Marcu, W. J. Snyder, and W. S. Grundfest, "Time-resolved fluorescence spectra of arterial fluorescent compounds: reconstruction with the Laguerre expansion technique.," Photochem. Photobiol. **71**, 178–87 (2000).

124. J. A. Jo, Q. Fang, and L. Marcu, "Ultrafast Method for the Analysis of Fluorescence Lifetime Imaging Microscopy Data Based on the Laguerre Expansion Technique.," IEEE J. Quantum Electron. **11**, 835–845 (2005).

125. J. A. Jo, Q. Fang, T. Papaioannou, J. D. Baker, A. H. Dorafshar, T. Reil, J.-H. Qiao, M. C. Fishbein, J. a Freischlag, and L. Marcu, "Laguerre-based method for analysis of time-resolved fluorescence data: application to in-vivo characterization and diagnosis of atherosclerotic lesions.," J. Biomed. Opt. **11**, 021004 (2006).

126. Y. Chen and A. Periasamy, "Characterization of two-photon excitation fluorescence lifetime imaging microscopy for protein localization.," Microsc. Res. Tech. **63**, 72–80 (2004).

127. P. R. Barber, S. M. Ameer-Beg, J. D. Gilbey, R. J. Edens, I. Ezike, and B. Vojnovic, "Global and pixel kinetic data analysis for FRET detection by multi-photon time-domain FLIM," Proc. SPIE **5700**, 171–181 (2005).

128. S. L. Jacques, "How tissue optics affect dosimetry of photodynamic therapy.," J. Biomed. Opt. **15**, 051608 (2010).

129. M. S. Patterson and B. W. Pogue, "Mathematical model for time-resolved and frequency-domain fluorescence spectroscopy in biological tissues," Appl. Opt. **33**, 1963–1974 (1994).

130. J. Wu, F. Partovi, M. S. Field, and R. P. Rava, "Diffuse reflectance from turbid media: an analytical model of photon migration.," Appl. Opt. **32**, 1115–21 (1993).

131. K. Vishwanath, B. Pogue, and M. Mycek, "Quantitative fluorescence lifetime spectroscopy in turbid media : comparison of theoretical , experimental and computational methods," Phys Med Biol **47**, 3387–3405 (2002).

132. K. Vishwanath and M.-A. Mycek, "Time-resolved photon migration in bi-layered tissue models.," Opt. Express **13**, 7466–82 (2005).

133. T. Pyka, R. Schulz, A. Ale, and V. Ntziachristos, "Revisiting the normalized Born approximation: effects of scattering.," Opt. Lett. **36**, 4329–31 (2011).

134. S. V Patwardhan and J. P. Culver, "Quantitative diffuse optical tomography for small animals using an ultrafast gated image intensifier.," J. Biomed. Opt. **13**, 011009 (2008).

135. A. H. Andersen and A. C. Kak, "Simultaneous algebraic reconstruction technique (SART): a superior implementation of the art algorithm," Ultrason. Imaging **6**, 81–94 (1984).

136. A. T. N. Kumar, S. B. Raymond, B. J. Bacskai, and D. A. Boas, "Comparison of frequency-domain and time-domain fluorescence lifetime tomography.," Opt. Lett. **33**, 470–2 (2008).

137. A. T. Kumar, S. B. Raymond, G. Boverman, D. A. Boas, and B. J. Bacskai, "Time resolved fluorescence tomography of turbid media based on lifetime contrast.," Opt. Express **14**, 12255–70 (2006).

138. G. O. Fruhwirth, S. Ameer-Beg, R. Cook, T. Watson, T. Ng, and F. Festy, "Fluorescence lifetime endoscopy using TCSPC for the measurement of FRET in live cells.," Opt. Express **18**, 11148–58 (2010).

139. K. König, "Clinical multiphoton tomography.," J. Biophotonics **1**, 13–23 (2008).

140. K. Konig and I. Riemann, "High-resolution multiphoton tomography of human skin with subcellular spatial resolution and picosecond time resolution.," J. Biomed. Opt. **8**, 432–9 (2003).

141. H. Xie, J. Bec, J. Liu, Y. Sun, M. Lam, D. R. Yankelevich, and L. Marcu, "Multispectral scanning time-resolved fluorescence spectroscopy (TRFS) technique for intravascular diagnosis.," Biomed. Opt. Express **3**, 1521–33 (2012).

142. P. A. A. De Beule, C. Dunsby, N. P. Galletly, G. W. Stamp, A. C. Chu, U. Anand, P. Anand, C. D. Benham, A. Naylor, and P. M. W. French, "A hyperspectral fluorescence lifetime probe for skin cancer diagnosis.," Rev. Sci. Instrum. **78**, 123101 (2007).

Chapter 3.

Paper II – Monitoring Photosensitizer Uptake Using Two-Photon Fluorescence Lifetime Imaging Microscopy

Shu-Chi Allison Yeh[1], Kevin R. Diamond[3], Michael S. Patterson[1,3], Zhaojun Nie[1], Joseph E. Hayward[2,3] and Qiyin Fang[1,2,*]

[1]School of Biomedical Engineering, McMaster University, 1280 Main Street West, Hamilton, Ontario, L8S 4K1, Canada

[2]Department of Engineering Physics, McMaster University, 1280 Main Street West, Hamilton, Ontario, L8S 4K1, Canada

[3]Department of Medical Physics and Applied Radiation Sciences, McMaster University, 1280 Main Street West, Hamilton, Ontario, L8S 4K1, Canada

Published in Theranostics; 2(9):817-826, 2012

Introduction to paper II

In this chapter, photosensitizer-molecular interactions were studied *in vitro* using fluorescence lifetime imaging microscopy (FLIM). As a relatively new technique, FLIM may provide additional information on biochemical and physiological state of the targeted fluorophores and their microenvironments. PDT efficacy relies on the interplay between localized drug and light. Monitoring TRF for the subcellular location of photosensitizers yield information regarding the drug binding status, potential formation of photoproduct and aggregates, and may be eventually beneficial for probing cell damages.

In this work, a prostate cancer cell line (Mat-Lylu) was incubated with a FDA-approved photosensitizer, Photofrin®. We hypothesize that the fluorescence lifetime of photosensitizers will go through changes during drug uptake, from cellular membrane, cytoplasm, to mitochondria. The drug will be redistributed after mitochondrial depolarization, which initiates apoptosis. We analyzed the fluorescence decays using a bi-exponential model, followed by segmentation analysis of localized lifetime parameters. When Photofrin® was localized at the cell membrane, the slow lifetime component was found to be significantly shorter (4.3 ± 0.5 ns) than those at other locations (cytoplasm: 7.3 ± 0.3 ns; mitochondria: 7.0 ± 0.2 ns, $p < 0.05$).

This work shows that the time-resolved fluorescence imaging may change according to the subcellular location and the drug structure. The targeted audience of this work include researchers who are also investigating PDT dosimetry, photosensitizer-molecular interactions, and/or time-resolved fluorescence-based biomedical applications. This manuscript was prepared by me and revised by all of the co-authors.

Contents of Paper II

Abstract

Photodynamic Therapy (PDT) provides an opportunity for treatment of various invasive tumors by the use of a cancer targeting photosensitizing agent and light of specific wavelengths. However, real-time monitoring of drug localization is desirable because the induction of the phototoxic effect relies on interplay between the dosage of localized drug and light. Fluorescence emission in PDT may be used to monitor the uptake process but fluorescence intensity is subject to variability due to scattering and absorption; the addition of fluorescence lifetime may be beneficial to probe site-specific drug-molecular interactions and cell damage. We investigated the fluorescence lifetime changes of Photofrin® at various intracellular components in the Mat-LyLu (MLL) cell line. The fluorescence decays were analyzed using a bi-exponential model, followed by segmentation analysis of lifetime parameters. When Photofrin® was localized at the cell membrane, the slow lifetime component was found to be significantly shorter (4.3 ± 0.5 ns) compared to those at other locations (cytoplasm: 7.3 ± 0.3 ns; mitochondria: 7.0 ± 0.2 ns, $p < 0.05$).

3.1. Introduction

Photodynamic therapy (PDT) is a cancer treatment for various types of invasive tumors. The main advantages of PDT over traditional cancer treatments are attributed to the localized effects of the photochemical reactions. It involves the administration of a photosensitizer, followed by the activation of the drug by light that initiates the "phototoxic effect" – the coupling of drugs in the triplet excited state with ground state oxygen molecules. This reaction leads to the generation of the highly cytotoxic singlet oxygen ($^1O_2$) species, which has an extremely short lifetime and distribution radius, enabling localized therapeutic effects [1]. However, the therapeutic efficacy of PDT depends strongly on the local concentration of the photosensitizer and amount of light it absorbs, thus the current clinical standard of using prescribed drug and light dosages is insufficient. PDT dose is influenced by factors such as different drug uptake rates, tissue optical properties, variable tissue oxygenation, as well as unexpected photophysical and photochemical changes of the photosensitizing agents [2]. As a result, real-time monitoring of the drug distribution and its interactions with surrounding tissue has become a valuable approach in order to determine the dosage more accurately. Some potential dosimetric approaches using the steady-

state fluorescence spectra of photosensitizers have been studied to determine the effective PDT dosage. Explicit dosimetry measures each dose factor independently by modeling input parameters (*e.g.* the photosensitizer concentration, light fluence, and oxygenation within the targets) to retrieve the proper PDT dose. In order to incorporate all of the dose determining factors into a single metric, including PDT pathways that may affect the individual treatment outcome, implicit dosimetry correlating photobleaching and cell viability has also been investigated [2–7]. Although these techniques tackled the underlying photochemistry and photobiology of the excited photosensitizers in the tumor site, the measured steady-state fluorescence intensity still suffered from artifacts arising from the heterogeneity of tissue optical properties [8], local environment, unknown chromophores with overlapped spectra, and the geometry of excitation and detection [9]. That is, the measured intensity does not truly represent what happens inside the tumor and direct measurements of tissue optics are still required. Therefore, under- or over-estimation of the drug concentration may happen due to individual variability if it is estimated by the amplitude of fluorescence signal alone. These problems may be overcome by the addition of time-resolved features (lifetime, fitting coefficients, etc.), which are independent of signal intensity [10]. Fluorescence lifetime, defined as how long a fluorophore remains in its excited state, is sensitive to intermolecular interactions and changes of microenvironment while it is independent of intensity variations and the problems suffered by steady-state fluorescence techniques. Fluorescence lifetime imaging microscopy (FLIM) makes it possible to distinguish these factors and reveal the drug interactions with the cellular environment [11]. Previous studies have shown that photosensitizers' fluorescence lifetimes go through significant changes when bound to intracellular components. For example, the fluorescence lifetimes of photosensitizers such as Photofrin®, 5-ALA, and mTHPC were all shortened *in vitro* compared to those in solution [12–17]. These changes in lifetime provide opportunities to monitor the binding states of photosensitizers, and the microenvironment. In particular, it is known that drug distribution and its cytotoxicity have a strong correlation [18–21] . Despite this correlation, the relationship between lifetime changes and drug localization has not been well studied. Thus, characterizing the fluorescence decay time of the photosensitizer localized at a specific intracellular component may not only differentiate between different species of photosensitizers (*e.g.* monomeric or aggregated forms) located in a particular intracellular microenvironment [13], but also reveal the drug-molecular interacting process of PDT drug inside cells. In addition, as the conventional one-photon technique is subject to scattering and out of focus signals that confound fluorescence emission from various intracellular sources, two-photon laser excitation takes advantage of nonlinear optical effects from near-IR ultrafast lasers to confine the imaging spot size to femto-liter volumes with less scattering effect at this spectral window [22,23]. These small volumes enable more accurate data interpretation and analysis. Eventually, it is possible that the

combination of steady-state and time-resolved fluorescence could be correlated to cell viability, which may be a valuable tool for real-time PDT dosimetry.

The purpose of this study is to investigate how fluorescence lifetime changes when a photosensitizer is bound to specific intracellular components at specific stages of cellular uptake. Photofrin® (porfimer sodium) was used in this study as it is a photosensitizing agent used widely in PDT to treat solid tumors [1].

3.2. Materials and Methods

We characterized the time-lapse fluorescence intensity and lifetime distribution of Photofrin® (Axcan Pharma Inc., Mont-Saint-Hilaire, QC, Canada) in Mat-LyLu (MLL) rat prostate adenocarcinoma cell line. Cells were incubated with Photofrin® at 5 μg/mL for times ranging from 0.5 hour to 18 hours. The confocal microscope was used for visualizing the intracellular drug location and two-photon fluorescence lifetime imaging was performed for tracking fluorescence lifetime changes *in vitro*. The fluorescence lifetime information was correlated with the subcellular locations of the photosensitizer.

3.2.1. Cell culture

Mat-LyLu is a rat prostate adenocarcinoma cell line used in previous studies [5,14]. The cells were incubated in 25 cm^2 sealed vials [35-3108, Becton Dickinson Falcon™, NJ, USA] with 3.5 mL of medium that contains RPMI medium 1640 (11875-093, Gibco-BRL, Gaithersburg, MD, USA) with 2% antibiotic/antimycotic (15240-095, Gibco-BRL), 1% hepes buffer (15630-105, Gibco-BRL), and also supplemented with 10% Fetal Bovine Serum (FBS) (10437-010, Gibco-BRL) at 37 ºC in a water jacketed CO_2 incubator (Forma Series II, Thermo Fisher Scientific Inc, Waltham, MA, USA). Cells were passaged every 2 to 3 days until it reached about 60% of confluence.

3.2.2. Experimental preparation

Cells were removed from the original culture vials using 0.5% of 10X Trypsin-EDTA (15400-054, Gibco-BRL), and then seeded on a 25 mm glass coverslip (pre-washed with 99.9% ethanol (34964, Sigma Aldrich) to remove any possible coatings that may affect cell attachment and growth) in culture medium in a 35 × 10 mm dish. After 6 hours of incubation, the medium was replaced by one containing Photofrin® solution. To dilute Photofrin® properly, a stock solution of 2.5 mg/mL of the photosensitizer dissolved in PBS (14200-075, Dulbecco's Phosphate Buffered Saline 10X Gibco-BRL) was diluted in the culture medium to a final concentration of 5μg/mL. Cells were incubated in the Photofrin® containing medium for the specified periods and then the coverslip was rinsed with PBS twice and placed in a metal chamber for imaging. 1 mL of Hanks buffer

solution with Ca^{2+} was added into the chamber to prevent cells from drying and undergoing apoptosis during imaging.

3.2.3. Confocal imaging and two-photon fluorescence lifetime imaging

The time-dependent Photofrin® fluorescence emission was collected by a laser scanning confocal microscope (TSC SP5 & DMI 6000 B, Leica, Wetzlar, Germany) with a 63X oil-immersed objective lens. A built-in Argon-ion laser operating at 514 nm was used in combination with the emission range from 600 - 750 nm. The FLIM microscope was coupled to a Ti:Sapphire laser (Chameleon-Ultra, Coherent, Santa Clara, CA, USA) emitting at 810 nm with 80 MHz repetition rate. An integrated TCSPC module (SPC-830, Becker & Hickl GmbH, Berlin, Germany) was used to record fluorescence decay kinetics throughout 64 time channels. The fluorescence lifetime system has been described in a previous publication [14]. The average power used for fluorescence lifetime acquisition was around 45 mW with 1.5 ps pulse duration at the objective plane, which yields a peak power density of approximately 1.5×10^{11} W cm^{-2}. The total pixel dwell time for 60 seconds of acquisition was approximately 915 μs, which renders the total fluence of 4350 J/cm^2 with the pixel size of 0.96 x 0.96 μm^2.

The images were acquired after 1 hour and 18 hours of incubation to characterize initial uptake of Photofrin® and prolonged incubation, respectively. In addition, data were acquired every 30 minutes from 2 hours to 6 hours of incubation to examine the uptake process *in vitro* in more detail.

3.2.4. Data analysis

Time-lapse FLIM data were fitted with a bi-exponential model using the vendor supplied software (SPCImage, v3.0.8.0, Becker and Hickl). The sample measured decay trace and its fitting curve from a single pixel were demonstrated in **Fig. 3.1**. The retrieved individual lifetime and amplitude parameters of every pixel were then imported to MATLAB (Mathworks, Natick, MA) for futher analysis using a program developed in-house. Three repeated trials for each incubation period were acquired, with each trial containing multiple regions of interest. From each lifetime image, the mean value and standard deviation of individual parameters such as the bi-exponential lifetime components (τ_2, τ_1), and corresponding coefficients (A_2, A_1) of every pixel in the image were plotted. Using these values, the weighted mean and standard deviation of three repetitive measurements were calculated. The regions of interest, for example, mitochondria or cytoplasm, were segmented based on intensity. The segmentation was only performed on images collected at 4 hours and 4.5 hours of incubation, where the Photofrin® localization was undergoing a "transition" stage, thus the FLIM images showed lifetime values from different locations. The classification of the intracellular components was first visually verified based on preliminary confocal images as shown in **Fig 3.2(a)**, where the cells were stained with MitoTracker®

Green (FM 7514, Invitrogen) to reveal the mitochondrial distribution. The segmentation was then done based on thresholding the histogram of pixel intensity (photon counts/ pixel) in the intensity images. Intensity values ranging from 15 - 60 counts per pixel were classified as "cytoplasm", and greater than 60 counts per pixel were classified as mitochondria. Sample confocal and segmentation images are shown in **Fig. 3.2(c)** and **3.2(d)**. As the signal of Photofrin® is extremely low and comparable with the autofluorescence at the beginning of incubation (less than 1 hour), the cell membrane was selected using the Matlab® built-in periphery detection function (*bwperim*) instead of segmentation.

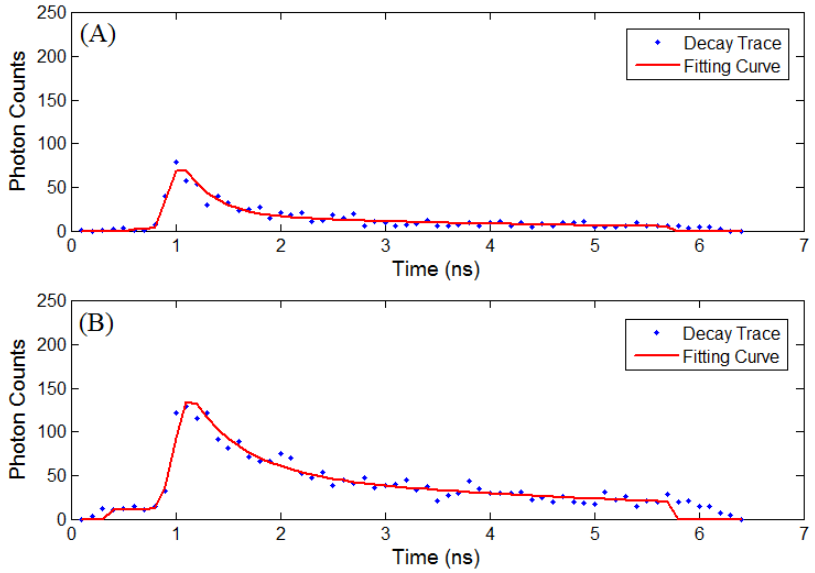

Figure 3.1(A) Sample measured decay trace (blue dotted line) and the fitting curve (red line) from a pixel in data at 2.5 hours of incubaton. Data was exported from the SPCImage software and plotted in Matlab. Each data point represents the total photon counts collected in that time channel. (B) Sample measured data and fitting curve from a pixel in data at 4.5 hours of incubaton. It is noted that the peak intensity increases with the cellular uptake.

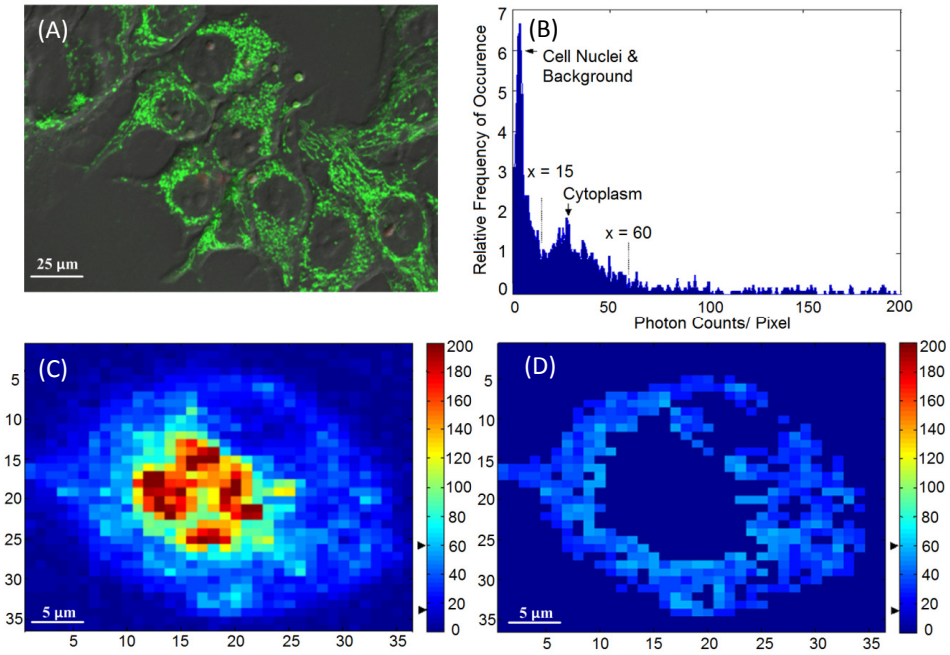

Figure 3.2 (A) A sample confocal image showing the distribution of mitochondria. MLL cells were stained with 100 nM of MitoTracker® Green, as indicated by the green color. (B) Histogram (photon count per pixel) used for segmentation of FLIM images. Based on the morphological features shown in confocal images, the main peak corresponds to the lower pixel intensities from the cell nuclei, and the minor peak corresponds to the intensities from the cytoplasmic region, as indicated by the arrows and the range covered by the dashed lines. (C) Original intensity image of a single cell. The cell was stained with Photofrin® for 4.5 hours, when Photofrin® presented at both mitochondrial and cytoplasm regions. Note the image was from a small area of a field of view, therefore the image seems pixelated. The thresholds used to segment the cytoplasmic region were marked by the black arrows on the color bar (D) The segmentation was performed based on the morphological features and histogram, where signals with intensity > 60 counts/pixel (mitochondria) and < 15 counts/ pixel (cell nucleus and background) were eliminated.

3.3. Results

Steady-state confocal images showed the location and cellular uptake rate of Photofrin® matched the literature, where Photofrin® first binds to the plasma membrane, then moves towards cytoplasm, and finally targets the inner membrane of the mitochondria [20,24,25]. These confocal results were also consistent with the FLIM images when cells were stained with 20 µg/mL of Photofrin® as shown in **Fig. 3.3**.

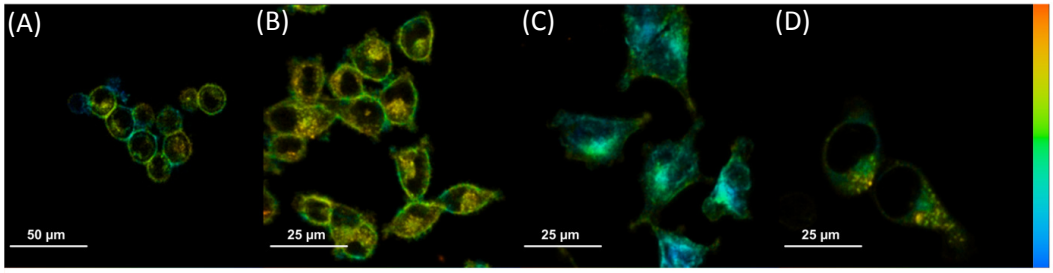

Figure 3.3 Sample time-lapse average lifetime images of Photofrin® (20 µg/mL) uptake by MLL cells between 1-18 hours. The color legend illustrates the corresponding lifetime values ranging from 1 ns (red) to 10 ns (blue). The pixels corresponding to the photosensitizer in the lifetime images are co-localized with the signal of the steady-state fluorescence images (data not shown). (A) The image shows Photofrin® uptake by the cell membrane at 1 hour of incubation; (B) 2 to 4 hours of incubation. This image was acquired at 2.5 hours of incubation when Photofrin® started to migrate into the cytoplasm; (C) Photofrin® has localized at the peri-nuclear region after 6 hours of incubation; and (D) After 18 hours of incubation, granular spots have appeared in the cells and the redistribution of the drug after prolonged incubation was observed.

The FLIM datasets acquired at different incubation times were then classified into four categories based on the intracellular distribution: namely membrane, cytoplasm, mitochondria, and redistribution groups. Various sources of fluorescence may contribute to the total exponential decay signal, such as photoproducts, different molecular constituents of Photofrin®, and autofluorescence. Rather than use the average fluorescence lifetime to monitor the Photofrin® uptake process, the fluorescence lifetimes and amplitudes were plotted separately. **Fig. 3.4** shows the slow lifetime component of Photofrin® when it is localized at different intracellular components over various incubation periods. The values of the longer lifetime component (τ_2) are consistent with previous spectral-resolved FLIM studies, where the fluorescence signals of photoproducts and aggregated Photofrin® (emission range at 651 nm – 687 nm) increased after irradiation and exhibited long lifetime components of approximately 8 ns [13,16]. In **Fig. 3.4**, τ_2 did not change significantly from 2 hours to 18 hours of incubation. The individual standard deviation of τ_2, however, was reduced from around 1 ns to 0.4 ns after 4.5 hours of incubation, when Photofrin® was localized in the mitochondrial regions. The overlap of cytoplasmic and mitochondria groups at 4 hours and 4.5 hours of incubation were analyzed based on the segmentation technique. At the transition stage, the values of fluorescence lifetime and standard deviation between two groups were similar. It should be noted that Photofrin® exhibited the slow decay time (τ_2) of 4.3 ± 0.5 ns when it was bound to the cell membrane. The significant lifetime change compared to all other incubation periods ($p < 0.01$ except for redistribution group where $p < 0.05$) suggested that

the differences between the cell membrane microenvironment and other regions may result in more quenching of the fluorescence.

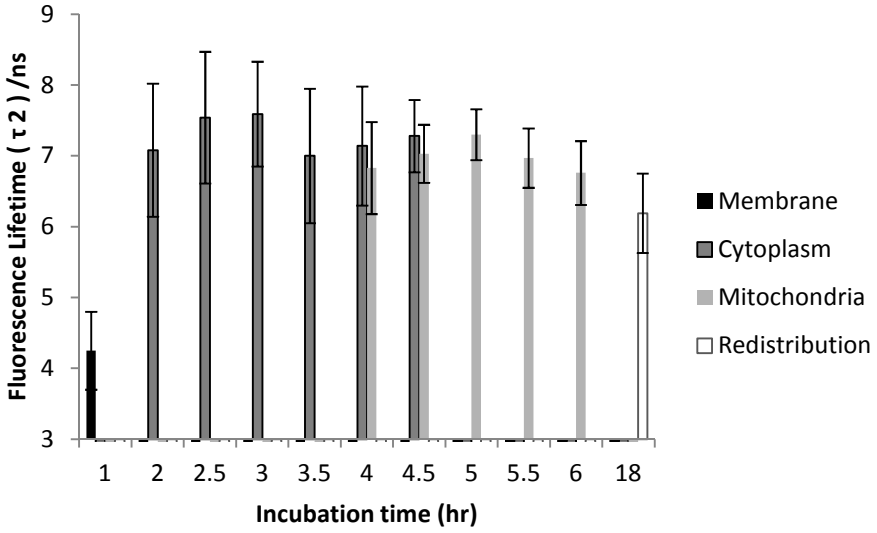

Figure 3.4 Distribution of τ_2 (slow component) as a function of different incubation times. The four different locations (cell membrane, cytoplasm, mitochondria, and redistribution) were determined based on the preliminary results from confocal images. Image segmentation was performed at 4 hours and 4.5 hours of incubation when Photofrin® localized at the mitochondria and cytoplasm. Significant short τ_2 was observed (4.3 ± 0.5 ns) in the cell membrane group ($p < 0.05$), while Photofrin® exhibited the mean lifetime of 7.1 ± 0.3 ns for the remaining intracellular locations. It was observed that the standard deviation was reduced when Photofrin® localized at the mitochondria.

The time-lapse τ_1 (short lifetime component) of Photofrin® was plotted in **Fig. 3.5**. It should be noted that all values of τ_1 are less than 1.0 ns and mostly at 0.5 ± 0.1 ns when Photofrin® localized at the mitochondrial region. Although τ_1 was found to be significantly shorter when comparing data at 1 hour and 3 hours of incubation ($p < 0.01$), it was also observed that the lifetime values in the cytoplasm group fluctuated more than other groups. The relatively small variations of short lifetime components over incubation time suggested that τ_1 may not be a good option for monitoring cellular uptake of Photofrin®.

Fig. 3.6 and **Fig. 3.7** show the normalized coefficients, A_1 and A_2, of the short and long lifetime components. As seen in **Fig. 3.6**, the significant increase of A_2 from 19% to 35% ($p < 0.01$) was observed when cells are taking up more Photofrin® over time, supporting the assertion that more aggregates and photoproducts of Photofrin® are formed after irradiation. At 18 hours, however, the images showed depolarization and swelling of mitochondria, therefore the

Photofrin® might be released and redistributed throughout the cells again. At early incubation times when intracellular concentrations of Photofrin® were low, the autofluorescence, mainly short component of porphyrin species that exhibit 1.7 ns of average fluorescence lifetime in the non-stained control group (with 70 % of τ_1 centered at 0.8 ns, and 30 % of τ_2 centered at 3.5 ns, data not shown), contributed more to the short lifetime component than Photofrin® itself. Therefore, as the τ_1 is very close to the system response (0.2 ns), it may contain contributions from short autofluorescence signals and estimation uncertainties, especially in the case of low signal from Photofrin®. This can be seen in **Fig. 3.7**, where the short lifetime component contributed the most at the beginning of the incubation, and as the intracellular Photofrin® concentration increased, the relative amplitude A_1 decreased from 81% to 65%.

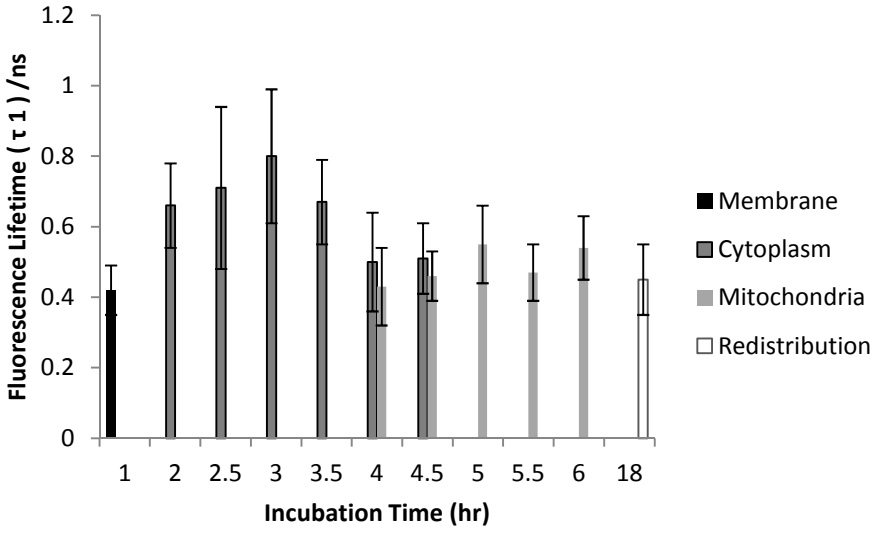

Figure 3.5 Distribution of τ_1 as a function of different incubation times. All values of τ_1 are less than 1.0 ns and at 0.5 ± 0.1 ns when Photofrin® localized at the mitochondrial region.

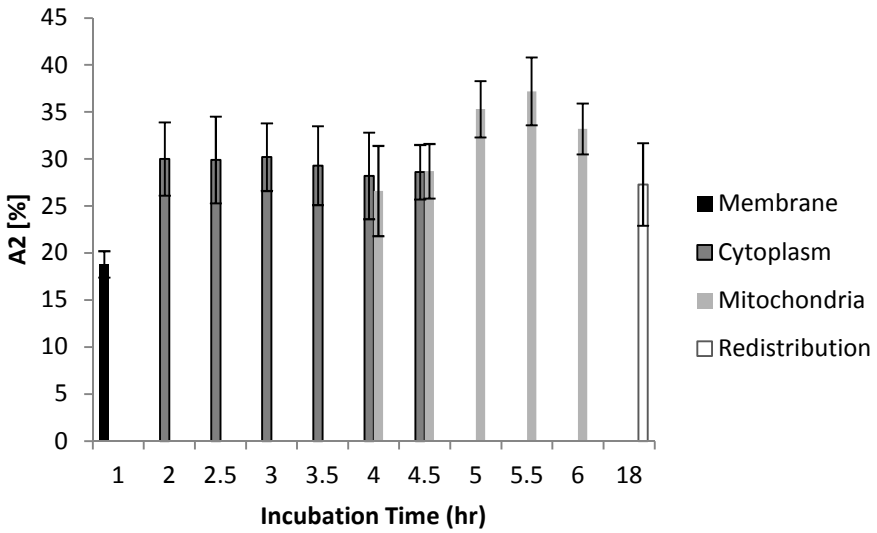

Figure 3.6 Distribution of A_2 as a function of different incubation time. A_2 was increased from 19% to 35% as cells took up more Photofrin® as the incubation time increased, suggesting contribution of τ_2 (mostly from photoproducts of Photofrin® under strong irradiation) increased. However, at the time of 18 hours, the images showed depolarization and swelling of mitochondria, therefore the Photofrin® may have been released and redistributed throughout the cells again.

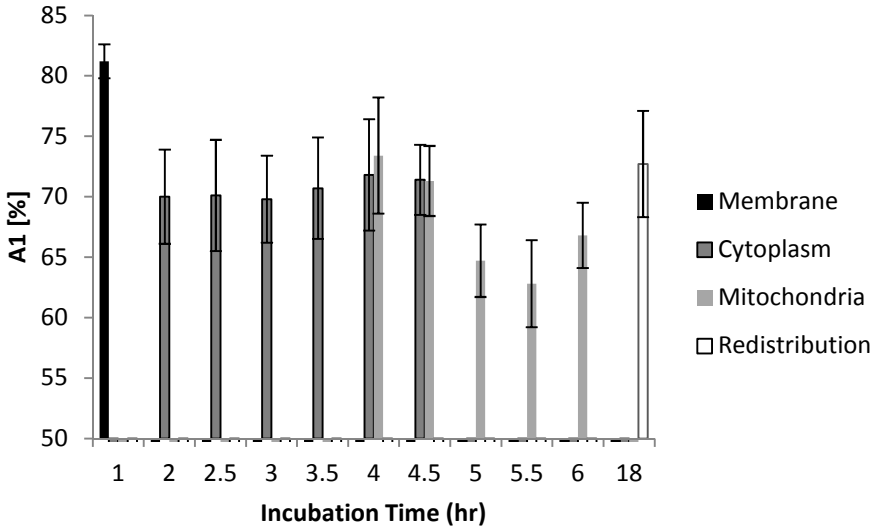

Figure 3.7 Distribution of A_1 as a function of different incubation time. At 1 hour of incubation, because only trace of Photofrin® was taken up by the cells, short lifetime components such as autofluorescence and system response may contribute more signal than Photofrin® itself. As the intracellular Photofrin® concentration increased, the short component decreased from 81% to 65%. It should be noted that the A_1 increased after prolonged incubation.

3.4. Discussion and Conclusion

The hypothesis of this study is that FLIM is a potential complementary tool for dosimetry, that not only demonstrates the location and intensity of the drug, but also reveals the drug-cell interaction status. The changes in lifetime at different intracellular locations may then be correlated with cell viability in the future PDT studies. Using a two-photon FLIM system, fluorescence lifetimes of Photofrin® in MLL cells decay bi-exponentially, with a slow component (τ_2) that was found to be significantly shorter when localized at the cell membrane, and then increase when reaching their intracellular targets, all with a large amount (70%) of fast component (τ_1) ranging from 0.3 – 1.0 ns.

The measured τ_2 of Photofrin® agrees well with the reported values (8.0 ± 0.6 ns) of its photoproduct and aggregates at various subcellular locations [13]. Based on the spectrally-resolved studies done by Rueck *et al.,* Photofrin® monomer in human HepG2 cells exhibited a slow decay time of 13.3 ± 0.3 ns; however, this was not observed in the present study. The measured values of τ_1 are also consistent with previous studies, which correspond to extremely short-lived components of Photofrin® aggregates that exhibited 0.1 to 1.2 ns fluorescence lifetimes under strong irradiation [16,26], autofluorescence of porphyrins [14,27].

In general, there are some factors that have an impact on the measured τ_2 and τ_1. For example, the drug concentration could yield different dark toxicity and phototoxicity. It has been reported that dark toxicity would exist when the Photofrin® concentration was more than 2 μg/mL [28]. Moreover, the relatively high laser power (6500 J/cm^2 and 4350 J/cm^2 for membrane and other groups, respectively) used to increase acquired photon counts may increase photodestruction of the monomers and photoproduct formation, which explains why monomer fluorescence lifetime was not observed in this study. The influence of phototoxicity was also discussed in another *in vitro* study of localized Photofrin®, where reduced cell viability was demonstrated using the two-photon fluence from 1600 J/cm^2 to 6300 J/cm^2 [29]. Therefore, in the present study, potential dark toxicity and the phototoxicity could lead to earlier onset of apoptosis, which was reported to be correlated with higher amounts of autofluorescence signal at the peri-nuclear regions [30,31]. As a result, the increased autofluorescence (the short lived porphyrin species [27]), and the photoproducts all potentially result in shortened lifetimes and large A_1 values [16] compared to the previous report [13]. In addition, due to the limitation of photon counts, only bi-exponential analysis was performed; therefore, the measured individual parameters are the average of a range of lifetimes distributed in the cell [13,14,16,26]. The localized lifetime values are discussed in the following sections.

When Photofrin® was bound to the plasma membrane, the increase of the short lifetime component (which can also be seen in **Fig. 3.7**) might be due to: (i) the binding of Photofrin® to specific receptors on the cell membrane, and more likely, (ii) photobleaching of the monomers, formation of photoproduct, and consequently the increase of the short components due to increased light exposure (over 90 s imaging, which correspond to 6500 J/cm^2). The shortening of the fluorescence lifetimes at this stage of uptake could be particularly interesting because the plasma membrane-based regime might also play an important role in cell killing during PDT. This was also revealed in a previous study, where immediate ROS generation and fast activation of cascade apoptosis signalling were observed when Photofrin® targeted the cell membrane of the A431 cell line. However, the cell morphology seemed to be more necrotic than apoptotic [21,32]. The effect on cell viability of membrane-localized Photofrin® should be investigated further in future studies.

The individual standard deviation of the fluorescence lifetime measured in the cytoplasmic group was large compared to other groups. The variability exists for a variety of reasons. First, Photofrin® was still under the uptake process so the distribution and concentration of drug would be variable and low. In other words, the measured lifetimes of Photofrin® will be more affected by other contributions such as autofluorescence, which may lead to large variations of τ_2 and τ_1. The contribution of Photofrin® was also reflected in the A_1 and A_2 plots, where A_1 decreased over time whereas A_2 increased as more Photofrin® was taken by the cells. Second, cytoplasm is a relatively more hydrophilic environment than the cell membrane and mitochondria. Photofrin® in this environment tends to form various kinds of aggregates, which is reflected by the large standard deviation observed in the cytoplasm group in both **Fig. 3.4** and **Fig. 3.5**. When looking at the lifetime values after segmentation, as observed from the datasets at 4 and 4.5 hours of incubation, there was not much difference between cytoplasmic and mitochondrial groups. This may have been a result of Photofrin® not being bound stably to mitochondrial inner membrane at 4 hours of incubation, which increased the standard deviation of the fluorescence lifetime of the mitochondrial group. In contrast, there was very little Photofrin® in the cytoplasm at 4.5 hours of incubation, which reduced the variations of the cytoplasm group. Although mitochondria location was confirmed by the MitoTracker Green, visual determination may also pose a source of error. In addition, the non-linear curve fitting process with lower signal-to-noise ratio (SNR) could also pose intrinsic inaccuracy in lifetime estimation. To tackle this issue, the SNR values were calculated by taking the ratio of the peak intensity of the decay curve to the root mean square of the noise before the rising edge of the decay curve. Average values from multiple cells of the four groups were compared in **Table 3.1**. It is noted that the values increase with the cellular uptake process when Photofrin® moved towards mitochondria (from 24.5 to 32.2), then drop back to 24.9 after prolonged incubation and redistribution of the drug. Therefore, in terms of the

possible contributions to differences of standard deviation between cytoplasmic and other groups, we would still consider the variability of microenvironment more than the discrepancy in SNR.

Table 3.1 The SNR values from different intracellular groups.

Intracellular Groups	SNR
Cell Membrane	24.5
Cytoplasm	26.9
Mitochondria	32.2
Redistribution	24.9

Measurements taken at the redistribution time point (18 hours of incubation) were inconclusive due to effects of Photofrin® dark toxicity. Photofrin® was redistributed throughout the cells at this stage, as seen in the confocal and lifetime images, where the cytoplasmic granularity suggests that cell damage had also occurred [33]. Therefore, as observed in all figures, the standard deviation of individual lifetimes increased slightly. Although the dying cells may have exhibited higher autofluorescence signal, the individual lifetimes were not shortened significantly, likely due to an elevated intracellular Photofrin® concentration after prolonged incubation [29,34]. However, the reciprocal changes of A_1 (autofluorescence) and A_2 (Photofrin) after the drug arrived its intracellular target (mitochondria) can still be seen in **Fig. 3.6** and **Fig. 3.7**, where the increased contribution of A_2 and decrease of A_1 were observed after 5 hours of incubation.

In conclusion, we investigated the time-lapse fluorescence lifetime changes of Photofrin® and studied the location-wise differences based on segmentation of the regions of interest. This study provided a different approach of assessing photobiology and photochemistry of the photosensitizer *in vitro*, and also rendered a potential application of using the plasma membrane-based FLIM as an indicator of cell apoptotic or necrotic responses. Current results showed the measured fluorescence lifetimes were significantly shorter when Photofrin® localized to the plasma membrane, while no significant difference was observed between the cytoplasm and mitochondria. Other photosensitizers may exhibit similar fluorescence lifetime characteristics *in vitro*, but it is necessary to be further verified. Future work may include: verifying the current study using Photofrin® in highly controlled, simulated plasma membrane environment; studying the effects of plasma membrane-mediated PDT in three dimensional cell cultures; investigation of cell line and photosensitizer variability; and combining the current work with an endomicroscopy technique, bringing FLIM-based PDT dosimetry towards tissue level.

References

1. Wilson BC, Patterson MS. The physics, biophysics and technology of photodynamic therapy. Phys Med Biol.2008; 53:R61–109.

2. Wilson BC, Patterson MS, and Lilge L. Implicit and Explicit Dosimetry in Photodynamic Therapy : a New Paradigm. Laser Med Sci. 1997;3:182–99.

3. Wilson BC, Patterson MS. The physics of photodynamic therapy. Phys Med Biol. 1986;31:327–60.

4. Dysart JS, Patterson MS, Farrell TJ, et al. Relationship between mTHPC fluorescence photobleaching and cell viability during in vitro photodynamic treatment of DP16 cells. Photochem Photobiol. 2002;75:289–95.

5. Dysart JS, Patterson MS. Characterization of Photofrin photobleaching for singlet oxygen dose estimation during photodynamic therapy of MLL cells in vitro. Phys Med Biol. 2005;50:2597–616.

6. Sheng C, Hoopes PJ, Hasan T, et al. Photobleaching-based dosimetry predicts deposited dose in ALA-PpIX PDT of rodent esophagus. Photochem Photobiol. 2007;83:738–48.

7. Georgakoudi I, Foster TH. Singlet oxygen- versus nonsinglet oxygen-mediated mechanisms of sensitizer photobleaching and their effects on photodynamic dosimetry Photochem Photobiol. 1998;67:612–25.

8. Diamond KR, Patterson MS, Farrell TJ. Quantification of fluorophore concentration in tissue-simulating media by fluorescence measurements with a single optical fiber. App Opt. 2003;42:2436–42.

9. Cormier JF, Fortin M, Fréchette J, et al. The effects of self-absorption and detection geometry on fluorescence intensity and decay lifetime. Proc SPIE. 2005;5702:123.

10. Diamond KR, Pawel PM, Hayward JE, et al. Quantification of fluorophore concentration in vivo using two simple fluorescence-based measurement techniques. J Biomed Opt. 2005;10:024007-1-10

11. Suhling K, French PMW, Phillips D. Time-resolved fluorescence microscopy. Photochem Photobiol Sci. 2005;4:13–22.

12. Rueck A. FLIM and SLIM for molecular imaging in PDT. Proc SPIE. 2005;5700:182–7

13. Rueck A, Huelshoff CH, Kinzler I, et al. SLIM : A New Method for Molecular Imaging. Microsc Res Techniq. 2007;492:485–92.

14. Russell JA, Diamond KR, Collins TJ, et al. Characterization of Fluorescence Lifetime of Photofrin and Delta-Aminolevulinic Acid Induced Protoporphyrin IX in Living Cells Using Two-Photon Excitation. IEEE J Quantum Elect. 2008;14:158–66.

15. Connelly JP, Botchway SW, Kunz L, et al. Time-resolved fluorescence imaging of photosensitiser distributions in mammalian cells using a picosecond laser line-scanning microscope. J Photochem Photobiol A Chem. 2001;142:169–75

16. Koenig K, Wabnitz H, Dietel W. Variation in the fluorescence decay properties of haematoporphyrin derivative during its conversion to photoproducts. J Photochem Photobiol B Biol. 1990;8:103–11.

17. Lassalle H-P, Wagner M, Bezdetnaya L, et al. Fluorescence imaging of Foscan and Foslip in the plasma membrane and in whole cells. J Photochem Photobiol B Biol. 2008;92:47–53.

18. Saczko J, Mazurkiewicz M, Chwiłkowska A, et al. Intracellular distribution of Photofrin in malignant and normal endothelial cell lines. Folia Biol. 2007;53:7–12

19. Morgan J, Oseroff AR. Mitochondria-based photodynamic anti-cancer therapy. Adv Drug Delv Rev. 2001;49:71–86.

20. Hilf R. Mitochondria are targets of photodynamic therapy. J Bioenerg Biomembr. 2007;39:85–9.

21. Hsieh Y-J, Wu C-C, Chang C-J, et al. Subcellular localization of Photofrin determines the death phenotype of human epidermoid carcinoma A431 cells triggered by photodynamic therapy: when plasma membranes are the main targets. J Cell Physiol. 20;194:363–75.

22. Karotki A, Khurana M, Lepock JR, et al. Simultaneous two-photon excitation of photofrin in relation to photodynamic therapy. Photochem Photobiol. 2006;82:443–52.

23. Zipfel WR, Williams RM, Webb WW. Nonlinear magic: multiphoton microscopy in the biosciences. Nat Biotechnol. 2003; 21:1369–77.

24. Oleinick NL, Morris RL, Belichenko I. The role of apoptosis in response to photodynamic therapy: what, where, why, and how. Photochem Photobiol Sci. 2002;1:1–21

25. Morgan J, Potter WR, Oseroff a R. Comparison of photodynamic targets in a carcinoma cell line and its mitochondrial DNA-deficient derivative. Photochem Photobiol. 2000;71:747–57.

26. Schneckenburger H, Steiner R, Rueck A. In vivo photoproduct formation during PDT with ALA-induced endogenous porphyrins. J Photochem Photobiol B: Biol. 1993;18:287–90.

27. Koenig K, and Schneckenburger H. Laser-induced autofluorescence for medical diagnosis. J Fluoresc. 1994;4:17-40

28. Singh G, Jeeves WP, Wilson BC, et al. Mitochondrial photosensitization by Photofrin II. Photochem Photobiol. 1987;46:645–9.

29. Khurana M, Collins HA, Karotki A, et al. Quantitative in vitro demonstration of two-photon photodynamic therapy using photofrin and visudyne. Photochem Photobiol. 2007;83:1441–8.

30. Levitt JM, Baldwin A, Papadakis A, et al. Intrinsic fluorescence and redox changes associated with apoptosis of primary human epithelial cells. J Biomed Opt. 2006;11:064012-1-10

31. Dittmar R, Petier E, Zandvoort M, et al. Assessment of cell viability in three-dimensional scaffolds using cellular auto-fluorescence. Tissue Eng Pt C-Meth. 2012;18:198-204

32. Kessel D, Luo Y, Deng Y, et al. The role of subcellular localization in initiation of apoptosis by photodynamic therapy. Photochem Photobiol. 1997;65:422-426.

33. Biesele JJ, Goldhaber P. A study of cytoplasmic lipid granularity in tissue culture cells. Cancer Res. 1955;15:767–73.

34. Kabe Y, Ohmori M, Shinouchi K, et al. Porphyrin accumulation in mitochondria is mediated by 2-oxoglutarate carrier. J Biol Chem. 2006; 281:31729–35.

Chapter 4.

Paper III – Effects of incomplete decay in fluorescence lifetime estimation

Regina Won Kay Leung,[1,2,+] Shu-Chi Allison Yeh,[3,+] and Qiyin Fang[1,3,*]

[1]*Department of Engineering Physics, McMaster University.*

[2]*Institute of Biomaterials & Biomedical Engineering, University of Toronto,164 College Street, Toronto, Ontario M5S 3G9, Canada*

[3]*School of Biomedical Engineering, McMaster University.*

[+] *Contributed equally,* [*] *qiyin.fang@mcmaster.ca*

Published in Biomedical Optics Express; 2(9):2517-2531, 2011

Introduction to paper III

Typical time-domain fluorescence lifetime techniques assume that each subsequent decay is independent. In this chapter, we studied the scenario when such assumption is invalid and the effect of incomplete fluorescence decay on the accuracy of fluorescence lifetime estimation. We also developed an analytical model to correct such effects.

Fluorescence lifetime imaging has been used extensively to probe biological microenvironment and interactions in biomedical sciences. For example, the photosensitizer studies we mentioned in the previous chapters. Fluorescence lifetime measurement can be achieved by the use of high repetition rate lasers. However, when the inter-pulse duration is too short to allow for complete fluorescence decay, the decay tails from previous excitation pulses can superimpose onto the subsequent measurement. As a result, the effect of incomplete decay distorts the measured decay curves and leads to inaccurate lifetime estimation.

We first developed a robust time-domain mathematical platform allowing accurate simulation of the process and manipulations of a number of parameters. This mathematical model was then validated using both simulation and experiments. Then, the effect of incomplete fluorescence decay on the accuracy of fluorescence lifetime estimation was characterized using this model. Based on these results, analytical solutions were developed to correct the distorted fluorescence lifetime for the typical a bi-exponential decay scenario.

This work is useful for researchers using ultrafast laser to study fluorophores with slow decay profiles, particularly for photosensitizers and newly developed nanomaterials in biomedical applications. It may also be beneficial for readers who work on time-domain instrumentation and software development to take the fluorescence lifetime distortion into account. The manuscript was equally contributed by Regina Leung and I, and edited by Dr. Qiyin Fang.

Contents of Paper III

Abstract

Fluorescence lifetime imaging has emerged as an important microscopy technique, where high repetition rate lasers are the primary light sources. As fluorescence lifetime becomes comparable to intervals between consecutive excitation pulses, incomplete fluorescence decay from previous pulses can superimpose onto the subsequent decay measurements. Using a mathematical model, the incomplete decay effect has been shown to lead to overestimation of the amplitude average lifetime except in mono-exponential decays. An inverse model is then developed to correct the error from this effect and the theoretical simulations are tested by experimental results.

4.1. Introduction

Fluorescence lifetime imaging microscopy (FLIM) has become a powerful imaging tool in cell and molecular biology research [1], drug discovery [2], and clinical diagnosis [3]. Fluorescence lifetime can be defined as the average time fluorophores stay in the excited state after excitation and described by multiple exponential decays [4]. Given sufficient signal, fluorescence lifetime is independent of fluorescent intensity such that it has been used to complement steady state imaging modalities, which are based on intensity and spectral features [4]. FLIM based techniques have been extensively investigated in a number of applications including Fluorescent Resonant Energy Transfer (FRET) [5, 6, 16, 17], ion mapping of intracellular environment [7, 8], as well as clinical diagnosis for malignant tumours [9, 10] and dosimetry for drug administration [11, 15].

In time-domain measurement, a short-pulsed laser is used to excite the fluorophores and the fluorescent emission is measured as a function of intensity decay over time [4]. The fluorescence decay may be modeled as the summation of multiple exponential components, as shown in **Eq. (4.1)**.

$$F(t) = a_1 e^{-t/\tau_1} + a_2 e^{-t/\tau_2} + a_3 e^{-t/\tau_3} + \cdots \qquad \textbf{(4.1)}$$

Where $F(t)$ is the measured fluorescence intensity as a function of time t; τ_i are the individual exponential components; and a_i are the coefficients of each exponential term. The measured intensity decay is a convolution of $F(t)$ with the

Instrument Response Function (IRF), thus deconvolution is sometimes necessary to recover the *F(t)* when the IRF is not negligible [4].

Typical FLIM systems use either Time Correlated Single Photon Counting (TCSPC) based point scanning method [6, 11, 12, 15] or ICCD-based wide-field imaging technique [3, 7, 9, 13]. In TCSPC, only the first photon of a pulse is recorded. To build a probability histogram for each pixel in an image, a large number of pulses are needed. In ICCD based techniques, each pulse excites the whole field-of-view while a large number of excitation pulses are also needed to achieve sufficient signal-to-noise ratio (SNR). Consequently, both techniques require high repetition rate light source and detection systems in order to accurately determine the fluorescence lifetime while achieving sufficient imaging frame rate. Since short, sub-nanosecond pulsed excitation is also required in time-domain systems, mode-locked Ti:Sapphire lasers have become the most commonly used excitation sources in current FLIM systems. New picosecond diode lasers with various excitation wavelengths also holds promise for several biological applications.

In Ti:Sapphire lasers, the repetition rate is typically limited to 70-100 MHz due to the mode-locking mechanism. This limitation has caused concerns in measuring longer decays where the average fluorescence lifetime is comparable to the period of the excitation pulses [4, 13]. It has been advised that the interval between two excitation pulses should be more than four [4] or five [13] times of the average fluorescence lifetime in order to accurately estimate the lifetime from experiments. That is, if a fluorophore's lifetime is longer than 3 ns and a 80 MHz (12.5 ns between excitation pulses) laser is used, the tails of decay curves from previous excitation periods may contribute significantly to the current decay curve, which may lead to inaccurate lifetime estimation [13,14]. This "incomplete decay" effect is illustrated in **Fig. 4.1**. To simplify the illustration, the commonly seen noise background or instrument offset is ignored here.

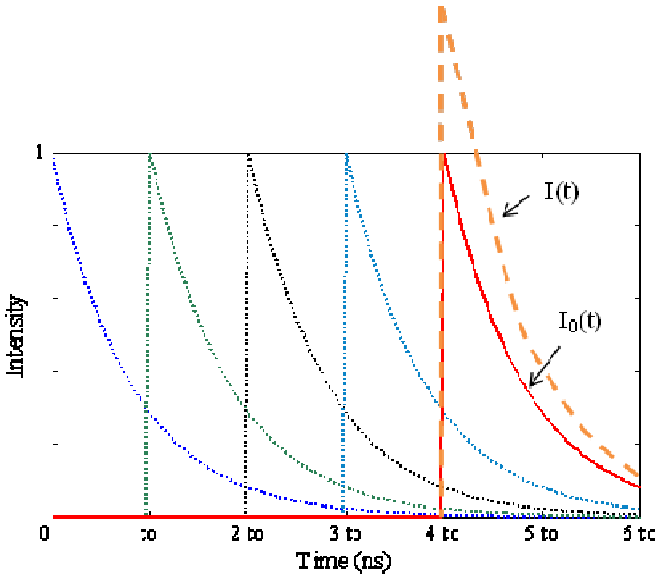

Figure 4.1 Simulated effect of incomplete decay on the measured decay curve is illustrated, where the tails of multiple previous decay curves (short dashed lines) excited by a high repetition rate light source contribute significantly to the current original curve, $I_0(t)$(solid line) , which lead to the distorted measured decay curve, I(t) (long dashed line) that can cause inaccurate lifetime estimation. t_0 is the time interval between two consecutive excitation pulses. Note that the incomplete decay caused by the laser excitation prior to the current one contributes the most to the current measured decay curve as illustrated in the last decay curve.

Fig.4.1 simulated effect of incomplete decay on the measured decay curve is illustrated, where the tails of multiple previous decay curves (short dashed lines) excited by a high repetition rate light source contribute significantly to the current original curve, $I_0(t)$(solid line) , which lead to the distorted measured decay curve, I(t) (long dashed line) that can cause inaccurate lifetime estimation. t_0 is the time interval between two consecutive excitation pulses. Note that the incomplete decay caused by the laser excitation prior to the current one contributes the most to the current measured decay curve as illustrated in the last decay curve.

In practice, many fluorophores have long lifetimes that are subjected to the influence of the incomplete decay effect when excited by high repetition rate lasers. For example, a clinically-approved photosensitizer for photodynamic therapy (PDT), Photofrin®, is a typical long-lived fluorophore with its average lifetime of around 13 ns in bulk solutions or 6 -10 ns in live cells [11,15]. Incomplete decay may also cause problems in applications using short lifetime fluorophores. An example is FLIM based Föster Resonant Energy Transfer or FLIM-FRET, where protein-protein interactions is calculated from small changes of donor fluorophore lifetimes [16]. Many FRET pairs exhibit bi-exponential decays with fluorescence lifetimes of 2 - 4 ns [17], while the lifetime change in the order of 0.1 - 0.2 ns is critical.

The inaccurate lifetime estimation due to the ultrafast repetitive excitation is generally mentioned [4, 18] and Barber *et. al,* initially reported an analytical model in a conference paper [19] to describe the "incomplete decay" effect. This original work is crucial towards designing time-domain instrumentations and selection of light sources. In practical situations, however, excitation repetition rate is not a typical selectable feature. In addition, a large number of data has already been acquired using high repetition rate excitation sources. In this report, we established an analytical model similar to Barber *et. al.*'s to simulate the effects of the incomplete decay and quantitatively determine the influence of the incomplete decay to the accuracy of lifetime parameter estimation either in noise-free or noisy conditions. The theoretical simulation is experimentally tested using standard fluorophores with a multiphoton microscope and a 80MHz Ti:Sapphire laser. Most importantly, correction methods were developed to recover original lifetime parameters from the measured lifetime values. **Table 4.1** illustrated the abbreviations used in the rest of this article.

Table 4.1 Definition of the abbreviations for lifetimes

Abbreviations	***Definition***
τ_0	Original amplitude weighted lifetime
τ_{id}	Simulated measured amplitude weighted lifetime due to incomplete decay alone
τ_{idn}	Simulated measured amplitude weighted lifetime due to incomplete decay and with noise

4.2. Materials and Methods

4.2.1. Analytical model of incomplete decay

The analytical model describing the incomplete decay effect is first reported by Barber *et. al.* in Ref [19]. As shown in **Fig. 4.1**, the original fluorescence intensity decay $I_0(t)$ is different from the measured decay curve $I(t)$, where the period of the excitation laser pulses are short compared to the fluorophore's lifetime. If $I_0(t)$ is represented with N exponential terms, it can be described as:

$$I_0(t) = A_{01}e^{-t/\tau_{01}} + A_{02}e^{-t/\tau_{02}} + \ldots + A_{0i}e^{-t/\tau_{0i}} + \ldots + A_{0N}e^{-t/\tau_{0N}} \quad \textbf{(4.2)}$$

where for the i^{th} term, τ_{0i} is the lifetime component. Then, the original amplitude weighted lifetime τ_0 is determined by [4]:

$$\tau_0 = A^n{}_{01}\tau_{01} + A^n{}_{02}\tau_{02} + \ldots + A^n{}_{0N}\tau_{0N} \quad \textbf{(4.3)}$$

where A^n_{0i} is the normalized coefficient defined as $A^n_{0i} = A^n_{0i} \Big/ \sum_{i=1}^{N} A^n_{0i}$.

Similarly, the experimentally measured fluorescence decay *I(t)* and estimated lifetime τ are [4]:

$$I(t) = A^n{}_1 e^{-t/\tau_1} + A^n{}_2 e^{-t/\tau_2} + \ldots + A^n{}_N e^{-t/\tau_N} \quad \textbf{(4.4)}$$

$$\tau = A^n{}_1\tau_1 + A^n{}_2\tau_2 + \ldots + A^n{}_N\tau_N \quad \textbf{(4.5)}$$

where $A^n{}_i$ is the normalized coefficient defined as $A^n_i = A^n_i \Big/ \sum_{i=1}^{N} A^n_i$

Both the measured and original multi-exponential decay curves are characterized by their corresponding coefficients and lifetime components. To demonstrate how incomplete decay influences fluorescence lifetime measurement and estimation, a forward model was developed while assuming the original parameters (A_{01}, A_{02},… , A_{0N}, $\tau_{01},\tau_{02},\ldots,\tau_{0N}$) are known and that the measured parameters affected by incomplete decay (A_1, A_2,… , A_N, $\tau_1,\tau_2,\ldots,\tau_N$) are unknown. In practice, one would always obtain the measured values experimentally and try to estimate the original set of decay parameters. An inverse model was then derived from the forward model and assumes the opposite: the measured parameters are known and the original parameters are unknown. The goal of the inverse model is to predict the original lifetime parameters from the measured data by correcting errors in lifetime estimation due to incomplete decay.

Please note that in the following analysis, we made an assumption that there are an unlimited number of fluorophores available in the system, while only a small number of them are excited at any given time. In practice, this assumption is probably valid especially for multiphoton FLIM measurements while only the focal plane is excited by high repetition rate (70-100 MHz) mode-locked Ti: Sapphire lasers. In these cases, photobleaching is also not significant. One should note that especially in TCSPC measurements where a large number of excitation pulses are used, this assumption may be invalid.

4.2.1.1. Forward Model

From **Fig. 4.1**, as a result of incomplete decay, *I(t)* is a summation of $I_0(t)$ and the tails of the *n* previous decay curves where $I_0(t)$ is the original decay curve,

I(t) is the resulting measured decay curve, and t_o is the time interval between two consecutive excitation pulses:

$$I(t) = \lim_{n\to\infty}[I_0(t) + I_0(t+t_o) + \ldots + I_0(t+nt_o)] \quad \textbf{(4.6)}$$

Substituting in **Eq. (4.2)** into **Eq. (4.6)** to get,

$$I(t) = \lim_{n\to\infty}\left(\sum_{i=1}^{N} A_{0i}e^{-\frac{t}{\tau_{0i}}} + \sum_{i=1}^{N} A_{0i}e^{-\frac{t+t_0}{\tau_{0i}}} + \ldots + \sum_{i=1}^{N} A_{0i}e^{-\frac{t+nt_0}{\tau_{0i}}}\right) = \sum_{i=1}^{N}\left(A_{0i}e^{-\frac{t}{\tau_{0i}}} \cdot \sum_{n=0}^{\infty} e^{-\frac{nt_0}{\tau_{0i}}}\right) \quad \textbf{(4.7)}$$

Since $\sum_{n=0}^{\infty} r^n = 1/(1-r)$ for $|r|<1$, While $|e^{-t_0/\tau_{0i}}| < 1$ as t_o and τ_{0i} are always positive, the final expression for *I(t)* can be significantly simplified to [20]

$$I(t) = \sum_{i=1}^{N} \frac{A_{0i}}{1-e^{-t_0/\tau_{0i}}} e^{-t/\tau_{0i}} \quad \textbf{(4.8)}$$

Therefore, by comparing **Eq. (4.8)** with **Eq. (4.4)**, the measured parameters can now be expressed as a function of the original parameters where

$$A_i = \frac{A_{0i}}{1-e^{-t_0/\tau_{0i}}} \quad \textbf{(4.9)}$$

$$\tau_i = \tau_{0i} \quad \textbf{(4.10)}$$

The measured amplitude weighted lifetime due to the effect of incomplete decay (τ_{id}) can be calculated from original parameters by substituting **Eq. (4.9)** and (**4.10)** into **Eq. (4.5)**:

$$\tau_{id} = \sum_{i=1}^{N} \frac{A_{0i}/(1-e^{-t_0/\tau_{0i}})}{\sum_{k=1}^{N} A_{0k}/(1-e^{-t_0/\tau_{0k}})} \tau_{0i} \quad \textbf{(4.11)}$$

Finally, to quantify the difference between measured and original amplitude weighted lifetimes, the fractional error is defined as:

$$\%E = \frac{\tau_{id} - \tau_0}{\tau_0} \times 100\% \quad \textbf{(4.12)}$$

4.2.1.2. Inverse Model

The inverse model is derived from the forward model by rearranging **Eq. (4.9)** and (**4.10)** to describe original parameters in terms of measured parameters as shown in **Eq. (4.13)** and (**4.14)**.

$$A_{0i} = A_i(1 - e^{-\frac{t_o}{\tau_i}}) \tag{4.13}$$

$$\tau_{0i} = \tau_i \tag{4.14}$$

As shown in **Eq. (4.15)**, the original amplitude weighted lifetime can be expressed in terms of the measured parameters by substituting **Eq. (4.13)** and (**4.14)** into **Eq. (4.3)** as indicated by:

$$\tau_0 = \sum_{i=1}^{N} \frac{A_i(1 - e^{-t_0/\tau_i})}{\sum_{k=1}^{N} A_k(1 - e^{-t_0/\tau_i})} \tau_i \tag{4.15}$$

Finally, to quantify the difference between original and measured amplitude weighted lifetimes, the fractional error is defined as:

$$\%E = \frac{\tau_0 - \tau_{id}}{\tau_{id}} \times 100\% \tag{4.16}$$

The inverse analytical model can be applied directly to the measured parameters to correct for the effects of incomplete decay and obtain the original amplitude weighted lifetime value. The analytical model is also further examined to create guidelines for lifetime measurements to determine whether or not incomplete decay is significant to require correction.

From the results given by **Eq. (4.8)**, **Eq. (4.15)**, and **Eq. (4.16)** in the mono-exponential decay case, incomplete decay does not affect the estimated amplitude weighted lifetimes (τ_{id}) since the τ_{id} is the same as the original individual lifetime while the coefficient is normalized.

As most of the commonly used fluorophores exhibit multiple-exponential decay, this study focuses on how the incomplete decay contributes to incorrect lifetime estimation in the bi-exponential cases, which is mostly seen in practical FLIM experiments. Nonetheless, the inverse model can be applied to more complex cases where more than two exponential components are present. The general analytical model for multi-exponential incomplete decay developed above can be applied to the specific bi-exponential case as shown below where $N = 2$.

Expressing the measured coefficients and component lifetimes affected by incomplete decay in terms of the original parameters using **Eq. (4.9)** and (**4.10)**:

$$A_1 = \frac{A_{01}}{1 - e^{-\frac{t_o}{\tau_{01}}}} \quad \textbf{(4.17)}$$

$$A_2 = \frac{A_{02}}{1 - e^{-\frac{t_o}{\tau_{02}}}} \quad \textbf{(4.18)}$$

$$\tau_1 = \tau_{01} \quad \textbf{(4.19)}$$

$$\tau_2 = \tau_{02} \quad \textbf{(4.20)}$$

The measured amplitude weighted lifetime is given by:

$$\tau_{id} = A^n{}_1 \tau_1 + A^n{}_2 \tau_2 \quad \textbf{(4.21)}$$

$$\tau_{id} = \frac{\frac{A_{01}}{1 - e^{-t_o/\tau_{01}}}}{\frac{A_{01}}{1 - e^{-t_o/\tau_{01}}} + \frac{A_{02}}{1 - e^{-t_o/\tau_{02}}}} \tau_1 + \frac{\frac{A_{02}}{1 - e^{-t_o/\tau_{02}}}}{\frac{A_{01}}{1 - e^{-t_o/\tau_{01}}} + \frac{A_{02}}{1 - e^{-t_o/\tau_{02}}}} \tau_2 \quad \textbf{(4.21a)}$$

where the measured amplitude weighted lifetime (τ_{id}) as shown in **Eq. (4.21a)** is expressed in terms of the original parameters by substituting **Eq. (4.17)** to **Eq. (4.20)** into **Eq. (4.21)**. Again, applying the general analytical model developed above, the inverse model is applied to the bi-exponential case where *N = 2* to obtain the following equations to express the original parameters in terms of measured parameters:

$$A_{01} = A_1 (1 - e^{-\frac{t_o}{\tau_1}}) \quad \textbf{(4.22)}$$

$$A_{02} = A_2 (1 - e^{-\frac{t_o}{\tau_2}}) \quad \textbf{(4.23)}$$

$$\tau_{01} = \tau_1 \quad \textbf{(4.24)}$$

$$\tau_{02} = \tau_2 \quad \textbf{(4.25)}$$

The original amplitude weighted lifetime is:

$$\tau_0 = A_{01} \tau_{01} + A_{02} \tau_{02} \quad \textbf{(4.26)}$$

$$\tau_0 = \frac{A_1(1-e^{-t_o/\tau_1})}{A_1(1-e^{-t_o/\tau_1})+A_2(1-e^{-t_o/\tau_2})}\tau_{01} + \frac{A_2(1-e^{-t_o/\tau_2})}{A_1(1-e^{-t_o/\tau_1})+A_2(1-e^{-t_o/\tau_2})}\tau_{02} \quad \textbf{(4.26a)}$$

where the original amplitude weighted lifetime as shown in **Eq. (4.26a)** is expressed in terms of the measured parameters by substituting **Eq. (4.22)** to (**4.25)** into **Eq. (4.26)**.

4.2.1.3. Incomplete decay simulations

To further investigate the analytical models and develop guidelines to determine the significance of incomplete decay on amplitude weighted lifetime measurements, bi-exponential incomplete decay curves of different lifetimes are simulated in Matlab under various conditions. Conditions include varying the repetition rate, coefficients, and differences in lifetime components. The fractional error between the original (τ_0) and simulated measured amplitude weighted lifetime (τ_{id}) as defined in **Eq. (4.12)** or (**4.16)** is calculated using the derived analytical models and examined under each condition.

4.2.2. Noise simulation

To understand the effect of the incomplete decay in practical experiments, noise simulation has been performed to see whether lifetime estimation error caused by random experimental noise is comparable to errors from incomplete decay. Typical experimental noise sources in FLIM measurements include shot noise (Poisson noise) from the photo detector, digitization error from the digitizer, ambient light, and other electronics noise from the amplification process. In general, the signal amplitude is low and instrumentation noises significantly surpassed the shot noise. In this work, we assume the errors arise from these processes are independent of each other. Consequently, although each process may have a different error distribution, the overall error can be considered to be Gaussian [21]. Therefore, in the noise simulation, Gaussian noise is generated and added to the simulated mono- and bi-exponential incomplete decay curves at different SNR values. Specifically, the SNR is defined as the average signal amplitude divided by random Gaussian noise with standard deviation "sd" [22]. Curve fitting was then performed on the noisy simulated curves to determine the lifetime parameters and the fractional errors.

To simulate mono- and bi-exponential incomplete decay curves, all the parameters were defined according to the experimental conditions. For mono-exponential, two cases were simulated: Case 1 with τ_1 = 1.5 ns and Case 2 with τ_2 = 4.9 ns which correspond to the lifetimes of Rhodamine B (RdmB) and Lucifer Yellow (LY) respectively. For bi-exponential, various cases were generated with different A_1:A_2 ratios where A_1 ranged from 0.1 – 0.9 and A_2 is normalized to be

$1 - A_1$. In all the cases, the original coefficient values were chosen such that $A_1 + A_2 = 516$, $\tau_1 = 1.5$ ns (RdmB), and $\tau_2 = 4.9$ ns (LY). The absolute original coefficient values were set as 516 based on typical original peak decay intensities obtained from the real TCSPC experiments; however, it will not affect the actual calculation of amplitude weighted lifetime, where the normalized coefficients were used. Although the fitting coefficient A in mono-exponential decay is not critical, we performed and plotted simulation to demonstrate the effect of noise on parameter estimations.

Gaussian noise was then generated with a mean of 0 and a standard deviation (SD) based on the signal to noise ratio (SNR) where SNR was defined as the average signal amplitude divided by SD of random Gaussian noise. The range of SNR in our simulations ranged from 16-182 and was determined by our typical experimental data measured using a 2-photon microscope and a TCSPC FLIM module. The generated Gaussian noise at various SNR is then added to the simulated incomplete decay curves.

Curve fitting to the simulated data was then performed using the curve fitting toolbox (Matlab v2010, Mathworks, Natick, MA), where the non-linear least squares method using the Trust-Region algorithm was applied. Fitted parameters (A_1, A_2, τ_1, τ_2) were used to calculate lifetime values and the fractional error for various SNR. The fractional error between the data with and without the noise is defined as $(\tau_{idn}-\tau_0)/\tau_0 * 100$, where τ_{idn} represents the amplitude weighted average lifetime of the noisy incomplete decay curve and τ_0 represents the amplitude weighted average lifetime of the original decay curve.

4.2.3. Time-domain multi-photon fluorescence lifetime measurements

To validate the theoretical model and simulations, we measured the fluorescence lifetime of standard fluorophores using two fluorescence lifetime measurement modalities: a time-domain FLIM microscope using 80 MHz laser excitation and a second set of measurements using a frequency domain lifetime fluorometer.

The time-domain FLIM instrument is a two-photon microscope (TSC SP5 & DMI 6000 B, Leica, Wetzlar, Germany) equipped with the TCSPC fluorescence lifetime acquisition module (SPC-830, Becker & Hickle GmbH, Berlin, Germany) and a femtosecond mode-locked Ti:Sapphire laser pulsing at 80 MHz (Chameleon-Ultra, Coherent. Santa Clara, CA). In this system, fluorescence emission channels are selected by a prism and several variable-width slits in front of detectors. The fluorescence intensity decay was fitted to a bi-exponential decay model using the Matlab curve fitting toolbox to calculate the lifetime parameters.

The frequency domain instrument is a lifetime fluorometer (ChronosFD, ISS, Champaign, IL) using a laser diode centred at 470 nm (90099, ISS) with the

modulation frequency between 8 to 200 MHz. The fluorescence was transmitted through a band pass filter centred at 580 nm (580/DF30, XF3022, Omega Optical, VT), and the detected signal was analyzed using the included software (Vinci, ISS) to retrieve the time-domain parameters.

Two standard fluorescence dyes, Lucifer yellow (LY) (L0259, Sigma-Aldrich, St. Louis, MO) with a lifetime of 4.9 ns and Rhodamine B (RdmB) (R6626, Sigma-Aldrich) with a lifetime of 1.5 ns were diluted in purified water to the concentration of 2 μM. The two fluorescence dyes were then mixed at appropriate ratios and their lifetimes are measured using both instruments for comparison. In the frequency-domain measurements, Coumarin 6 (546283, Sigma-Aldrich) was used as a reference dye with the fluorescence lifetime of 2.5 ns and excitation and emission spectra overlapping with LY and RdmB. It was diluted in 99.9 % Ethanol (34964, Sigma Aldrich) to appropriate concentration that provides comparable signals with respect to the samples. To provide references for the original amplitude weighted lifetime calculation, the fluorescence lifetimes of LY and RdmB were then retrieved by mono-exponential fitting using Vinci (data not shown). In the time-domain measurements, the samples were illuminated with the laser at 860 nm and the emission channel was set from 500 nm to 700 nm to ensure the optimum excitation and detection efficiency. Three separate measurements have been performed and all the acquisition parameters remained the same throughout the acquisition processes to eliminate artefacts from sources other than the incomplete decay. Quantum efficiency correction was also performed after the data acquisition by comparing the integrated photon intensities of each fluorescence dye; therefore the real contribution of individual lifetimes can be restored.

4.3. Results

4.3.1. Simulated results of the incomplete decay

According to **Eq. (4.8)**, incomplete decay only affects the coefficient values, while the measured individual lifetime components are the same as the original individual lifetime components, as indicated in **Eq. (4.9)** and (**4.10**). Therefore, amplitude weighted lifetime estimation for mono-exponential decay is unaffected by incomplete decay because its amplitude weighted lifetime estimation does not depend on the coefficient. For bi-exponential decays, however, the measured amplitude weighted lifetime (τ_{id}) does depend on the coefficients A_1 and A_2, where $\tau_{id} = A_1\tau_1 + A_2\tau_2$. Thus, measured parameters from bi-exponential decay must be interpreted carefully and corrected for incomplete decay. The rest of the report will focus on examining the analytical model for incomplete decay for bi-exponential cases. The illustration of the effect of incomplete decay on mono- and bi-exponential decay is shown in **Fig. 4.2** where both the original (τ_0)

and measured (τ_{id}) decay curves are shown on a linear and log scale. As shown in **Fig. 4.2**, incomplete decay only affects the estimation of amplitude weighted lifetimes for bi-exponential decays. **Table 4.2** shows the time-domain parameters distorted by the incomplete decay in mono- and bi-exponential cases used in **Fig. 4.2**.

The difference between the i^{th} measured and original coefficients which is defined as the fractional error $E_i = (A_i - A_{0i})/ A_{oi}$ where i = 1, 2 for bi-exponential cases. According to **Eq. (4.9)**, E_i can be rewritten as:

$$E_i = \frac{1}{1 - e^{-t_0/\tau_i}} - 1 \qquad \textbf{(4.27)}$$

As a result of the dependence of amplitude weighted lifetimes on the individual coefficients given by **Eq. (4.20)**, parameters that result in less than 5% fractional errors between the individual measured and original coefficients which would then result in less than 5% uncertainty in lifetime estimations are investigated. Given the typical temporal resolution of about 200 ps in time-domain instruments, we consider 5% uncertainty in lifetime estimation can be considered as acceptable error. As a result, when the fractional error caused by incomplete decay is less than 5 %, it is considered insignificant and can be neglected. One should note that this 5% cutoff value is somewhat arbitrary and, depending on the application, it should be used with caution. Consequently, since the magnitude of the i^{th} fractional error (E_i) is only dependent on the i^{th} individual lifetime (τ_i), the threshold value of individual lifetimes($\tau_{i(thld)}$) that would give fractional errors of 5 % is determined by rearranging **Eq. (4.26)**. The threshold value is expressed as:

$$\tau_{i(thld)} = -\frac{t_o}{\ln(0.05/1.05)} \qquad \textbf{(4.28)}$$

Also, as shown in **Eq. (4.27)**, E_i is a monotonically increasing function with respect to τ_i, which means if $\tau_i < \tau_{i(thld)}$, the estimation errors due to incomplete decay are less than 5 % and may be negligible. The $\tau_{i(thresh)}$ values corresponding to various laser repetition rates are shown in **Table 4.3**. As expected, the higher the repetition rate, the lower the threshold individual lifetime value, and thus the more likely incomplete decay will cause fractional errors between coefficients and cause errors in lifetime parameter estimation.

It is also useful to note that the fractional error E_i scales linearly with the laser repetition period t_o and thus the individual threshold lifetime values ($\tau_{i(thld)}$) that would give fractional errors of 5% can instead be expressed as a fraction of the repetition period, $t_o/ \tau_{i(thld)}$. This threshold ratio between repetition period t_o and threshold lifetime value $\tau_{i(thld)}$ can be denoted as $R_{i(thld)}$. By re-arranging **Eq. (4.28)**, $R_{i(thld)} = t_o/ \tau_{i(thld)} = -\ln(0.05/1.05) = 3.045$. Since E_i is a monotonically decreasing function with respect to t_o/ τ_i, this means that as long as the time interval between laser pulses (t_o) is 3 times longer than the individual lifetime τ_i,

the estimation errors due to incomplete decay are less than 5% and may be negligible.

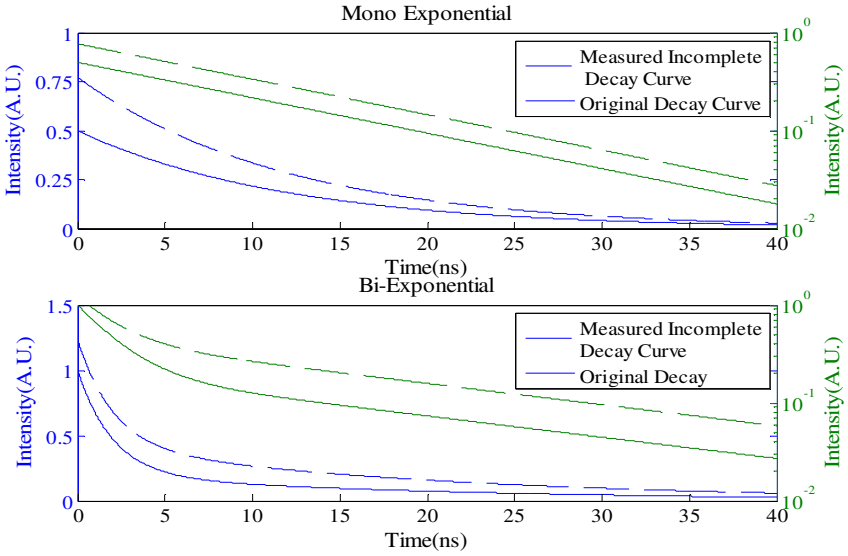

Figure 4.2 Simulation of the original (solid line) and measured (dashed line) decay curves for both mono-exponential (top) and bi-exponential (bottom) cases at repetition rate of 80 MHz (12.5 ns). For the mono-exponential case, τ_{01} = 12 ns, A_{01} = 0.5. For the bi-exponential case, τ_{01} = 2 ns, τ_{02} = 20 ns, A_{01} = 0.8, A_{02} = 0.2. The corresponding log scale plots of each decay curve are also shown as the top two curves of each graph with the log plot axis on the right.

Fig. 4.2. Simulation of the original (solid line) and measured (dashed line) decay curves for both mono-exponential (top) and bi-exponential (bottom) cases at repetition rate of 80 MHz (12.5 ns). For the mono-exponential case, τ_{01} = 12 ns, A_{01} = 0.5. For the bi-exponential case, τ_{01} = 2 ns, τ_{02} = 20 ns, A_{01} = 0.8, A_{02} = 0.2. The corresponding log scale plots of each decay curve are also shown as the top two curves of each graph with the log plot axis on the right.

When the individual lifetimes are longer than those specified in **Table 4.3** for corresponding repetition rates, the superposition from previous decay can affect lifetime parameter estimation significantly. To develop guidelines that determine the significance of incomplete decay in lifetime measurements, it is of great interest to investigate incomplete decay in various experimental conditions (e.g. repetition rate, coefficients, difference in lifetime components).

Table 4.2 Original and measured parameters for mono- and bi-exponential decay

Mono- Exponential		Bi-exponential	
Original	Measured (τ_{id})	Original	Measured (τ_{id})
$A_{01} = 0.50$	$A_1 = 0.77$	$A_{01} = 0.80$	$A_1 = 0.80$
$\tau_{01} = 12$ ns	$\tau_1 = 12$ ns	$A_{02} = 0.20$	$A_2 = 0.43$
$\tau_0 = 12$ ns	$\tau_{id} = 12$ ns	$\tau_{01} = 2.0$ ns	$\tau_1 = 2.0$ ns
		$\tau_{02} = 20$ ns	$\tau_2 = 20$ ns
		$\tau_0 = 5.6$ ns	$\tau_{id} = 8.29$ ns

Table 4.3 Threshold amplitude averaged lifetime values (for bi-exponential decay) at various time windows (t_o) between consecutive excitation pulses

$\mathbf{t_o}$ **(ns)**	$\boldsymbol{\tau_{i(thresh)}}$ **(ns)**
10 (100 MHz)	3.28
12.5 (80 MHz)	4.11
16.7 (60 MHz)	5.49
25 (40 MHz)	8.21
50 (20 MHz)	16.4

As shown in **Fig. 4.3**, the fractional error between original and measured amplitude weighted liftimes as defined in **Eq. (4.12)** corresponding to a set of original parameters *($A_{01} = A_{02} = 0.5$*, $\tau_{01} = 1$ ns, *τ_{02}* varies from 0 to 20 ns) was plotted with respect to *τ_2* at various repetition rates as shown by the multiple curves. It was observed that at each *τ_2* value, the error increased as the repetition rate increased. For example, the error of the τ_{id} at *τ_2* of 20 ns at the highest repetition rate (100 MHz) resulted in the maximum error of all cases with 40% error from the original average lifetime value (*τ_0*). **Fig. 4.3** also illustrated the negligible incomplete decay effect when $\tau_1 = 1$ ns and $\tau_2 < \tau_{i(thld)}$; the error is always less than 5%. Similarly, **Fig. 4.3** illustrates that when the time window between laser excitation pulses (*t_o*) is around three times longer than both τ_1 and τ_2, the error due to incomplete decay is less than 5%.

The effect of measured coefficients and lifetime component values on the absolute fractional error between τ_{id} and τ_0 values as defined in **Eq. (4.16)** was also investigated at a constant repetition rate of 80 MHz as shown in **Fig. 4.4**. **Fig. 4.4** shows a contour plot where the y-axis corresponds to *A_1* and is varied from 0 to 1 (*$A_2 = 1 - A_1$*) and the x-axis corresponds to the difference between measured lifetime components (*τ_1* - *τ_2*) where *τ_2* (10 ns) was chosen to be constant and *τ_1*

varies from τ_2 - *8 (2 ns)* to τ_2 + *8* (18 ns). The varying gray scale colour of the contour map corresponds to the calculated absolute fractional errors for the various corresponding measured coefficient and lifetime component values where the darker the colour, the larger the error.

Examining the effect of measured coefficients on the fractional error for the bi-exponential case, it can be seen from **Fig. 4.4** that regardless of the values of the measured lifetime components, the error increases (grayscale colour becomes darker) as A_1 approaches 0.5. In other words, since $A_2 = 1 - A_1$, the fractional error increases as A_1 and A_2 approach 0.5.

However, the nature of this error trend is not symmetric with respect to A_1. The behavior, as observed in **Fig. 4.4**, follows this pattern: if $\tau_2 > \tau_1$ (negative difference), the maximum error tends to occur at values greater than $A_1 = 0.5$ whereas if $\tau_2 < \tau_1$ (positive difference), maximum error tends to occur at values less than $A_1 = 0.5$. Therefore, it is difficult to determine *the specific* A_1 values that would give the maximum error for all cases. However, it is clear that the error from incomplete decay increases for measured coefficients that converge towards 0.5. It is also interesting that although all cases of measured parameters in **Fig. 4.4** followed this error trend with respect to amplitude variations, the magnitude of the error varied drastically between different cases. The reason for this large difference between different cases of measured parameters (lifetime components) will be investigated in the following section.

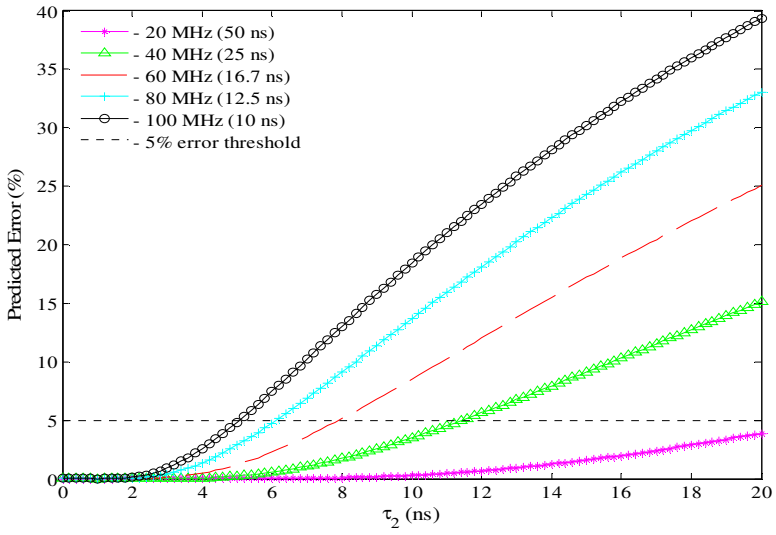

Figure 4.3 The predicted fractional errors defined by **Eq. (4.12)** are plotted as a result of incomplete decay at various original amplitude weighted lifetime values at various repetition rates for bi-exponential decays. For each curve, τ_1 remains constant at 1 ns and τ_2 is varied from 0 to 20 ns as shown on the x-axis. The coefficients are fixed at $A_{o1} = A_{o2} = 0.5$.

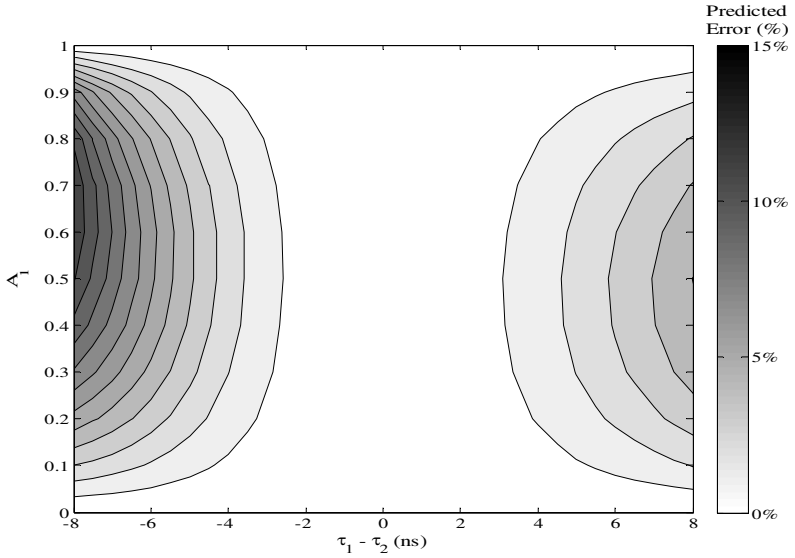

Figure 4.4 Illustrating the dependence and trends of absolute fractional error (as defined in **Eq. (4.16)**) on measured coefficient and lifetime component values using a contour plot. Y-axis corresponds to A_1 and is varied from 0 to 1 ($A_2 = 1 - A_1$). X-axis corresponds to the difference between measured lifetime components (τ_1 - τ_2) where τ_2 (10 ns) was chosen to be constant and τ_1 varies from τ_2 - 8 (2 ns) to τ_2 + 8 (18 ns). The varying gray scale colour of the contour map corresponds to the calculated absolute fractional errors where the larger the error, the darker the gray scale colour as defined by the color bar.

As shown in **Fig. 4.4**, the absolute fractional error between measured (τ_{id}) and original (τ_0) amplitude weighted lifetime values (as defined by **Eq. (4.16)**) also depends on the measured lifetime components. However, where incomplete decay has an effect, the error does not depend on the magnitude of the measured lifetime components but actually on the differences between the measured lifetime components (τ_1 - τ_2). It can be observed from **Fig. 4.4** that as the difference between τ_1 and τ_2 increases, the error increases as well. The error trend is not symmetric with respect to the difference between measured lifetime components where positive differences will result in lower error values. This is an indication that larger lifetime component values with the same differences will result in relatively lower fractional error values. Moreover, **Fig. 4.4** demonstrate that in cases with small differences in measured lifetimes (i.e. 4 ns), incomplete decay effects may be negligible (< 5 %) for all possible coefficient values, which further verifies the threshold values determined by the model.

4.3.2. The dependency of measured lifetimes (τ_{idn}) on the SNR level

In practical FLIM measurements, the data always includes significant amounts of noise. We performed noise simulation in our model to investigate how noise affects the estimation of amplitude weighted lifetime values. To do this, the simulated noisy incomplete decay curves with the SNR varying from 16 to 182 for various A_{01}:A_{02} ratios (τ_{01} = 1.5 ns (RdmB), and τ_{02} = 4.9 ns (LY)) were fitted using the nonlinear least squares algorithm to obtain the predicted measured amplitude weighted lifetimes (affected by incomplete decay) with noise (τ_{idn}).The corresponding residuals were plotted (data not shown) and at each SNR level showed no pattern, indicating the good quality of fitting process. The original amplitude weighted lifetime values (τ_0) for various A_{01} to A_{02} ratios were also calculated for the original decay signal. Using the inverse model on $\tau_{idn,}$ the corrected amplitude weighted lifetimes were obtained (τ_{corr}). The original amplitude weighted lifetime (τ_0), predicted measured amplitude weighted lifetimes (with noise) (τ_{idn}), and corrected amplitude weighted lifetimes (τ_{corr}) for various A_{01}:A_{02} ratios at SNR = 16 are shown in **Table 4.4** below. As shown in **Table 4.4**, it is demonstrated that the corrected amplitude weighted lifetimes (τ_{corr}) by the inverse model under low SNR = 16 are almost equivalent to the original amplitude weighted lifetimes (τ_0) (less than 1% difference). This further verifies the accuracy of the inverse model and indicates that the effect on estimation error from noise itself is actually minor in comparison with the effect of incomplete decay and is always negligible. This shows that the correction for incomplete decay is indeed necessary.

Table 4.4 Simulation values: Original amplitude weighted lifetime (τ_0), predicted measured amplitude weighted lifetimes (with noise) (τ_{idn}), and corrected (on τ_{idn}) amplitude weighted lifetimes (τ_{corr}) for various A_{01}:A_{02} ratios at SNR = 16 (τ_{01} = 1.5 ns (RdmB), and τ_{02} = 4.9 ns (LY))

Original		***Predicted Measured***	***Correction using inverse model on τ_{idn}(ns)***
A_{01} *(%)*	τ_0 *(ns)*	τ_{idn} *(ns)*	τ_{corr} *(ns)*
0	4.90	4.90	4.90
25	4.05	4.14	4.09
50	3.20	3.29	3.23
75	2.35	2.42	2.37
100	1.50	1.50	1.50

4.3.3. Experimental results

The fluorescence lifetimes of Lucifer yellow (LY) and Rhodamine B (RdmB) were measured by the time domain TCSPC and the frequency domain ChronosFD systems, which correspond to cases with incomplete decay (in TCSPC, 80MHz laser is used) and without (in the ChronosFD), respectively. The average lifetime of LY is 5.07 ns ± 0.30 ns (TCSPC) and 4.9 ns ± 0.06 ns (ChronosFD), respectively when fitted with mono-exponential model. RdmB exhibits a fast decay with the fluorescence lifetimes at 1.55 ns ± 0.13 ns and 1.50 ns ± 0.03 ns respectively. In order to determine the original amplitude weighted lifetimes (τ_0) without the effects of incomplete decay, the dye mixture was calculated with respect to the original fluorescence lifetime of each dye obtained from the frequency domain system (4.9 ns and 1.5 ns). Also, to determine the real relative contribution of RdmB and LY (ie correct original coefficients to obtain real original coefficients), the quantum efficiency (QE) of each fluorescence dye was also determined by taking the average of integrated photon intensities from three repetitive LY and RdmB measurements using TCSPC. The results showed the relative QE of RdmB is 36 % against LY. Therefore, the quantum efficiency corrected original coefficients can represent the real relative contribution of RdmB ($QE_c\ A_{01}$) and LY ($QE_c\ A_{02}$) where $QE_c\ A_{02} = 1 - QE_c\ A_{01}$.

Table 4.5 lists the quantum efficiency corrected amplitude weighted lifetimes obtained from frequency domain measurements (τ_0), the TCSPC measurements (τ_{idn}), and correction of τ_{idn} using the inverse model (τ_{corr}). Except for the measurement at $QE_c\ A_{01} = 59.1\%$ ($\tau_0 = 2.89$ ns), the measured TCSPC lifetime (τ_{idn}) consistently overestimated the original amplitude weighted lifetime of the solution (τ_0) as obtained from the frequency domain system. The overestimation of measured amplitude weighted lifetime values is predicted and agrees with the incomplete decay model. Using the inverse model, the measured amplitude weighted lifetime values (τ_{idn}) were corrected and is close enough to the original amplitude weighted lifetime (τ_0) to be within the uncertainties of the experimental measurement. Differences between τ_0 and τ_{idn} ($Diff_{id}$) and between τ_0 and τ_{corr} ($Diff_{corr}$) were evaluated to see whether lifetime estimation error caused by incomplete decay is comparable to errors from random experimental noise. As shown in **Table 4.5**, $Diff_{id}$ is always larger than $Diff_{corr}$ for all mixtures indicating that the effect on estimation error from incomplete decay is larger than the effect on error from noise and that the correction for incomplete decay is indeed necessary. The outlier value at 59.1% ($\tau_0 = 2.89$ ns) may be due to low SNR in the experimental measurements, which led to large uncertainties in lifetime estimation for bi-exponential decays.

Table 4.5 Experimental values: Time domain amplitude weighted lifetimes of Lucifer Yellow (LY) and Rhodamine B (RdmB) mixture solution were measured experimentally using TCSPC (τ_{idn}) and frequency domain lifetime spectrometer (τ_0). Based on the inverse model, the TCSPC measurements were corrected (τ_{corr}) based on an 80MHz repetition rate excitation. Differences between τ_0 and τ_{idn} ($Diff_{id}$) and between τ_0 and τ_{corr} ($Diff_{corr}$) were evaluated to see whether lifetime estimation error caused by incomplete decay is comparable to errors from random experimental noise.

Frequency domain measurements		***TCSPC with 80 MHz excitation***	***Correction using inverse model on τ_{idn}***	***Differences in τ values***	
$QE_c\ A_{01}$ *(%)*	τ_0 *(ns)*	τ_{idn} *(ns)*	τ_{corr} *(ns)*	$Diff_{id}= \tau_{idn}- \tau_0$ *(ns)*	$Diff_{corr}= \tau_{corr} - \tau_0$ *(ns)*
0	4.90	5.07	5.07	0.17	0.17
8.2	4.62	4.85	4.76	0.23	0.14
19.4	4.24	4.84	4.34	0.60	0.10
35.2	3.70	3.79	3.76	0.09	0.06
59.1	2.89	2.55	2.49	-0.34	-0.40
100	1.50	1.55	1.55	0.05	0.05

4.4. Discussion and Conclusion

Applications of fluorescence lifetime in imaging and spectroscopy have become an active research and technology development area owning to the recent advances of short pulsed lasers and high speed photo detection systems. One of the key technologies that pushing FLIM into a user friendly microscopy modality is the development of turn-key Ti:Sapphire laser systems. Although their high repetition rate enables fast image/data acquisition the short interval between consecutive excitation pulses causes concerns that fluorescence lifetime may not be accurately estimated.

In this report, we developed a general mathematical model to quantitatively estimate how incomplete fluorescence decay affects the measured fluorescence decay curves and subsequent estimation of lifetime values. In addition, an inverse model allows the correction of errors caused by incomplete decay. Specifically, the simulation results show that incomplete decay does not affect estimation of individual lifetime component in multi-exponential decays but rather the coefficient terms, which in turn lead to underestimation of average lifetime. As expected, the extent of error strongly depends on the ratio of amplitude weighted lifetime and the interval between excitation pulses. For example, in the case of bi-exponential decay excited at 80MHz, if both lifetime components are less than 4 ns, the simulation results suggest that the error can be neglected and no correction is required. If at least one lifetime component is larger than 4 ns, the measurement errors would be significant but can be corrected by the proposed mathematical model. Taking individual parameters into account, our results demonstrated that the fractional error between the original and

measured lifetime values (E_{id}) became significant with (i) increased laser repetition rate, (ii) converge of coefficients to be equal, and (iii) increased difference between individual lifetime components, while the error is not significantly increased by the noise. These facts offer guidelines that allow researchers to have a better idea for measurement values that may require correction for incomplete decay.

The incomplete decay effect is most profound for fluorophores with long lifetimes such as Photofrin® and ALA induced protoporphyrin IX (PpIX), which are clinically approved photosensitizers with fluorescence lifetimes of more than 10 ns [11]. As a result, invalid interpretation of experimental results can easily happen when the average lifetimes of photosensitizers are measured by short-pulsed lasers with repetition rate more than 20 MHz.

It should be noted that artifacts in lifetime estimation from incomplete decay effect is not significant in microscopy where the lifetimes of most fluorescence probes are short. Nonetheless, in the case of FLIM-FRET, where the majority acceptor-donor pairs have average lifetimes of less than 4 ns while exhibit bi-exponential decay [17], small errors in lifetime estimations may be critical since 5 % of lifetime change may corresponding to significant errors in inter-molecular distance calculation.

In addition to applications in microscopy, quantitative analysis of incomplete decay is also useful in other time-domain fluorescence techniques. For example, Yuan et. al. described a technique that uses fibers with different lengths to multiplex multiple spectral channels of fluorescence decay using a single detector [23]. The multiplexed fluorescence decays were separated by the different propagation time introduced by the different fiber lengths. The detected signal is the superposition of signals from decays from adjacent pulses and also suffers from the incomplete decay effect. The inverted model from this work can also correct the superposition of incomplete decays in this case to provide more accurate lifetime estimation.

It should be noted that the reported results were simulated in a scenario with the assumptions that photobleaching is insignificant and the instrumental response function (IRF) is negligibly small. In practice, these assumptions may break down. Therefore, future work includes investigating the models with photobleaching effect and convolution of IRF.

References

1. K. Suhling and D. Phillips, “Time-resolved fluorescence microscopy”, Photochem. Photobiol. Sci., **4**, 13-22 (2005).

2. M.T. Kelleher, G. Fruhwirth, G. Patel, E. Ofo, F. Festy, P.R. Barber, S. M. Ameer-Beg, B. Vojnovic, C. Gillett, A. Coolen, G. Kéri, P. A. Ellis, and T. Ng, "The potential of optical proteomic technologies to individualize prognosis and guide rational treatment for cancer patients," Targeted Oncology, **4**, 235-252 (2009)

3. I. Munro, J. McGinty, N. Galletly, J. Requejo-Isidro, P. M. P. Lanigan, D. S. Elson, C. Dunsby, M. A. A. Neil, M. J. Lever, G. W. H. Stamp, P. M. W. French, "Toward the clinical application of time-domain fluorescence lifetime imaging," Journal of Biomedical Optics, **10**, 051403-1-9, (2005)

4. J. R. Lakowicz, Principles of Fluorescence Spectroscopy, 3rd ed. (Kluwer Academic/Plenum, New York, 2006), Chap. 4.

5. G.O. Fruhwirth, S. Ameer-Beg, R. Cook, T. Watson, T. Ng, and F. Festy. , "Fluorescence lifetime endoscopy using TCSPC for the measurement of FRET in live cells," Optics Express, **18**, 11148-11158 (2010).

6. T. Ng, A. Squire, G. Hansra, F. Bornancin, C. Prevostel, A. Hanby, W. Harris, D. Barnes, S. Schmidt, H. Mellor, P. I. H. Bastiaens, P. J. Parker. "Imaging protein kinase Cα activation in cells," Science, **283**, 2085–2089 (1999)

7. J.R. Lakowicz, H. Szmacinski, K. Nowaczyk, W.J. Lederer, M.S. Kirby, and M.L. Johnson, "Fluorescence lifetime imaging of intracellular calcium in COS cells using Quin-2," Cell Calcium, **15**, 7-27 (1994)

8. A.V. Agronskaia, L. Tertoolen, and H.C. Gerritsen, "Fast fluorescence lifetime imaging of calcium in living cells," Journal of Biomedical Optics, **9**, 1230-1237 (2004)

9. G. Wagnières, J. Mizeret, A. Studzinski, and H. van den Bergh, " Frequency-domain fluorescence lifetime imaging for endoscopic clinical cancer photodetection: apparatus design and preliminary results," J. Fluoresc., **7**, 75-83 (1997)

10. Y. Sun, N. Hatami, M. Yee, K. Phipps, D. S. Elson, F. Gorin, R. J. Schrot, and L. Marcu, "Fluorescence lifetime imaging microscopy for brain tumor image-guided surgery," Journal of Biomedical Optics, **15**, 056022-1-5 (2010).

11. J. A. Russell, K. R. Diamond, T. Collins, H. F. Tiedje, J. E. Hayward, T. J. Farrell, M. S. Patterson, Q. Fang, "Characterization of Fluorescence Lifetime of Photofrin and Delta-Aminolevulinic Acid Induced Protoporphyrin IX in Living Cells using Single and Two-photon Excitation," IEEE Journal of Selected Topics in Quantum Electronics, **14**, 158-166 (2008)

12. W. Becker, A.Bergmann, C. Biskup, "Multispectral Fluorescence Lifetime Imaging by TCSPC," Microscopy Research and Technique **70**, 403-409 (2007).

13. H.C. Gerritsen, "High-speed fluorescence lifetime imaging," Proc. SPIE, **5323**, 77-86 (2004)

14. W. Becker, The bh TCSPC Handbook, 3rd Edition, (Becker & Hickl GmbH, 2008)

15. A. Ruck, CH.Hulshoff, I.Kinzler, W. Becker, and R. Steiner, "SLIM: a new method for molecular imaging", Microscopy Research and Technique **70**, 485-492 (2007)

16. E.A. Jares-Erijman and T.M. Jovin, "Imaging molecular interactions in living cells by FRET microscopy," Current Opinion in Chemical Biology, **10**, 409-416 (2006)

17. Y. Chen and A. Periasamy, "Characterization of two-photon excitation fluorescence lifetime imaging microscopy for protein localization," Microscopy Research and Technique, **63**, 72-80 (2004)

18. P.R. Barber, S.M. Ameer-Beg, J.Gilbey, L.M. Carlin, M.Keppler, T.C.Ng and B. Vojnovic, "Multiphoton time-domain fluorescence lifetime imaging microscopy: practical application to protein-protein interactions using global analysis", J.R. Soc. Interface, **6**, 93-105, (2009)

19. P.R. Barber, S.M. Ameer-Beg, J. Gilbey, R. J. Edens, I. Ezike, and B. Vojnovic, "Global and pixel kinetic data analysis for FRET detection by multi-photon time-domain FLIM," Proc. SPIE, **5700**, 171-181 (2005)

20. J. Stewart, Calculus: early transcendentals,5^{th} ed. (Thomson/Brooks/Cole, Belmont, CA, 2003)

21. J.R. Taylor, An introduction to error analysis. 2nd ed. (University Science Books, Sausalito, 1997)

22. Schroeder, D. J., Astronomical optics. (Academic Press, San Diego, 2000), Chap. 17

23. Y. Yuan, T. Papaioannou, and Q. Fang, "Single-shot acquisition of time-resolved fluorescence spectra using a multiple delay optical fiber bundle," Optics Letters, **33**, 791-793 (2008)

Chapter 5.

Paper IV – 5-ALA induced PpIX as a Fluorescence Marker for Quantitative Image Analysis of High-Grade Dysplasia in Barrett's Esophagus Cellular Models

Shu-Chi Allison Yeh[1], Samir Sahli[2], David W. Andrews[3], Michael S. Patterson1[4], David Armstrong[5], JohnProvias[6], and Qiyin Fang[1,2,*]

[1]*McMaster University, School of Biomedical Engineering.*

[2]*McMaster University, Department of Engineering Physics.*

[3]*Sunnybrook Research Institute, 2075 Bayview Ave., Toronto, ON, M4N 3M5*

[4]*McMaster University, Department of Medical Physics and Applied Radiation Sciences.*

[5]*McMaster University, Division of Gastroenterology, Department of Medicine.*

[6]*McMaster University, Department of Pathology.*

Accepted with revision, Journal of Biomedical Optics; January, 2015

Printed with permission

Introduction to paper IV

Early detection/diagnosis and intervention of high-grade dysplasia (HGD) in Barrett's esophagus (BE) is considered to be critical in treatment of esophageal cancer. We proposed the concept of integrated detection and treatment of HGD using endomicroscopy. In this chapter, in a proof-of-principle *in vivo* cell imaging study, we developed image processing and analysis techniques to detect HGD cells from benign BE cells using morphological features in confocal images.

Currently, clinical diagnosis and treatment procedures for HGD in BE are separated by *in vivo* endoscopic screening and *ex vivo* histopathological analysis. This results in significant sampling and relocation errors during intervention, leading to increased risks of developing esophageal cancer.

We report using a FDA-approved photosensitizer, 5-ALA, as a fluorescent contrast agent for cellular level classification of high-grade dysplasia (HGD) in Barrett's esophagus (BE). The cell nucleus stain is one of the gold standards for diagnosis of HGD in BE. Using a clinically approved photosensitizer holds a particular advantage because it can highlight nucleus morphology without adverse effects from mutagenic DNA targeting stains, and still yield comparable information to histological standards. More importantly, morphological / textural feature extraction, and classification using supervised learning approach provide a more robust detection that mitigates inter- and intra-observer variation during diagnosis. Our results demonstrate sensitivity of 95% and specificity of 87% for detection of HGD.

This work shows a new application of PDT photosensitizers as a nucleus contrast for automatic detection. It may be beneficial for readers who work on cancer diagnosis using any contrast agent, and/or endomicroscopy-based instrumentation development and fluorescence studies on gastrointestinal neoplasia. The manuscript was written by me and edited by all of the co-authors.

Contents of Paper IV

Abstract

Early detection and treatment of high-grade dysplasia (HGD) in Barrett's esophagus (BE) may reduce the risks of developing esophageal adenocarcinoma. Confocal endomicroscopy (CLE) has shown advantages over routine white-light endoscopic surveillance with biopsy for histological examination; however, CLE is compromised by insufficient contrast, and by intra- and inter-observer variation. In this study, a FDA-approved PDT photosensitizer was used to reveal morphological and textural features similar to those found in histological analysis. These features were then combined with machine learning for a more robust detection of HGD. Our results showed 95% sensitivity and 87% specificity using the optimal feature combination and can be further extended to 3D cellular models.

5.1. Introduction

Esophageal adenocarcinoma (EAC) is a malignant cancer with a low 5-year survival rate of 12% due to the limitation of early diagnosis. [1–3] EAC is associated with high-grade dysplasia (HGD) in a setting of Barrett's esophagus (BE), a pre-malignant condition in which the normal squamous epithelium is replaced by intestinal metaplasia that may eventually progress, via low grade dysplasia (LGD) to HGD. [4] Although endoscopic surveillance is performed regularly on patients with BE in an attempt to achieve early diagnosis, substantial sampling and relocation errors still exist due to the nature of the random four-quadrant biopsy protocol and temporal separation of the diagnostic and treatment procedures. [5] Therefore, integrated real-time diagnosis and treatment ("seek-and-treat") is an ideal strategy to overcome these challenges. Optical biopsy is an emerging technique that probes the optical properties of targeted lesions during the examination, with the potential for achieving real-time diagnosis. [3,6] However, there are still certain major challenges when investigating BE. In general, the diagnostic accuracy of point-spectroscopy is strongly affected by patient-to patient variability. [5] Also, insufficient sensitivity and specificity are found particularly in autofluorescence BE imaging due to poor signal-to-noise ratio. [7] To overcome these limitations, *in vivo* histology, using subcellular resolution microscopic imaging and an suitable exogenous contrast agent holds advantages in showing real time cytological information of clinical histology

standards, in which HGD cells are characterized by certain cytological features of atypia, including, particularly, the nucleus pattern as well as loss of cell polarity, crowded cell nucleus distribution, overlapping of the cell borders, nuclear pleomorphism with irregular nucleus shape and size, enlarged cytoplasm to nucleus ratio, nuclear stratification, etc. On the contrary, intestinal metaplasia demonstrates well-spaced, rounder and more basally-oriented nuclei; gross observation shows non-distorted architecture, existence of goblet cells and less stratified morphology. [8,9]

In recent years, machine learning has emerged as a potential technique to automate the detection of pre-malignant lesions. [10,11] Muldoon *et al*. used HRME (high-resolution microendoscopy) and a nucleus contrast agent, proflavin, to perform automatic imaging recognition of neoplastic lesions and obtained sensitivity and specificity of 0.87 and 0.85, respectively. [10] Although these cellular resolution technologies have been extensively investigated and have demonstrated desirable sensitivity and specificity, use of a contrast agent capable of highlighting HGD remains controversial. For example, nucleus stains exhibit better cytological patterns to identify HGD, [9] but are considered mutagenic. Other commercial dyes are relatively safer but yield poor selectivity for HGD area. [12] Common markers for the GI tract and their properties are summarized in **Table 5.1**; unfortunately, most do not provide sufficient contrast for the identification of HGD. [5,10,12–17]

As a result, FDA-approved PDT (photodynamic therapy) photosensitizers that cause fluorescence of mitochondria become attractive alternatives to "nucleus" contrast agents, and the fluorescence lifetime of photosensitizers may also be an additional contrast for probing cellular uptake [18]. More importantly, PDT photosensitizers also provide potential treatment selectivity. [19,20] In addition, the development of automatic recognition based on cellular features can be a promising technique to mitigate variability in subjective observation and improve detection sensitivity and specificity. To study this "seek and treat" strategy, we started with a well-characterized *in vitro* BE model [21] that demonstrated cell line competition in 2D and 3D co-culture [22,23] with close cytogenetic similarities to BE *in vivo* [21,24] and less experimental variability than animal models. [23,25] The eventual goal of this study is to translate knowledge gained from this co-culture platform to clinical data for detecting HGD using clinically available CLE [26]. In a pilot study, using 5-ALA induced protoporphyrin IX (PpIX) as a contrast agent, we began with morphological and textural features at a single-cell level in mono-culture, and the capability of generalizing the training algorithm was further evaluated in co-culture, which could be further extended to be compatible with histology standards [9] using high-density cell culture.

Table 5.1 Common contrast agents in esophageal chromoendoscopy

Contrast Agents	Properties and Applications
Fluorescein	Highlights vasculature and intrer-cellular space. Goblet cells and epithelial mucin appear dark. [12,13]
Methylene Blue	Highlights actively absorbing columnar epithelium but with little discrimination for HGD. [16,17]
Toluidine Blue	Stains nuclei of columnar cells. [17]
Lugol's Solution	Stains only normal mucosa for its affinity to iodinated agents. [14]
Cresyl Violet	Stains the cytoplasm and, also, highlights cell nuclei; the staining pattern is not discriminative. [15,26]
Acriflavin	Stains cell nuclei directly, but is considered to be mutagenic. [10]
Acetic Acid	Highlights columnar mucosa, but low specificity for HGD. [5]
Indocyanine Green	Less used in chromoendoscopy, but only for marking locations. [17]

5.2. Materials and Methods

We studied 5-ALA induced PpIX synthesis in both metaplasia and HGD cell lines to investigate its potential as a contrast agent to highlight cellular patterns in CLE. Then, imaging analysis was performed to extract morphological and texture features based on PpIX fluorescence. Finally, we trained the support vector machines (SVM) to classify co-cultured cells and the classification performance was characterized.

5.2.1. Mono-culture and Co-culture

CP-A (non-dysplastic metaplasia, ATCC® CRL-4027™) and CP-B (high-grade dysplasia, ATCC® CRL-4028™) are two well-characterized, hTERT immortalized human Barrett's esophageal cell lines [21–23] that were selected as an *in vitro* platform to study the fluorescence pattern of 5-ALA induced PpIX. In order to provide the ground truth for the classification results in co-culture, parental CP-A cells were further transfected with a cytosolic mCerulean3 construct to achieve cyan fluorescence that does not overlap with the PpIX spectrum. The stably transfected CP-A cells were expanded using the complete culture medium containing 5 µg/mL selective antibiotics (Blasticidin S HCl, R210-01, Gibco®, Canada), and further purified using a flow cytometer (FACSCanto™, BD Biosciences, CA). Stable cells were then maintained using complete medium supplemented with 3 µg/mL of Blasticidin S.

The complete medium used for all cell lines was composed of MCDB 153 base medium (M7403, Sigma), supplemented with 5% Fetal Bovine Serum (16000-036, Gibco®), 0.25 µg/ml Amphotericin B (A2942, Sigma), 1% Penicillin/Streptomycin (15140-122, Gibco®), 0.4 µg/ml Hydrocortisone (H0888,

Sigma), 140 µg/ml bovine pituitary extract (P1476, Sigma), 20 mg/L Adenine(A8626, Sigma), 0.1% Insulin-transferrin-sodium selenite (I1884, Sigma), 20 ng/ml Recombinant EGF (E9644, Sigma), 4mM Glutamine, and 1nM Cholera Toxin (C8052. Sigma). Cells were grown in a 25 cm^2 culture flask and maintained at 37 ºC in a water jacketed CO_2 incubator (Forma Series II, Thermo Fisher Scientific Inc, Waltham, MA). The subculturing procedures followed the recommendation from ATCC, where cells were immersed in 1 mL Trypsin-EDTA solution (2.5X, 0.5%, 15400-054, Gibco®) until fully detached; neutralized by complete culture medium followed by a mandatory centrifugation process at 125g in order to re-suspend cells in fresh trypsin-free culture medium.

5.2.2. Sample Preparation

5-ALA (A3785, Sigma) is a photosensitizing agent, but it served as a fluorescent marker to highlight cell mitochondria and create nucleus contrast in this study. A 100 mM stock solution dissolved in PBS (14190-144, Gibco®) was stored in aliquots in the dark. A working concentration of 0.5 mM was prepared before every experiment by further diluting the stock solution in the serum-free complete culture medium. Cells were seeded on glass-bottom dishes (P35G-1.5-14-C, MatTek, MA) one day before the experiment. Before imaging acquisition, individual cell lines were incubated with 5-ALA for various periods of time between 3 to 6 hours to yield different mitochondrial PpIX concentrations for training of the classification algorithm. This variable was introduced intentionally to characterize intracellular PpIX concentration, and account for variability in fluorescence intensity during classification. Co-culture preparation used a total of 0.3 x 10^5 cells containing mCerulean-CP-A and parental CP-B in 1:1 with the incubation of 5-ALA for 6 hours.

5.2.3. Imaging Acquisition

The fluorescence emission of 5-ALA induced PpIX was collected between 625 nm – 750 nm by a laser scanning confocal microscope (TCS SP5 & DMI 6000 B, Leica, Wetzlar, Germany) equipped with an Argon-ion laser operating at 514 nm. The emission spectral band starting from 625 nm was used to maximize the detected PpIX intensity whilst avoiding overlap with the m-cerulean spectrum. A 63X objective lens was used to yield a field of view (FOV) of 246 µm x 246 µm with lateral resolution of approximately 300 nm, comparable to current confocal endomicroscopy systems. [12] The acquisition channel for transfected CP-A cells in co-culture used 458 nm laser excitation with the emission spectral range of 465 nm to 500 nm to match the fluorescence emission peak of m-cerulean. Sample fluorescence images of both cell lines in monoculture and co-culture are demonstrated in **Fig. 5.1** and **5.2**.

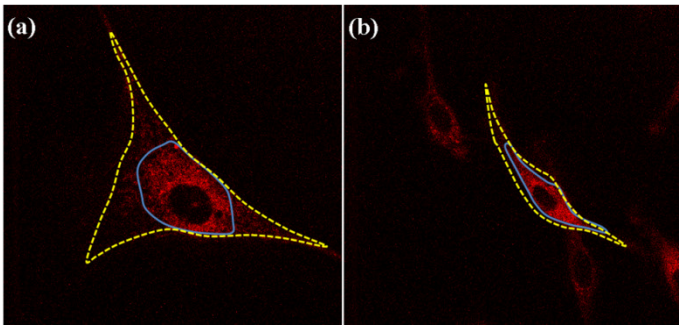

Figure 5.1 Sample CP-A and CP-B cells labelled with the fluorescent PpIX in mono-culture conditions. Cells were loaded with 5-ALA and the PpIX fluorescence was examined within 6 hours of incubation. The fluorescent area (mitochondria distribution) is highlighted by the solid line and the real cell shapes based on the bright field images are indicated by the dashed line. PpIX fluorescence thus yielded distinct morphological and textural patterns in (a) CP-A cells and (b) CP-B cells, where CP-A cells yielded a more concentrated fluorescence accumulation towards the peri-nuclear region, while CP-B cells demonstrated a more elongated shape. Further imaging processing and segmentation was performed for classification of CP-B cells.

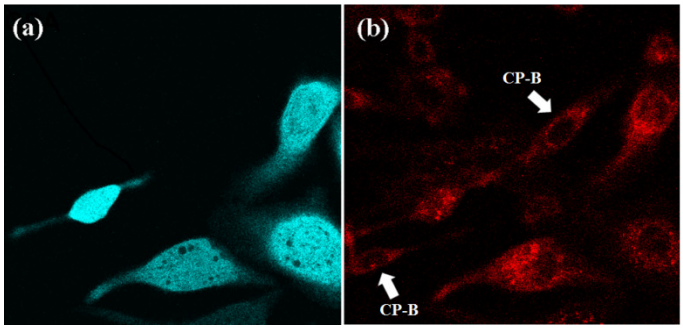

Figure 5.2 In co-culture condition, stably transfected CP-A cells were used for validation of the classification results; therefore, the CP-A cells in the co-culture image can be identified based on the images acquired from the emission band of 465 nm to 500 nm (CP-A-m-cerulean channel).

5.2.4. Quantifying Intracellular PpIX in mono- and co-culture

To investigate the feasibility of using PpIX as a contrast agent, the cellular uptake was compared for metaplastic and high-grade dysplastic cells. Both cell lines were incubated with 5-ALA solution for a specified time and fluorescence images were acquired every hour using both one-photon (5.92 J/cm^2) and two-photon excitation (9911 J/cm^2) until the intracellular PpIX reached a plateau. PpIX intensities in co-culture were only compared at 6 hours of incubation. All acquisition parameters including the fluence, magnification, emission spectral range and the detector gain remained the same in repetitive trials using different batches of cells. The acquired images were pre-processed with consistent

preprocessing procedures to segment out the fluorescent area using Matlab (Mathworks, Natick, MA), then the average PpIX intensity per pixel was plotted against the incubation period.

5.2.5. Segmentation and Feature Extraction

Fluorescent PpIX served as the main fluorescence marker to highlight cell mitochondria and create nucleus contrast. The imaging data were imported to Matlab for further image processing and extracting quantitative features. Due to the low signal to noise ratio provided by PpIX, all fluorescence images were preprocessed to reduce the shot noise and uneven background. Contrast was enhanced by three iterative adjustment of imaging threshold, followed by further smoothing and morphological operations to segment out binary images of each cell. The segmentation results are demonstrated in **Fig. 5.3**. Then, mitochondrial distribution was analyzed using various morphological features based on the binary images to illustrate the shape eccentricity, irregularity, and the nucleus to mitochondria ratio [9,27]. PpIX fluorescence patterns of each cell were explored using statistical calculation of the intensity histogram. Further textural analysis was achieved using the gray-level co-occurrence matrix (GLCM) [28] along perpendicular and diagonal axes of the bounding box to extract intensity contrast, correlation, homogeneity and energy. The key features and their descriptions are summarized in **Table 5.2**.

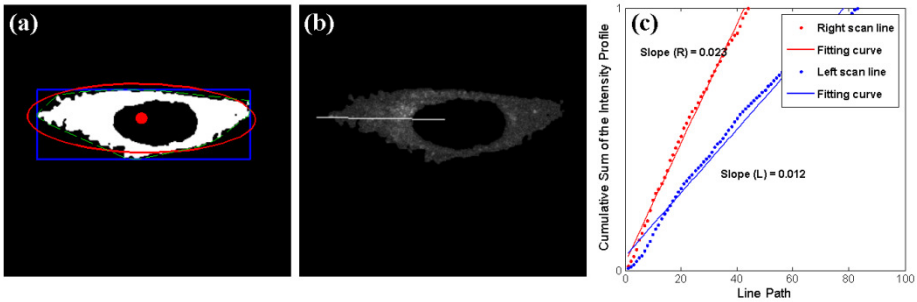

Figure 5.3 Examples of morphological and textural features. (a) A binary image is used to extract morphological features. The bounding box, convex area (area within dashed lines), and the ellipse are noted. (b) The original 8-bit image of mitochondria distribution was obtained based on the binary mask. This image shows the line used for extracting line scan intensity profile, as listed in Table 5.2. (c) The intensity contrast can be revealed based on the slope of cumulative intensity along the line a small value was a result of higher contrast close to the cell nucleus. The slope (L) is from the line shown in 5.3(b), and the slope (R) is obtained from the line in opposite direction.

Table 5.2 List of features

Morphological Features	**Descriptions**
Eccentricity of the ellipse[1]	Measuring the ratio of the length between the two foci to the major axis length of the ellipse. Larger values indicate slender shapes
Major to minor axis ratio[5]	Measuring the two axes of the ellipse. Larger values indicate slender shapes.
Extent[7]	Calculated by the binary pixel area divided by the bounding box area. Slender cells with various orientation lead to smaller values.
Solidity[6]	Calculated by the binary pixel area divided by the convex area to demonstrate shape irregularity.
Roundness	$(4\pi \times \text{Area}) / (\text{Perimeter}^2)$. The value of 1 indicates a perfect circle
Nucleus to mitochondria ratio[3]	The binary pixel area of the segmented cell nucleus to PpIX localized mitochondria
Intensity/ Textural Features	**Descriptions**
Line scan intensity profile[2*]	The intensity profile along the line from the centroid to one end of the ellipse. A single value of slope was obtained to represent the intensity increment along the line.
Standard deviation[8]	Standard deviation of the pixel intensity in the segmented region shown in Fig. 5.3(b).
Smoothness[10]	$1- 1/(1+\sigma^2)$. σ represents variance of intensity histogram.
Third moment[9]	Measuring the symmetricity of intensity histogram of the segmented region.
Entropy	The randomness of intensity values within the segmented region
GLCM Contrast[2*]	The contrast of pixel intensity to adjacent pixels over the segmented area
GLCM Correlation	The correlation of neighbor pixel intensity over the segmented regions
GLCM Homogeneity	The closeness of the gray-level co-occurrence matrix elements to its diagonal
GLCM Energy[4]	The sum of the squared elements of the matrix over the entire region

Note: Superscript numbers indicate the recruiting sequence during feature reduction, as described in Sec. 5.2.6. * showed comparable discriminant capability returned by sequential forward feature selection.

5.2.6. Feature Reduction and Classification

125 datasets containing 62 CP-B and 63 CP-A cells from mono-culture were used for training the SVM to achieve the desired generalization capability and prediction of high-grade dysplastic (CP-B) cells in co-culture. Vectors of 15 features were selected to characterize the cells; however, most of the features contain redundant information that is highly correlated. Therefore, reduction of feature dimensionality was first performed using a built-in forward sequential selection (FSS) algorithm (*sequentialfs*), where the best combination of feature subsets can be selected for classification. In the feature selection process, individual features were sequentially recruited for classification and tested for prediction accuracy using 10-fold cross-validation. This operation splits the whole training set into 10 subgroups, followed by iterative classification on every single subgroup using the training algorithm obtained from the other nine-tenths of datasets. This feature reduction step renders a combination of feature subsets that yields the smallest misclassification error (as shown in **Fig. 5.4a**).

Using the best feature subsets returned from the feature selection step, support vector machines (SVM) were then trained to classify each cell in the co-culture to CP-A (metaplasia) or CP-B (HGD). In particular, SVM mapped the input features to a higher dimensional space to find the best hyperplane that yields the largest margin between the two classes. The RBF (Gaussian radial basis function) kernel was applied to deal with potential non-linear relationships between the feature attributes and the class, thus yielding a soft margin. [29] Given the training sets, the RBF kernel radius (R) and the box constraint (C) were optimized using 5-fold cross-validation. A total of 109 CP-A and 135 CP-B cells in co-culture were used for testing the classification performance. The classification sensitivity was defined as the ratio of correct HGD detection to true CP-B numbers, and the specificity corresponds to the ratio of correct metaplasia detection to true CP-A numbers. Performance of the classification algorithm was further demonstrated by plotting the receiver operating characteristic (ROC) curve and represented by the area under the curve (AUC), as shown in **Fig. 5.5 – 5.7**.

5.3. Results

5.3.1. Evaluation of Time-lapse PpIX fluorescence intensity

To evaluate the use of 5-ALA for detection of dysplastic cells, we first characterized the cellular uptake behavior of the two cell lines. The intracellular PpIX intensities were calculated against the incubation time using mono-culture, and the co-culture intensity difference was compared after 6 hours of incubation. The comparison of PpIX fluorescence intensities between metaplasia and HGD cell lines is shown in **Fig 5.4(a) and 5.4(b)**. The results showed that CP-B cells reached maximum PpIX concentration faster (within 3 hours) than CP-A cells, where the PpIX intensities at 3 hours were 32 ± 3 in CP-B and 23 ± 2 counts in CP-A using 1-photon excitation ($p < 0.01$). The data acquired using 2-photon

excitation demonstrated a similar trend. In addition, it was clearly shown that there was no selective accumulation of PpIX in HGD cells with neoplastic characteristics; instead, both cell lines exhibited similar saturation intensities after 5 hours of 5-ALA incubation. As shown in **Fig. 5.4(c)**, the lack of selectivity ($p = 0.51$) was also observed in co-culture environment, where the PpIX intensities in both cell lines agreed with the mono-culture results. Although we are comparing metaplasia versus high grade dysplasia, the results are consistent with a previous study that BE tissue exhibited a faster PpIX accumulation within 4 hours compared to normal epithelium, and the eventual maximum intensity was higher in normal epithelium. The conversion and saturation intensity of PpIX may depend on the activity and amount of ferrochelatase [20,30]

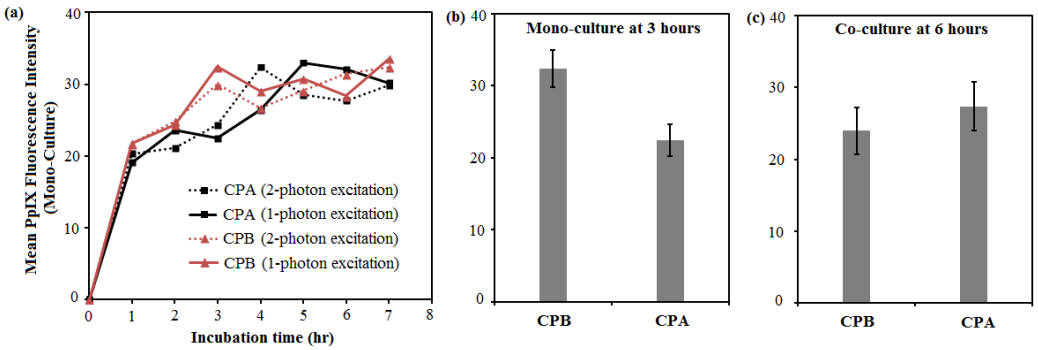

Figure 5.4 (a) The averaged intracellular PpIX intensity of each cell line in monoculture was plotted against the incubation time from 0 to 7 hours using one-photon (solid line) and two-photon excitation (dotted line). It was noted that CP-B cells exhibit a higher PpIX intensity than CP-A, where the PpIX intensities in CP-B and CP-A are 32±3 and 23±2 counts, respectively using 1-photon excitation at 3 hours of incubation. The intracellular PpIX intensity eventually reached a plateau. The standard deviation of each data point was not shown in the figure for easy visualization. (b) PpIX intensity of CP-B and CP-A in monoculture measured at 3 hours ($P < 0.01$) using 1-photon excitation. (c) Intracellular PpIX intensities were compared between the two cell lines grown in co-culture environment after 6 hours of 5-ALA incubation ($p = 0.51$). The error bars represent the standard deviation of the mean.

5.3.2. Reduction of Dimensionality

The rank of features in the recruiting process is indicated by the superscript numbers in **Table 5.2**. During sequential feature recruiting from the mono-culture training group, combinations of a range of feature numbers were examined for their classification performance. As shown in **Fig. 5.5(a)**, the misclassification rates (MCR) were plotted against the feature numbers selected sequentially from mono-culture. The same subsets of feature combination returned by feature selection were then tested in co-culture classification. It is noted that the MCR converged to 0.10 when more than 4 features were used for the mono-culture group, while only 2 features (eccentricity and line scan intensity profile) were required to produce the MCR of 0.09 when the same feature subsets

were used in co-culture classification. With the reduced feature dimensionality, the performance of SVM for co-culture classification was further demonstrated in **Fig. 5.5(b)**, where ROC curves were plotted for various feature numbers. The best prediction performance using two features achieved the AUC of 0.95. There is a trend that the error of co-culture classification is almost doubled after 3 features. This could be due to the fact that the other features are not so representative and also added noises to the datasets. Extraction of features can be a time-consuming task since that requires computing geometric, intensity and texture features from each individual cell. Obtaining such a high AUC with only two features selected via sequential feature recruiting is a promising result since the SVM can now only use these two identified features for classifying CPA versus CPB cells in the context of 2D co-culture. From computational point of view, this result opens the way for online implementation of CPA-CPB classification, which may be beneficial for validation *in vivo* as a logical next step.

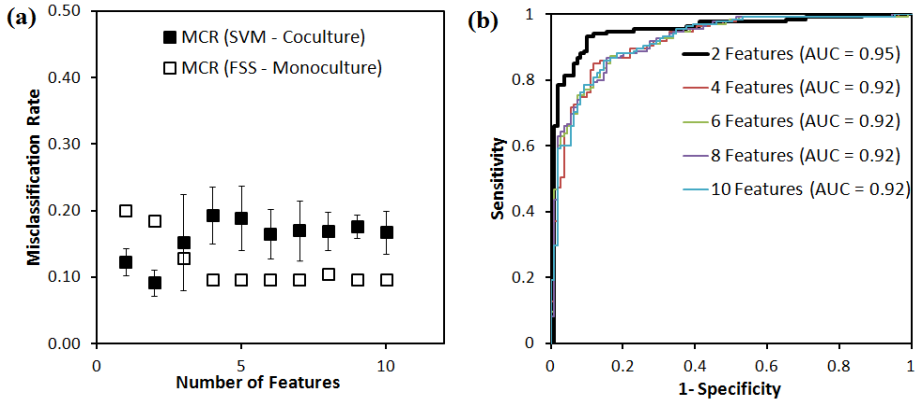

Figure 5.5 (a) Misclassification rates were plotted against up to 10 features used for classification. The results from the training set using mono-culture yielded the MCR of 0.10 when 4 features were used. It is noted that classification results using the same feature subsets in co-culture yielded the MCR of 0.09 when only the eccentricity and line scanned intensity profile were employed. The error bars represent standard deviation of co-culture testing sets from 3 separate acquisition trials. (b) ROC curves were obtained from SVM classification on all co-culture samples, and the AUC of 0.95 can be achieved using the two features returned by feature selection, as indicated by the bold black line.

5.3.3. Classification Performance Using Support Vector Machines

Without any specified stopping criterion, the feature selection process returned the subsets including eccentricity and line scan intensity profiles, or eccentricity and the GLCM contrast. **Fig. 5.6** and **5.7** demonstrate the training results using mono-culture cells and the corresponding classification results on the co-culture cells, where CP-A and CP-B were seeded in the same dish. **Fig. 5.6** shows the training results based on eccentricity and GLCM intensity contrast

using the SVM with a Gaussian kernel. The two optimized parameters, *R* (2.21) and *C* (1.07), account for the radius of the Gaussian kernel and the imbalance of group population, respectively. Although the training result demonstrates sensitivity of 90% and specificity of just 74%, the combined classification results from all co-culture images of repetitive trials showed 94% sensitivity and 82% specificity. The ROC curves that demonstrate the trade-off of sensitivity and specificity are shown in **Fig 5.8**. **Fig 5.7** shows the training results based on eccentricity and the slope obtained from the line scan profile. This training result was obtained with sensitivity of 95% and specificity of 70% with *R* and *C* of 2.17 and 0.78, respectively; however, the classification produce an improved prediction on the co-culture set, for which 95% sensitivity and 87% specificity were obtained with an AUC of 0.95 (**Fig. 5.8**). **Table 5.3** summarizes the classification results from both mono-culture and co-culture, indicating a good generalization capability of the classifier from mono-culture to co-culture environment.

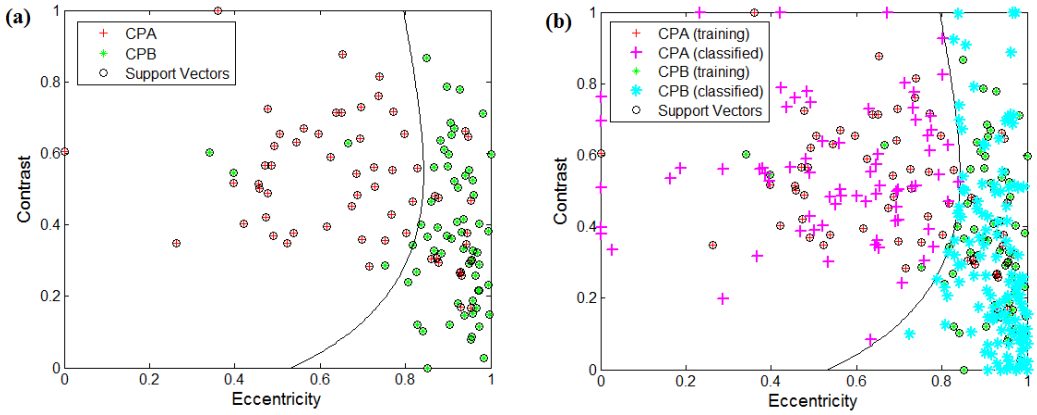

Figure 5.6 (a) The training results based on eccentricity and intensity contrast, which yields sensitivity of 90% (True CP-B) and specificity of 74% (True CP-A) (b) The training model was tested on a combination of co-culture imaging trials. The classification results demonstrated 94% sensitivity and 82% specificity, with the AUC of 0.94.

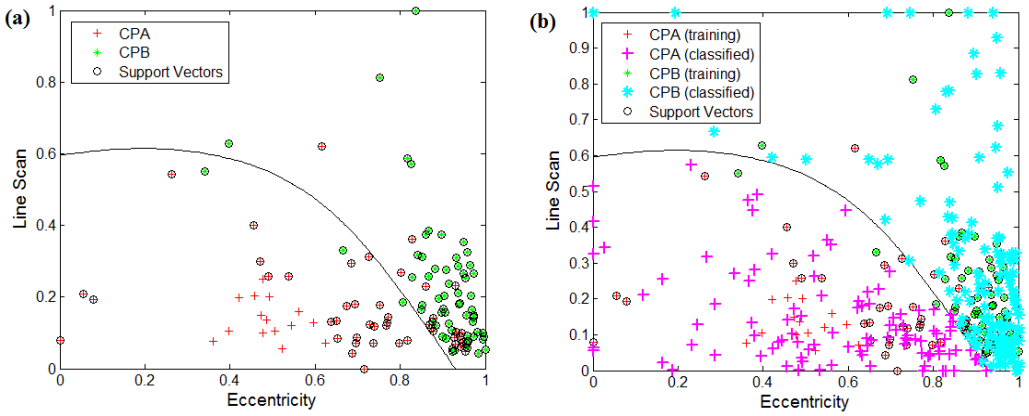

Figure 5.7 (a) The training results based on eccentricity and the slope obtained from the line scan profile using the same training set and testing set. This training showed sensitivity of 95% (True CP-B) and Specificity of 70% (True CP-A) (b) The results from co-culture images showed 95% sensitivity and 87% specificity.

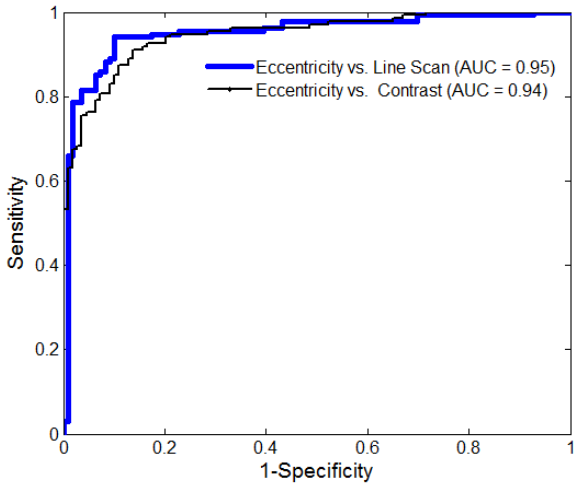

Figure 5.8 Performance of SVM using two features: the combination of eccentricity and intensity contrast (AUC = 0.94), and the combination of eccentricity and the slope obtained from the line scan intensity profiles (AUC = 0.95).

Table 5.3 Summary of the classification results

Features	Groups	Sensitivity	Specificity
Eccentricity vs. Contrast	Mono-culture	90%	74%
	Co-culture	94%	82%
Eccentricity vs. Line Scan	Mono-culture	95%	70%
	Co-culture	95%	87%

5.4. Discussion

We used a PDT photosensitizing agent, 5-ALA to induce PpIX as a fluorescence marker to highlight mitochondria and generate nucleus contrast in Barrett's esophageal cell lines. Imaging contrast induced by PpIX is promising for its safety compared to regular nucleus stains, and its ability to delineate the nucleus in contrast to the highlighted mitochondria. Our results indicated that the HGD cells (CP-B) can be distinguished from metaplastic (CP-A) cells based on their mitochondrial distribution (morphology) and intensity patterns, with an ROC curve AUC of 0.95. Although the current study was based on an *in vitro* platform, the feasibility of using photosensitizers as contrast agents for automatic detection of pre-malignant cells in co-culture has been demonstrated. The quantitative imaging analysis and classification yielded a better selectivity when compared with previous clinical studies solely based on 5-ALA preferential uptake, [31] where the confounding PpIX fluorescence found in non-dysplastic regions led to high misclassification errors. The current study also provides promising results when compared with the previous imaging analysis study using other contrast agents *in vivo*, [10] but an extension from the current study to 3D environment is necessary for a more direct comparison.

Due to the first use of 5-ALA for automatic detection, we started with investigating the cellular uptake behavior in mono-culture and co-culture environments. The intensity variation over time and the lack of selective uptake both reveal the need for robust detection algorithms based on morphological and textural features. For example, in clinical applications, the inadequate detection accuracy may be attributed to lack of drug selectivity, [32] varied uptake rate, and artifacts from detection geometry. [33] In other words, training procedures that took the intensity variation into account may improve the classifier. Feature extraction and classification in this study were initially performed at the single-cell level in an attempt to have a thorough understanding of the morphological and cellular textural features that could potentially be retained in the next step that will conform to histological standards. [9] In order to establish a connection towards the 3D model, we also acquired images of high density cell culture, where the cell-cell interaction is more prominent and could yield distinct distribution patterns for classification. **Fig. 5.9** demonstrates high-density mono-culture and co-culture images stained with fluorescent PpIX. It is clear that the nucleus contrast highlighted by PpIX can yield compatible features with both single-cell features and histology guidelines. For example, the intrinsically greater eccentricity and more homogeneous intensity distribution of HGD cells were still observed in high cell density environment (**Fig. 5.9(b)**), which actually serves as hidden information to describe more randomly orientated nuclei and overlapped structure in a region of HGD. More importantly, irregular nucleus size, orientation, and the formation of crowded and non-uniform stratified pattern were observed in CP-B (**Fig. 5.9(b)**) compared to CP-A cells (**Fig. 5.9(a)**), which is consistent with histological analyses. [8,9] This preliminary study thus provides baseline features

for investigating high density and multi-layered cell culture for identification of HGD regions as indicated in **Fig. 5.9(c)**.

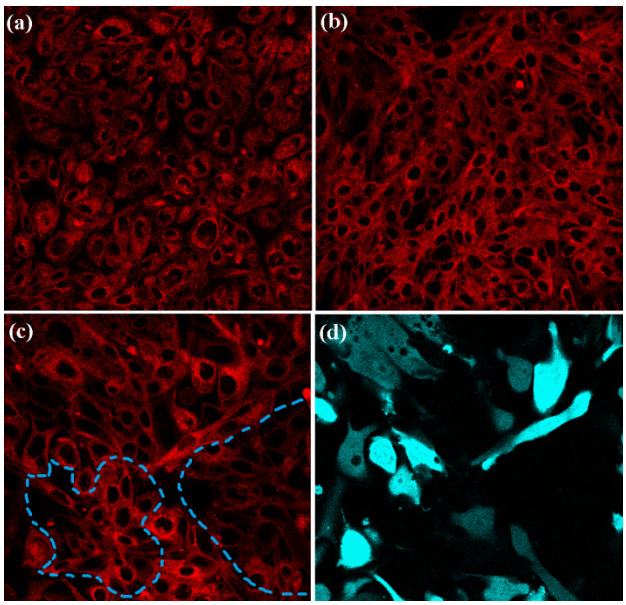

Figure 5.9 Sample images of high density mono-culture and co-culture cells incubated with 5-ALA for 6 hours. (a) mono-layer CP-A (metaplasia) cells. (b) CP-B cells (HGD) that always form nodes of multiple layers before expanding. (c) Co-culture image containing both CP-A and CP-B cells where certain CP-B areas are highlighted by the dashed line. (d) The same field of view as (c) where CP-A cells were stably transfected with mcerulean-3 for the ground truth channel.

In this study, higher sensitivity and lower specificity were observed during the training process but the specificity was increased during the classification using co-culture datasets. From a drug uptake perspective, a maximum level of PpIX can be accumulated in mitochondria within 5 to 6 hours. The more accumulation of PpIX in mitochondria, the better intensity contrast of mitochondrial distribution can be achieved. This phenomenon improves the classification of CP-A cells that exhibit greater intensity contrast compared to CP-B. It may be beneficial to further investigate the classification results on the testing co-culture sets at various incubation times. Moreover, it is also observed that the use of fewer features can achieve better classification performance in co-culture compared to mono-culture, as shown in **Fig. 5.5(a)**. It may be attributed to the fact that co-culture environment provides a better control over experimental variability on both cell lines. Therefore, comparable classification performance can be achieved using simpler feature combinations.

Relatively small numbers of cells were used to develop the classification algorithms. A larger sample population more likely represents population variability better. To conquer this issue, mono-culture and co-culture images in this study were obtained from multiple independent experiments using different batches of cells growing in identical condition with the same imaging acquisition

settings. Individual cell lines from various batches were observed to have very similar morphology and drug uptake rate, suggesting a consistency in morphological and fluorescence intensity patterns within each cell line. Furthermore, the use of stably transfected CP-A cells could also lead to additional variability of CP-A cells. However, the transfection-associated changes in morphology and intensity texture can be validated by preliminary flow cytometry results: the forward scattering (size) and the side scattering (granularity) of transfected cells yielded a totally different distribution pattern from CP-B cells, but the same distribution as CP-A cells (**Fig 5.10**). In other words, the transfection did not alter cell morphology and granularity considerably. This can also be observed in **Fig 5.6** and **Fig 5.7** where the CP-A (training set) and transfected cells (in co-culture testing set) in the classification showed significantly overlapped distribution.

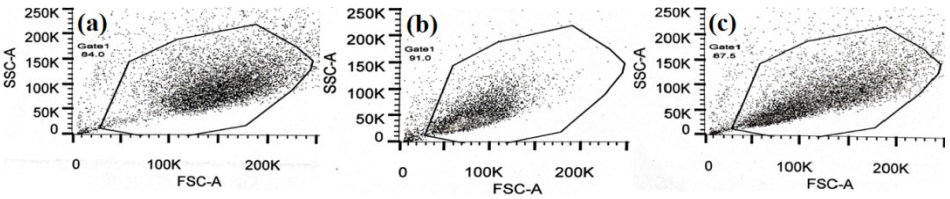

Figure 5.10 Cell size and granularity demonstrated by the flow cytometry measurements. (a) Parental CP-A cells (b) Parental CP-B cells, and (c) Co-culture of transfected CP-A and parental CP-B cells using 1:1 seeding ratio. The same gate was used to collect the cell count and the CP-A cells were also separated by the m-cerulean emission. Both transfected and parental CP-A showed overlapping distributions in terms of size and granularity, in which the granularity is associated with the fluorescence intensity contrast in the cell. On the contrary, CP-B cells are of small cell size and less granularity than CP-A cells.

It should be noted that BE *in vivo* is a highly heterogeneous environment where different types of cells co-exist. In this case, the discrimination would not only be between two cell lines, but multiple. In clinical practice, the endoscopist take biopsy samples based on visual observation of "metaplasia", characterized by salmon pink color different from other normal squamous epithelium. Within metaplasia tissue, the pathologist has to confirm the presence of HGD, as metaplasia and dysplasia are not easily distinguished by wide field observation. Therefore, we aim to distinguish these two very similar cell lines (metaplasia and HGD) as a starting point, which essentially could be a more challenging task compared to classification between normal and BE cells.

5.5. Conclusion

In conclusion, this preliminary study suggests that using a clinically approved photosensitizer as a contrast agent with the aid of machine learning may

be a feasible approach for robust determination of HGD or pre-malignant cells. This approach overcomes the poor selectivity of clinical photosensitizers for BE, provide safer nucleus contrast detection and, potentially, reduce inter-observer variability. This is the first time that a PDT photosensitizer was employed as a potential contrast agent; therefore, we investigated the cellular uptake patterns, and extracted features at a single cell level. However, the experimental methodology and the classifier were designed to account for intensity variations that can be challenging *in vivo*. This two-dimensional cell culture platform, thus, served as a baseline research tool for us to tackle cell behavior and relevant features in organotypic models. Optimization of a 5-ALA based classification algorithm using high-density 2D and 3D co-culture is currently under investigation. In addition, using the PDT photosensitizer may provide potential selectivity in treatment due to a faster PpIX accumulation in HGD cells. Therefore, it might be interesting to investigate the potential benefits for integrated strategies that combine detection and treatment.

References

1. G. Portale, J. A. Hagen, J. H. Peters, L. S. Chan, S. R. DeMeester, T. A. K. Gandamihardja, and T. R. DeMeester, "Modern 5-year survival of resectable esophageal adenocarcinoma: single institution experience with 263 patients.," J. Am. Coll. Surg. **202**, 588–96; discussion 596–8 (2006).

2. E. Sihvo, M. Luostarinen, and J. Salo, "Fate of patients with adenocarcinoma of the esophagus and the esophagogastric junction: a population-based analysis.," Am. J. Gastroenterol. **99**, 419–24 (2004).

3. N. Thekkek, S. Anandasabapathy, and R. Richards-Kortum, "Optical molecular imaging for detection of Barrett's-associated neoplasia.," World J. Gastroenterol. **17**, 53–62 (2011).

4. S. J. Spechler, "The Natural History of Dysplasia and Cancer in Barrett's Esophagus," J. Clin. Gastroenterol. **36**, 2–5 (2003).

5. B. C. Wilson, "Detection and treatment of dysplasia in Barrett's esophagus: a pivotal challenge in translating biophotonics from bench to bedside.," J. Biomed. Opt. **12**, 051401 (2007).

6. T. D. Wang and J. Van Dam, "Optical biopsy: a new frontier in endoscopic detection and diagnosis.," Clin. Gastroenterol. Hepatol. **2**, 744–53 (2004).

7. M. A. Kara, R. S. DaCosta, C. J. Streutker, N. E. Marcon, J. J. G. H. M. Bergman, and B. C. Wilson, "Characterization of tissue autofluorescence in Barrett's esophagus by confocal fluorescence microscopy.," Dis. Esophagus **20**, 141–50 (2007).

8. R. Fiocca, L. Mastracci, M. Milione, P. Parente, and V. Savarino, "Microscopic esophagitis and Barrett's esophagus: the histology report.," Dig. Liver Dis. **43 Suppl 4**, S319–30 (2011).

9. J. R. Goldblum, "Barrett's esophagus and Barrett's-related dysplasia.," Mod. Pathol. **16**, 316–24 (2003).

10. T. J. Muldoon, N. Thekkek, D. Roblyer, D. Maru, N. Harpaz, J. Potack, S. Anandasabapathy, and R. Richards-Kortum, "Evaluation of quantitative image analysis criteria for the high-resolution microendoscopic detection of neoplasia in Barrett's esophagus.," J. Biomed. Opt. **15**, 026027 (2010).

11. and R. R.-K. N. Thekkek, D.M. Maru, A.D. Polydorides, M.S. Bhutani, S. Anandasabapathy, "Pre-Clinical Evaluation of Fluorescent Deoxyglucose as a Topical Contrast Agent for the Detection of Barrett ' s-Associated Neoplasia During Confocal Imaging," Technol. Cancer Res. Treat. **10**, 431–441 (2011).

12. M. I. Canto, "Endomicroscopy of Barrett's Esophagus.," Gastroenterol. Clin. North Am. **39**, 759–69 (2010).

13. M. B. Wallace, P. Sharma, C. Lightdale, H. Wolfsen, E. Coron, A. Buchner, M. Bajbouj, A. Bansal, A. Rastogi, J. Abrams, J. E. Crook, and A. Meining, "Preliminary accuracy and interobserver agreement for the detection of intraepithelial neoplasia in Barrett's esophagus with probe-based confocal laser endomicroscopy.," Gastrointest. Endosc. **72**, 19–24 (2010).

14. T. M. Hitoshi Shiozaki, Hideaki Tahara, Kenji Kobayashi, Hiroshi Yana, Shigeyuki Tamura, Haruhiko Imamoto, Tokiharu Yano, Kunihiko Oku, Mikiyo Mitata, Kiniji Nishiyama, kazuko Kubo, "Endoscopic screening of early esphageal cancer with the lugol dye method in patients with head and neck cancers," Cancer **66**, 2068–2071 (1990).

15. Y. Amano, Y. Kushiyama, S. Ishihara, T. Yuki, Y. Miyaoka, N. Yoshino, N. Ishimura, H. Fujishiro, K. Adachi, R. Maruyama, M. A. K. Rumi, and Y. Kinoshita, "Crystal violet chromoendoscopy with mucosal pit pattern diagnosis is useful for surveillance of short-segment Barrett's esophagus.," Am. J. Gastroenterol. **100**, 21–6 (2005).

16. L. M. Wong Kee Song, D. G. Adler, B. Chand, J. D. Conway, J. M. B. Croffie, J. a Disario, D. S. Mishkin, R. J. Shah, L. Somogyi, W. M. Tierney, and B. T. Petersen, "Chromoendoscopy.," Gastrointest. Endosc. **66**, 639–49 (2007).

17. M. I. Canto, "Staining in gastrointestinal endoscopy: the basics.," Endoscopy **31**, 479–86 (1999).

18. S.-C. A. Yeh, K. R. Diamond, M. S. Patterson, Z. Nie, J. E. Hayward, and Q. Fang, "Monitoring photosensitizer uptake using two photon fluorescence lifetime imaging microscopy.," Theranostics **2**, 817–26 (2012).

19. C. J. Kelty, S. L. Marcus, and R. Ackroyd, "Photodynamic therapy for Barrett's esophagus: a review," Dis. Esophagus **15**, 137–144 (2002).

20. C. J. Kelty, N. J. Brown, M. W. R. Reed, and R. Ackroyd, "The use of 5-aminolaevulinic acid as a photosensitiser in photodynamic therapy and photodiagnosis," Photochem. Photobiol. Sci. **1**, 158–168 (2002).

21. M. C. A. Palanca-Wessels, A. Klingelhutz, B. J. Reid, T. H. Norwood, K. E. Opheim, T. G. Paulson, Z. Feng, and P. S. Rabinovitch, "Extended lifespan of Barrett's esophagus epithelium transduced with the human telomerase catalytic subunit: a useful in vitro model.," Carcinogenesis **24**, 1183–90 (2003).

22. L. M. F. Merlo, R. E. Kosoff, K. L. Gardiner, and C. C. Maley, "An in vitro co-culture model of esophageal cells identifies ascorbic acid as a modulator of cell competition.," BMC Cancer **11**, 461 – 471 (2011).

23. R. E. Kosoff, K. L. Gardiner, L. M. F. Merlo, K. Pavlov, A. K. Rustgi, and C. C. Maley, "Development and characterization of an organotypic model of Barrett's esophagus.," J. Cell. Physiol. **227**, 2654–9 (2012).

24. M. C. Palanca-Wessels, M. T. Barrett, P. C. Galipeau, K. L. Rohrer, B. J. Reid, and P. S. Rabinovitch, "Genetic analysis of long-term Barrett's esophagus epithelial cultures exhibiting cytogenetic and ploidy abnormalities," Gastroenterology **114**, 295–304 (1998).

25. Y. Su, X. Chen, M. Klein, M. Fang, S. Wang, C. S. Yang, and R. K. Goyal, "Phenotype of columnar-lined esophagus in rats with esophagogastroduodenal anastomosis: similarity to human Barrett's esophagus.," Lab. Investig. **84**, 753–65 (2004).

26. R. Kiesslich, L. Gossner, M. Goetz, A. Dahlmann, M. Vieth, M. Stolte, A. Hoffman, M. Jung, B. Nafe, P. R. Galle, and M. F. Neurath, "In vivo histology of Barrett's esophagus and associated neoplasia by confocal laser endomicroscopy.," Clin. Gastroenterol. Hepatol. **4**, 979–87 (2006).

27. R. C. Gonzalez and R. E. Woods, *Digital Image Processing, Chapter 11*, 3nd ed. (Prentice Hall, 2008), pp. 795 – 860.

28. G. B. F. Argenti, L. Alparone, "Fast algorithms for texture analysis using co-occurence matrices," Vol. 137 (1990).

29. C. Hsu, C. Chang, and C. Lin, "A Practical Guide to Support Vector Classification," **1**, 1–16 (2010).

30. R. Ackroyd, N. Brown, D. Vernon, D. Roberts, T. Stephenson, S. Marcus, C. Stoddardl, and M. Reed, "5-aminolevulinic acid photosensitization of dysplastic Barrett's esophagus: a pharmacokinetic study," Photochem Photobiol. **70**, 656–662 (1999).

31. E. Endlicher, R. Knuechel, T. Hauser, R. Szeimies, J. Schölmerich, and H. Messmann, "Endoscopic fluorescence detection of low and high grade dysplasia in Barrett's oesophagus using systemic or local 5-aminolaevulinic acid sensitisation," Gut **48**, 314–319 (2001).

32. R. Bonnett, "Photosensitizers of the Porphyrin and Phthalocyanine series for photodynamic therapy," Chem. Soc. Rev. 19–33 (1995).

33. J. L. Sandell and T. C. Zhu, "A review of in-vivo optical properties of human tissues and its impact on PDT," **4**, 773–787 (2012).

Chapter 6.

Paper V – 5-aminolevulinic Acid for Quantitative Seek-and-Treat of High-Grade Dysplasia in Barrett's Esophagus Cellular Models

Shu-Chi Allison Yeh[1], Celine S.N. Ling[2], David W. Andrews[3], Michael S. Patterson[4], Kevin R. Diamond[4], Joseph E. Hayward[4], David Armstrong[5], and Qiyin Fang[1,2,*]

[1]McMaster University, School of Biomedical Engineering.

[2]McMaster University, Department of Engineering Physics.

[3]Sunnybrook Research Institute, 2075 Bayview Ave., Toronto, ON, M4N 3M5

[4]McMaster University, Department of Medical Physics and Applied Radiation Sciences.

[5]McMaster University, Division of Gastroenterology, Department of Medicine.

In Press, Journal of Biomedical Optics; January, 2015

Printed with permission

Introduction to paper V

This chapter focuses on the treatment aspect of the "seek and treat" concept. We characterized the dose response curves of Barrett's esophagus cell lines to 5-ALA and various irradiation regimes. This is considered a complementary study to the BE detection part using quantitative image processing.

Although PDT has been used clinically as one of the treatment approaches for BE, in a macroscopic way. This is the first time to study the treatment efficacy at the microscopic level, in order to characterize cell responses when the photosensitizer is used as a contrast agent for automatic detection. We compared the difference in viability between high-grade dysplasia (HGD) and metaplastic cell lines by retrieving dose response curves. In addition, in order to investigate the optimal cellular-based treatment, we also compared irradiation regimes with or without mitochondrial activation, using one-photon or two-photon light sources. We found that HGD cells are more sensitive to the treatment due to more photosensitizer accumulation at earlier time. Also, treatment involving more activation of mitochondria provides the best killing efficacy.

This work shows that PDT can lead to various extent of cell death between cell lines, and between treatment strategies. It may be beneficial for readers who work on cellular-based ablation with the aid of photosensitizers or other therapeutic contrast agents. The manuscript was written by me and edited by all of the co-authors.

Contents of Paper V

Abstract

High-grade dysplasia (HGD) in Barrett's esophagus poses increased risk in developing esophageal adenocarcinoma. To date, early detection and treatment of HGD regions is still challenging due to the sampling error from tissue biopsy and relocation error during the treatment after histopathological analysis. In this study, CP-A (metaplasia) and CP-B (high-grade dysplasia) cell lines were used to investigate the "seek and treat" potential using 5-ALA induced PpIX. The PDT photosensitizer then provides both phototoxic effect and additional image contrast for automatic detection and real-time laser treatment. Complementary to our studies on automatic classification, this work focused on characterizing subcellular irradiation and the potential phototoxicity on both metaplasia and HGD. The treatment results showed that the HGD cells are less viable than metaplastic cells due to more PpIX production at earlier times. Also, due to mitochondrial localization of PpIX, better killing effect was achieved by involving mitochondria or whole cells compared to just nucleus irradiation in the detected region. With the additional toxicity given by PpIX and potential morphological/textural differences for pattern recognition, this cellular platform serves as a platform to further investigate real time "seek and treat" strategies in 3D models for improving early detection and treatment of Barrett's esophagus.

6.1. Introduction

Barrett's esophagus (BE) is a precancerous condition occurring in the lower esophagus, where the original squamous epithelium undergoes metaplastic transformation and is replaced by the intestinalized columnar cells. [1,2] BE can progress through low-grade dysplasia to high-grade dysplasia (HGD), which significantly increases the risk of developing esophageal adenocarcinoma if early treatment is not provided. [3–5] Although various interventions have been studied extensively, [6–11] the diagnostic techniques are still inadequate and suspected areas of HGD may be missed because of sampling errors for the initial biopsies or because of an inability to locate the same target areas on repeat endoscopy. This is a common problem because pathological analysis following four-quadrant biopsy is the current gold standard for evaluating suspected lesions. Because it can take several days to process, stain and examine the biopsies, diagnosis and treatment are commonly separated into two steps, which leads to difficulties in accurate relocalization of the lesions in separate procedures. [4] Optical biopsy is an emerging technique that takes advantages of distinct tissue optical properties of

targeted lesions to enable real-time diagnosis. [12] In particular, the cellular-based optical biopsy retrieves subcellular Barrett's-associated characteristics by the use of point spectroscopy or endomicroscopy. [4,13] However, there are substantial challenges in detecting dysplasia in Barrett's esophagus with optical biopsy including poor signal-to-noise ratio and low specificity in fluorescence endoscopy imaging [14] and significant patient-to-patient variability. [4] To address these challenges, microscopic-based visualization of subcellular morphology with the addition of an exogenous contrast agent is desirable to enhance the contrast between normal, metaplastic and HGD regions. Aiming for translation of such techniques to future clinical applications, using fluorescence from FDA approved photosensitizers as a contrast agent becomes an attractive option. [15,16] In addition, the use of photosensitizers may provide additional treatment efficacy. In other words integrated detection and treatment can be achieved using well-characterized light illumination immediately following a robust detection with quantitative feature extraction and classification (**Chapter 5**). Palanca-Wessels *et al*. have developed metaplasia (CP-A) and HGD (CP-B, CP-C and CP-D) cell strains from Barrett's esophagus. The morphological features and cellular behaviors of these cell lines have been investigated along with normal squamous epithelial cells in both co-culture and organotypic culture models. [17–19] Therefore, these cell lines could potentially serve as a cellular-based platform to study the integrated early detection and treatment of Barrett's Esophagus.

In this study, we have focused on characterizing the subcellular irradiation efficacies in order to understand the potential PpIX phototoxicity on both metaplasia and HGD cell lines after detection. The microscopic images obtained at subcellular resolution would be comparable to microendoscopic technologies in development. [13,20,21] Among potential PDT "contrast agents," 5-aminolevulinic acid (5-ALA) is an endogenous heme precursor that localizes well in mucosal tissues. [10] It produces preferential accumulation of cytotoxic protoporphyrin IX (PpIX) at the mitochondrial membranes, [22,23] which can potentially lead to treatment selectivity; more importantly, PpIX provides nucleus contrast for detection of HGD [13]. To date, although 5-ALA has been studied extensively for treating BE *in vivo,* limited selectivity was noted for dysplastic cells. [11,24–29] Our goal is to use the BE cellular platform to investigate the feasibility of integrated detection and treatment. The quantitative imaging analysis, feature extraction, and classification have been investigated in our group, followed by the characterization of localized, subcellular treatment efficacy in this study to examine the optimal irradiation scheme.

6.2. Materials and Methods

We characterized the dose response curves of two Barrett's esophagus cell lines (CP-A and CP-B) to various doses of light fluence using one-photon and two-photon irradiation. Three irradiation regimes were applied at each light dose

in the presence or absence of 5-ALA in order to investigate the treatment efficacy as a result of targeted subcellular PDT.

6.2.1. Cell Culture

CP-A (non-dysplastic metaplasia, ATCC® CRL-4027™) and CP-B (high-grade dysplasia, ATCC® CRL-4028™) are both hTERT-immortalized epithelial cells derived from human esophagus. [17] These well-characterized pre-malignant cell lines were selected as an *in vitro* platform to study subcellular treatment efficacy. Both cell lines were cultured under identical conditions using the same batch of MCDB 153 base medium (M7403, Sigma), supplemented with 5% Fetal Bovine Serum (16000-036, Gibco®, Canada), 0.25 µg/ml Amphotericin B (A2942, Sigma), 1% Penicillin/Streptomycin (15140-122, Gibco®), 0.4 µg/ml Hydrocortisone (H0888, Sigma), 140 µg/ml bovine pituitary extract (P1476, Sigma), 20 mg/L Adenine (A8626, Sigma), 0.1% Insulin-transferrin-sodium selenite (I1884, Sigma), 20 ng/ml Recombinant EGF (E9644, Sigma), 4mM Glutamine (G7513, Sigma), and 1nM Cholera Toxin (C8052. Sigma). Cells were maintained at 37 ºC in a water-jacketed CO_2 incubator (Forma Series II, Thermo Fisher Scientific Inc, Waltham, MA) and passaged as recommended by ATCC. All experimental data were acquired using cells within 10 passages after cryopreservation to minimize the variability due to cell degradation. [30]

6.2.2. Experimental Preparation

In this study, 5-ALA (A3785, Sigma) served as a fluorescent marker as well as a PDT photosensitizer. A stock solution of 100 mM 5-ALA dissolved in PBS (14190-144, Gibco®) was prepared and stored in 1 ml aliquots in the dark. Fresh photosensitizer-containing medium was prepared by further diluting the stock solution in the serum-free complete culture medium to a working concentration of 0.5 mM that provides sufficient contrast without yielding dark toxicity.

Cells were detached from a 25 cm^2 culture flask with 2.5 X Trypsin-EDTA solutions (0.5%, 15400-054, Gibco®). Centrifugation process at 125g was used to re-suspend cells in fresh trypsin-free culture medium. A total of 1×10^5 cells were seeded on a gridded glass-bottom dish (P35G-2-14-CGRD, MatTek, MA) 24 hours before the experiment. The culture medium was then replaced by the 0.5 mM 5-ALA-containing medium for a specified incubation period before the experiment. Samples were rinsed with Hanks balanced salt solution (14025-092, Gibco®) supplemented with 20 mM of Hepes buffer (15630-106, Gibco®) before imaging, and were immersed in 1 mL of Hanks-Hepes buffer during the imaging acquisition procedures.

6.2.3. Imaging Acquisition

The fluorescence emission of 5-ALA induced PpIX was collected by a laser scanning confocal microscope (TSC SP5 & DMI 6000 B, Leica, Wetzlar, Germany) equipped with an argon-ion laser operating at 514 nm for one-photon irradiation, and a femtosecond Ti:sapphire laser (Chameleon-Ultra, Coherent, Santa Clara, CA) pulsing at 810 nm for two-photon excitation. The emission spectral band was set as 600 – 750 nm to maximize the detected PpIX intensity, in combination with a transmitted light detector to acquire bright field images.

6.2.4. Subcellular PDT Treatment

Both cell lines were incubated with 5-ALA for 3 hours before imaging and subcellular treatment. The light fluence levels used for imaging and dose response curves are summarized in **Table 6.1**, where the fluence was calculated based on the average power (P) measured at the sample plane, total exposure time (t), and the field of view (FOV): 246 x 246 μm^2. In order to understand the cytotoxic roles played by light fluence and PpIX and eventually to select an appropriate ablative approach, the dose response curves were compared between three treatment schemes selected manually based on the bright-field and 5-ALA images using the built-in software of the microscope: (i) Nucleus treatment: only cell nuclei were illuminated; (ii) Mitochondrial treatment: only a portion of peri-nuclear region highlighted by PpIX was irradiated, with the size of the irradiation field being similar to its cell nucleus; (iii) Whole cell treatment: the light was applied through the whole FOV without any selection. All treatment schemes were applied at the focal plane of the cells only, which focused on the center section of approximately 1 micron in thickness. To compare the treatment efficacy after various regimes, a cell viability dye, propidium iodide (P3566, Invitrogen, Canada) at a working concentration of 300 ng/ mL was used to stain the nuclei of cells which had a compromised cell membrane at 2 hours after the initial irradiation. The fluorescence intensity from propidium iodide (PI) was collected using the excitation light at 488 nm in combination with the emission range of 600 - 700 nm. Therefore, dead cells are highlighted by PI, and the cell viability was obtained based on the ratio of the remaining cells (non-stained by PI) to the original cell count in the same FOV indicated by the gridded dish. Cell counts were obtained with the highlight of PpIX fluorescence in the experimental groups, or using the bright-field images in the control groups. Cells were grown to a density that precluded cell overlap to yield accurate counting results.

Table 6.1 Light doses applied to cell imaging (*) and dose response curves.

One –photon excitation		Two-photon excitation	
P (μW) × t (s)	**Fluence (J/cm^2)**	**P (mW) × t (s)**	**Fluence (J/cm^2)**
0.15 × 6.4	0.002*	45 × 1.28	124*
28 × 5.12	0.24	45 × 5.12	495
70 × 10.24	1.18	45 × 25.6	2478
70 × 25.6	2.96	45 × 51.2	4955
70 × 51.2	5.92	45 × 102.4	9910

6.3. Results

6.3.1. Fluorescence of PpIX

Sample PpIX fluorescence images of metaplastic (CP-A) and HGD (CP-B) cells are shown in **Fig. 6.1.** Differences in cell line morphology were observed when cell mitochondria were highlighted by PpIX; CP-A cells showed dense mitochondrial distribution close to the peri-nuclear region demonstrating a rounder shape, whilst the mitochondria of CP-B cells spread out through the cells demonstrating a more elongated morphology. Further analysis of the cellular fluorescence images identified a small set of features that differentiated metaplastic (CP-A) and dysplastic (CP-B) cells with a sensitivity of 95% and specificity of 87%, yielding an AUC of 0.95 for the ROC curve (**Chapter 5**).

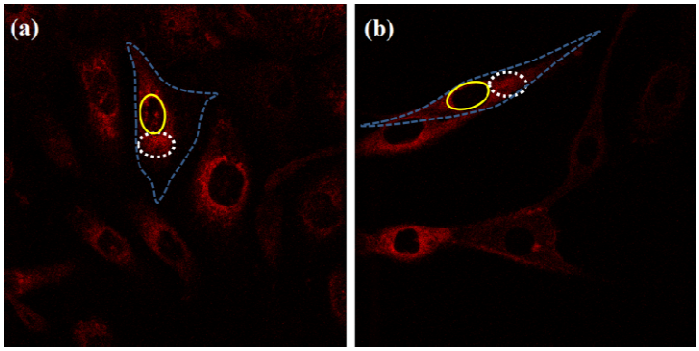

Figure 6.1 Sample PpIX fluorescence images of metaplastic (CP-A) and HGD (CP-B) cells. (a) CP-A cells were incubated with 5-ALA for 6 hours. (b) CP-B cells were incubated with 5-ALA for 3 hours. The red pseudo-color at the mitochondria was PpIX fluorescence excited by an Argon ion laser at 514 nm and collected at the spectral range between 600 – 750 nm. Cell regions selected for PDT treatment were highlighted, including cell nuclei (solid line), partial mitochondria (dotted line), and the whole cell region that can be visualized in bright field images (dashed line).

6.3.2. Subcellular irradiation

Light treatment was given at 3 hours after 5-ALA incubation, where the metaplastic and HGD cells exhibited significantly different intracellular PpIX intensity ($p < 0.01$) in our imaging analysis study (data not shown). We employed various regimes to investigate and characterize their treatment efficacy, which could be relevant when the cellular-based treatment or ablation is integrated with endomicroscopic technology. **Fig. 6.2** to **Fig. 6.5** demonstrate the dose response curves of CP-B (HGD) and CP-A (metaplasia) cells to various laser irradiation doses using 514 nm (**Fig. 6.2 – 6.3**) or 810 nm (**Fig. 6.4 – 6.5**) irradiation, and the cell survival rate associated with three subcellular treatment approaches.

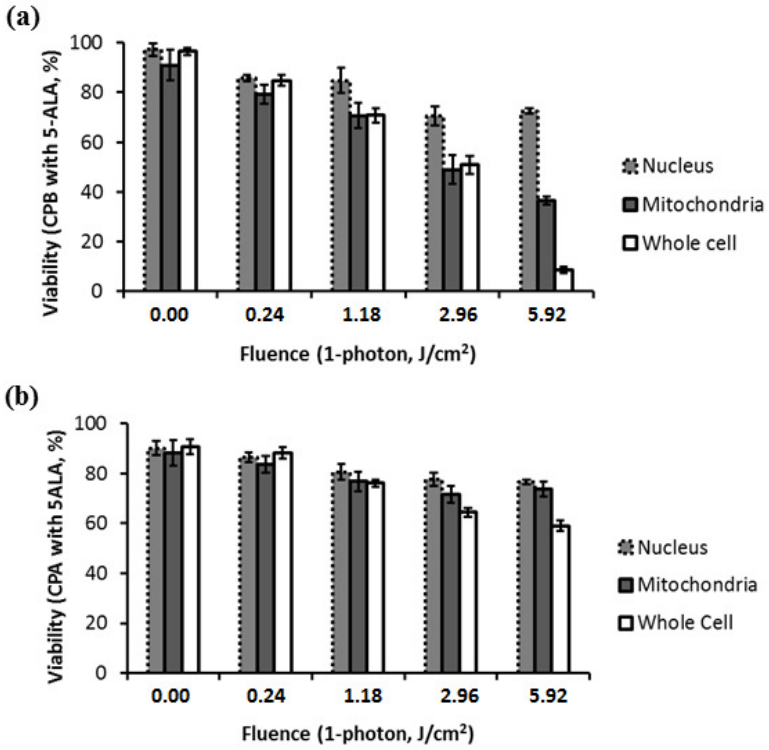

Figure 6.2 Cell survival rates of ALA-stained (a) HGD and (b) metaplasia cells after various subcellular treatment regimes are plotted against five laser irradiation fluences operating at 514 nm, ranging from the fluence for imaging acquisition (0.002 J/cm^2) to 5.92 J/cm^2. Error bars in all figures represent weighted standard deviation from three repetitive trials of each set.

Since both drug and light contribute to cell toxicity, the following comparisons of PDT treatment responses were made: (i) the dose responses of different cell lines, (ii) the dose responses of subcellular treatment, (iii) 5-ALA groups and control groups without drug administration, and (iv) the effect of one-photon and two-photon illumination.

When comparing the dose response between two different cell lines incubated with 5-ALA (**Fig. 6.2**), it was observed that the HGD cells (CP-B) exhibited a significantly lower survival rate than CP-A cells when the light fluence is greater than 2.96 J/cm^2 ($p < 0.01$): CP-B cells showed an approximately 20% reduction in viability comparing to CP-A cells when using either mitochondria or whole cell treatment. When a light fluence of 5.92 J/cm^2 was given, CP-B cells were observed to be 37 % and 51 % less viable than CP-A cells with the mitochondria and whole cell treatment, respectively. These facts suggested the dysplastic cell line was more sensitive to the treatment. The proportional cytotoxic contribution from the light irradiation and the photosensitizer will be discussed further when comparing 5-ALA groups to control groups.

Various extents of phototoxic effects from subcellular PDT treatment were also observed. In general, when cells were incubated with 5-ALA, whole cell and mitochondrial irradiation yielded better efficacy when compared with nucleus treatment. This trend is obvious when the light dose is higher than 2.96 J/cm^2 for CP-B ($p < 0.01$) and 5.92 J/cm^2 in CP-A ($p < 0.01$). This indicates that the irradiation regime involving mitochondria may enhance treatment efficacy in HGD while keeping most of metaplasia cells unharmed. For example, when mitochondria of CP-B and CP-A were both irradiated with light at 5.92 J/cm^2, CP-B cells were observed to be less viable ($p < 0.01$). This selectivity may be further enhanced when integrated with quantitative feature extraction and detection.

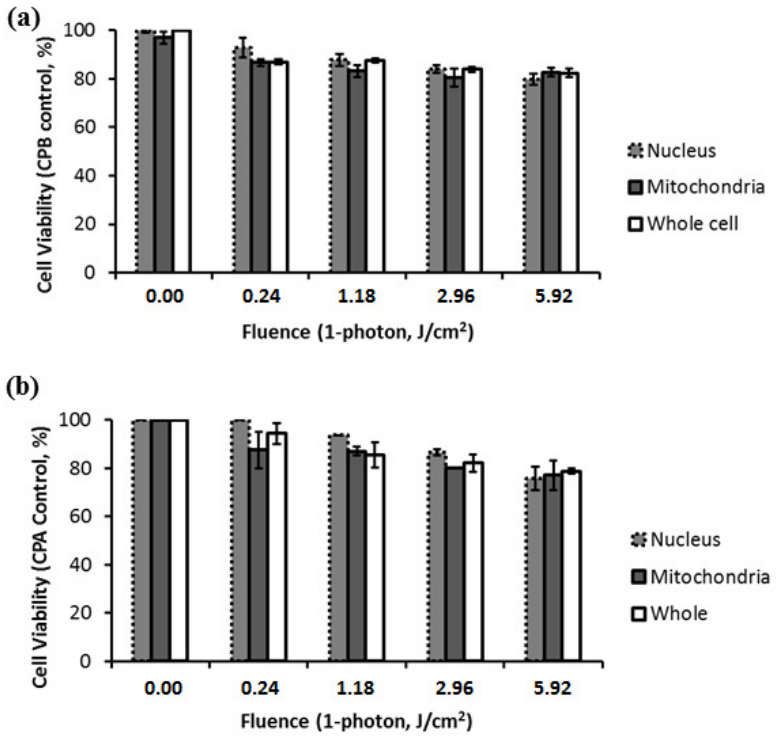

Figure 6.3 Cell survival rates of non-stained (a) HGD and (b) metaplasia cells after various subcellular treatment regimes were plotted against five laser irradiation fluence levels operating at 514 nm, ranging from the dose of imaging acquisition (0.002 J/cm^2) to 5.92 J/cm^2.

The dose response curves were also collected using cells without 5-ALA administration (**Fig. 6.3**). The results observed from non-stained CP-A and CP-B cells indicated that both cell lines had equivalent responses to the photothermal and photochemical laser effect in no-drug controls. Both cell lines were observed to have greater than 80% of viability with good morphological appearance after being exposed to the a high fluence of 5.92 J/cm^2, indicating the light-induced photochemical and photothermal reactions at this level corresponded to approximately 20% cell death, with no difference observed between cell lines and subcellular regimes ($p > 0.05$). In other words, when comparing the results with 5-ALA groups, 20% of cell death caused by mitochondrial and whole cell treatment was attributed to the laser effect, which agrees with the observed 20% cell death from the nucleus-only treatment in the 5-ALA group. The relationships between different treatment regimes are described and summarized in **Table 6.2**.

Table 6.2 The difference in cell viability between treatment regimes using 1-photon PDT (5.92 J/cm^2)

Comparison	Viability		Notes
CPA to PpIX	$CPA_{PpIX\text{-}Whole}$ 59%	$CPA_{control\text{-}whole}$ 79%	-20% due to CPA responses to PpIX[1]
	$CPA_{PpIX\text{-}mito}$ 74%	$CPA_{PpIX\text{-}nucleus}$ 77%	-3% (PpIX was partially activated)[2]
CPB to PpIX	$CPB_{PpIX\text{-}Whole}$ 8%	$CPB_{control\text{-}whole}$ 82%	-74% due to CPB responses to PpIX[3]
	$CPB_{PpIX\text{-}mito}$ 37%	$CPB_{PpIX\text{-}nucleus}$ 72%	-35% (PpIX was partially activated)[4]
Cell sensitivity	$CPB_{PpIX\text{-}whole}$ 8%	$CPA_{PpIX\text{-}whole}$ 59%	CP-B are more sensitive to treatment[5]
	$CPB_{PpIX\text{-}mito}$ 37%	$CPA_{PpIX\text{-}mito}$ 74%	CP-B are more sensitive to treatment[6]
Cell to light fluence	$CPA_{control\text{-}nucleus}$ 75%	$CPA_{PpIX\text{-}nucleus}$ 77%	Laser effect dominates[7]
	$CPB_{control\text{-}whole}$ 82%	$CPA_{control\text{-}whole}$ 79%	Equivalent response to laser fluence[8]

$^{(1\text{-}8)}$ subscript numbers in the table correspond to the item numbers discussed in the main text

As demonstrated in **Fig. 6.4** and **Fig. 6.5**, the dose response curves were also collected using two-photon irradiation. The relationships between different treatment regimes are described and summarized in **Table 6.3**. It was noted that the dose response curves were consistent with the results obtained from one-photon treatment, where CP-B cells were more susceptible to PpIX phototoxicity. In addition, because the focal volume of two-photon irradiation is much smaller than one-photon irradiation, the difference in viability of CP-B caused by PpIX was observed to be smaller than it was with one-photon treatment, as summarized in items 3 and 4 of **Table 6.2**. This was consistent with one-photon treatments for 5-ALA stained HGD showing better efficacy than 2-photon treatment, as observed in **Fig. 6.2** and **Fig. 6.4** ($p < 0.05$). CP-A cells showed similar viability between one- and two-photon regimes, which could be attributable to less intracellular PpIX concentration or more resistance to the photosensitizing toxicity.

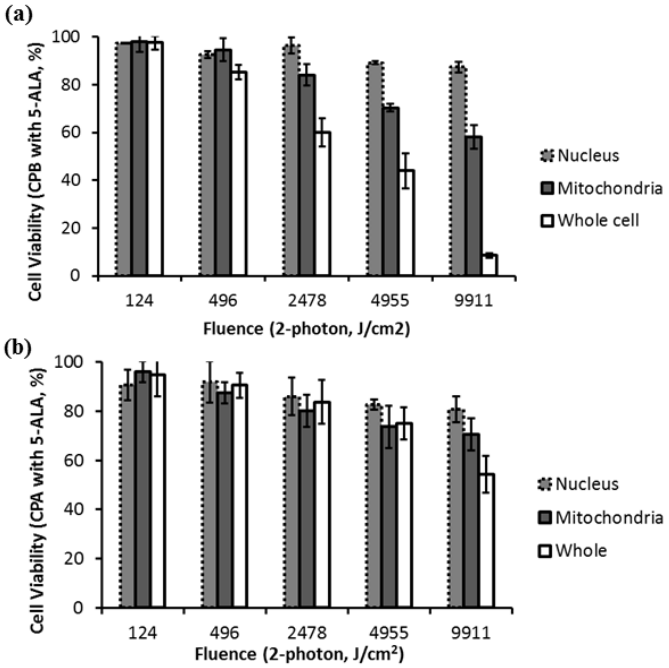

Figure 6.4 (a) HGD and (b) metaplasia cells after various subcellular treatment regimes were plotted against five fluence levels operating at 810 nm, ranging from the dose for imaging acquisition (124 J/cm^2) to 9911 J/cm^2.

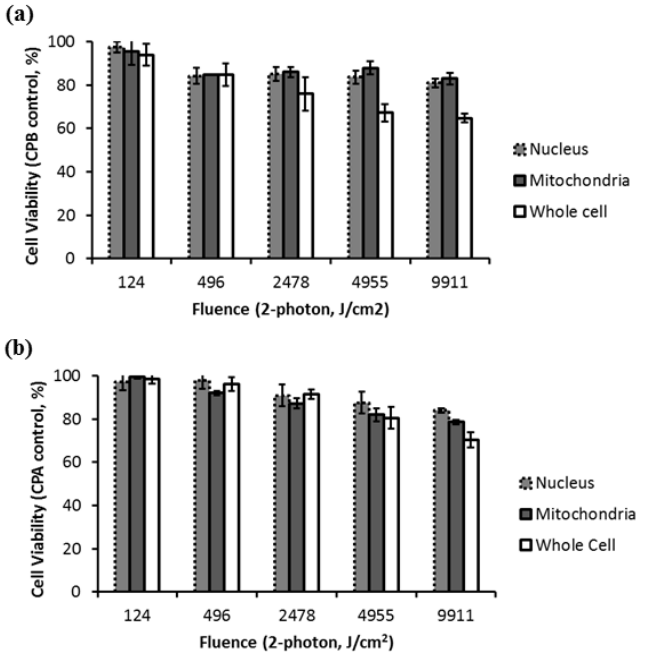

Figure 6.5 (a) Non-stained HGD and (b) metaplasia cells after various subcellular treatment regimes were plotted against five fluence levels operating at 810 nm.

Table 6.3 The difference in cell viability between treatment regimes using 2-photon PDT (9911 J/cm^2)

Comparison	Viability		Notes
CPA to PpIX	$CPA_{PpIX\text{-}Whole}$ 54%	$CPA_{control\text{-}whole}$ 70%	-16% due to CPA responses to PpIX[1]
	$CPA_{PpIX\text{-}mito}$ 71%	$CPA_{PpIX\text{-}nucleus}$ 81%	-10% (PpIX was partially activated)[2]
CPB to PpIX	$CPB_{PpIX\text{-}Whole}$ 9%	$CPB_{control\text{-}whole}$ 65%	-54% due to CPB responses to PpIX[3]
	$CPB_{PpIX\text{-}mito}$ 58%	$CPB_{PpIX\text{-}nucleus}$ 87%	-29% (PpIX was partially activated)[4]
Cell sensitivity	$CPB_{PpIX\text{-}whole}$ 9%	$CPA_{PpIX\text{-}whole}$ 54%	CP-B are more sensitive to treatment[5]
	$CPB_{PpIX\text{-}mito}$ 58%	$CPA_{PpIX\text{-}mito}$ 71%	CP-B are more sensitive to treatment[6]
Cell to light fluence	$CPA_{control\text{-}nucleus}$ 81%	$CPA_{PpIX\text{-}nucleus}$ 84%	Laser effect dominates[7]
	$CPB_{control\text{-}whole}$ 70%	$CPA_{control\text{-}whole}$ 66%	Equivalent response to laser fluence[8]

(1- 8) subscript numbers in the table correspond to the item numbers discussed in the main text

6.4. Discussion

In this study, subcellular irradiation of two Barrett's esophagus cell lines were investigated as a potential *in vitro* model for "seek and treat" of esophageal dysplasia. It has also been demonstrated that intracellular PpIX could serve as a contrast agent to highlight both types of esophageal cells (**Fig. 6.1**), while acting as a photosensitizer for selective treatment (**Fig. 6.2** and **6.4**). Imaging processing and classification has been performed in co-culture model (**Chapter 5**). The specific PDT efficacy achieved by subcellular irradiation was also characterized and correlated with the relative amount of intracellular PpIX activation and the light fluence applied to the cells. Using confocal fluorescence images of these cells, we found both CP-B and CP-A cells achieved their maximum PpIX formation at mitochondria within 5 to 6 hours, while the dysplastic cells (CP-B) demonstrated faster PpIX production than the metaplastic cells (CP-A), especially at 3 hours of incubation (data presented in **Chapter 5**). Treatment was given and characterized at an earlier time frame (3 hours); therefore, even a false positive of detection occurs, it may not be harmful for the falsely treated metaplastic cells.

Correlating the discrepancy of intracellular PpIX to treatment efficacy, CP-B cells were found to be more susceptible to PpIX activation when different light fluence and subcellular treatment regimens were given. In contrast, both non-stained cell lines were observed to demonstrate similar viability when the same fluence was applied. According to the results from **Fig. 6.2** to **Fig. 6.5**, comparison between groups and the corresponding explanations were summarized in **Table 6.2**. It is clear that the viability reduction between the 5-ALA groups and control (non-stained) groups was solely due to the photosensitizing effects from PpIX. This conclusion is further supported when comparing the viability between the nucleus treatment and mitochondrial treatment because nucleus treatment irradiated the part "without PpIX". As shown in **Table 6.2** from items 1 – 4 of one-photon irradiation, it was observed that CP-B cells demonstrated 51% lower viability than CP-A cells after PpIX activation. This was consistent with the comparison between 5-ALA incubated CP-A and CP-B cells with whole cell and mitochondrial irradiation (items 5 and 6 in **Table 6.2**). Although cell death was attributed to both photothermal and photochemical interactions, an additional 50% decrease in CP-B viability compared to CP-A cells may have been related to the discrepancy in intracellular PpIX intensity, where approximately 50% more PpIX intensity was observed in CP-B cells at 3 hours of incubation (data presented in **Chapter 5**). It should be noted that the difference in survival rate can also be affected by the intrinsic PDT resistance and sensitivity of CP-A and CP-B, respectively. However, CP-B viability is comparable to the previous 5-ALA based cell study in well-oxygenated environment. [31] Furthermore, equivalent cell responses to laser irradiation were found to be consistent between group comparisons as shown in items 7 – 8 of **Table 6.2**. The nucleus treatment on 5-ALA and non-stained groups caused no difference in viability, and the whole cell treatment between both no-drug controls also led to less than 5% difference in viability. **Table 6.3** summarizes the results from two-photon PDT, which are similar to the one-photon irradiations except that the CP-B was less susceptible to the treatment, as PpIX was activated less efficiently. For instance, in items 1 and 3 of **Table 6.3**, CP-B only yielded approximately 40% decrease in viability when compared to CP-A (16 % vs. 54 %), which could also be partly attributed to the discrepancy of intracellular PpIX (23%, data presented in **Chapter 5**) and the intrinsic cell responses. The biological (cytotoxic) effect that is linearly proportional to the photosensitizer concentration was also in agreement with previous fluorescence-based studies on pharmacokinetics and localization of PpIX accumulation *in vivo*. In those studies, the PDT induced necrosis was significantly greater than in the control group and the intra-tissue PpIX fluorescence was correlated with the tissue damage after treatment. [32,33]

When comparing whole cell treatment to mitochondrial treatment on 5-ALA stained cells, it is necessary to account for the ratio of the photosensitized areas because only a partial activation was used in mitochondrial treatment. We compared the ratio of activated area and the corresponding changes in cell

survival rate to obtain a more valid comparison of the two subcellular regimes. **Table 6.4** showed the calculated values and standard deviation measured from multiple regions of interest, suggesting that both whole cell and partial mitochondrial treatment achieved comparable PDT efficacy although the whole cell treatment resulted in a lower survival rate due to additional energy deposition. Moreover, according to the treatment efficacy measured from single-plane one-photon (~0.8 micron in thickness) and two-photon (up to 0.5 micron in thickness [34]) subcellular treatment at the fluence range, it is straightforward to come up with an assumption that one-photon excitation demonstrated a better killing efficacy as more PpIX along the light path was excited to induce the phototoxic effect. However, it should be noted that the photosensitizing effect would not be proportional to the fluence if the fluence rate applied to the sample depleted the ground state photosensitizers. The fluence rates used in this study were up to 0.12 W/cm^2 in one-photon treatment, which have negligible depletion effects on ground state photosensitizers in either high or low oxygen condition. [35] On the other hand, two-photon excitation with the fluence rate of 96.8 W/cm^2 exceeded the reported limit, thus it was possible that the ground state photosensitizer was depleted during the treatment. [35]

Table 6.4 Scaling factors for whole cell and mitochondrial treatment

Groups	**Fractional Area (Partial / Total Activation of PpIX)**	***Fractional Changes in Survival Rate**
One-photon excitation	**45 ± 11%	47 % ± 4 %
Two-photon exciation		54 % ± 11%

* Calculated using the ratios of item 4 to item 3 (Table 6.2 and 6.3, values in "notes"). **Calculation from a single plane. The one-photon excitation volume will be further affected by the sample thickness.

Propidium iodide was used as a necrotic stain to quantify cell death a short period of time after irradiation (2 hours). It has been reported that apoptosis could be the main biological effect induced by PDT, while it depends on the cell types, overall doses, *etc*; [36,37] As the cell morphological features shown in **Fig. 6.6**, cells tended to demonstrate a necrotic cell death within 2 hours after exposure to a high fluence. This phenomenon could be the consequence of PpIX induced oxidative stress [38]. This agreed with a previous report that oxidative stress induced necrosis happens shortly after irradiation; the affected cells change morphology in less than one hour and go through necrosis within two hours. [39]

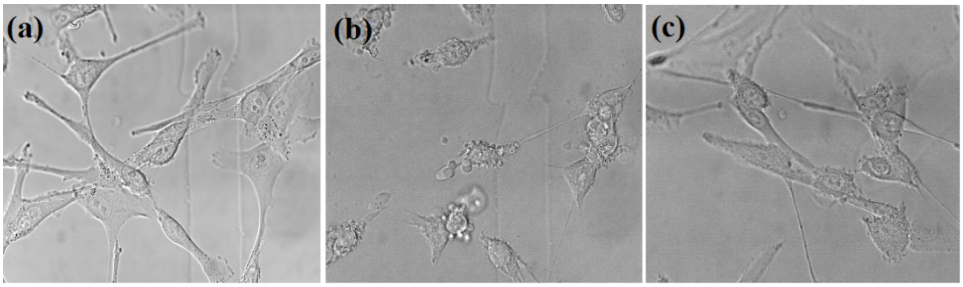

Figure 6.6 Sample bright field images of 5-ALA loaded CP-B cells seeded on the glass-bottom dishes after exposed to various treatment regimes. (a) Cells remained the same morphology after exposed to the fluence level of imaging acquisition, suggesting a negligible adverse effect at this light dose (b) CP-B cells were observed to exhibit necrotic cell death at 2 hours after whole cell irradiation with the fluence of 5.92 J/cm^2; (c) Nucleus treatment on the 5-ALA loaded cells did not induce significant cell death when the mitochondria-localized PpIX was not activated.

6.5. Conclusion

In conclusion, the pre-malignant Barrett's esophagus cell lines provide a platform to investigate detection and treatment strategies using a PDT photosensitizer. In addition to the distinct morphological patterns revealed by PpIX fluorescence imaging, this study demonstrated potential subcellular treatment strategies and their corresponding efficacies for cellular-based PDT, which will be an important component in real-time integrated detection and treatment of Barrett's esophagus using endomicroscopic technology. Our results demonstrated that HGD cells were less viable than metaplastic cells after PDT due to increased accumulation of PpIX at earlier times. More importantly, whole cell and mitochondrial treatment induced comparable PDT effect while nucleus irradiation only exhibited little phototoxicity. With the aid of automatic detection, this indicates that appropriately-targeted irradiation schemes directed at mitochondria may further enhance treatment selectivity without introducing excessive phototoxicity for non-HGD cells. Verifying these strategies in a co-culture platform and three dimensional cell cultures will be the logical next step complementary to quantitative imaging processing and classification.

References

1. S. J. Spechler, "The Natural History of Dysplasia and Cancer in Barrett's Esophagus," J. Clin. Gastroenterol. **36**, 2–5 (2003).

2. C. J. Kelty, S. L. Marcus, and R. Ackroyd, "Photodynamic therapy for Barrett's esophagus: a review," Dis. Esophagus **15**, 137–144 (2002).

3. J. Rees, P. Lao-Sirieix, A. Wong, and R. Fitzgerald, "Treatment for Barrett's oesophagus (Review)," in *The Cochrane Collaboration* (John Wiley & Sons, Ltd, Etobicoke, 2011).

4. B. C. Wilson, "Detection and treatment of dysplasia in Barrett's esophagus: a pivotal challenge in translating biophotonics from bench to bedside.," J. Biomed. Opt. **12**, 051401 (2007).

5. R. E. Sampliner, B. Fennerty, and H. S. Garewal, "Reversal of Barrett's esophagus with acid suppression and multipolar electrocoagulation: preliminary results," Gastrointest. Endosc. **44**, 532–535 (1996).

6. G. S. Dulai, D. M. Jensen, G. Cortina, L. Fontana, and A. Ippoliti, "Randomized trial of argon plasma coagulation vs. multipolar electrocoagulation for ablation of Barrett's esophagus," Gastrointest. Endosc. **61**, 232–240 (2005).

7. A. Larghi, C. J. Lightdale, L. Memeo, and G. Bhagat, "EUS followed by EMR for staging of high-grade dysplasia and early cancer in Barrett's esophagus," **62**, (2005).

8. P. K. Nijhawan and K. K. Wang, "Endoscopic mucosal resection for lesions with endoscopic features suggestive of malignancy and high-grade dysplasia within Barrett's esophagus.," Gastrointest. Endosc. **52**, 328–32 (2000).

9. D. Mitton and R. Ackroyd, "Photodynamic therapy in oesophageal carcinoma : an overview A brief history of photodynamic therapy," Photochem. Photobiol. Sci. **3**, 839–850 (2004).

10. C. J. Kelty, N. J. Brown, M. W. R. Reed, and R. Ackroyd, "The use of 5-aminolaevulinic acid as a photosensitiser in photodynamic therapy and photodiagnosis," Photochem. Photobiol. Sci. **1**, 158–168 (2002).

11. P. Hinnen, F. W. M. De Rooij, W. C. J. Hop, A. Edixhoven, H. Van Dekken, J. H. P. Wilson, and P. D. Siersema, "Timing of 5-aminolaevulinic acid-induced photodynamic therapy for the treatment of patients with Barrett's oesophagus," J. Photochem. Photobiol. B Biol. **68**, 8–14 (2002).

12. T. D. Wang and J. Van Dam, "Optical biopsy: a new frontier in endoscopic detection and diagnosis.," Clin. Gastroenterol. Hepatol. **2**, 744–53 (2004).

13. R. Kiesslich, L. Gossner, M. Goetz, A. Dahlmann, M. Vieth, M. Stolte, A. Hoffman, M. Jung, B. Nafe, P. R. Galle, and M. F. Neurath, "In vivo histology of Barrett's esophagus and associated neoplasia by confocal laser endomicroscopy.," Clin. Gastroenterol. Hepatol. **4**, 979–87 (2006).

14. M. A. Kara, R. S. DaCosta, C. J. Streutker, N. E. Marcon, J. J. G. H. M. Bergman, and B. C. Wilson, "Characterization of tissue autofluorescence in Barrett's

esophagus by confocal fluorescence microscopy.," Dis. Esophagus **20**, 141–50 (2007).

15. J. A. Russell, K. R. Diamond, T. J. Collins, H. F. Tiedje, J. E. Hayward, T. J. Farrell, M. S. Patterson, and Q. Fang, "Characterization of fluorescence lifetime of Photofrin and delta-aminolevulinic acid induced protoporphyrin IX in living cells using single and two-photon excitation," IEEE J. Quantum Electron. **14**, 158–166 (2008).

16. A. Ruck, C. Hulshoff, I.Kinzler, W. Becker, and R. Steiner, "SLIM : A new method for molecular imaging," Microsc. Res. Tech. **70**, 485–492 (2007).

17. M. C. A. Palanca-Wessels, A. Klingelhutz, B. J. Reid, T. H. Norwood, K. E. Opheim, T. G. Paulson, Z. Feng, and P. S. Rabinovitch, "Extended lifespan of Barrett's esophagus epithelium transduced with the human telomerase catalytic subunit: a useful in vitro model.," Carcinogenesis **24**, 1183–90 (2003).

18. R. E. Kosoff, K. L. Gardiner, L. M. F. Merlo, K. Pavlov, A. K. Rustgi, and C. C. Maley, "Development and characterization of an organotypic model of Barrett's esophagus.," J. Cell. Physiol. **227**, 2654–9 (2012).

19. L. M. F. Merlo, R. E. Kosoff, K. L. Gardiner, and C. C. Maley, "An in vitro co-culture model of esophageal cells identifies ascorbic acid as a modulator of cell competition.," BMC Cancer **11**, 461 – 471 (2011).

20. K. B. Dunbar, P. Okolo, E. Montgomery, and M. I. Canto, "Confocal laser endomicroscopy in Barrett's esophagus and endoscopically inapparent Barrett's neoplasia: a prospective, randomized, double-blind, controlled, crossover trial.," Gastrointest. Endosc. **70**, 645–54 (2009).

21. M. I. Canto, "Endomicroscopy of Barrett's Esophagus.," Gastroenterol. Clin. North Am. **39**, 759–69 (2010).

22. P. Hinnen, "Biochemical aspects of ALA-PDT basic mechanisms and optimization for the treatment of Barrett's oesophagus," Erasmus University Rotterdam, Retrieved from http://hdl.handle.net/1765/22851 (2001).

23. J. C. Kennedy, R. H. Pottier, and D. C. Pross, "Photodynamic therapy with endogenous protoporphyrin IX: basic principles and present clinical experience.," J. Photochem. Photobiol. B. **6**, 143–8 (1990).

24. P. E. Claydon and R. Ackroyd, "5-Aminolaevulinic acid-induced photodynamic therapy and photodetection in Barrett's esophagus," Dis. Esophagus **17**, 205–212 (2004).

25. C. J. Kelty, R. Ackroyd, N. J. Brown, S. B. Brown, and M. W. R. Reed, "Comparison of high- vs low-dose 5-aminolevulinic acid for photodynamic therapy of Barrett's esophagus.," Surg. Endosc. **18**, 452–8 (2004).

26. R. Ackroyd, N. Brown, D. Vernon, D. Roberts, T. Stephenson, S. Marcus, C. Stoddardl, and M. Reed, "5-aminolevulinic acid photosensitization of dysplastic Barrett's esophagus: a pharmacokinetic study," Photochem Photobiol. **70**, 656–662 (1999).

27. C. J. Kelty, R. Ackroyd, N. J. Brown, T. J. Stephenson, C. J. Stoddard, and M. W. R. Reed, "Endoscopic ablation of Barrett's oesophagus: a randomized-controlled trial of photodynamic therapy vs. argon plasma coagulation.," Aliment. Pharmacol. Ther. **20**, 1289–96 (2004).

28. R. L. P. van Veen, M. C. G. Aalders, K. L. Pasma, P. D. Siersema, J. Haringsma, W. van de Vrie, E. E. E. Gabeler, D. J. Robinson, and H. J. C. M. Sterenborg, "In situ light dosimetry during photodynamic therapy of Barrett's esophagus with 5-aminolevulinic acid.," Lasers Surg. Med. **31**, 299–304 (2002).

29. H. C. Wolfsen, "Present Status of Photodynamic Therapy for High-Grade Dysplasia in Barrett's Esophagus," J. Clin. Gastroenterol. **39**, 189–202 (2005).

30. M. C. Palanca-Wessels, M. T. Barrett, P. C. Galipeau, K. L. Rohrer, B. J. Reid, and P. S. Rabinovitch, "Genetic analysis of long-term Barrett's esophagus epithelial cultures exhibiting cytogenetic and ploidy abnormalities," Gastroenterology **114**, 295–304 (1998).

31. J. S. Dysart and M. S. Patterson, "Photobleaching kinetics, photoproduct formation, and dose estimation during ALA induced PpIX PDT of MLL cells under well oxygenated and hypoxic conditions.," Photochem. Photobiol. Sci. **5**, 73–81 (2006).

32. A. Johansson, G. Palte, O. Schnell, J.-C. Tonn, J. Herms, and H. Stepp, "5-Aminolevulinic acid-induced protoporphyrin IX levels in tissue of human malignant brain tumors.," Photochem. Photobiol. **86**, 1373–8 (2010).

33. A. Kim, M. Brantsch, C. Niu, Z. B. Moses, P. A. Valde, D. Tosteson, B. C. Wilson, K. D. Paulsen, D. W. Roberts, and B. T. Harris, "5-aminolevulinic acid-induced protoporphyrin IX concentration correlates with histopathologic markers of malignancy regions of increasing malignancy," **13**, 846–856 (2011).

34. W. R. Zipfel, R. M. Williams, and W. W. Webb, "Nonlinear magic: multiphoton microscopy in the biosciences.," Nat. Biotechnol. **21**, 1369–77 (2003).

35. M. A. Weston and M. S. Patterson, "Monitoring oxygen concentration during photodynamic therapy using prompt photosensitizer fluorescence.," Phys. Med. Biol. **58**, 7039–59 (2013).

36. D. Kessel, Y. Luo, Y. Deng, and C. K. Chang, "The role of subcellular localization in initiation of apoptosis by photodynamic therapy.," Photochem. Photobiol. **65**, 422–6 (1997).

37. N. L. Oleinick, R. L. Morris, and I. Belichenko, "The role of apoptosis in response to photodynamic therapy: what, where, why, and how," Photochem. Photobiol. Sci. **1**, 1–21 (2002).

38. C. H. Kim, C.-W. Chung, K. H. Choi, J.-J. Yoo, D. H. Kim, Y.-I. Jeong, and D. H. Kang, "Effect of 5-aminolevulinic acid-based photodynamic therapy via reactive oxygen species in human cholangiocarcinoma cells.," Int. J. Nanomedicine **6**, 1357–63 (2011).

39. T. Vanden Berghe, N. Vanlangenakker, E. Parthoens, W. Deckers, M. Devos, N. Festjens, C. J. Guerin, U. T. Brunk, W. Declercq, and P. Vandenabeele, "Necroptosis, necrosis and secondary necrosis converge on similar cellular disintegration features.," Cell Death Differ. **17**, 922–30 (2009).

Chapter 7.

Conclusions and future work

7.1. Summary

Fluorescence of PDT photosensitizers has been an important tool in PDT drug monitoring and dosimetry [1–5], and also provides certain contrast for visual determination of neoplastic margins [6–9] . In this dissertation, we use the fluorescence of photosensitizers, and investigate two potential clinical applications – (i) PDT dosimetry, and (ii) integrated detection and treatment of Barrett's Esophagus (BE).

As for PDT dosimetry, we provided a review of TRF studies associated with PDT photosensitizers, and specified certain challenges and advancement to date. The goal of this review is to help people in the field grasp the current status of TRF-PDT, and bring up research questions and logical next steps for clinical translation. Experimental validation was also performed *in vitro* to study fluorescence lifetime changes of photosensitizers when going through various drug-molecular bindings during uptake processes. It is interesting to see that the fluorescence lifetimes measured in subcellular organelles correspond well to various contributions from molecular binding, photoproducts, and aggregate formation. This study also showed the potential effect of photobleaching of monomers when longer exposure time was used. In addition to experimental validation, we also studied one of the challenges rising from time-domain TRF techniques, where the measured TRF parameters can be distorted when long-lived fluorophores (*e.g.*) are used. An appropriate correction based on the proposed analytical solutions enables more accurate estimation of the measured results. Overall, it is important to note that TRF studies up to date still lack correlation between TRF measurements and treatment effects, which is actually the most important consideration when proposing TRF as a tool for dosimetry; therefore, we will further discuss about this issue in **Section 7.2.1**.

Another application is based on the subcellular "location" of fluorescent photosensitizers. Mitochondrial targeting of 5-ALA induced PpIX provides a unique advantage: being a nucleus contrast without inducing DNA mutation. The nucleus pattern is essential in histopathological analysis when diagnosing Barrett's Esophagus, a pre-cancerous lesion of esophageal adenocarcinoma. Hence, the nucleus pattern is also one of the desired features when people are developing diagnostic tools using optical biopsy. We take advantage of the fluorescence contrast provided by PpIX to acquire morphological and textural features of cells. With the help of statistical classification using support vector machines (SVM), it is possible to achieve more robust detection of high-grade dysplasia (HGD) compared to existing optical biopsy approaches. We also characterized the potential toxicity and treatment effects given by PpIX in an attempt to provide well characterized treatment regimens when using PpIX as a contrast agent. Integrated detection and treatment is then feasible using confocal endomicroscopy, which enables a more precise management of the lesion. The purpose of current studies is to examine the feasibility of the concept. Going back to the topic of clinical translation, significant efforts should be put, including the employment of larger sample population into experimental models closer to real situation, and real-time detection algorithms. We will discuss about these issues and potential future work in **Section 7.2.2**.

Overall, this thesis reports two applications using fluorescence of photosensitizers. These are valuable as they serve as feasibility studies for proof-of-concept, and may eventually enhance the overall cancer detection and treatment accuracy noninvasively. In **section 7.2,** we discuss about potential challenges, ongoing studies and future work of these two applications.

7.2. Discussions and future work

7.2.1. TRF for PDT dosimetry

As discussions associated with each paper (**Chapter 2 - 4**) have been included in individual chapters, here we focus on the discussion about certain underlying questions when using TRF for PDT dosimetry. A straightforward question coming from TRF for PDT dosimetry is: What is the actual relationship between the measured TRF components and treatment effects? In other words, is there a unique TRF element that can be directly correlated to treatment progress? There are two potential parameters that can be employed from TRF measurements, including contributions of various components, and the drug-molecular binding conditions. For example, there may be fractional changes of each time-resolved component (*e.g.* photosensitizer monomer, photoproducts, autofluorescence, *etc*.) during the cellular uptake or treatment progress, and these changes could be further correlated to the final treatment efficacy. This can be seen in **Chapter 3**

that shows significant changes in photosensitizer contribution (coefficients of τ_2) during cellular uptake, corresponding to more drug-molecular interactions and photoproducts. Correlation between TRF parameters and cell viability will be a logical next step for **Chapter 3**. In fact, it may be possible to use just one parameter, "averaged fluorescence lifetime" that can be calculated based on individual lifetime and coefficient [10], and correlate it with tissue responses, so that one parameter can represent all. As the averaged value is from proportional changes of several lifetime components in biological environment, including changes of photosensitizers, autofluorescence, and physiological conditions, there may not be such a specific element whose decay alone would correspond to the treatment final effect. Correlating the measured TRF parameters with treatment effects will require more experimental validation either *ex vivo* or *in vivo*.

Studies to date, although mostly *in vitro* and do not provide a systemic connection between measurements and treatment outcome, fluorescence lifetimes of specific components have been well characterized in cellular environment. Therefore, these studies can be helpful for future TRF-PDT studies to interpret the results. For example, dose interdependencies have been considered as important variables during PDT dynamics, as stated in **Chapter 2**. Previous studies have shown that TRF is able to reflect these interdependencies, including vascular responses that affect perfusion and oxygen supply, O2 depletion from photosensitizers or high fluence, photosensitizer depletion and photobleaching from high fluence, and uptake variation. We discussed about the effects of uptake variation and photosensitizer depletion on lifetime estimation *in vitro* in **section. 2.3.1**, and also summarized potential fluorescence lifetime components existing in cells. These factors are further validated in **Chapter 3** that studies TRF changes during cellular uptake of Photofrin® in a prostate cancer cell line. In **section 2.3.2,** we also reviewed the potential effects from oxygen depletion and vascular responses *in vivo*. So far, there is no quantitative data verifying how each *in vivo* variable affects the measured TRF lifetime and coefficients; however, this analysis should be an ongoing direction along with the development of robust data analysis and time-resolved fluorescence tomography.

Moreover, when TRF is used for dosimetry, what guidelines should be used to constitute an "optimal dose"? Several indicators should be taken into account to constitute an optimal dose using TRF, including cellular responses (necrosis/apoptosis), and vascular responses. It is noted that apoptosis and necrosis can start in a time frame of 1 to 4 hours, but vascular responses can happen within 15- 30 minutes that causes insufficient supply of oxygen. In other words, TRF may be able to probe the effect of oxygen during the treatment; however, cellular responses (apoptosis/necrosis) should be correlated with some "real time" indicators such as singlet oxygen quenching effect, photoproduct formation, binding to targeted molecules, and mitochondrial function. As mentioned in previous paragraphs, these correlations are logical next steps and will need to be verified *in vivo*. Moving forwards, how does TRF information

avoid overdose and underdose? Overdose could be a relatively minor problem in cancer treatment when compared to underdose, although it is critical in certain applications such as brain tumor. However, the overdose problem is not only caused by the PDT dose factors and interdependencies, but also caused by intrinsic tumor selectivity of photosensitizers. For example, both Photofrin® and 5-ALA-PpIX have been reported to also stain normal tissue to some extent [11,12], which may yield inaccurate tumor margins and potential collateral damages. This will require the use of more selective photosensitizers, or computer-aided diagnostic criteria and other features that are independent of fluorescence intensity. The latter option is also the motivation of **Chapter 5** (though a different application), and one of the reasons to use intensity-independent TRF measurements. On the contrary, underdose is critical in cancer management. Underdose could be associated with depletion of effective photosensitizers. This leads to the reduced contribution of photosensitizer monomers, and can reduce the averaged fluorescence lifetime significantly while the steady-state intensity may not change much due to spectral overlap between the photosensitizer and its photoproducts. It is noted that photobleaching, the decrease of fluorescence intensity, can be due to more amount of cytotoxic oxygen species, indicating greater treatment effect in aerobic conditions. In other words, the combination of TRF and intensity parameters can be helpful to delineate the results. Another factor leading to underdose is the depletion of oxygen or insufficient oxygen supply. This actually could lead to increase of photosensitizer lifetime, and less quenching of fluorescence intensity. However, it is not clearly known/studied so far that how prominent oxygen quenching can affect the average lifetime, and which lifetime component can be used to account for this effect. Advancement in data analysis and more *in vivo* validation would be valuable to investigate this issue. Overall, it is true that *in vitro* results may not be carried completely towards *in vivo* measurements as there is whole lot more complexity present *in vivo*. However, well controlled *in vitro* experiments are able to study most of variants in biological environment that potentially affect the measured TRF parameters, and this is valuable information when delineating *in vivo* results in the next step.

Eventually, how would TRF be employed clinically and what are the challenges in terms of clinical translation? Potential challenges and ongoing studies include the capability of accurate and robust multi-exponential analysis for TRF data of low SNR, and the need of appropriate modeling and reconstruction of tomographic maps. Taking data analysis as an example, an inverse model was proposed to correct the measured TRF parameters (**Chapter 4**), but we only focused on bi-exponential analysis, which may not be sufficient in practice. To date, estimation of multiple exponential component beyond bi-exponential decay is difficult and usually with large estimation error. Nonetheless, the forward analytical model and the inverse model are generally applicable to more than bi-exponential decay. In general, improvement in data analysis and tomographic

modeling helps explain relative contributions, location, and changes of multiple fluorophores, which render a list of dosimetric indicators described in **Table 2.5**, including cell function, photosensitizer and oxygen status, and drug-molecular bindings.

In addition to improvement in "reliability" in data analysis, there are two advancements for potential clinical translation. The first one is FLIM endoscopy, which enables data acquisition of gastrointestinal tract – one of clinical indications of Photofrin®. Another one is hyperspectral TRF, which further deals with problems of multiple fluorophores in a biological system. Hyperspectral TRF provides more thorough information, but for sure, significant effort is required for reduction of data dimension, feature extraction, and final data interpretation in terms of PDT dosimetry. In conclusion, these are feasible requirements to bring TRF towards clinical applications, and therefore research in this field is still under development for two-photon endoscopy [13–15], hyperspectral TRF [16], TRF data analysis [17,18], and TRF tomography [19,20].

7.2.2. Integrated diagnosis and treatment for BE

To study the feasibility of using photosensitizers for integrated detection and treatment for clinical applications, *in vitro* characterization is a logical first step towards *in vivo* and clinical models. Current work answered certain important research questions at this characterization (*in vitro*) stage. (i) Photosensitizers may not demonstrate sufficient selectivity. In other words, what image features can we use to robustly perform quantitative image processing and detection of HGD? (ii) Photosensitizers produce phototoxicity as well. How to characterize cell responses to this type of new "contrast agent"? When laser ablation or PDT is used, what type of treatment strategy is the most efficient way of cell killing? These questions are answered in **Chapter 5 and 6**. Although performed using low density cell culture, current work is valuable as: (i) we characterized PpIX fluorescence in Barrett's cell lines and studied its morphological and textural features; (ii) the detection is independent of fluorescence intensity. Therefore, it accounts for individual variation of drug uptake that always occurs *in vivo*; (iii) the optimal features obtained from feature selection, including eccentricity (morphological) and intensity contrast (textural), are comparable with histological standards [21]. This combination can also be extended to applications in high-density co-culture; (iv) we characterized cellular responses to PpIX activation and irradiation of various subcellular targets. This is an important complementary aspect for integrated detection and treatment, so that an efficient treatment strategy can be given immediately after detection. All of these demonstrate that it is promising to extend current work for the next stage.

Going beyond current work, a logical next step is to combine detection and treatment with increased sample population (high density cells in high content

screening), 3D cellular culture, or animal studies. It can be an obvious question that fluorescent background or fluence distribution can be changed significantly in 3D models and even worse *in vivo* due to interference from tissue optical properties. One of the advantages of current work is to use PDT photosensitizers as the contrast agent for pattern recognition of HGD region (**Chapter 5**), not to quantify its true intensity. This can be applied to images acquired from confocal microendoscopy, where nucleus patterns can be clearly resolved and processed. In terms of treatment perspectives, **Chapter 6** only studies cellular responses to PDT. Laser ablation was not performed in current work because of the lack of high power lasers on site. However, it is certainly feasible and can also be coupled with fiber optics for endoscopic applications [22,23]. Therefore, it will be valuable to characterize the dose of laser ablation [24] when cells are stained with photosensitizers, as it may provide less collateral damages and offers more predictable cell responses compared to photochemical effects from PDT. Although it may sacrifice a certain portion of benign cells due to the false-positive detection, this damage is actually not that critical when the treatment is performed at the cellular level. With a typical epithelial layer of 500 microns, it is possible to mitigate this challenge by the use of multi-photon illumination to obtain well-sectioned images [25]. Image processing of multi-photon co-culture images using high-density cell culture are currently performed, as shown in the discussion of **Chapter 5**. So far, we have not proceeded to organotypic models, but z-stack imaging acquisition on high-density co-culture was performed to investigate potential image features for detection, as shown in **Fig. 7.1**. It is clear that the HGD (CP-B) cell line tends to form stratified layers and irregular nucleus morphology compared to single-layered, oval-shaped CP-A nuclei. This agrees well with histological standards as well as the image features obtained from current work (**Chapter 5**). For example, it can be observed that a greater eccentricity in HGD is related to irregular morphological patterns seen in high-density co-culture. In addition, a higher intensity contrast of the whole cell (or less homogeneity) from mitochondrial distribution is still clearly seen in non-HGD (CP-A) cells. Although the original feature combinations still exist, it is still useful to determine boundaries of HGD in real applications. This requires further feature sets describing boundary conditions for the training of SVMs. In addition to morphological and textural features, TRF parameters may potentially provide additional features for classification and treatment monitoring. The rationale is that TRF is dependent on cell metabolism (alteration in autofluorescence) and drug interaction with individual cell lines (alteration in photosensitizer fluorescence).

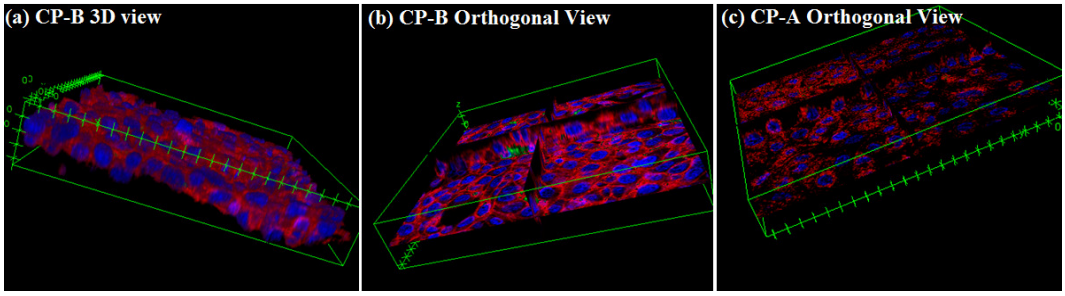

Figure 7.1. 3D representation of CP-A and CP-B cells using image J. Cells were stained with PpIX and Hoechst 33258 to highlight mitochondria and nuclei, respectively. (a) 3D volume (246 µn x 246 µn x 30 µn) of CP-B cells. (b) Orthogonal view of the CP-B volume from 4(a). (c) Orthogonal view of CP-A volume.

7.2.3. Using cellular models for large-scale studies

Overall, characterizing fluorescence of photosensitizers in cellular models is valuable for proof-of-concept in a more controlled experimental setting, as demonstrated in **Chapters 3, 5**, and **6**, but these models suffers from variability rising from complex biological systems. Therefore, once the small-scale experiments verify the research concepts, large sample population is required to yield statistical significance. A possibility to include large sample population using cellular models is the use of high-content screening (HCS), which can be used to acquire high throughput confocal fluorescence and time-resolved fluorescence images [26,27]. HCS utilizes arrayed cells in multi-well plates to build large-scale cell biological studies, and is an automated process from sample preparation, image acquisition, to data archiving. Typically, it allows a throughput of $> 10^6$ cells from each experiment. This is a significant larger amount compared to conventional microscopic imaging of less than a hundred cells per image. The number of cells is further reduced when high magnification objectives are used (*e.g.* a 63X objective lens is used in current work, yielding just tens of cells). The automated process also reduces the experimental variability introduced by manual operation from each repetitive measurement. More importantly, HCS is able to incorporate several experimental variables identified in the small-scale studies to yield more comprehensive results.

Taking TRF studies as an example, the experimental variables include cell lines, types of photosensitizers and PDT reactions, drug concentrations, drug incubation time, oxygenation conditions, light exposure, and so on. Such variables are listed in **Chapter 2**. These parameters are difficult to be systemically examined *in vitro*, and can be complicated by complex microenvironment *in vivo*.

Therefore, before the maturation of TRF data analysis and tomography, HCS could be a good option to investigate these dose variables.

HCS can also be a good transition for the BE project (**Chapters 5 - 6**) before *in vivo* models are available. As mentioned, the logical next step is to combine the detection and treatment in an experiment. HCS allows for large-scale analysis of cell morphology, fluorescence patterns, and additional features such as TRF parameters. Treatment, ideally in laser ablation schemes, can be programmed after detection of HGD cells in co-culture, which yield statistical results of killing rates. Another bonus given by HCS is that cell competition behaviors in co-culture [28] can be more easily studied compared to conventional microscopic techniques. Cell competition in co-culture include changes in proliferation speed, drug uptake rate, and viability of individual cell line, and the competition behaviors could be altered by the original cell density in co-culture [29]. For example, it has been observed that high density BE cell culture (monolayer) exhibits higher PpIX intensity compared to low density cell culture (data not shown).That being said, it is challenging for small-scale experiments to investigate this population effect. Although flow cytometry can provide data from large sample population and has been tried earlier to study cell competition effects (data are not included in the thesis), spatial information provided by HCS is particularly important in the BE project.

7.3. Conclusion

In conclusion, this thesis provided two potential clinical applications by information from fluorescence of photosensitizers. The review and first-stage studies using cellular models are presented in each paper from **Chapters 2 – 6**, and the preliminary results are promising. Ongoing studies such as advancement in instrumentation, data processing, and the development of experimental models make it more feasible for clinical translation.

References

1. K. R. Diamond, M. S. Patterson, and T. J. Farrell, "Quantification of fluorophore concentration in tissue-simulating media by fluorescence measurements with a single optical fiber.," Appl. Opt. **42**, 2436–42 (2003).

2. K. R. Diamond, P. P. Malysz, J. E. Hayward, and M. S. Patterson, "Quantification of fluorophore concentration in vivo using two simple fluorescence-based measurement techniques.," J. Biomed. Opt. **10**, 024007 (2005).

3. J. S. Dysart and M. S. Patterson, "Photobleaching kinetics, photoproduct formation, and dose estimation during ALA induced PpIX PDT of MLL cells under well oxygenated and hypoxic conditions.," Photochem. Photobiol. Sci. **5**, 73–81 (2006).

4. J. S. Dysart and M. S. Patterson, "Characterization of Photofrin photobleaching for singlet oxygen dose estimation during photodynamic therapy of MLL cells in vitro.," Phys. Med. Biol. **50**, 2597–616 (2005).

5. B. C. Wilson, M. S. Patterson, and L. Lilge, "Implicit and explicit dosimetry in photodynamic therapy : a new paradigm," Lasers Med. Sci. **12**, 182–199 (1997).

6. C. J. Kelty, S. L. Marcus, and R. Ackroyd, "Photodynamic therapy for Barrett's esophagus: a review," Dis. Esophagus **15**, 137–144 (2002).

7. W. Stummer, U. Pichlmeier, T. Meinel, O. D. Wiestler, F. Zanella, and H.-J. Reulen, "Fluorescence-guided surgery with 5-aminolevulinic acid for resection of malignant glioma: a randomised controlled multicentre phase III trial.," Lancet Oncol. **7**, 392–401 (2006).

8. P. a Valdés, A. Kim, F. Leblond, O. M. Conde, B. T. Harris, K. D. Paulsen, B. C. Wilson, and D. W. Roberts, "Combined fluorescence and reflectance spectroscopy for in vivo quantification of cancer biomarkers in low- and high-grade glioma surgery.," J. Biomed. Opt. **16**, 116007 (2011).

9. P. J. Muller and B. C. Wilson, "Photodynamic therapy of brain tumors--a work in progress.," Lasers Surg. Med. **38**, 384–9 (2006).

10. J. R. Lakowicz, *Principles of Fluorescence Spectroscopy*, 3rd ed. (Springer, 2006).

11. S. M. Hahn, M. E. Putt, J. Metz, D. B. Shin, E. Rickter, C. Menon, D. Smith, E. Glatstein, D. L. Fraker, and T. M. Busch, "Photofrin uptake in the tumor and normal tissues of patients receiving intraperitoneal photodynamic therapy.," Clin. cancer Res. **12**, 5464–70 (2006).

12. A. Johansson, G. Palte, O. Schnell, J.-C. Tonn, J. Herms, and H. Stepp, "5-Aminolevulinic acid-induced protoporphyrin IX levels in tissue of human malignant brain tumors.," Photochem. Photobiol. **86**, 1373–8 (2010).

13. D. R. Rivera, C. M. Brown, D. G. Ouzounov, W. W. Webb, and C. Xu, "Multifocal multiphoton endoscope.," Opt. Lett. **37**, 1349–51 (2012).

14. K. König, "Clinical multiphoton tomography.," J. Biophotonics **1**, 13–23 (2008).

15. M. C. Skala, K. M. Riching, D. K. Bird, A. Gendron-Fitzpatrick, J. Eickhoff, K. W. Eliceiri, P. J. Keely, and N. Ramanujam, "In vivo multiphoton fluorescence

lifetime imaging of protein-bound and free nicotinamide adenine dinucleotide in normal and precancerous epithelia.," J. Biomed. Opt. **12**, 024014 (2007).

16. Z. Nie, R. An, J. E. Hayward, T. J. Farrell, and Q. Fang, "Hyperspectral fluorescence lifetime imaging for optical biopsy.," J. Biomed. Opt. **18**, 096001 (2013).

17. J. Phipps, Y. Sun, R. Saroufeem, N. Hatami, M. C. Fishbein, and L. Marcu, "Fluorescence lifetime imaging for the characterization of the biochemical composition of atherosclerotic plaques.," J. Biomed. Opt. **16**, 096018 (2011).

18. L. Marcu, "Fluorescence lifetime techniques in medical applications.," Ann. Biomed. Eng. **40**, 304–31 (2012).

19. A. T. N. Kumar, S. B. Raymond, B. J. Bacskai, and D. A. Boas, "Comparison of frequency-domain and time-domain fluorescence lifetime tomography.," Opt. Lett. **33**, 470–2 (2008).

20. R. E. Nothdurft, S. V Patwardhan, W. Akers, Y. Ye, S. Achilefu, and J. P. Culver, "In vivo fluorescence lifetime tomography.," J. Biomed. Opt. **14**, 024004 (2009).

21. J. R. Goldblum, "Barrett's esophagus and Barrett's-related dysplasia.," Mod. Pathol. **16**, 316–24 (2003).

22. A. Uchugonova, M. Lessel, S. Nietzsche, C. Zeitz, K. Jacobs, C. Lemke, and K. König, "Nanosurgery of cells and chromosomes using near-infrared twelve-femtosecond laser pulses.," J. Biomed. Opt. **17**, 101502 (2012).

23. C. L. Hoy, N. J. Durr, P. Chen, W. Piyawattanametha, H. Ra, O. Solgaard, and A. Ben-Yakar, "Miniaturized probe for femtosecond laser microsurgery and two-photon imaging.," Opt. Express **16**, 9996–10005 (2008).

24. A. Vogel and V. Venugopalan, "Mechanisms of pulsed laser ablation of biological tissues.," Chem. Rev. **103**, 577–644 (2003).

25. W. R. Zipfel, R. M. Williams, and W. W. Webb, "Nonlinear magic: multiphoton microscopy in the biosciences.," Nat. Biotechnol. **21**, 1369–77 (2003).

26. V. C. Abraham, D. L. Taylor, and J. R. Haskins, "High content screening applied to large-scale cell biology," Trends Biotechnol. **22**, 15–22 (2004).

27. P. R. Barber, G. P. Pierce, S. M. Ameer-Beg, D. R. Matthews, L. M. Carlin, M. Keppler, M. Kelleher, F. Festy, C. Gillett, R. Springall, T. C. Ng, and B. Vojnovic, "Towards high-throughput FLIM for protein-protein interaction screening of live cells and tissue microarrays," IEEE Int. Symp. Biomed. Imaging 356–359 (2008).

28. L. M. F. Merlo, R. E. Kosoff, K. L. Gardiner, and C. C. Maley, "An in vitro co-culture model of esophageal cells identifies ascorbic acid as a modulator of cell competition.," BMC Cancer **11**, 461 – 471 (2011).

29. Y. Miki, K. Ono, S. Hata, T. Suzuki, H. Kumamoto, and H. Sasano, "The advantages of co-culture over mono cell culture in simulating in vivo environment.," J. Steroid Biochem. Mol. Biol. **131**, 68–75 (2012).